TIP CLEARANCE CONTROL CONCEPTS IN GAS TURBINE H.P. COMPRESSORS

Godwin I. Ekong

A thesis submitted for the degree of Doctor of Philosophy

Department of Engineering and Design, School of Engineering and Informatics

University of Sussex

August 2013

CONTENTS

Declaration

I hereby declare that this thesis has not been submitted, either in the same or different form, to this or any other university for a degree.

Godwin I. Ekong

August 2013

Acknowledgements

I would like to thank Prof. Peter Childs for offering me the study opportunity in the first place. I am indebted to my supervisor Dr Christopher Long for his guidance and support throughout the course of this research. Special thanks to Professor Naser Sayma for his support and encouragement. I would like to express my thanks to my former supervisor Dr. Nick Atkins, for his assistance throughout the various stages of this research. I would like to give my thanks also to Mr. Simon Davies for his assistance in the rig design and to Alan Banks for maintaining my computer in a working state. I would also like to express thanks to all my fellow postgraduates in TFMRC for their support. Thanks also to Rolls-Royce plc NEWAC Team for their help and guidance on the direction of my work.

I would like to express my thanks and gratitude to Akwa Ibom State Government, Nigeria for sponsoring my study. Special thanks to His Exc. Arc (Obong) Victor B. Attah for his vision in the training. My sincere thanks go to Dr. L. O. Asuquo for his support and encouragement. Worthy of thanks are Prof. A. H. Ekpo, Engr. (Prof.) Charles Uko, Mr. P. J. Effiong, Mr. Edem Esara, Hon. Fidelis Ekpo and others for their support and encouragement. Finally, special thanks go to my mother Mrs Afiong Ita Ekong, siblings Grace, Emah, Imoh, Uduak, Gloria spouse Adim, Uncles Mike Emah, Dominic Emah friends Abraham, Attih, Ubong, Idongesit, Unwana, Augustine Ekpo, Mr Ekpo, Mr Ikoedem, Dr. Obotowo, Rev Ekereobong Moses, Nsimah, Joseph and fellow staff for their prayers and support throughout my stay in the United Kingdom.

UNIVERSITY OF SUSSEX

Godwin Ita Ekong **Doctor of Philosophy**

TIP CLEARANCE CONTROL CONCEPTS IN GAS TURBINE H.P. COMPRESSORS

Summary

This thesis describes the development of concept and the evaluation for the reduction and control of tip clearance in HP compressors. The potential method of tip clearance improvement was the reduction in the disc time constant by improving drum heat transfer using radial inflow of air. A passive clearance control scheme was employed in this research. This involves the control of disc and casing thermal response during engine transient by increasing the heat transfer coefficient of the drum. This will speed up the thermal response of the drum hence controlling the clearance between casing and the blade tip during engine transient. A sensitivity analyses were performed to determine the quantitative effect of heat transfer coefficient on the time constant of the disc hence the effect on tip clearance during engine transient in a square cycle using a finite element compressor drum and casing models of RB211 524 and Trent 1000 engines. Measured disc surface temperatures were used to analyse the disc time constant. The results show

that an increase in heat transfer coefficient reduces the drum time constant. It produces a reduction in cruise clearance and impacts positively on compressor operability. The effect was improved significantly with radial inflow injection on the time constant of the disc and hence the effect on tip gap from a transient cycle.

A finite element model of the multiple cavity rig which incorporates a rotor and an inner shaft scaled down from a Rolls Royce Trent aero-engine to a ratio of 0.7:1 was also used to simulate flow conditions in the HP compressor cavity equivalent to the Trent 1000 aero-engine, with a rotational speed of up to 10000 rpm. The idle and maximum take-off conditions in the square cycle correspond to in-cavity rotational Reynolds numbers of $3.1\times10^{6} \leq \mathrm{Re}_{\varphi} \leq 1.0\times10^{7}$. The project involves modelling of radial inflow regimes of 1.6%, 2%, 3%, 4%, and 6% and the use of a lumped parameter model and experimental data to demonstrate proof of concept. The results shows that 6% radial inflow is capable of reducing the cavity disc time constant by approximately 44% during acceleration at high power and 39% during deceleration at low power with a time constant reduction factor of 2 during acceleration and 1.8 during deceleration.

NOMENCLATURE

Symbol	Description	Units
a	Inner radius	[m]
A	Surface area	[m^2]
A_a	Half cone angle	[rad]
A_{an}	Shaft annulus area	[m^2]
A_c	Cross-sectional area of the shroud-cavity	
A_j	Over-shroud cavity has a nozzle of area	
b	outer radius	[m]
C	Conductance	[W/m^2K]
C	Specific heat	[J/ (kgK)]
C_p	Specific heat at constant pressure	[J/kg K]
C_v	Specific heat at constant volume	[J/kg K]
D	Diameter of holes	[m]
E	Young modulus	[N/m^2]
E	Thermal energy	[J]
G	Gab ratio (G = s/b)	
h	Heat transfer coefficient	[W/m^2 K]
H	Vickers micro-harness	[HV]
H	Enthalpy	[J]
k	Harmonic mean conductivity on either side	[N/m]

k	Scaling constant	
k	Thermal conductivity	[W/ (m.K)]
L	Length	[m]
m	Mass	[kg]
$\dot{m}_1$	Leakage flow	
$\dot{m}$	Mass flow rate	[kg/s]
$\dot{m}_{ent}$	Axial entrainment mass flow	
$\dot{m}_j$	Jet flow	
N	Rotational speed	(rad/s)
P	Static pressure	[Pa]
Q	Heat added	[J]
q_x	Heat transfer rate or flux	[W/m^2]
R	Gas constant	J/kg K
r	Independent of the radial position	
ri	Inner radius	[m]
r_m	Pitch circle radius	[m]
ro	Outer radius	[m]
r_s	Shaft radius	[m]
s	Cavity width	[m]
T	Know temperature	[K]
T_1	Inlet or upstream temperature	[K]
T_2	Exit or downstream temperature	[K]
T26	Inlet or upstream temperature	[K]
T30	Exit or downstream temperature	[K]

ΔT	Change in temperature	[K]
T_f	Fluid temperature	[K]
T_s	Surface temperature	[K]
T_R	Temperature of radiator	[K]
T_∞	Bulk temperature	[K]
T_o	Total temperature	[K]
T_{stag}	Stagnation temperature	[K]
U	Internal energy	[J]
V	Volume	[m^3]
V_{act}	The actual volume of n holes	
V_{abs}	Absolute velocity	
v_j	Jet with velocity	
V_{rel}	Relative fluid velocity	
V_{swept}	The swept volume between r_0 and r_i	
W	Stream mass flow rate	[Mg/s]
W	Mean bulk axial velocity of the throughflow	[m/s]
X	Scaling factor	
x	Distance or length	[m]
Δx	Distance in the x-direction	[m]
X_{air}	The fraction of air	
X_{mat}	The fraction of material	
Q_{Grey}	Heat flow rate from a grey body	
d_{tran}	Transient thermal growth of drum	
T_{max}	Drum stage temperature at maximum take off	

T_{stage}	Stage temperature for Idle, MTO and Cruise
αd	Coefficient of thermal expansion for the drum material
$\alpha d_{\text{var}iable}$	Variable coefficient of thermal expansion for the drum material
d_{tran}	Transient thermal growth of drum
C_{tran}	Transient thermal growth of casing

Greek Symbols

α	Coefficient of linear thermal expansion [K^{-1}]
$\alpha_{\max}$	Values of the coefficient of thermal expansion at maximum take off
α_T	Value of the coefficient of thermal expansion with respect to temperature
β	Volume expansion coefficient of the fluid [1/K]
δ	Clearance displacement
δ_c	Casing displacement
δ_{CBC}	Cold build clearance displacement
δ_{close}	Closure displacement
δ_{FHR}	Full hot re-slam displacement
δ_{MAX}	Worst point after maximum take-off point in the cycle
δ_r	Rotor displacement

δ_{th}	Thermal expansion of the drum	
$\delta d_{th\max}$	Drum thermal growth at maximum take off	
Δ	Change	
ε	Emissivity	
γ	Ratio of specific heat	
μ	Dynamic viscosity	[kg/m s]
υ	Kinematic viscosity	[m^2/s]
ω	Angular velocity	[rad/s]
Ω	Rotational speed	[rad/s]
π	Constant	
$\Re$	Universal gas constant	[J/ molK]
ρ	Density	[kg/m^3]
σ	Roughness of the contacting materials	[m]
σ	Stefan Boltzmann constant	[W/m^2K^4]
σ	Ratios of gap to axial chord length at the rotor tip	
τ	Time constant	[s]
ξ_{1-2}	Grey body view factor	

Dimensionless Groups

$Bi = \frac{hL_c}{k}$	Biot Number
$C_{w,out}$	Non-dimensional entrained mass flow rate
$\mathrm{Gr}_X = \frac{g\beta(T_s - T_{ref})X^3}{\nu^2}$	Grashof number
$Nu = \frac{qr}{k\Delta T}$	Local Nusselt number
$\Pr = \frac{\mu C_p}{k}$	Prandtl number

$Ra = Gr.\Pr$	Rayleigh number
$\mathrm{Re}_{\phi} = \frac{\Omega r^2}{\nu}$	Local rotational Reynolds number
$\mathrm{Re}_{z} = \frac{W d_h}{\nu}$	Axial Reynolds number
$\mathrm{Ro} = \frac{\mathrm{W}}{\Omega \mathrm{a}}$	Rossby number

Subscripts

0	Total
an	Annulus
atm	Atmospheric
av	Average
b	bore
ent	Axial entrainment
I	Inner
in	Inlet
o	Outer
out	Outlet
r	Radial
R	Radiator
rad	Radiation
s	Surrounding
s	Shaft
sh	Shroud
ϕ	Tangential
∞	Outside the boundary layer
z	Axial
Ø	Rotational

Acronyms

AC	Alternating current
ACC	Active clearance control
AutoCAD	Automatic computer aided design
CAD	Computer aided design
CBC	Cold Build Clearance
CF	Centrifugal force
CFD	Computational fluid dynamics
CO_2	Carbon (IV) oxide
CZ	Convecting Zones
db	Database
DBD	Dielectric barrier discharge
dbtemp	Database temperature
DDRAM	Design Definition Review and Audit Meeting
DPR	Diagnostic Problem Report
Dred	Design Rationale editor
DSJ	Directed Synthetic Jet
DU	Thermal Ducts
ER	External Radiation
FHRS	Full Hot Re-Slam
FRGEND	Forced convection correlation for rotating flow
GE	General Electric
HP	High pressure
HPC	High pressure compressor
HPT	High pressure turbine
HTML	Hyper Text Markup Language
IGES	Initial Graphics Exchange Specification
IPC	Intermediate pressure compressor
IPT	Intermediate pressure turbine
IR	Internal Radiation
LDA	Laser Doppler Anemometry

LPC	Low pressure compressor
LPT	Low pressure turbine
.mat file	Material file
MCR	Multiple cavity rig
MP	Model point
MTO	Maximum Take-Off conditions
MNUN	Forced convection correlation
NASA	National Aeronautics and Space Administration
NEWAC	NEW Aero Engine Core Concepts
NGV	Nozzle guide vane
NO_x,	Nitrogen oxide
NSJ	Normal Synthetic Jet
NUS	Natural convection correlations for upper surface of plates
NVP	Natural convection correlation for vertical plates or cylinder
PCC	Passive clearance control
RPM	Revolution per minute
SDJ	Steady Directed Jet
SFC	Specific fuel consumption
ST	Thermal Streams
STEP	Standard for the Exchange of Product
TAMB	Atmospheric temperature
TBC	Thermal barrier coating
TFMRC	Thermo-Fluid Mechanics Research Centre
TP	Thickness property
TRIZ	Theory of inventive problem solving
LPT	Low pressure turbine
HPT	High pressure turbine
IPT	Intermediate pressure turbine
US	United States
VO	Thermal Voids

LIST OF FIGURES

LIST OF TABLES

CHAPTER ONE

1. Introduction

A gas turbine engine is an internal combustion engine consisting of a compressor, combustion chamber and a turbine. A typical gas turbine engine used in this study is the Trent 1000 jet engine shown in Figure 1.1. Figure 1.1 shows a cut away diagram of Rolls- Royce Trent 1000 jet engine indicating the different compressor and turbine section of the engine. These are Fan or Low pressure compressor (LPC), Intermediate pressure compressor (IPC), High pressure compressor (HPC), High pressure turbine (HPT), Intermediate pressure turbine (IPT) and Low pressure turbine (LPT).

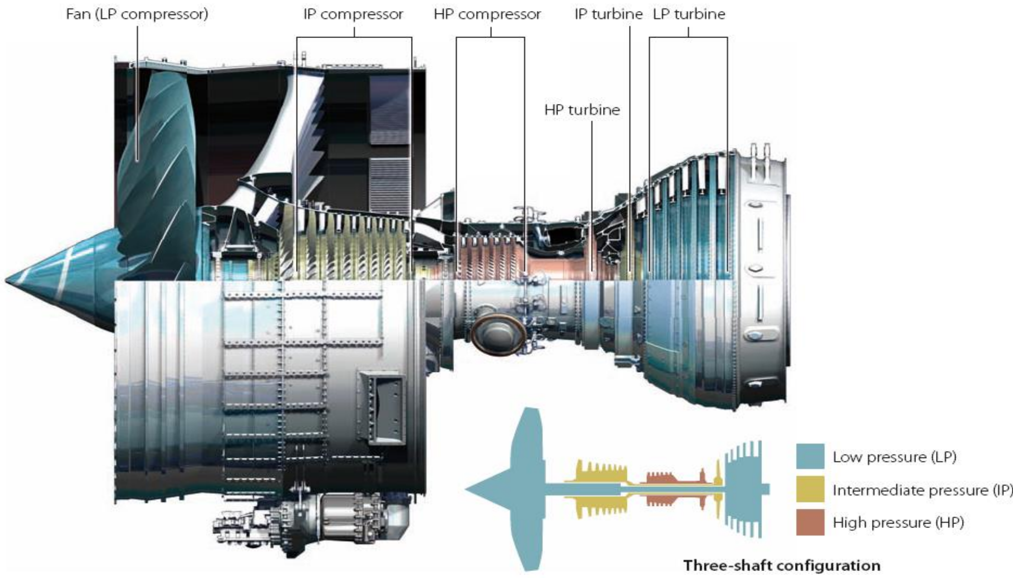

Figure 1.1: Trent 1000 jet engine with stages' delivery pressures, courtesy of Rolls-Royce plc

The efficiency of the gas turbine engine such as used in aircraft depend in some measure on the clearance between the rotor blade tips and the surrounding engine casing shroud such as the clearance between the compressor blade tips and the compressor casing. In an effort to maintain a high level of compressor efficiency, gas turbine engines manufacturers have endeavoured to maintain the closest possible clearance between rotating compressor parts and surrounding casing structure. This is so because any air leakage there between signifies a loss of energy in the system. If the clearance is too large, more of the engine air will escape through the gap between the rotor blade tips and the surrounding casing shroud, thereby decreasing the engine's efficiency. If the clearance is too small, the rotor blade tips may rub the surrounding casing shroud during certain engine operating conditions such as acceleration and deceleration. This can lead to the deformation of casing, vibration of blades and in some cases the blade can fracture. During these changes in engine conditions from idle to maximum take-off, the rim of a compressor disc responds considerably more quickly to changes in the temperature of the main flow than the disc cob. The resultant radial temperature gradients result in high stresses and reduced disc life. Furthermore, the compressor drum responds more slowly to changes in annulus air temperature, and particularly the disc cobs, than the surrounding engine casing. These differential expansions and contractions lead to changes in the blade tip clearances. The reductions in blade tip clearance in compressor of gas turbine engine will improve engine efficiency both at steady state and during transient operation. An efficient control method for the tip clearance is also essential for engine stability. This would reduce compressor surge occurrence during the engine transient operation.

Compressor surge is the complete breakdown of compression during transient operation cause by aerodynamic instability within the system. This is a total breakdown of the continuous steady flow through the entire compressor. During surging, the earlier compressed air is expelled through the engine intake. This is due to the failure of compressor to continue compressing the already-compressed air in the system. The evidence of surge is by a reversal of flow in a compressor accompanied by high vibration, a loud bang, increase in exhaust temperature and rotor speed, and loss of thrust. Surging results in damage to the compressor parts such as blades and thrust bearings.

Tip clearance in the axial flow compressor of aero-engines is also of critical importance in terms of both performance and cost of operation of the aircraft. As the clearance between the compressor blade tips and the casing increases, the aerodynamic efficiency will decrease. Figure 1.2 shows the variation of efficiency with clearance. It indicates that the larger the clearance the lower the efficiency and the lower the clearance the higher the efficiency.

The decrease in aerodynamic efficiency will result in an increase in the specific fuel consumption and operating costs, which are very importance to civil airline operators and their customers alike. In practice a 1% reduction in specific fuel consumption (SFC) for a large passenger aircraft could save "560 tonnes of fuel per annum and reduce direct operating costs by 0.5%" (Childs et al. 2006). It is therefore important to reduce the uncertainties associated with engine optimisation such as large tip clearance.

The aim of this research is to develop a concept for controlling the compressor tip clearance throughout the engine operating cycle during engine transient operation. This is achieved by reducing the high pressure compressor (HPC) drum time constant. The drum time constant is reduced by increasing the heat transfer coefficient of the drum through the introduction of the radial inflow into the drum cavity. Increasing the thermal response of the high pressure compressor (HPC) drum reduces the reslam characteristic of the drum, thereby reducing the cold build clearance (CBC), leading to a reduction in cruise clearance and a reduction of clearance at first acceleration.

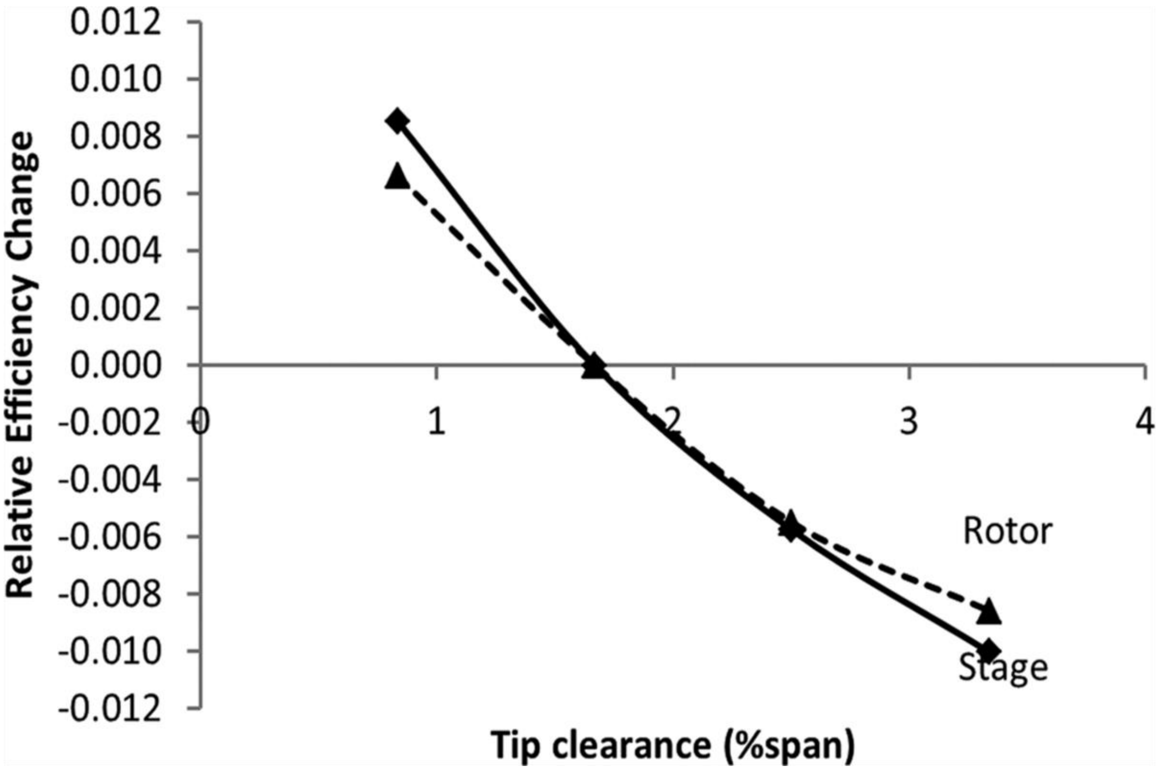

Figure 1.2: A schematic diagram showing the efficiency variation with tip clearance for medium tip gap (Sakulkaew et al. 2013)

The multiple cavity rig (MCR) is used for the study. It is a representative of real aero-engine geometry and operates at engine non-dimensional conditions. The work reported here is part of the wider 6th Framework European Project NEWAC (NEW Aero Engine Core Concepts), which aims to develop alternative engine configurations in order to achieve significant and durable reduction of pollution. The technology will be applied to the rear stages of a modern high pressure compressor as these stages are more exposed to tip clearance problems. This is to a certain extent due to larger thermal expansion resulting from higher gas temperatures, and also owing to the higher impact on the aerodynamic losses due to smaller blades in the later stages.

The lumped parameter method is employed to predict closures and clearance behaviours at any point in the cycle during engine transient operation, and the experimental data obtained by Dr. Nick Atkins as part of the wider NEWAC programme from the multiple cavity rig are validated against the two-dimensional finite element thermo-mechanical model of the rig to explore the physical principles and demonstrate proof of concepts.

A review of previous work is presented in Chapter 2, and the finite element analysis program SC03 model of the rig is described in Chapter 3. The 1 -dimensional analysis is presented in chapter 4. Sensitivity analysis using HP compressors drum and casing models of RB211-524 and Trent 1000 engine are described in Chapter 5 while the 2D thermal modelling prediction are validated against the lumped parameter model results and experimental data as well as a discussion of the results of the matching are discussed in Chapter 6. In Chapter 7, 2-dimensional thermal modelling of the multiple cavity rig and the results of the modelling showing the effect of radial inflow in the cavity are discussed and a summary of the main conclusions and recommendations for future work are presented in Chapter 8.

Chapter 2

2. Review of previous work and background information on tip clearance control

This chapter presents insight into previous investigations carried out in the field of tip clearance control in axial compressors. This is preceded by presentation of the basic terminology specific to the axial compressor. This chapter is divided into four main sections. The axial compressor overview is described in section 2.1, literature particular to compressor clearance control and tip clearance flows in gas turbines is reviewed in section 2.2, tip clearance control patent review is presented in section 2.3, fluid dynamics and heat transfer in rotating disc systems are discussed in section 2.4 through to 2.6, rotating cavity with radial inflow is presented in section 2.7 while section 2.8 examines rotating cavity with axial throughflow and the summary is presented in section 2.9.

2.1 Compressor Overview

A compressor is a device that imparts energy to fluid flow and as a result increases the pressure of the working fluid passing through it. During this process, the volume of the working fluid is reduced and the temperature is increased. Compressors are divided into two broad groups; namely positive displacement and dynamic compressors. The dynamic type compressor is subdivided into centrifugal and axial compressors. These are commonly used in gas turbines with the latter being the focus of the research. For details on axial compressor design and operation, the reader is referred to Cumpsty (1989), Wilson (1993), Saravanamuttoo et al. (2001), Aungier (2003), Boyce (2003) and Rolls-Royce (2005).

2.1.1 Axial compressor

Axial compressors are rotating aerofoil based compressors where the working fluid mainly flows parallel to the axis of rotation. They produce a continuous flow of compressed gas, and have the advantages of high efficiencies and a large mass flow capability, in relation to their cross section. For high pressure rises to be achieved in axial compressors, several rows of aerofoil are required making them more complex and expensive than other compressor designs. An axial compressor consists of a series of stages, each stage comprised of a row of rotor blades followed by a row of stator blades Saravanamuttoo et al. (2001). These series of stages are required to achieve the desired overall pressure ratio. They are mounted with bearings, which are aided by the casing structure, which integrates stator vanes aerofoil cross sections that are aligned axially behind the rotor blades Rolls-Royce (2005).

An axial compressor may have a single spool or multi-spools depending on the number of rotor and stator assemblies. In some cases, additional rows of stator blades, called inlet guide vanes (IGVs) are included to guide the air to the first row of rotor blades.

- **Single spool:** A single spool compressor is a compressor with one rotor and stator assembly with as many stages as needed to achieve the desired pressure ratio and all the airflow passes through the compressor. Figure 2.1 shows a single spool comprises of a single compressor driven by a single turbine.

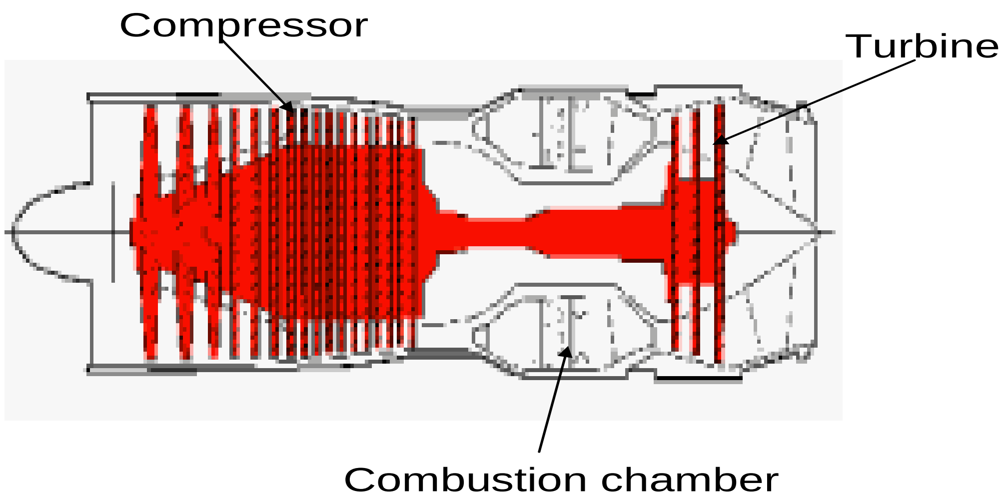

Figure 2.1: A single spool courtesy of Thai Technics (2001)

- **Multi-spool:** This consists of two or more rotor blade assemblies each driven by their own turbine at an optimum speed to achieve a higher-pressure ratio and to give the compressor a greater operating flexibility. Figure 2.2 shows a multi-spool comprising of a twin-spool in which the low pressure compressor is connected to the low pressure turbine while the high pressure compressor is connected to the high pressure turbine.

A multi-spool such as the twin-spool is most suitable for by-pass type engines where the low pressure (LP) or front compressor is designed to handle a larger mass airflow than the HP compressor. In this manner, a percentage of the air from the LP compressor passes into the HP compressor while the remaining part of the air called the by-pass flow is ducted around the HP compressor and finally, both flows mix again in the exhaust system before passing to the propelling nozzle Rolls-Royce (2005).

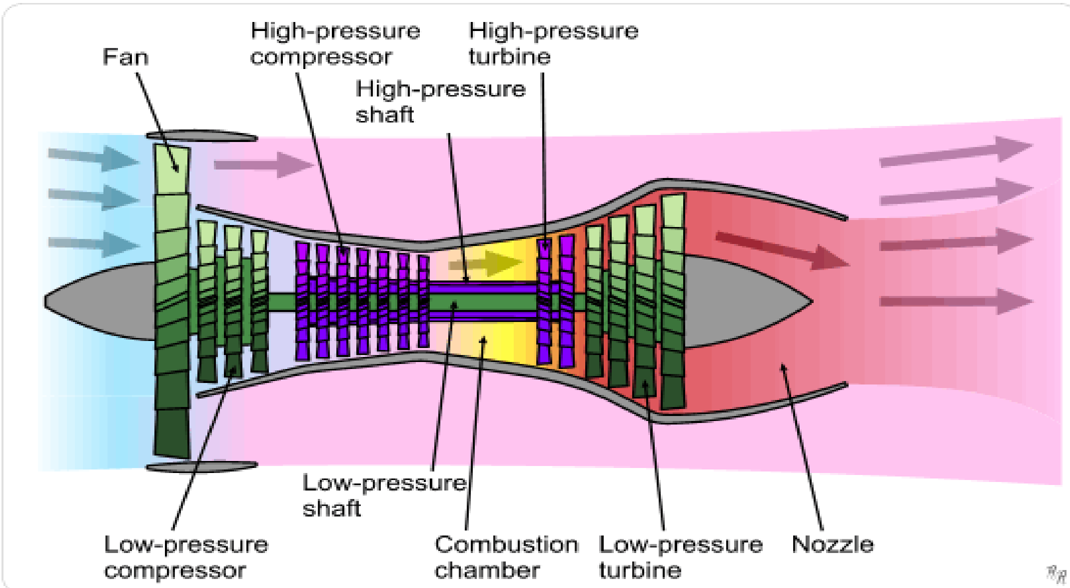

Figure 2.2: A multi-spool courtesy of Wikipedia

The length of the blades, annulus area of an axial compressor is gradually reduced from the front to the rear of the compressor to maintain the axial velocity at a near constant level Boyce (2003). The compressor rotor is driven by the turbine through a connecting shaft, which rotates at a high speed causing air to be induced continually into the compressor. The air is drawn into the compressor through the engine intake as the rotor rotates and the working fluid principally flows parallel to the axis of rotation. The rotor blade imparts energy to the air thereby causing the pressure to rise; the air pressure and temperature continue to increase as the air passes each stationary stator which is located downstream of each rotor that redirects the flow onto the next set of rotor blades. Finally, at the last stator, all circumferential velocity, or whirl, from the air is removed leaving the core air to pass into the combustor pre-diffuser, before entering the combustor system Rolls-Royce (2005). An axial compressor produces a continuous flow of compressed air, hence having advantages of high efficiency and large mass flow capacity in relation to its cross section Rolls-Royce (2005).

Axial compressors are used widely in gas turbines, such as jet engines, high-speed ship engines and engines for power stations. A classic example of an axial compressor is the H.P. compressor. Figure 2.3a shows a schematic diagram of the internal layout of a H.P. compressor internal air system while Figure 2.3b shows a schematic diagram of clearance between rotor blade and the casing in an H.P. compressor. The H.P. compressor in Figure 2.3a consists of compressor disc, rotor, stator blade, rotor blade, the main flow through the compressor to the combustion chamber and the axial throughflow of cooling air. This throughflow cooling air extracted from stages of the intermediate pressure compressor and intended for the intermediate pressure turbine blades and seal, flows through the annular passage between the drive shaft and H.P. compressor disc bores. This throughflow may be heated by both convection and viscous dissipation as it travels along its route Long et al. (2007). Figure 2.3b shows a schematic diagram of clearance between rotor blade and casing in an H.P. compressor.

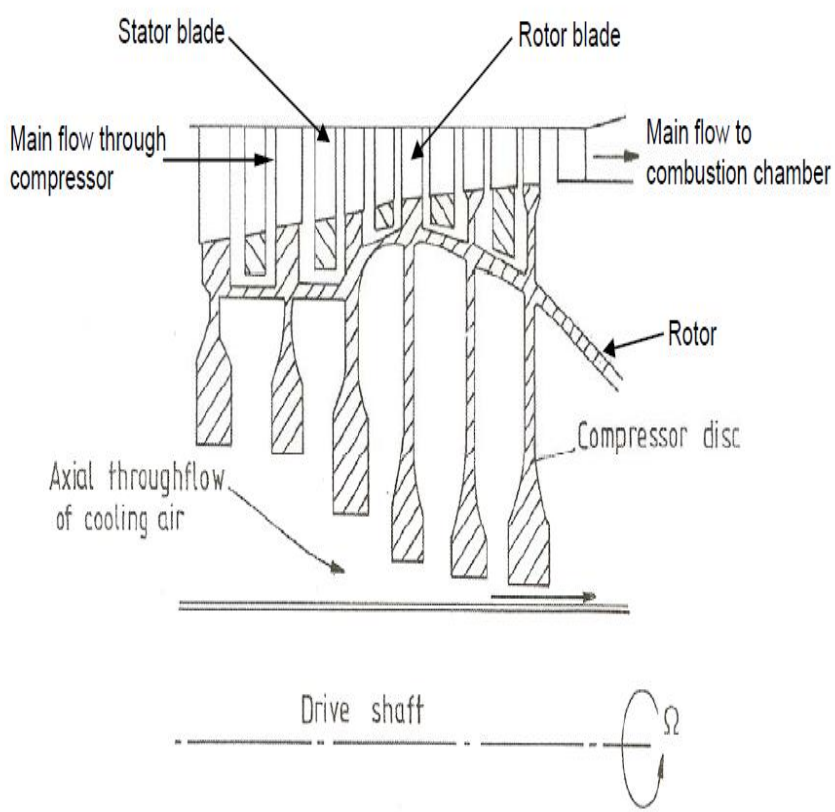

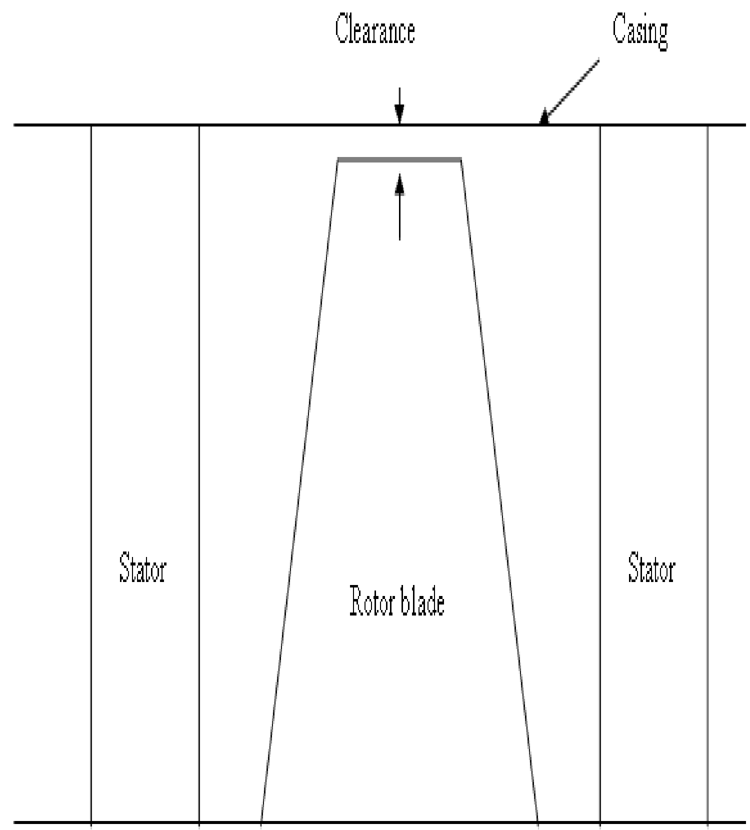

Figure 2.3a & b: 2.3a shows schematics of the Internal Layout of an HP Compressor (Long 1994) while 2.1b shows a schematic diagram of clearance between rotor blade and casing

2.1.2 Compressor characteristic

The compressor characteristic is the performance of the compressor with reference to different engine operating conditions. A typical compressor characteristic shows the delivery pressure ratio against the inlet mass flow following a constant rotational speed line. Figure 2.4 shows an operating curve of a gas turbine engine, which shows the relationship between the compression ratio of the engine and the mass airflow that must be maintained throughout the engine. If either of these factors goes out of limits, a compressor stall occurs and may in some cases lead to surge occurrence. When the engine is undergoing steady state operating conditions, the compressor will operate on the working line. However, during other engine operating conditions like acceleration, the compressor operating point can move above the working line. In view of the above, it is desirable to have a large operating margin (stability margin) to take care of transient operations. In a multi-stage compressor, each stage is being controlled by its own stage characteristics. It is important to match the stages to achieve low losses and sufficient operating range for off-design operation. A typical matching is where the front stages control the low-speed stability margin while the rear stages control the high-speed stability margin Rolls-Royce (2005).

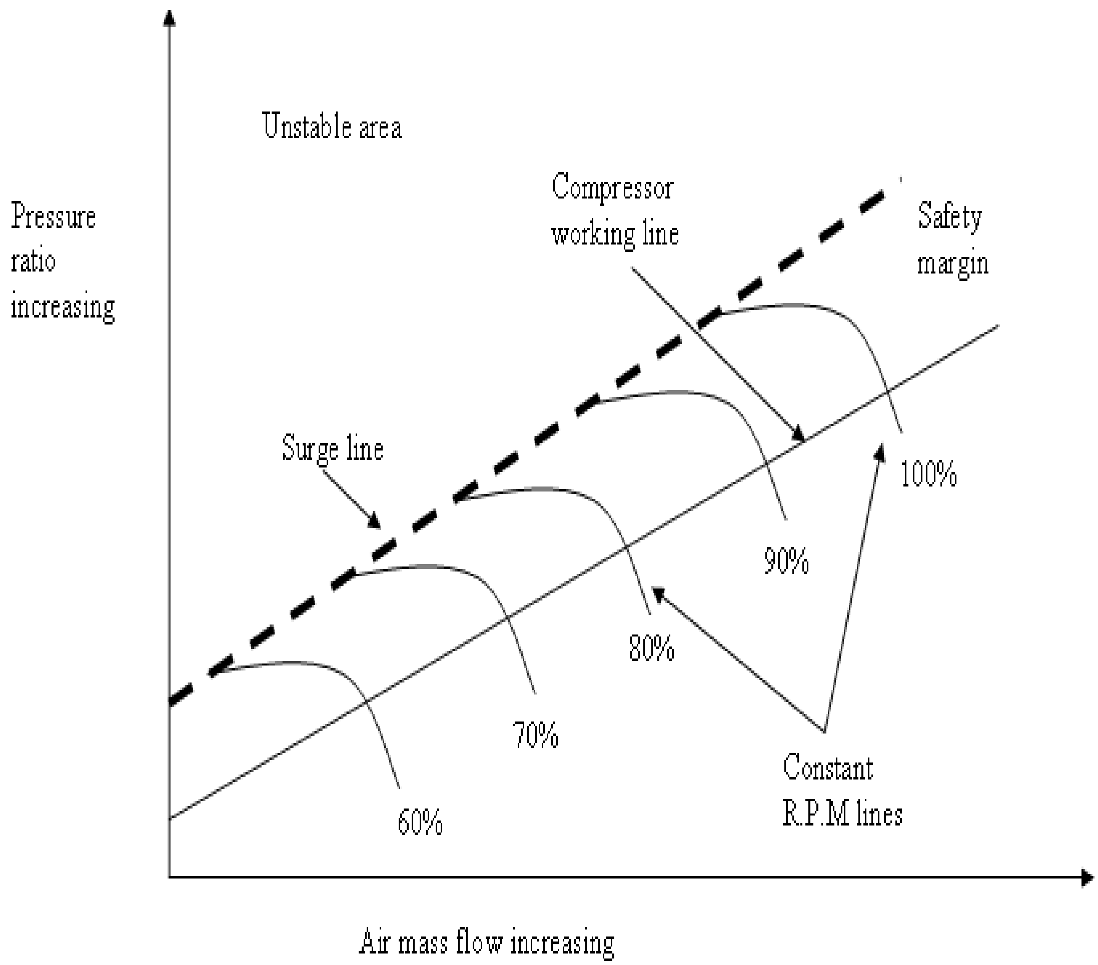

Figure 2.4: A Schematic Diagram of Compressor Characteristic Map (Rolls-Royce, 2005)

At a higher operating speed, if the operating condition of the compressor goes beyond the limits of the stability line, the rear stages become overloaded and immediately a breakdown of the airflow through the compressor occurs, giving rise to a phenomenon called surge. However, during low operating speeds, if the operating point moved beyond the stability line, the front stages of the compressor experience a phenomenon called rotating stall, which gives rise to a circumferentially non-uniform flow. This flow rotates around the annulus at 20 to 50 per cent of rotor rotational speed, and in the same direction

Rolls-Royce (2005). Rotating stall and surge are sources of blade vibration that can induce rapid aerofoil failure leading to the destruction of the compressor. Undesirable tip clearance in most cases contributes to the occurrence of surge and rotating stall. Consequently an active clearance control mechanism is necessary for optimum operation of the compressor.

2.1.3 Compressor clearance

Compressor clearance is the radial gap between the rotating blades and the casing of the aerofoil compressor. This clearance varies significantly during the various operating conditions of the engine namely: take-off, acceleration, cruise, deceleration and reacceleration due to the combined effects of centrifugal forces and thermal expansions. During transient operation, centrifugal forces on the rotor and different thermal expansions of blades, discs and the casing induce inertial and thermal stresses in an engine, which create deflections in components that can lead to loss in engine efficiency.

A cold engine is designed to have a large amount of compressor clearance, but this clearance diminishes as engine speed is increased from ground idle to maximum power during take off. During this process, the rotor and blade assembly expands rapidly, causing the rotating components to grow radially outward. The growth by rotor and blade are due to rotational forces and rapid heating. As the rotating component grows, the case and shroud assembly surrounding them also expands radially due to heating, but at a different rate (slower rate). This result in a minimum clearance condition called a pinch point Lattime and Steinetz (2002). After the pinch point, the casing which is less in mass acquires more heat quickly during acceleration and expands more than the disc having a heavier mass thereby increasing the clearance between the blade tip and the casing again. In a while after the casing expansion, the rotor starts to heat up at a slower rate than the casing thereby decreasing the clearance again. This continues until the engine approaches cruise condition, where the casing and rotor growth reaches thermal equilibrium which causes the tip clearance to remains relatively constant.

During deceleration from maximum take off to Idle at low speed the rotor shrinks quickly causing the rotor blade to move away from the casing thereby increasing clearance. The casing then loses heat quickly and contracts rapidly more than the disc thereby decreasing the clearance between them again in the compressor of the gas turbine engine. This continues until the engine approaches Idle condition, where the casing and rotor growth reaches thermal equilibrium which causes the tip clearance to remains relatively constant. Figure 2.5 shows the variation of closure with time over a square cycle of stage 1 HP compressor for RB211-524 engine with a maximum rotational speed of 10097 rpm, maximum inlet temperature of 544.3K and maximum outlet temperature 851.6K.

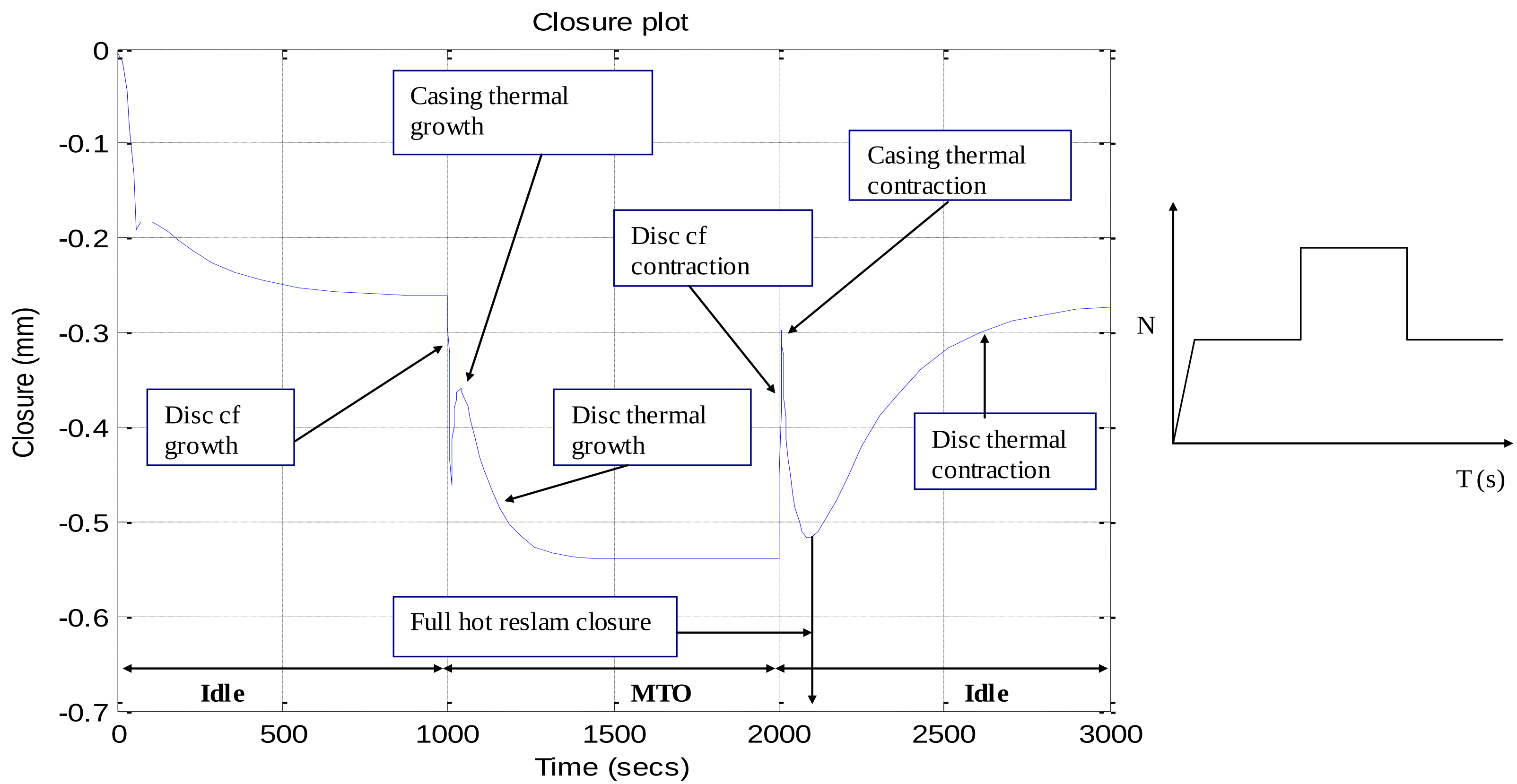

Figure 2.5: The variation of closure with time over a square cycle of stage 1 HP compressor for RB211-524 engine with a maximum rotational speed of 10097 rpm, maximum inlet temperature of 544.3K and maximum outlet temperature 851.6K

Closure is the relative movement between the blade tips and the casing in a gas turbine engine. A typical closure characteristic is shown in Figure 2.5. The running clearance is obtained by the addition of the cold build clearance (CBC) and the closure. The setting up of the CBC and calculation of clearance is dealt with in details in Chapter 5. The graph shows different thermal response characteristics of the stationary and rotating parts of the engine during transients. This includes disc centrifugal growth, casing thermal growth, disc thermal growth, disc centrifugal contraction, casing thermal contraction and disc thermal contraction. Also included in the graph is full hot re-slam closure.

It is considered useful at this instance to formally define the disc and casing response characteristics during transient operations. These transient operations includes start, stabilisation at idle, acceleration from idle to maximum take-off, stabilisation at maximum take-off, deceleration from maximum to idle and stabilisation at idle as shown in Figure 2.5. The engine start from 0s and between t =0s and t =1000s with speed of 6473.4 rpm is the first idle region, between t =1000s and t = 2000s is the maximum take-off (MTO) region with speed of 10096.7 rpm, and t = 2000s to t = 3000s with speed of 6473.4 rpm is the idle region. The engine finally come to rest after the transient at t = 3000s.

- **Disc centrifugal (CF) growth**: This indicates the radial growth of disc due to centrifugal acceleration of the disc as the engine start accelerating from idle position. During this period, the large cold closure in the engine between 0s and 1000s is reduced considerably.
- **Casing thermal growth:** Is the thermal expansion of the casing. The casing acquired heat quickly than the disc being lighter in mass than the disc as the

engine is accelerating to maximum take-off point. As the casing heats up, it expands and grows radially away from the rotating blade hence increasing the clearance exiting between the casing and the rotor blade within the next 10s from t = 1000s to t = 1010s mark. This gap starts reducing as the disc start to expand.

- **Disc thermal growth:** This is the thermal expansion of the disc. The disc with a heavier mass now start to acquire heat as the engine is accelerating and hence expands radially thereby causing the rotor blade to move radially. When this occurs, the gap is reduced until an equilibrium is reached and maintain till they finally stabilised at the stabilised maximum take-off point; in this case at t=2000s.
- **Disc centrifugal contraction:** This is the radial contraction of the disc due to the sudden withdraw of power from the engine hence slowing down the centrifugal acceleration of the disc. When this happens, the disc contracts causing the rotor blade to move away from the casing. This will open up the gap between the rotor blade and casing giving a large clearance again in the cycle. This occurs between t = 2000 and t = 2010s. This gap will start to narrow down again as the casing start to contract when it starts to lose its acquired heat.
- **Casing thermal contraction:** This is the sudden contraction of the casing as it starts to loose its acquired heat quickly due to its low mass resulting from low power in the engine. When this happens, the large gap starts to narrow down. This continues until there is equilibrium between the temperature of both the casing and the disc giving the tightest clearance after maximum take-off. This occurs between t = 2010s and t = 2060s giving the re-slam characteristic in the cycle. This gap further open up as the engine approach stabilised idle point.

- **Disc thermal contraction:** This occurs when the disc gradually losses heat as it cools down due to low power resulting in a large gap between the casing and the rotor blade. This gap continues to increase in sizes as the disc cool down gradually away from the casing. At an equilibrium temperature of both of them, the gap is maintained until it reaches the stabilised idle point. In this case is at t = 3000s.

These different thermal response characteristics of the stationary and rotating parts of the engine during engine transients give rise to complex tip clearance behaviour. This complex behaviour has a serious effect on engine operating parameters such as specific fuel consumption (SFC), surge margin, cruise clearance, turbine inlet temperature and indeed both overall efficiency gains and increased safety margins. A large clearance brings about a reduction in the overall efficiency of the compressor. Radomski (1982) carry out an investigation into the compressor clearance in high pressure compressor of CF6 jet engine for National Aeronautics and Space Administration (NASA) and came to the conclusion that a 1mm (0.040 in) reduction in clearance would produce a normalized average clearance change of 0.78%. This will give a corresponding increase in the compressor efficiency by 0.78% and a reduction in specific fuel consumption (SFC) of the fan engine by 0.38%.

In an axial flow compressor, a considerable percentage of efficiency loss arises in the blade tip region; here the complex flow that arises has been attributed to the interaction of the end-wall boundary layer and tip leakage flow. This complex flow behaviour at the blade tip is influenced by undesirable clearance between the rotating blade and the casing which must be controlled to achieve maximum engine efficiency. The gap between the rotor tips and the stationary casing wall in aerofoil compressors during engine operation must be controlled because it is a known source of losses in the compressor. This is so because the flow in the gap is not twirled by the blades and as such does not contribute to energy addition during compression process. This tip flow leaves the tip-gap as a vertical structure that generates pressure losses as it mixes with the main stream flow. These losses manifest in two forms namely; blockage and other losses resulting from fluid dynamic and thermodynamic effects. These various losses are recorded in the form of flow separation, stall and reduced rotor work efficiency which occurs as a result of the interaction between the clearance flow and the main flow of the compressor. This in turn affects significantly the performance and stability of the aerofoil compressor. The losses can be divided into two: (1) Losses encountered in the rotor and (2) Losses encountered in the stator. These losses can be described as disc friction loss, incidence loss, blade loading and profile loss, skin friction loss, clearance loss, wake loss, exit loss, stator profile loss and skin loss Boyce (2003).

In an effort to maintain a high degree of compressor efficiency, attempts have been made by gas turbine engine manufacturers to reduce the blade tip clearance as much as possible through active tip clearance control schemes. Active clearance control is any system that allows independent setting of a desired clearance at more than one operating point. This system makes use of fan air to cool the support flanges of the H.P. turbine casing. This reduces the casing and shroud diameters, and consequently blade tip clearance, during cruise conditions. Other forms of active control systems are magnetic and sensor actuation. Hence, a good clearance control scheme is an effort aimed at improving engine efficiency by controlling both transient and steady state tip clearance during engine operations. In the past, tip clearance control was focused on turbine/shroud relationship, but a recent development is the focus on compressor rotor/shroud and stator/rotor relationship. A good control method that reduces blade tip clearances significantly in aerofoil compressors will lead to a significant increase in the on-wing life of commercial aircraft, reduction in engine instability, reductions in specific fuel consumption (SFC) thus saving fuel costs, as a 1% reduction in SFC across the then current fleet could save a total of $160M per year in fuel costs Lattime and Steinitz (2002), reduction in air accident rate, increased economic and environmental benefits to the public due to reduction in emissions (NO_x, CO_2), increased payload and mission range capabilities, reduction in pressure losses and the overall increase in engine efficiency.

2.2 Compressor Clearance Control review

Many papers have been found which are relevant to the aerodynamic desensitisation of tip clearance flows. Aerodynamic desensitisation is the process of weakening the tip leakage vortex. Very few papers were found which relate directly to actual clearance control techniques. However, approximately 100 patents protecting various active and passive clearance control schemes have been found which and are presented in detail in appendix 2.1. This section summarises the literature relevant to aerodynamic desensitisation of tip clearance flows and other tip clearance control schemes.

2.2.1 Aerodynamic Desensitisation of Tip Clearance Flow

A number of strategies for desensitisation of tip clearance flow have been published over the past decades. The common objective among the authors is to reduce as much as possible the mass flow that passes through the tip clearance. The most common method is to modify blade tip geometry. This includes using squealer tips and tip platform extension such as adding winglet. These methods will change the discharge coefficient without affecting the pressure distribution around blade tip regions. Another method for controlling tip clearance flow and cooling the blade tip regions is by air injection. This air jet will hamper tip clearance flow and weaken the interaction between tip clearance flow and main passage flow, reduces tip clearance vortex and hence improving engine efficiency.

This section presents literature relevant to aerodynamic desensitisation of the tip flow under the following heading namely tips injection, squealer tip and tip platform extension. In an axial compressor, the pressure difference across the blade causes a leakage flow through the tip clearance from the pressure surface to the suction surface of the blade; this leakage causes blockages that eventually reduce the pressure rise capability and in turn affect the overall efficiency of the compressor Bae et al. (2003).

2.2.1.1 Tip Injection

Tip injection involves the injection of air into the gap between the blade tip and casing to reduce clearance. These include the injection of coolant from holes located on the blade tip, near the tip along the pressure side or along the suction surface. This is a reliable method to enhance compressor stability and will control the stage characteristics considerably by changing the radial work distribution. This can act as an obstruction to the tip clearance flow and will weaken the interaction between the passage flow and the tip clearance flow. It is also establish that tip injection causes the tip clearance loss to be less sensitive to the incidences. In addition, with injection, at all these incidences the heat transfer conditions are improved significantly on the blade tip surface in the middle and aft parts of blade Niu and Zang (2009). Thus, tip injection is proved to be an effective method of controlling tip clearance flow, even at off-design conditions.

Acharya et al. (2002) carried out a numerical simulation of film cooling holes on the tip of a gas turbine blade, and results on a flat tip, film coolant injection is shown to lower the local pressure ratio and alter the nature of the leakage vortex while a high film cooling effectiveness and low heat transfer coefficients are obtained along the coolant trajectory; these values increase slightly with increasing tip clearances. For a squealer tip, the flow inside the cavity exhibits stream wise directed flow; this alters the trajectory of the coolant jets and reduces their effectiveness.

Hohlfeld et al. (2003) investigated the effect of blowing from the dirt purge holes of a flat tip in a linear cascade with both numerical and experimental methods. Two different tip gaps of 0.56%C and 1.68%C were investigated. The results show that the flow ejected from the dirt purge holes is able to block the leakage flow in the tip gap and this blockage effect was more evident at the small tip gaps than at large ones.

Bae et al. (2003) examined tip clearance flow control using a fluidic actuator mounted on the casing and the application of three jets; Normal Synthetic Jet (NSJ), Directed Synthetic Jet (DSJ) and Steady Directed Jet (SDJ). The effectiveness of this three jet approach to tip clearance flow control was measured by (a) reduction of the tip leakage flow rate, (b) mixing enhancement between the defect region of the tip clearance vortex and the primary stream flow, and (c) stream wise momentum enhancement. Figure 2.6 shows a fluidic actuator mounted on the casing used in this study. When NSJ are injected, the momentum flux of NSJ modifies the streamline next to the casing wall therefore effectively reducing the tip clearance. The result of the experiment shows that the momentum flux of the NSJ reduces the rate of the leakage flow by modifying the streamline next to the casing wall thereby reducing the tip clearance effectively, while the DSJ causes a reduction in the flow blockage in the blade passage as the force-mixing of the jet with the main flow continues and finally the SDJ energises the retarded flow in the end-wall causing the flow to be more uniform, thereby controlling the tip clearance.

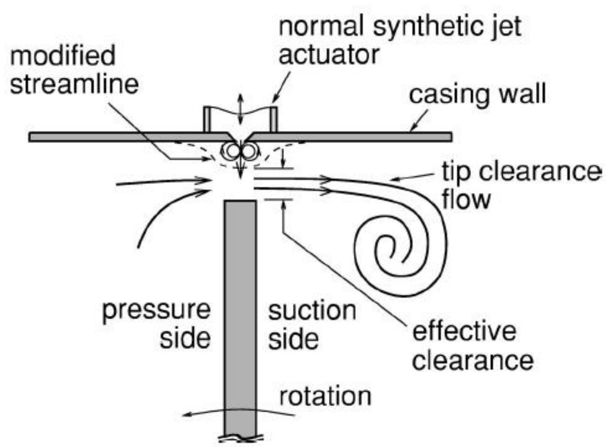

Figure 2.6: Illustration of Tip Leakage Flow Rate Reduction Scheme (Bae et al. 2003)

Rao and Camci (2004) performed an experimental study of a turbine tip desensitisation method based on tip coolant injection in a large-scale rotating turbine rig to ascertain the effect of injection mass flow rate and concluded that cooling injection could cause the tip clearance vortex and its associated losses to be reduced.

Cassina et al. (2007) carried out a numerical study on the suppression of flow instabilities in axial compressors using tip injection, with ten discrete injectors modelled as openings through the casing; a high pressure jet of air was supplied at angle 15° in radial direction. Analysing the results for various lengths and widths of the injector port, upstream axial position, injector mass flow rate and tangential flow angle, it was shown that the tip injection effectively actuated the low momentum fluid at the rotor tip, optimised width to length ratio of the injector port and thereby improved the stability margin.

Behr et al. (2007) examined the control of rotor tip leakage using cooling injection from the casing onto the rotor tip. The cooling air was injected from the casing into the opposing rotor turning direction through a rim array of ten holes open at equal distance per rotor pitch. The results showed that the interaction of the cooling air with the main air flow as it enters the tip of the rotor causes a reduction in the size, turbulence intensity and the rotor passage vortex, which in turn improved the isentropic efficiency of the stage.

Dobrzynski et al. (2008) studied experimentally the active flow control in a single-stage axial compressor using tip injection and end-wall boundary layer removal and came to the conclusion that tip injection as well as casing-wall boundary layer bleed are means to increase the operating range of the compressor. By energising the casing-wall boundary layer above the rotor leads to decreased blockage at the rotor tip section and hence to a shift of the radial aerodynamic loading distribution on rotor and stator. A further control is achieved by applying discrete tip injection with high injector exit velocities.

Curtis et al. (2009) carried out an experimental and computational investigation into the performance of an air-curtain seal used to control the leakage flow over the tip shroud of a turbine rotor.

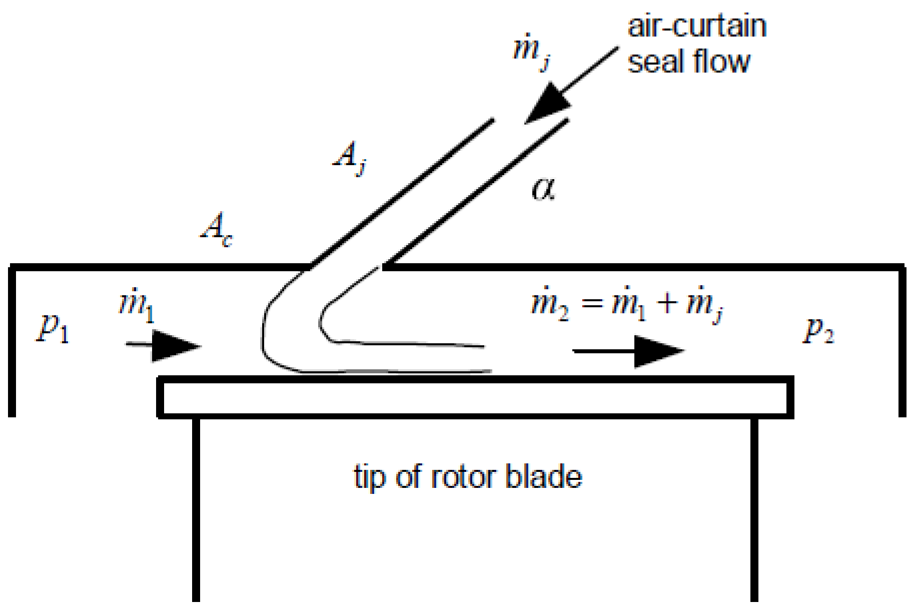

Figure 2.7: Simple Model for an Idealised Air-Curtain Seal (Curtis et al. 2009)

Figure 2.7 illustrates a simple two dimensional model of an idealised over-shroud cavity flow field. The over-shroud cavity has a nozzle of area A_j. The mass flow rate of the air-curtain is $\dot{m}_j$ and it enters the over-shroud cavity through a nozzle of area A_j, thus producing a jet with velocity v_j. The jet is at an angle α to the axial direction so that its momentum opposes the over-shroud leakage flow. The cross-sectional area of the shroud-cavity where the leakage and jet flows interact is A_c. The total mass flow rate entering the mainstream flow downstream of the shroud is given as $\dot{m}_2 = \dot{m}_1 + \dot{m}_j$, where the leakage flow is $\dot{m}_1$ and the jet flow is $\dot{m}_j$. The results show that a seal of this type has the potential to reduce or eliminate shroud leakage whilst having a practical level of clearance between the stationary and moving components.

Niu and Zang (2009**)** carried out a numerical investigation of an active tip clearance control method based on cooling injection from the blade tip surface.

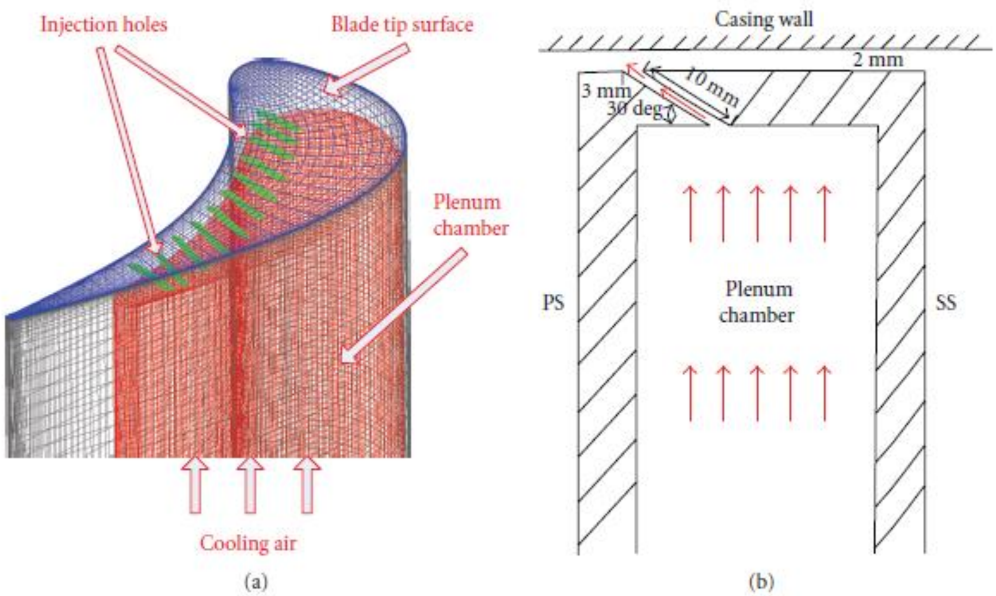

Figure 2.8: Schematic Diagram of Injection System. (Niu and Zang, 2009)

Figure 2.8 shows the schematic diagram of the injection system use in the current study. The cooling air entered the plenum chamber and homogenized there, then injected into the tip clearance passing through 11 holes which were 1mm in diameter. At all conditions, holes on the blade tip surface were located at a distance of 3mm from the pressure-side corner, directing toward the blade pressure side corner at an angle of 30◦ relative to the blade tip surface. The closer to the pressure-side corner the injection is located, the more it reduces total pressure losses at cascade exit and that tip injection reduces the tip clearance mass flow to the level with half tip clearance height. They concluded that injection location plays an important role in the redistribution of passage secondary flow.

2.2.1.2 Squealer tip

The Squealer is an extension done on the pressure or the suction surface toward the endwall or in some cases on both sides, radially outward from the blade tip. A squealer extension on the suction surface profile is called a suction-side squealer and a squealer extension on the pressure surface profile is called a pressure-side squealer. Squealers are valuable for the reason that they enhance the flow turning in the clearance region; decrease the mass flow through the clearance, causing a reduction in the force of the tip leakage vortex and assist in reducing the direct damage during blade rub with the endwall Ness II (2009). The overall significant of squealer is that they reduce the tip leakage flow loss.

Dey and Camci (2001) presented an experimental investigation of aerodynamic characteristics of full and partial-length squealer rims in a turbine stage. Their results show that the suction side partial squealers are aerodynamically superior to the pressure side squealers and the channel arrangement. The suction side partial squealers are capable of reducing the stage exit total pressure defect associated with the tip leakage flow to a significant degree. These results indicate that the use of "partial squealer rims" in axial flow turbines can positively affect the local aerodynamic field by weakening the tip leakage vortex. Papa et al. (2002) carried out an experimental investigation to measure average and local mass transfer coefficients on the tip of a gas turbine blade. Two different tip geometries were considered: a squealer tip and a winglet-squealer tip having a winglet on the pressure side and a squealer on the suction side of the blade. For both tip geometries the tip clearance level has a significant effect on the mass transfer distribution. The result shows that the squealer tip has a higher average mass transfer that sensibly decreases with gap level. Morris et al. (2005) carried out investigation into the use of active, blade mounted flow control to alter the tip flow field. In their study, a single dielectric barrier discharge plasma actuator was mounted to a turbine blade tip in a linear cascade facility. The actuator was configured to imitate a partial squealer geometry that is known to cause reduced losses as a passive control device. The active control results indicate that the actuators led to qualitative changes in the structure of downstream wake profiles as determined with a total pressure probe. These results were strongly dependent on the unsteady actuation frequency at fixed power. Azad et al. (2000) performed an experimental investigation on the effect of tip gap size and inlet turbulence intensity on detailed local heat transfer coefficient distribution on the plane tip surface of a gas turbine blade tip in five bladed stationary linear cascades at different Reynolds and Mach number conditions. Their results illustrate various regions of high and low heat transfer coefficient on the tip surface. They found that tip clearance has a significant influence on local tip heat transfer coefficient distribution and concluded that a larger tip gap generally resulted in a higher overall heat transfer coefficient due to the magnitude of the tip leakage flow. There is also an increase of about 15-20% in heat transfer intensity along the leakage flow path at higher turbulence intensity level from 6.1% - 9.7%. Papa et al. (2002) and Azad et al. (2000) measured heat transfer coefficients along the blade tip region. One location was at the thickest part of the blade which was shown to have low convective heat transfer coefficients as a result of low convective velocities. But, two regions with the highest heat transfer coefficients are the leading edge region and along the pressure side of the blade where the flow separation region is present. In their separate conclusions, overall heat transfer coefficients increased due to the larger leakage flows with a larger tip gap.

2.2.1.3 Tip platform extension

Tip platform extension is the method for desensitising tip clearance flow effects by design. This is also called a winglet and the extension is either towards the pressure side of the blade or the suction side of the blade. According to Dey and Camci (2001), it was envisaged that the extension will be most effective on the places on the blade where the pressure gradient were strongest. Tallman and Lakshminarayana (2001) made a numerical study of methods for desensitising tip clearance effects in turbines by tip surface chamfering and pointed out that chamfering the blade tip near the trailing edge of the gap led to a decrease in the size of the tip clearance vortex and its associated losses.

Saha et al. (2006) studied numerically blade tip leakage flow and heat transfer with pressure-side winglet and confirm the work of Dey and Camci that modification of blade tip geometry changes the discharge coefficient without affecting the pressure distribution around blade tip regions.

Kusterer et al. (2007) investigated how to reduce the tip clearance by design. They redesigned the blade by extending the tip region of the pressure side of the blade to winglets with the aim of having a reduction of mass flow in the radial gap between the blade tip and the casing as shown in Figure 2.9. Figure 2.9 shows the interaction of flow through the radial gap with a radial secondary flow, which is induced by the passage vortex, on the pressure side, and it interactions with the main flow and the secondary flows (mainly the passage vortex) on the suction side. This interactions cause tip leakage flow which creates the leakage vortex on the suction side as it is mixed with the main flow through the cascade.

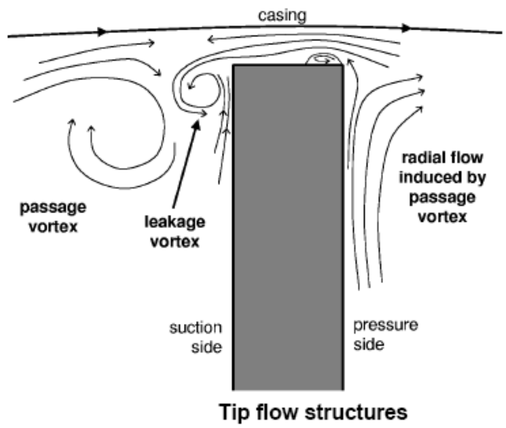

Figure 2.9: Diagram Showing Blade Tip Redesign without Modification (Kusterer et al. 2007)

The intensity of the leakage vortex strongly depends on the leakage mass flow rate, the velocity and their distribution along the blade chord. The quantity of leakage flow at positions in the front part induces higher loss than the portion in the rear part of the gap. This leakage mass flow can be reduced by means of geometric modifications inside or outside the radial gap as shown in Figure 2.10. In Figure 2.10, the blade tip is extended on the pressure side by a winglet like part with a constant thickness of the original trailing edge diameter at the tip edge. The geometric modification of the blade tip is to influence or guide the radial flow on the pressure side in a way that it is directed along the casing and away from the gap. Consequently, a reduced portion of this radial flow enters the tip clearance, but an increased amount is directed in opposite direction to the leakage flow. The resulting numerical analysis showed a reduction in the leakage vortex penetration of the main flow. According to the analysis, the leakage mass flow rate has been reduced by 7.2 % in blade 2 and 3.2 % in blade 3.

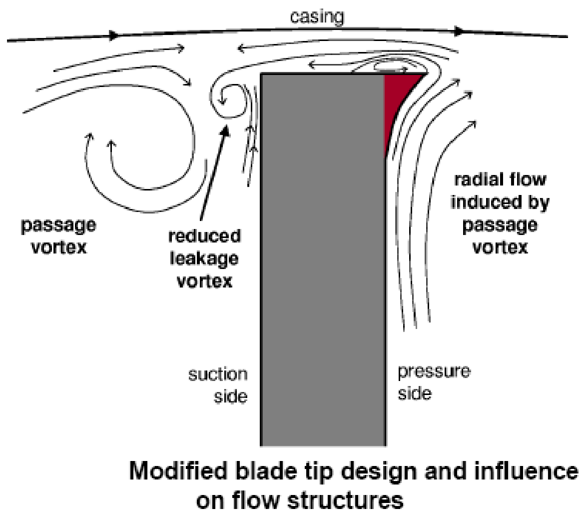

Figure 2.10: Diagram Showing Blade Tip Redesign with Modification (Kusterer et al. 2007)

2.2.1.4 Tip-gap geometry modification

Inoue et al. (2004) examined experimentally the effect of tip clearance on the occurrence of rotating stall, in a low-speed aerofoil compressor stage. The study was conducted for three axial gaps between the rotor and the front stator. The ratios of gap to axial chord length at the rotor tip are σ = 1.20, 0.75, and 0.35. The gap between the rotor and the rear stator was kept at 1.075 times the aerofoil chord length. The results shown by comparing the performance characteristic curve of pressure rise between small and large tip clearance indicate that the larger the gap the more possible the stall evolution.

Lu et al. (2005) carried out both numerical and experimental study of clearance levels and step profiles using eight different casing geometries to identify the effect of stepped tip gap on performance and flow field of a subsonic aerofoil-flow compressor rotor. In the analysis, it was concluded that pressure ratio, efficiency and stall margin of a subsonic rotor decrease with an increase in clearance, and that with increased tip gap over the aerofoil length of the rotor, the size and strength of the tip leakage vortex is increased, which in turn produces a larger source of low-energy blockage affecting the passage throughflow. However, if the stepped tip gap is included, it will alter the size and extent of the blockage to increase the passage throughflow area thereby yielding an improved performance of the compressor rotor.

Du et al. (2008) carried out a numerical investigation on the origination mechanism of unsteadiness in tip leakage flow for a transonic fan rotor. They observed that the self-induced unsteadiness of the tip leakage flows in this high-speed fan rotor is a result of dynamic interaction of two driving forces: the incoming main flow and the tip leakage flow. As these two flows impinge with each other at the tip region, an interface that separates the two flows is formed. It is found that among all the simulated cases, the self-induced unsteadiness exists when the size of the tip clearance equals or larger than design tip clearance of the computational model. It is further noticed that as the main flow rate is throttled down the tip leakage flow becomes comparatively stronger and leads to blockage of the main flow which can lead to compressor stall.

Deng et al. (2005) adopted numerical methods to clarify the unsteadiness of tip clearance flow in low-speed axial compressors, subjected to change in rotor performance and variable axial gap sizes between rotor and upstream and downstream stators. The result shows that within the computed range, there was a rise in pressure with a corresponding decrease of upstream axial gaps and none was observed with downstream stator meaning that the rotor performance is influenced more by upstream interaction than the downstream interaction.

Sirakov and Tan (2002) conducted an analysis using unsteady three-dimensional Reynolds averaged Navier-Stokes simulations to determine the effect of interaction between upstream wakes and rotor tip clearance flow in terms of average time performance. They concluded that strong interaction could decrease the tip region loss coefficient, and reduce the tip blockage and increase rotor passage static pressure rise coefficient.

2.2.2 Other tip clearance control methods

Other tip clearance control methods reviewed are mechanical and magnetic actuation, plasma actuation, the use of sensor and casing treatment schemes.

2.2.2.1 Mechanical, magnetic and sensor scheme

Spakovszky et al. (2001) documented the use of magnetic bearings for active modulation of HP compressor tip clearance for stall control. They carried out electro-magnetic and mechanical analysis of the magnetic bearing servo-actuator using the NASA Glenn high-speed single stage axial flow compressor to determine the benefit in stable compressor operating range. The simulation results yield a 2.3% reduction in stalling mass flow which is comparable to results with unsteady air injection. The results presented establish the viability of magnetic bearings for stall control in aero-engine high-speed compressors. Vakhtin et al. (2009) successfully built and tested a prototype sensor based on an interferometric ranging technique for monitoring tip clearances. The method provided measurement accuracy of better than ten micrometres. According to the designers, the mechanism is robust, inherently self-calibrating, and insensitive to environmental variations. The performance of the sensor was evaluated at both room temperature and inside a tube furnace to simulate the turbine environment. The spatial resolution, clearance measurement accuracy, clearance measurement range, and sensitivity of the prototype sensor were evaluated. The sensor system will provide a new tool for engine manufacturers to study and optimise blade tip clearance with high accuracy without the need for repetitive and cumbersome calibration procedures.

Jothiprasad et al. (2010) performed numerical simulations for the control of tip clearance flow in a low-speed axial compressor rotor with plasma actuation. This work investigates different dielectric barrier discharge (DBD) actuator configurations for affecting tip leakage flow and suppressing stall inception. The results show that the actuation reduced end-wall losses by increasing the static pressure of tip gap flow emerging from the blade suction side.

2.2.2.2 Casing treatment

Casing treatments can be used as an alternative to tip geometry modification. Casing treatment has been used to improve the control of stall in compressors. Beheshti et al. (2004) investigated numerically the effect of casing treatment on performance and stability of transonic axial compressors and found that casing treatment using slots and grooves increases the casing diameter of the area surrounding the rotor blade while the clearance remains constant and this reduces tip leakage flow through the end-wall zone and improves the compressor efficiency.

Lu et al. (2007) identified in their paper that the primary stall margin enhancement by casing treatment was made possible by the manipulation of tip clearance flow using slots and grooves in the shroud over the tips of compressor blades. A detailed computational analysis of flow interaction between the casing treatment and tip leakage flow under subsonic conditions shows that the use of circumferential grooves and axial skewed slots reposition the tip clearance vortex, delay the movement of the incoming/tip clearance flow interface thereby extending the compressor stall margin and thus delaying the inception of stall.

Zhao et al. (2010) performed a numerical investigation for the effects of circumferential grooves on the unsteadiness of tip clearance flow to enhance compressor flow instability. They concluded that circumferential groove casing treatment can suppress the unsteadiness of tip clearance flow by reducing the axial momentum of the flow, thereby changing the balance of the tip leakage flow and incoming main flow. The groove also reforms the tip region flow by inducing radial movement and tangential movement and hence, useful for improving compressor performance to intensify the radial and tangential movement.

2.3 Tip clearance control concepts patents

As stated in section 2.2, very few papers were found which relate directly to actual clearance control techniques. Nevertheless, 100 United State Patents and European Union patents protecting various active and passive clearance control concepts were reviewed. The concepts were compiled into the NEWAC Clearance control patent database which was useful for quick access to the patent space during the brainstorming phase of the

NEWAC project and for future reference as shown in Figure 2.11. The patents are given a category in terms of the type of clearance control system, the area of application in the engine, and clearance control techniques used. The most significant aspect in the patents review is their claims. The claims are the apparatus and methods used for solving problems. They concepts claims in the patents can generally be grouped into passive and active clearance control techniques. Section 2.3.1 described types of clearance control system while some of the patents reviews are deal with in details in section 2.3.2. The summary of others in terms of manufacturing company, year and a brief description of the patents and their claims are presented in Appendix 2.1

2.3.1 Types of clearance control system

There are two major clearance concepts group known as passive clearance control (PCC) and active clearance control (ACC) methods. These concepts can be further group into five categories, passive thermal, passive pneumatic active thermal, active mechanical and active pneumatic. For details on the five categories the reader is referred to Lattime and Steinetz (2002).

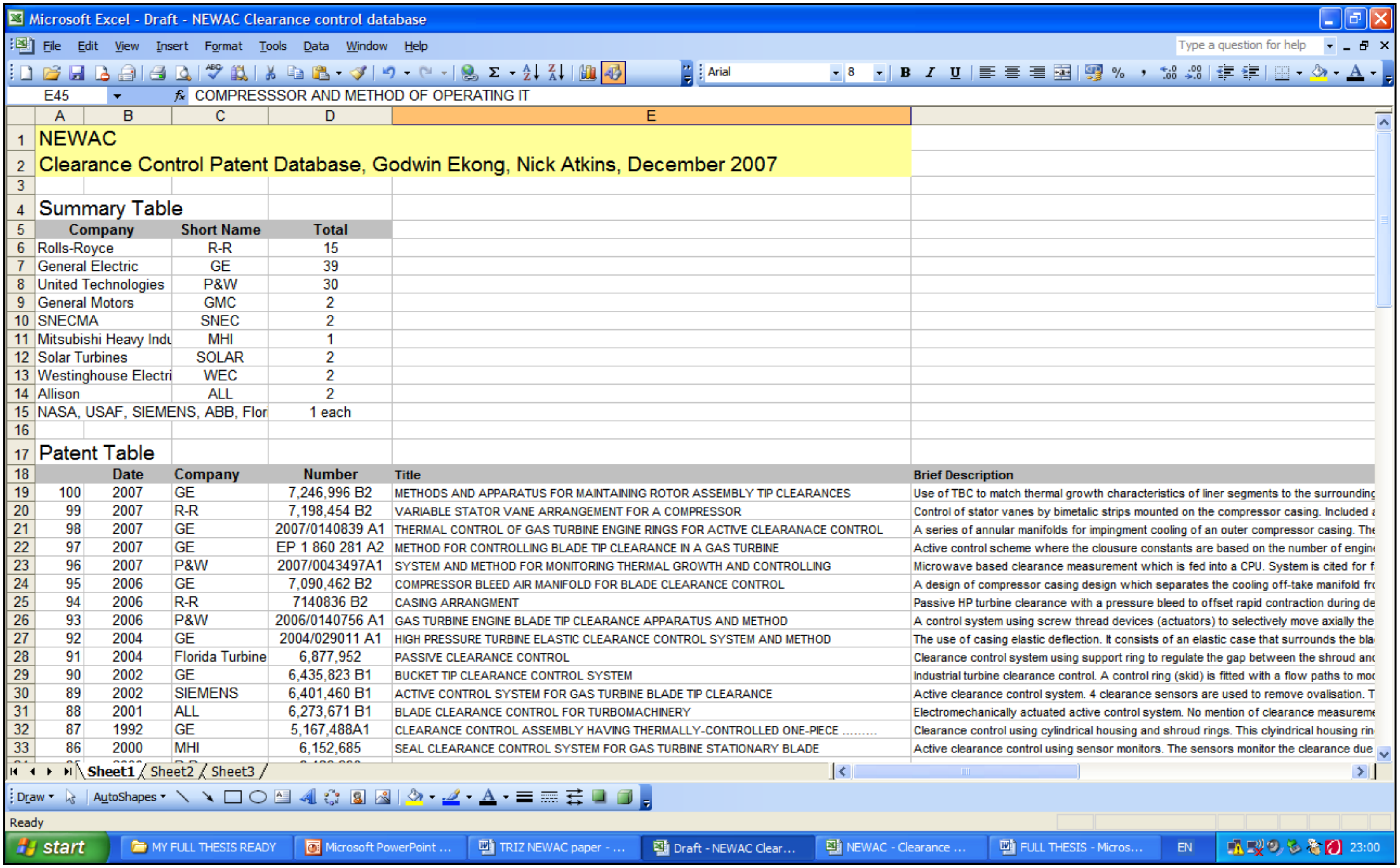

NEWAC

Clearance Control Patent Database, Godwin Ekong, Nick Atkins, December 2007

Summary Table

Company	Short Name	Total
Rolls-Royce	R-R	15
General Electric	GE	39
United Technologies	P&W	30
General Motors	GMC	2
SNECMA	SNEC	2
Mitsubishi Heavy Indu	MHI	1
Solar Turbines	SOLAR	2
Westinghouse Electri	WEC	2
Allison	ALL	2
NASA, USAF, SIEMENS, ABB, Flor		1 each

Patent Table

	Date	Company	Number	Title	Brief Description
100	2007	GE	7,246,996 B2	METHODS AND APPARATUS FOR MAINTAINING ROTOR ASSEMBLY TIP CLEARANCES	Use of TBC to match thermal growth characteristics of liner segments to the surrounding
99	2007	R-R	7,198,454 B2	VARIABLE STATOR VANE ARRANGEMENT FOR A COMPRESSOR	Control of stator vanes by bimetalic strips mounted on the compressor casing. Included
98	2007	GE	2007/0140839 A1	THERMAL CONTROL OF GAS TURBINE ENGINE RINGS FOR ACTIVE CLEARANACE CONTROL	A series of annular manifolds for impingment cooling of an outer compressor casing. The
97	2007	GE	EP 1 860 281 A2	METHOD FOR CONTROLLING BLADE TIP CLEARANCE IN A GAS TURBINE	Active control scheme where the clousure constants are based on the number of engin
96	2007	P&W	2007/0043497A1	SYSTEM AND METHOD FOR MONITORING THERMAL GROWTH AND CONTROLLING	Microwave based clearance measurement which is fed into a CPU. System is cited for f
95	2006	GE	7,090,462 B2	COMPRESSOR BLEED AIR MANIFOLD FOR BLADE CLEARANCE CONTROL	A design of compressor casing design which separates the cooling off-take manifold fr
94	2006	R-R	7140836 B2	CASING ARRANGMENT	Passive HP turbine clearance with a pressure bleed to offset rapid contraction during de
93	2006	P&W	2006/0140756 A1	GAS TURBINE ENGINE BLADE TIP CLEARANCE APPARATUS AND METHOD	A control system using screw thread devices (actuators) to selectively move axially the
92	2004	GE	2004/029011 A1	HIGH PRESSURE TURBINE ELASTIC CLEARANCE CONTROL SYSTEM AND METHOD	The use of casing elastic deflection. It consists of an elastic case that surrounds the bla
91	2004	Florida Turbine	6,877,952	PASSIVE CLEARANCE CONTROL	Clearance control system using support ring to regulate the gap between the shroud and
90	2002	GE	6,435,823 B1	BUCKET TIP CLEARANCE CONTROL SYSTEM	Industrial turbine clearance control. A control ring (skid) is fitted with a flow paths to mo
89	2002	SIEMENS	6,401,460 B1	ACTIVE CONTROL SYSTEM FOR GAS TURBINE BLADE TIP CLEARANCE	Active clearance control system. 4 clearance sensors are used to remove ovalisation. T
88	2001	ALL	6,273,671 B1	BLADE CLEARANCE CONTROL FOR TURBOMACHINERY	Electromechanically actuated active control system. No mention of clearance measureme
87	1992	GE	5,167,488A1	CLEARANCE CONTROL ASSEMBLY HAVING THERMALLY-CONTROLLED ONE-PIECE	Clearance control using cylindrical housing and shroud rings. This cylindrical housing rin
86	2000	MHI	6,152,685	SEAL CLEARANCE CONTROL SYSTEM FOR GAS TURBINE STATIONARY BLADE	Active clearance control using sensor monitors. The sensors monitor the clearance due

Figure 2.11: NEWAC Clearance control patent database

2.3.1.1 Passive clearance control system

A passive clearance control system is any system that sets the desired clearance at one operating point. Passive thermal scheme depend on material properties and engine operating temperatures to match the rotor and stator growths thus control tip clearance in a gas turbine engine. Passive control schemes include the use of slugging rings, directing of bleed air from the forward compressor stage over the casing of later stages during cruise operation in the engine. Another method is the use of hot gas from later stages to expand the casing when necessary, and then using colder air (even bypass in some cases) during cruise. The patent claims concerning passive control schemes are:

- The use of thermal barrier coating (TBC) on structural components to slow the thermal response
- Use of honeycomb to insulate parts of the structure
- Passive bimetallic control of stator vanes
- Pressure based system to balance rapid contraction during deceleration
- Thermal actuation schemes
- Numerous structural schemes to help thermal control
- Flanges with high expansion coefficient in a segmented impingement ring
- Bore ventilation schemes, including selective heating
- Metering of forward and rearward bleed air onto the compressor casing
- Passive control using a valve with passive thermal control
- Cam-based actuation
- Intersecting passage(s) to induce aerodynamic seals in passive control
- Passive system with a slugging ring

2.3.1.2 Active clearance control system

An active clearance control system is any system that allows the independent setting of a desired clearance at more than one operating point. Active clearance scheme make use of compressor and fan air to heat to expand or cool to contract shroud seal segment support to vary clearance. Active control schemes consist of both open loop and closed loop active systems. The open loop systems monitor the rpm and/or turbine inlet temperature. Others active control schemes uses delays to accommodate transient behaviour, with another making use of actual engine history (i.e. flight cycles) to modify the control parameters. The closed loop active systems directly monitor the tip clearance such as those using sensors. Active clearance control have the benefit of being able to be turned off when unneeded and turn on when required and can force the flow using either temporally steady or unsteady modes of operation Ness II (2009). The patent claims with active control schemes are:

- Many impingement manifold schemes (including use of bypass flow)
- Electric motor based system using axial movement and hade
- Pressure based system using axial movement and hade
- Pressure balance on thin outer casing (multiple patents)
- Electromechanical/Electromagnetic
- Fully active cooling of labseal gaps – thermal actuation
- External supplies of heat – electric and unspecified
- Magnetic bearings in fully active control – eccentricity only
- Electrical heating of compressor air for thermal control of clearances
- Fully active system with sensors and piezo actuation

- Modulation of casing temperature using a dual air source
- Plasma actuators

2.3.2 Review of patents

This section presents the review of some of the patent in detail taking into consideration their claims. The patents dealt with are Gaul, 1997, Albers et al., 2004, Mills et al., 1994, Deveau et al., 1985, Cline et al., 1982, Johnston et al., 1982 and Hallinger et al., 1976. Details of other patents can be found in appendix 2.1.

US 5667358 (Gaul, 1997) is a US patent claimed and protected by Westinghouse Electric (WEC). This is an active clearance control scheme controlled by heating a support ring. Figure 2.12 shows a plot of the blade tip clearance over time with and without the use of the blade tip clearance control method proposed by this invention.

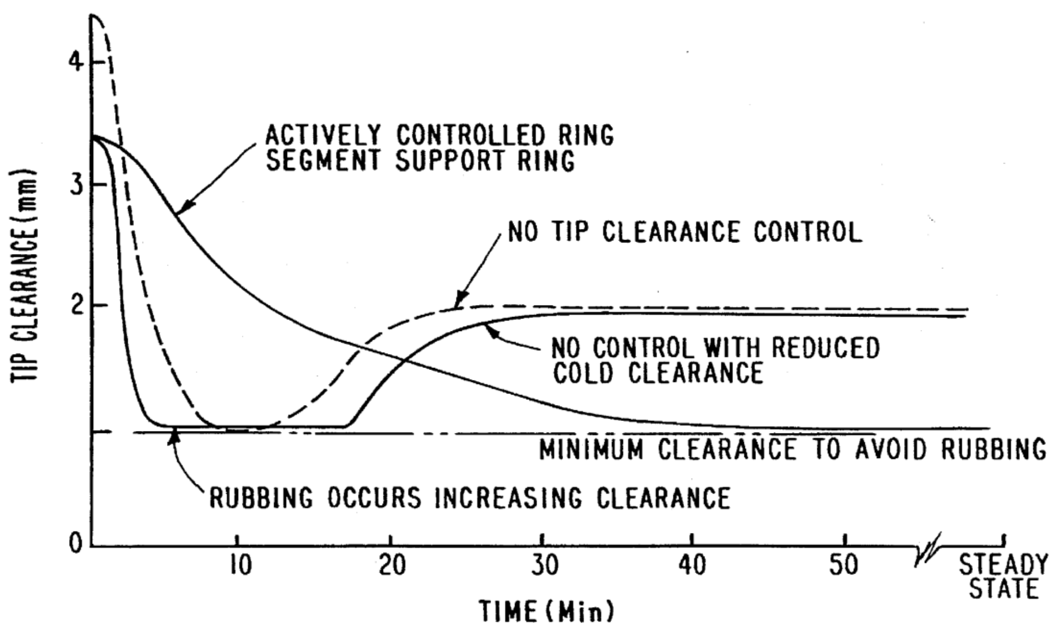

Figure 2.12: A plot of the blade tip clearance over time with and without the use of the blade tip clearance control method of the Gaul (1997) invention

During the transient period, the diameter of the outer gas path casing is increased. The outer casing is heated during transient periods to increase its diameter relative to the blade tip hence resulting in a reduction in the cold tip clearance and consequently providing a steady state running clearance.

US 029011 A1 (Albers et al., 2004) is a US patent claimed and protected by General Electric (GE), which involves the use of casing mechanical deflection to control clearance during engine transient operation. An elastic case surrounds the blade tip and shroud, and radially deflects in response to pressure differences. Figure 2.13 presents a thin case active clearance control according to this invention, while Figure 2.14 depicts a comparison between the radial deflection of the rotor and stator of this invention during the various engine operations.

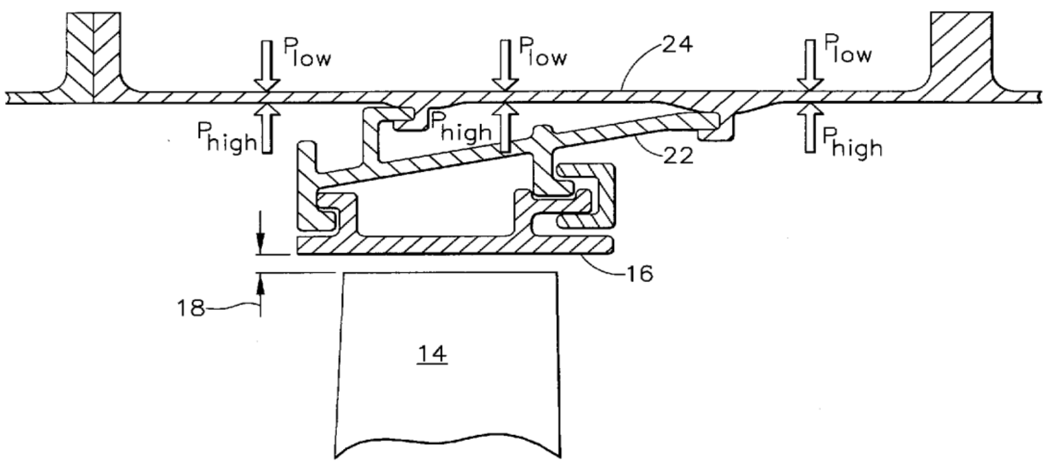

Figure 2.13: A thin case active clearance control according to the invention of Albers et al. (2004)

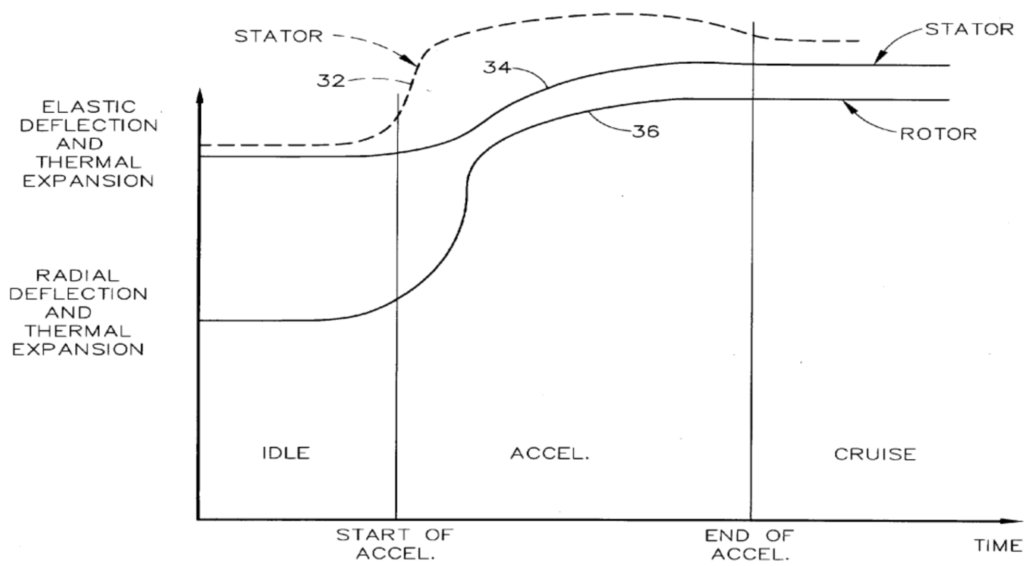

Figure 2.14: A comparison of the radial deflection of the rotor and stator of the invention of Albers et al. (2004) during different engine operations

US 5351732 (Mills et al., 1994) is a US patent claimed and protected by Rolls-Royce, which shows a thermal clearance control with logic control process that regulates the distribution of the cooling air from the forward to rearward regions of the engine casing. In this system, a casing cooling system operates in one of two conditions, such as the operation at engine cruise where all the cooling air is initially directed onto a specific region of the casing, and under full power conditions, where some of the cooling air is directed onto the specific region and the remainder is directed onto the remainder of the casing; this operation by the cooling system helps optimise the turbine blade and casing radial clearance. Figure 2.15 is an enlarged view of this invention which consists of a manifold (34) located radially outwardly of the portion of the casing (20) which surrounds the rotor blade (23). This manifold (34) is supported by a number of cooling air feed pipes (35) which are equally spaced around the turbine and supported by a cowling

(32). A sealing member (36) is located approximately half way along the axial length of the manifold to radially space apart the manifold and the casing.

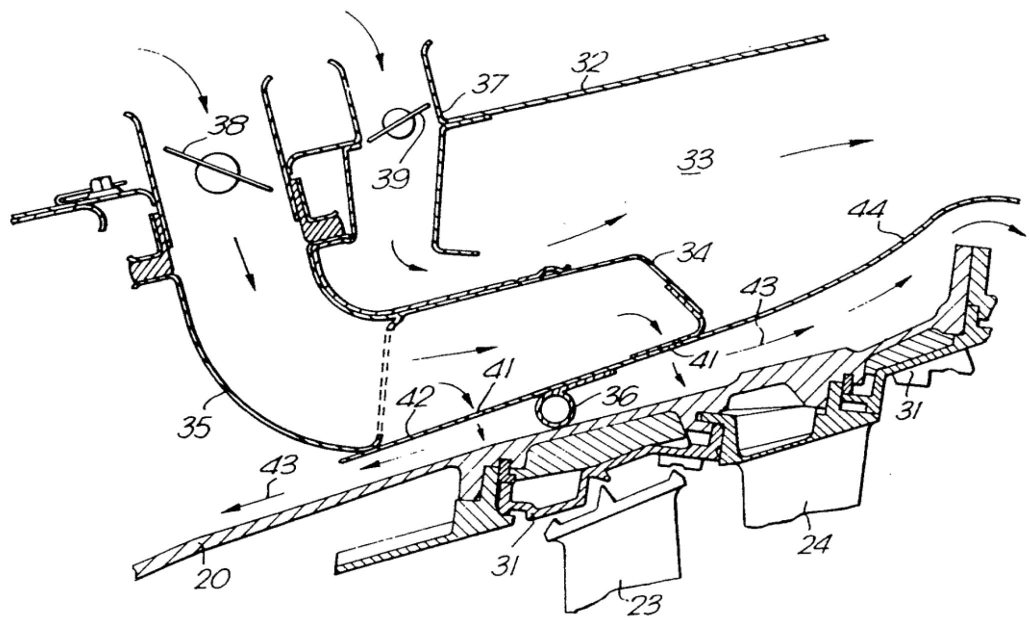

Figure 2.15: An enlarged view of the Mills et al. (1994) invention

US 4513567 (Deveau et al., 1985) is a US patent claimed and protected by United Technologies Corp. (Pratt & Whitney). In this patent, a dual air source is utilized for temperature modification of the casing in response to the engine operating conditions in order to control the clearance between the rotating and stationary elements of the engine. The concept employs casing heating and casing cooling in accordance with the engine cycle to achieve good clearance between the rotor and the casing supporting the seals. The modifying air comprises of different percentages of heating and cooling air ducted from the engine compressor to the casing segment to be cooled. Figure 2.16 shows a pinch point diagram illustrating the relative thermal growth between the rotor and stator of this invention.

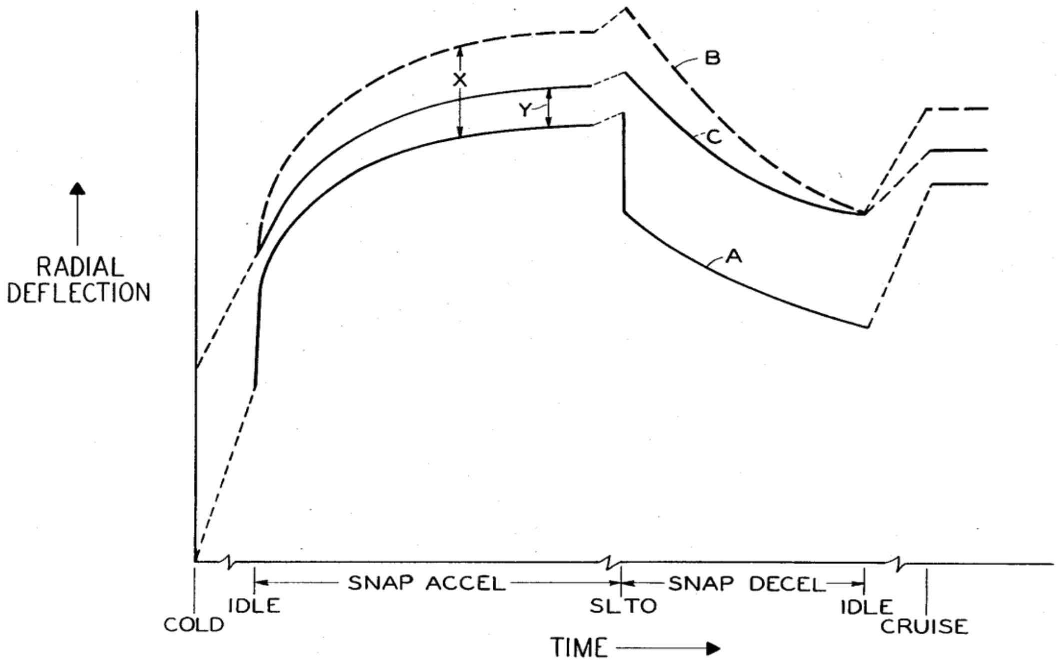

Figure 2.16: A pinch point diagram illustrating relative thermal growth between the rotor and stator of the Deveau et al. (1985) invention

As shown in Figure 2.16, the clearance varies widely over the operating range of the engine as the casing and rotor blades are subjected to different thermal conditions. The radial position of the rotor blade tips is indicated by curve A, while curve B represents the radial position of the outer seal at the corresponding turbine location of the rotor blade tips as a function of the engine operating condition. The position of the outer seal relative to the rotor blade tip is a function of the diameter of the engine case supporting the outer seal and of the temperature of the rotor blade. The gap (X) between the two curves A and B, shows the expected clearance between the rotor blade tip and the casing in an engine without the active clearance control scheme. However, using the active clearance control scheme of this invention with appropriate parameters, shaft RPM and flight Mach number, the radial position of the outer air seal is reduced, as represented by curve C, as it varies in respect to the engine operating. The gap (Y) represents the achievable clearance between the rotor blade tip and the corresponding outer air seal supported by the casing. This gives the minimum clearance necessary to avoid destructive disturbances during engine operation.

US 4363599 (Cline et al., 1982) is a US patent claimed and protected by General Electric (GE). In this claim, control rings are integrated into the turbine casing to expand and contract in order to control the clearance position of the turbine shroud. The invention consists of a number of control rings, integrated into the turbine casing, that thermally expand and contract. During engine operation, compressor air is ducted through internal passages in the rings to cause this expansion and contraction.

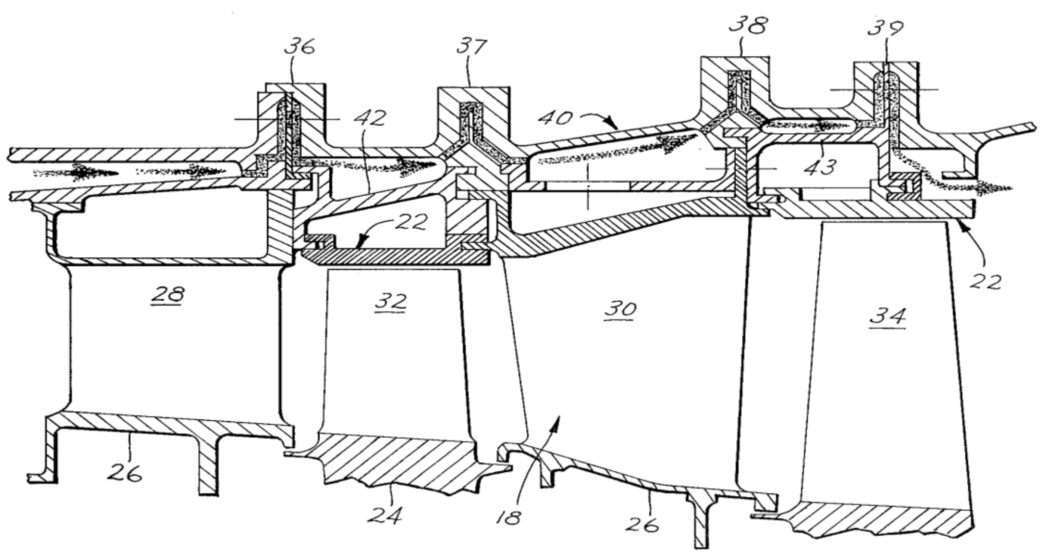

Figure 2.17: An enlarged sectional view of a high pressure turbine of a gas turbine engine incorporating one embodiment of the Cline et al. (1982) invention

Figure 2.17 shows an enlarged sectional view of a high pressure turbine of a gas turbine engine incorporating one embodiment with the control rings labelled 36, 37, 38 and 39. The system makes use of the pressure and temperature of the compressor air, together with the size, location and structure of the control rings, to match the thermal growth of the turbine, thus controlling clearance. In another embodiment, interstages bleed air from the upstream compressor stages could be used to control all or a number of selected rings. The radial movement of the control rings 36, 37, 38 and 39 is transferred to the turbine shroud (22) through the shroud supports (42 and 43). Each of the rings is carefully positioned radially outward of the side, and this allows the ring to directly affect the expansion and contraction of a shroud support, thereby controlling the clearance.

Figure 2.18 and Figure 2.19 shows the turbine stator and rotor profiles during acceleration and deceleration of the engine for the present invention.

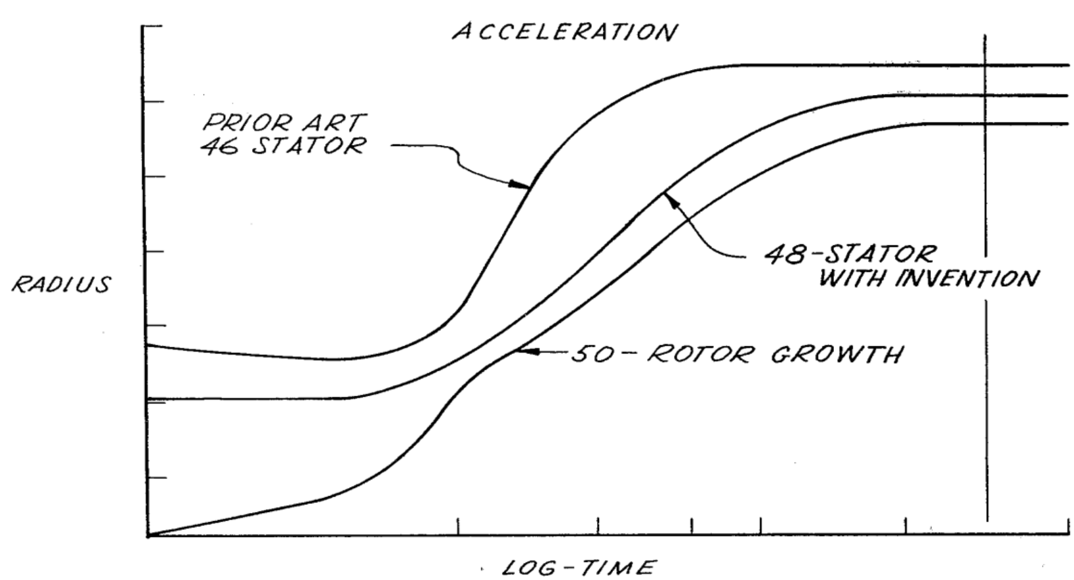

Figure 2.18: Graphical representation of turbine stator and rotor growth from idle engine to full throttle conditions Cline et al. (1982) invention

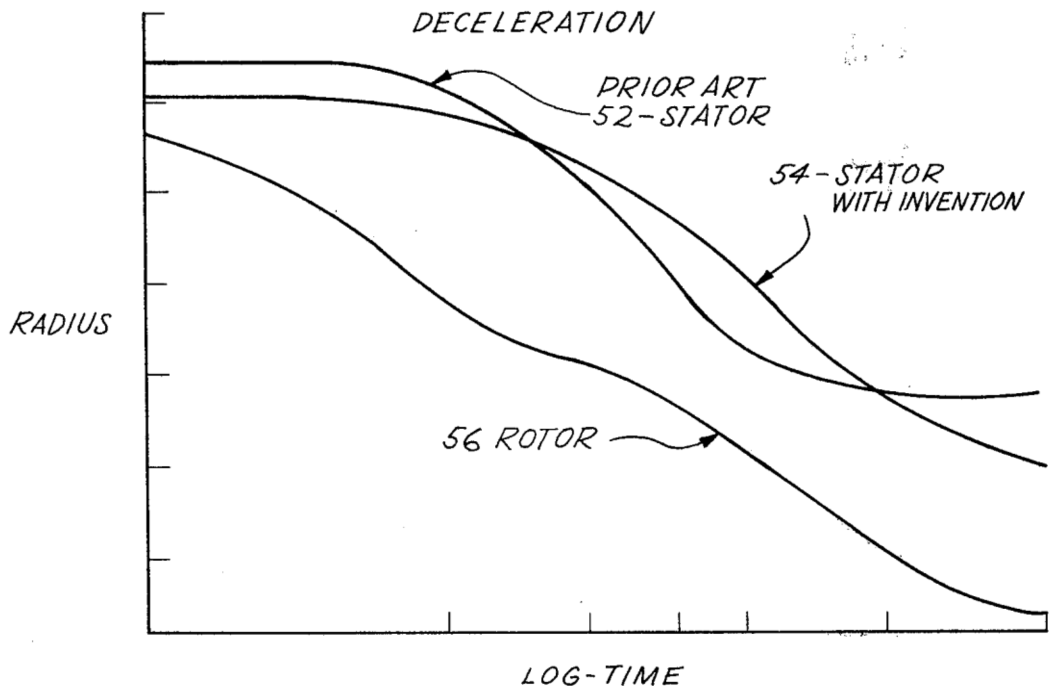

Figure 2.19: Graphical representation of turbine stator and rotor shrinkage from engine at full throttle to idle conditions Cline et al. (1982) invention

During acceleration, the stator profile (48) is reduced, thereby reducing the clearance between the engine stator and rotor. A similar effect is seen during deceleration, where the stator profile (54) is reduced, thereby reducing the clearance between the engine stator and rotor.

US 4329114 (Johnston et al., 1982) is a US patent claimed and protected by the National Aeronautics and Space Administration (NASA). This is an active clearance control system patent, The claim includes an improved clearance control system for turbomachinery, incorporating a number of rotor stages surrounded in close radial relationship by a stator structure. The improvement comprises of a means for introducing a flow of cooling air along an axial path at the outer surface of the stator structure to inhibit thermal expansion. The means for introducing the flow includes a method for bleeding fluid from the compressor, and a means for selectively diverting the flow of cooling air from the axial path during predetermined conditions of the turbomachine operation. This patent states that during steady state operation, cooling air is ducted from a low-pressure stage onto the casing of the higher-pressure stages, and a valve is provided to divert this cooling air during transients to slow the response of the casing. The valve is operated by a pneumatic or hydraulic energy source, based on the revolution per minute (rpm), via a controller. This arrangement is shown in Figure 2.20 and Figure 2.21.

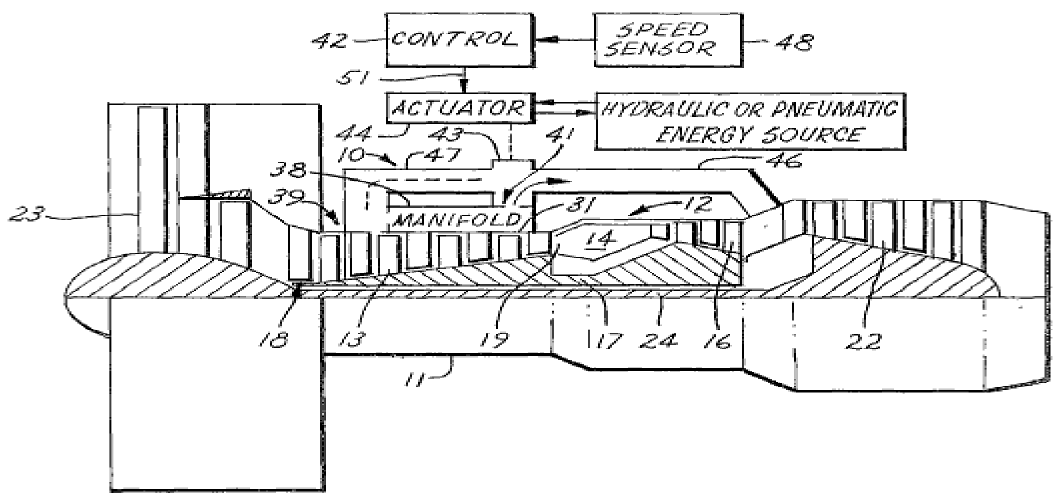

Figure 2.20: A schematic illustration of the gas turbine engine incorporating the Johnston et al. (1982) invention

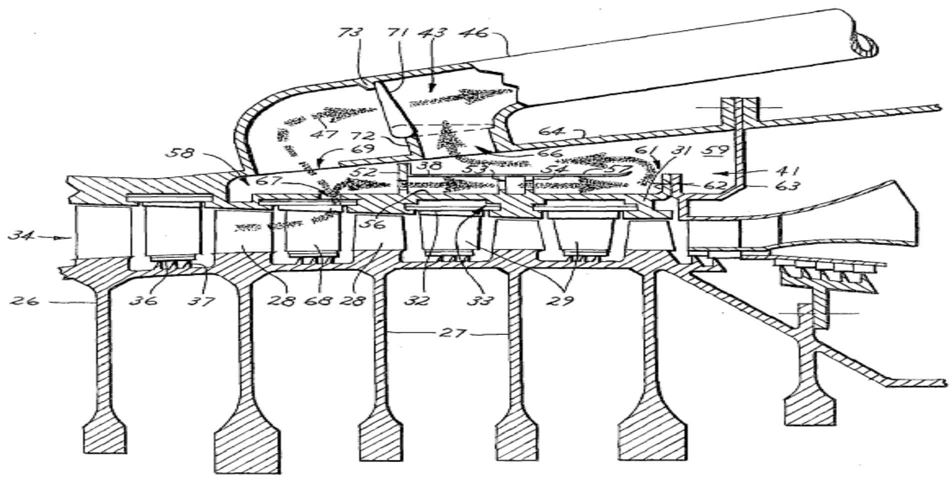

Figure 2.21: An axial cross-sectional view of the upper portion of the compressor incorporating the Johnston et al. (1982) invention

US 3975901 (Hallinger et al., 1976) is a US patent claimed and protected by SNECMA (SNEC). An element of this invention is to provide a device that will regulate clearance between the tips of the rotor blades and the adjacent wall of the stator of the turbine in a gas turbine engine. This involves a means for directing a gaseous flow against the wall in order to regulate its temperature. According to the invention, the system includes a proportioner with at least two inlet passages connected to gas sources at different temperatures, controlled by the thermal expansion of an obturator which is responsive to the temperature of the fluid passing through the turbine. During engine operation, the temperature of the gaseous flow is reduced when the obturator expands and thereby cools the stator when in a stable condition and heats it up during transient conditions, hence controlling the clearance (J) between the rotor blade tips and the adjacent wall of the stator of the turbine. Figure 2.22 shows an axial half–sectional view of a part of a gas turbine incorporating the regulating device called the proportioner (15) and the obturator (8).

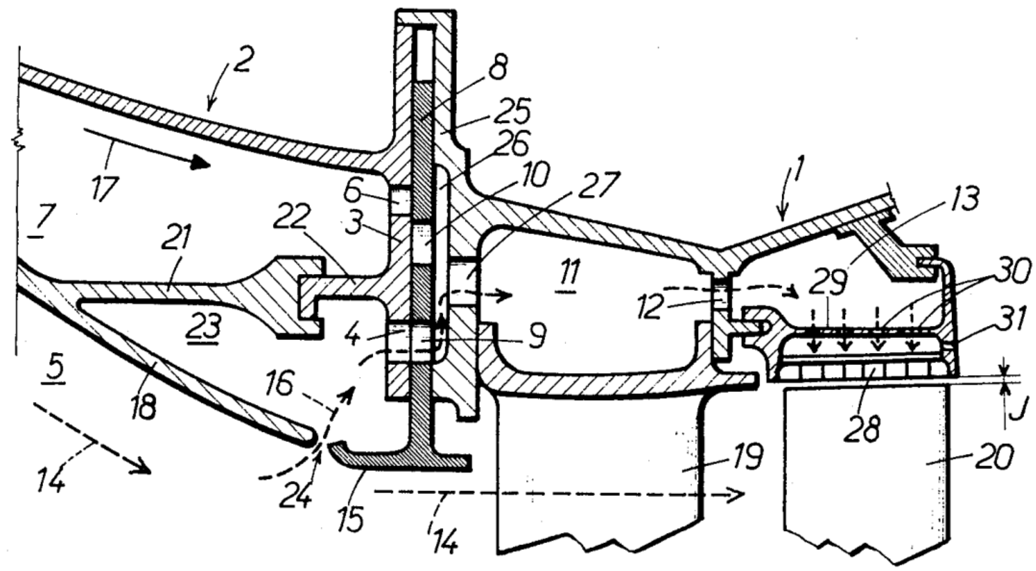

Figure 2.22: An axial half–sectional view of a part of a gas turbine incorporating the Hallinger et al. (1976) invention

2.3.2.1 Section Summary

This section has presented a patent review for tip clearance control in gas turbine engines. It provides information on the various way of controlling tip clearance in gas turbine engine. The patent search and review become imperative due lack of many open literatures on the actual method of controlling of tip clearance during engine transient. The patents were given correct interpretation in terms of the type of control system, the area of application on the engine, and the control scheme. These were grouped into passive clearance control system and active clearance control system. The results of the patent search and review are documented in NEWAC clearance control database and were very useful in the brainstorming phase of this project. It was during these sessions that the selection of the concept for the control of tip clearance reported in this study was chosen.

2.4 The Fluid Dynamics and Heat Transfer of Rotating Flows

A review of previous investigations on flow structures performed by other authors and researchers is presented here in order to get an idea of the flow field in a heated rotating cavity with axial throughflow and radial inflow as well as their effect on tip clearance in high pressure compressor during engine transient. In this section, the basic parameters relevant to rotating cavities and particularly to the case of rotating cavities with axial throughflow and radial inflow are explained, and the fluid dynamics and heat transfer of rotating flows are discussed. The rotating cavities with radial inflow and axial throughflow which are directly relevant to the research reported in this thesis are illustrated in Figure 2.23; the main features of these flows are discussed here and also to help in highlighting the complexity of the rotationally-induced buoyancy-driven flows. Only a brief review will be given here and the reader is referred to the work by Dorfman (1963), Chew (1982), Pincombe (1983), Long (1984), Farthing (1988), Owen and Rogers (1989), Tucker (1993), Owen and Rogers (1995) and Childs (2011) for more details of the study and the various rotating flow configurations. Identifying the flow structure and heat transfer inside a rotating cavity is important for designers since temperature gradients generate additional thermal stress and influence the linear expansion of the disc. This effect is notice during engine transient of (acceleration, deceleration and cruise).

During start and take-off condition the discs are colder than the incoming air, which is defined as an inverse temperature situation or heating flow. A normal temperature situation or cooling flow occurs during cruise and approach when the hot discs are cooled by air Günther – *W* et al. (2013).

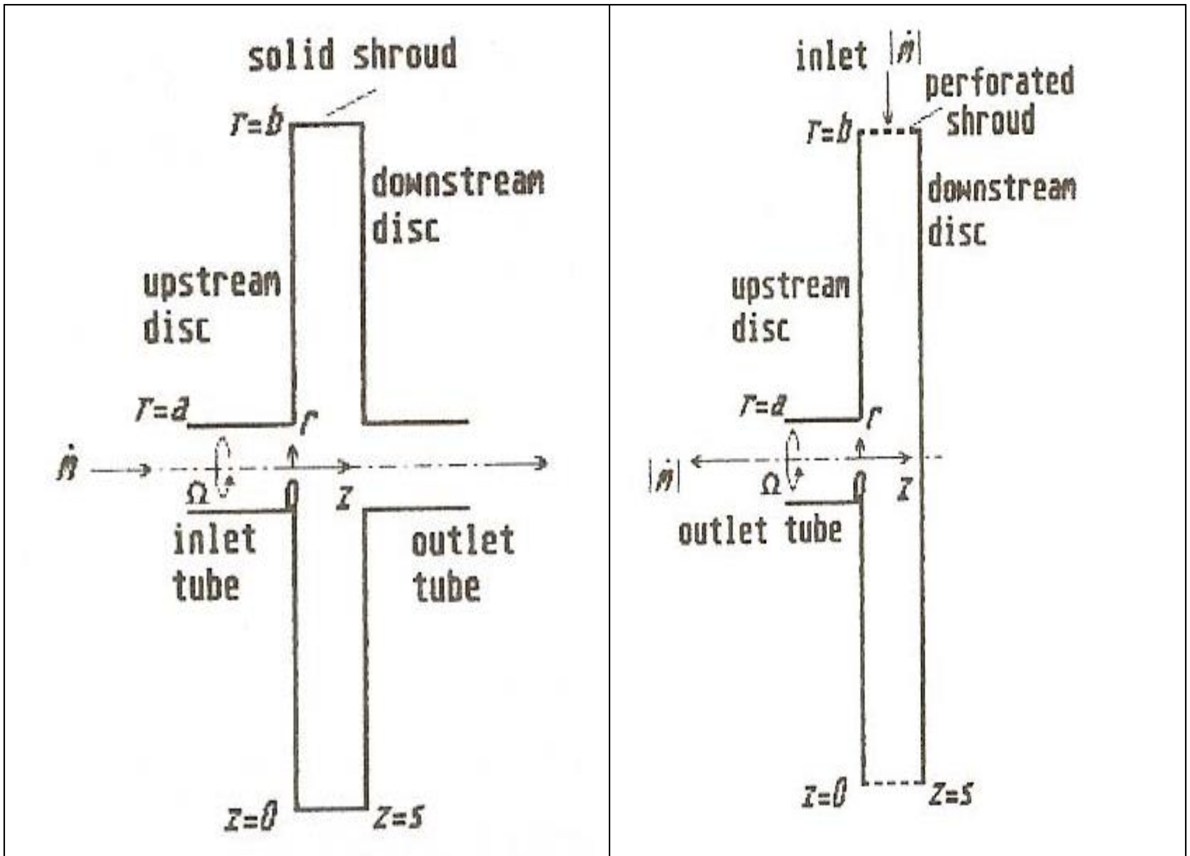

(a) Axial throughflow	(b) Radial inflow

Figure 2.23: Two types of cavity flow relevant to this thesis from Owen and Rogers (1995)

2.4.1 Parameters and Dimensionless Groups

The basic dimensionless flow parameters relevant to rotating cavities and particularly to the case of rotating cavities with axial throughflow and radial inflow which are useful for characterising the flow conditions within a rotating system are defined here. They are Reynolds number Re_ϕ, axial Reynolds number Re_z, Rossby number Ro_z and the Grashof number Gr. These non- dimensional parameters were matched to the multiple cavity rig conditions in Table 3.2 and use for the analysis in Chapter 6. Figure 2.21 illustrates a simplified model of a single rotating cavity with two discs separated from each other by a shroud of axial gap s. The outside radius of the discs is *b*, while the inside radius of the discs, or bore, is *a*. The gap ratio of the cavity *G* is defined as:

$$G = \frac{s}{b} \tag{2.1}$$

The cavity usually rotates around a central shaft of diameter r_s. This shaft can be stationary or may rotate. The rotational speed of the cavity is Ω and the bulk average velocity of the axial throughflow is W.

$$W = \frac{\dot{m}}{\rho A_{an}} \tag{2.2}$$

where $\dot{m}$ = mass flow rate of air that flow through the cavity

ρ = density of inlet air

$A_{an} = \left(a^2 - r_s{}^2\right)$ = shaft annulus area

For a fluid of kinematic viscosity ν (Long et al.), the rotational Reynolds number is defined as:

$$\mathrm{Re}_\phi = \frac{\Omega b^2}{\nu} \qquad \textbf{(2.3)}$$

The rotational Reynolds number Re_ϕ is the parameter that is relevant to the rotation of the cavity. The axial Reynolds numbers which is the parameter that characterises the axial throughflow of air is defined as:

$$\mathrm{Re}_Z = \frac{W d_h}{\nu} \qquad \textbf{(2.4)}$$

where d_h is the hydraulic diameter of the inlet. In case of a cavity without an inner shaft, $d_h = 2a$, while for one with an inner shaft of radius, r_s, $d_h = 2(a - r_s)$. Other non-dimensional parameters relevant to flow in rotating cavity are the Rossby number and the Grashof number. The Rossby number, Ro is defined as the ratio of the mean velocity of the throughflow to the tangential velocity of the disc at the bore radius:

$$Ro = \frac{W}{\Omega a} \qquad \textbf{(2.5)}$$

The Rossby number Ro links the effect of both rotation and the inertia of the throughflow. The Rossby number, Ro can also be expressed in terms of the rotational and axial Reynolds numbers as:

$$Ro = \frac{b^2 \mathrm{Re}_z}{2a(a - r_s)\mathrm{Re}_\phi} \qquad \textbf{(2.6)}$$

The Grashof number Gr is a non-dimensional quantity in fluid dynamics and heat transfer which approximates the ratio of the buoyancy to viscous force acting on a fluid. This is defined as:

$$Gr = \frac{\Omega^2 b \beta \Delta T L^3}{\nu^2} \qquad \textbf{(2.7)}$$

where β is the volume expansion coefficient. $\beta = \frac{1}{T}$ where T is the absolute temperature of the throughflow air. ΔT is the temperature difference between the supply air and the local surface temperature at the radius r considered, $\Delta T = (T_s - T_\infty)$. T_s is the surface temperature, T_∞ is the bulk temperature, b is the outer radius, v is the kinematic viscosity and L is the length. The length L can also be represented with y as $y = (b - r)$ which is the distance radially inward from the shroud. This is taken as the length parameter for this instance of Grashof number, with its value increasing against the gravitational field direction. In a rotating cavity application according to Farthing et al. (1992b), the term of Grashof number based on the radial distance along the disc surface is based on the local surface temperature and its relative centripetal acceleration by taking y as a height reference from the shroud. For a vertical plate, the flow transitions to turbulent around a Grashof number of 10^9

Another group of non-dimensional parameters are those relevant to thermal boundary layers and heat transfer in rotating cavity. These are the Prandtl number, Rayleigh number Ra and Nusselt number Nu.

The Prandtl number Pr is a dimensionless property of a fluid. It is the ratio of the kinematic viscosity to the thermal diffusivity at a given point. This is defined as:

$$\mathrm{Pr} = \frac{\nu}{\alpha} \qquad \textbf{(2.8)}$$

where v is the kinematic viscosity, defined as $\nu = \frac{\mu}{\rho}$ measure in m^2 / s and α is the thermal diffusivity, defined as $\alpha = \frac{k}{(\rho c_p)}$ measure in m^2 / s. The Prandtl number can also be defined as the ratio of viscous diffusion rate to thermal diffusion rate, given as $\left(\Pr = \frac{\mu c_p}{k} \right)$, where μ is dynamic viscosity in $Pas = (Ns)/m^2$, k is thermal conductivity in W/ (m K), c_p is specific heat $J/(kgK)$ and ρ is density in kg/m^3.

Increases of viscosity indicate an increase of δ and equally, the thickness of the thermal boundary layer is in relation with the thermal diffusivity. Prandtl number is important being a measure of the relative thickness of the velocity and thermal boundary layers.

Rayleigh number Ra is a non-dimensional parameter expressed as the product of the Grashof number and the Prandtl number.

$$Ra = Gr.\Pr \qquad \textbf{(2.9)}$$

For free convection near a vertical smooth surface (plate), the Rayleigh number Ra can also be written as:

$$Ra = Gr.\Pr = \frac{g.\beta}{\nu.\alpha} \Delta T.L^3 \qquad \textbf{(2.10)}$$

It is associated with buoyancy driven flow known as free convection or natural convection and also relates to the heat transfer within the fluid. If the Ra is less than the critical value for that fluid, heat transfer is primary in the form of conduction when it goes beyond the critical value; heat transfer is primarily in the form of convection.

The Nusselt number Nu is a dimensionless heat transfer coefficient. This is the ratio of convective heat transfer to conductive heat transfer through the fluid. Nusselt number can be thought of as the heat transfer coefficients multiply by the characteristic length divided by the thermal conductivity of the fluid. This is presented for a plate as:

$$Nu_L = \frac{hL}{k_f} \tag{2. 11}$$

The Nusselt number Nu_x denotes the heat transfer coefficient at x called the local Nusselt number where x is used for the characteristic dimension, Nu_L local Nusselt number value based on plate length, Nu_D local Nusselt number value based on cylinder diameter and Nu_{av} the average Nusselt number. The average Nusselt number can be expressed as a function of the Rayleigh number and the Prandtl number in the form of $Nu = f(Ra, \mathrm{Pr})$ for free convection and for forced convection, Nusselt number is a function of the Reynolds number and the Prandtl number in the form of $Nu = f(\mathrm{Re}, \mathrm{Pr})$. Empirical correlations that express the Nusselt number in the aforementioned forms used for heat transfer coefficient calculations in the models presented in this thesis are presented in Section 3.9.

2.5 The free disc

The fluid dynamics and heat transfer of the free disc have been studied extensively. It is a useful starting point for rotating flow theory is the so called free disc. The free disc is used to illustrate a rotating disc in a quiescent environment. A complete review has not been attempted here, and for a more detailed discussion on the subject of the free disc the reader is referred to Dorfman (1963), Owen and Rogers (1989), Owen and Rogers (1995) and Childs (2011). The work presented in this section is relevant to clearance control in H.P. compressors as it help to give an inside to fluid flow and heat transfer mechanism in H.P. compressor. The discs inside the rotating cavity behave as a free disc as such the free disc analysis is use as a starting point in this review.

A schematic diagram of the flow structure due to a free disc is shown in Figure 2.24. This is plane disc which has an outer radius b and rotates with angular velocity Ω around the z-axis, in an initially stationary fluid of density ρ, kinematic viscosity ν, thermal conductivity k and specific heat Cp.

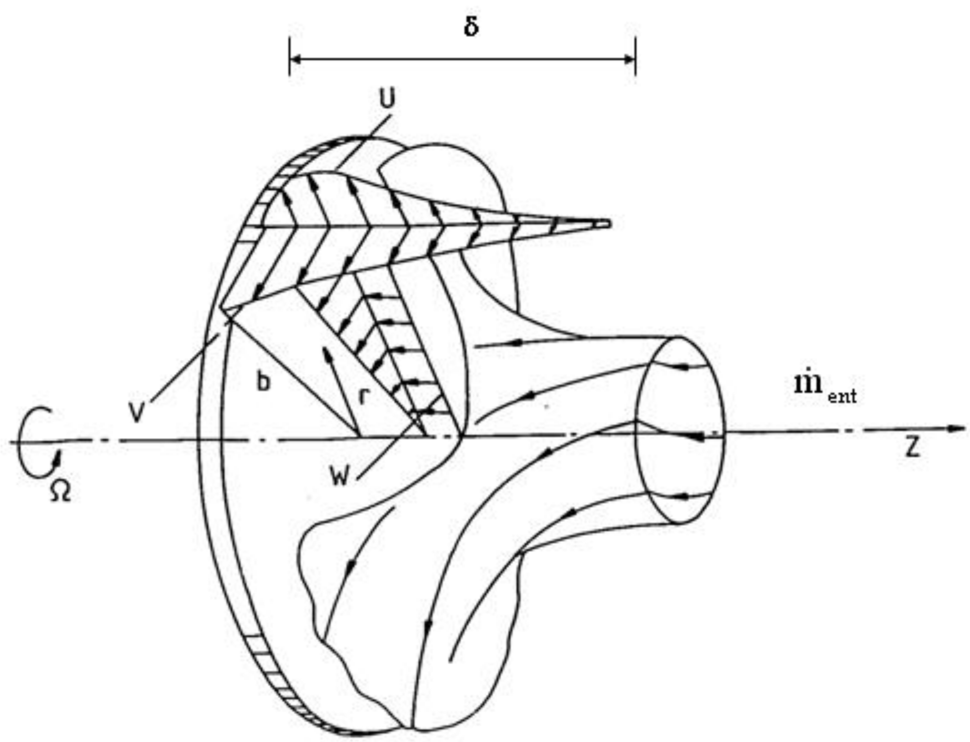

Figure 2.24: A Schematic Diagram of the Flow due to a Free Disc (Schlichtling, 1979)

In the area near the disc, the fluid has axial, radial and tangential velocity components W, U and V respectively relative to the stationary axis. As it rotates, the combination of viscous friction at the disc surface and centrifugal effect cause the flow to push radially outwards from the boundary layer that was formed on the disc. As the flow is pumped out radially outwards it is replaced by an axial entrainment flow into the boundary layer thereby maintaining mass continuity. The radial component of velocity is zero both on the disc and in the free stream and adjacent to the disc the radial and tangential velocities satisfy the no-slip condition. Rotating flows are frequently described by two main non-dimensional parameters namely the rotational Reynolds number $Re_{Ø}$, and the throughflow Reynolds number *Cw*. The rotational Reynods numbers was defined in Equation 2.7.

2.5.1 Fluid flow

In any fluid flow analysis, the flow must first be determined whether it is laminar or turbulent and this is controlled by the rotational Reynolds number.

Theodorsen and Regier (1944), Gregory, Stuart and Walker (1955) and Long (1984), in their studies concluded that turbulent flow over a free disc occurs for $Re_{\phi} > 3x10^5$. All groups of workers noted that transition occurred around local rotational Reynolds number of $Re_{\phi} = 3x10^5$. Hence, disc flow is laminar where $Re_{Ø} < 3 \times 10^5$, turbulent where $Re_{Ø} > 3 \times 10^5$ and the flow becomes transitional at $Re_{Ø} = 3 \times 10^5$.

The throughflow Reynolds number, C_w, is used to illustrate radial flow caused by rotation only or superimposed into the rotor-stator cavity. This is defined in Equation 2.12:

$$C_w = \frac{\dot{m}}{\mu b} \quad \textbf{(2.12)}$$

where $\dot{m}$ is the mass flow rate of fluid.

2.6 Heat transfer

Dorfman (1963) obtained an approximate solution of the energy equation assuming a power-law radial temperature distribution, $\Delta T = (T_s - T_{ref}) \propto (x)^n$. Given that T_s is the disc surface temperature and T_{ref} is the ambient fluid temperature and x = r / b. For laminar flow, $Re_Ø < 3 \times 10^5$, using Cochran's solution for tangential shear stress, Dorfman's results gives

$$Nu = 0.616\,\mathrm{Re}_\phi^{\,0.5}\,\mathrm{Pr}^{1/3} \quad \textbf{(2.13)}$$

$$Nu_{av} = 0.616\,\mathrm{Re}_\phi^{\,0.5}\,\mathrm{Pr}^{1/3} \quad \textbf{(2.14)}$$

For turbulent flow, $Re_Ø > 3 \times 10^5$, using Karman's results this gives

$$Nu = 0.0267\,\mathrm{Re}_\phi^{\,0.8}\,\mathrm{Pr}^{1/3} \quad \textbf{(2.15)}$$

$$Nu_{av} = 0.0232\,\mathrm{Re}_\phi^{\,0.8}\,\mathrm{Pr}^{1/3} \quad \textbf{(2.16)}$$

For laminar flow a non-unity Prandtl number and power-law temperature profiles, Dorman obtained approximate solutions of the energy equation as:

$$Nu = 0.308(n+2)^{0.5}\,\mathrm{Re}_\phi^{\,0.5}\,\mathrm{Pr}^{0.5} \quad \textbf{(2.17)}$$

$$Nu_{av} = 0.308(n+2)^{0.5}\,\mathrm{Re}_\phi^{\,0.5}\,\mathrm{Pr}^{0.5} \quad \textbf{(2.18)}$$

For turbulent flow ($\mathrm{Re}_\phi > 3\times10^5$), Dorfman employed von Kármán's equations to obtain the results for both local and average Nusselt numbers as:

$$Nu = 0.0197(n+2.6)^{0.2}\,\mathrm{Re}_\phi^{\ 0.8}\,\mathrm{Pr}^{0.6} \qquad \textbf{(2.19)}$$

and

$$Nu_{av} = 0.0197\frac{n+2}{(n+2.6)^{0.8}}\mathrm{Re}_\phi^{\ 0.8}\,\mathrm{Pr}^{0.6} \qquad \textbf{(2.20)}$$

where $Nu = \dfrac{qr}{k\Delta T}$ is the local Nusselt number and Nu_b is its value at r = b, $\mathrm{Pr} = \dfrac{\mu C_p}{k} \neq 1$ is the Prandtl number, q is the heat flux and k, and C_p are the fluid's thermal conductivity and specific heat capacity at constant pressure respectively. The average Nusselt (Nu_{av}) is the number given by: $Nu_{av} = \dfrac{q_{av}b}{k\Delta T_{av}}$ where q_{av} and ΔT_{av} are radially weighted averages. Dorfman's results show good agreement with the experimental data of Cobb and Saunders (1956) and Northrop and Owen (1988a). Dorfman's solutions of the energy integral equations provide the basic expressions for free disc heat transfer and are used as correlations for forced convection for rotating flow in the model.

2.7 The Rotating Cavity with a Radial Outflow or Inflow

The flow between two co-rotating turbine or compressor discs respectively can be modelled using a rotating cavity with a radial outflow or inflow. Figure 2.25 shows schematic diagrams of such flows structure for a cavity consisting essentially of two plane discs with an inner radius a, an outer radius b, a distance s apart, bounded by a circumferential shroud and rotating about the z-axis with a rotational speed Ω.

The flow structure is the same in both cases with the only difference being the direction of the flow. The flow can be divided into the following regions:

- The source region;
- The Ekman layers on the discs;
- The sink layer and;
- The interior or inviscid core where the axial and radial velocities are zero.

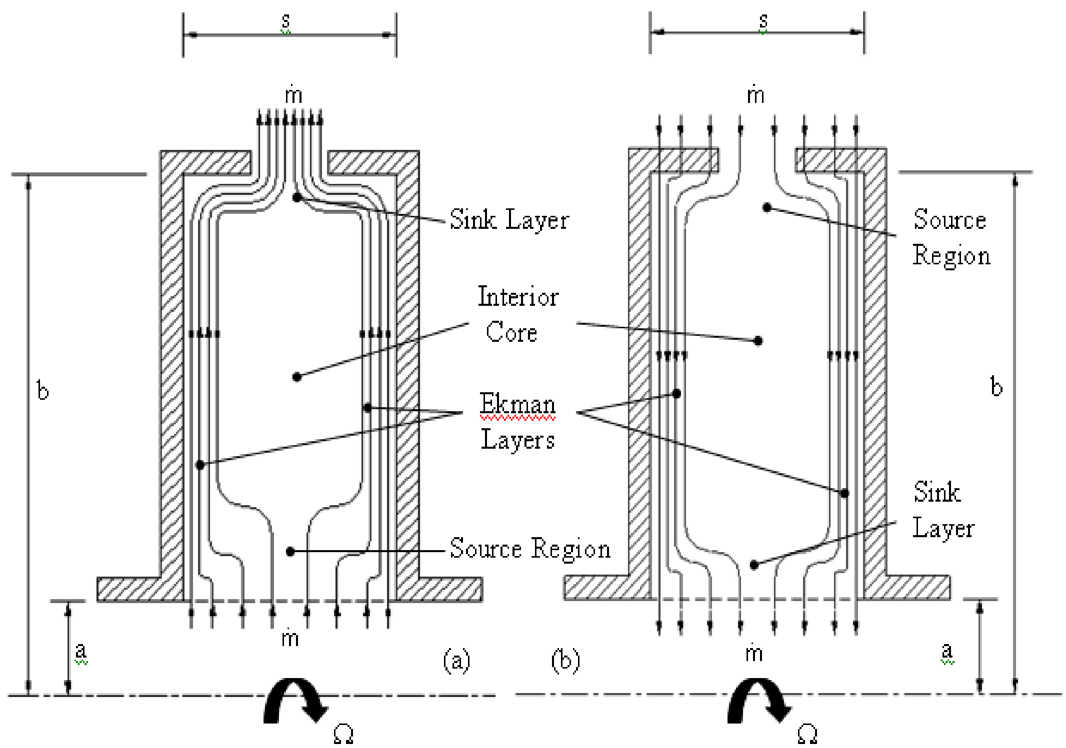

Figure 2.25: A Schematic Diagram of the Flow Structure in a Rotating Cavity for Radial (a) Outflow with a Radial Inlet and (b) Inflow with c = 1 (Owen and Rogers, 1989)

Motivated by geophysical flow, Hide (1968) investigated both theoretically and experimentally, laminar and isothermal radial outflow with a radial inlet in a rotating cavity. Four distinct regions were confirmed which he called the inner layer, Ekman layers, outer layer and potential core. Owen and Pincombe (1980) worked on flow visualisation and Laser Doppler Anemometer (LDA) measurements and the numerical predictions of Chew, Owen and Pincombe (1984) later confirmed Hide work and found out that the size of the source region increased with $C_{w,ent} = \frac{\dot{m}}{\mu_{ref} b}$ and decreased with $Re_{\phi,b}$.

For a given large value of C_w, for a given $Re_{\phi,b}$ the source region was observed to have filled the entire cavity and there will be no Ekman layers or interior core. Long and Owen (1986) observed similar flow structures for turbulent flow and the switch from laminar to turbulent flow was found to occur at $Re_\phi \approx 2\times10^5$ in the source region. Owen, Pincombe and Rogers (1985) established that in the Ekman layers transition to turbulence occurred when $Re_r = \frac{C_w}{2\pi x} \approx 180$, where $x = \frac{r}{b}$. Consequently, it is feasible for reverse transition to occur from turbulent to laminar flow inside the Ekman layers. Northrop and Owen (1988b) investigated a symmetrically heated rotating cavity with plane discs having the same temperature distribution on both discs for $1.2\times10^5 < Re_{\phi,b} < 3.2\times10^6$, $1400 < C_w < 14000$ and the flow structure was similar to that observed in the isothermal case. They established that the maximum value of the Nusselt number is obtained at a point close to the edge of the source region showing that it increased with an increase in radius and then decreased in the non-entraining Ekman layer and subsequently decreased sharply in the sink layer as the fluid moved away from the boundary layer. Furthermore, the local Nusselt numbers increased with an increase in C_w and $Re_{\phi,b}$.

2.7.1 The Rotating Cavity with a Radial Inflow

The flow structure in a rotating cavity with a superposed radial inflow is directly relevant to this research. In the diagram (Figure 2.25b), the flow enters the cavity at r = b with an amount of swirl which is equal in magnitude to swirl ratio c given as $c = \frac{V}{\Omega b}$, which depends on C_w, Re_ϕ and the shroud geometry.

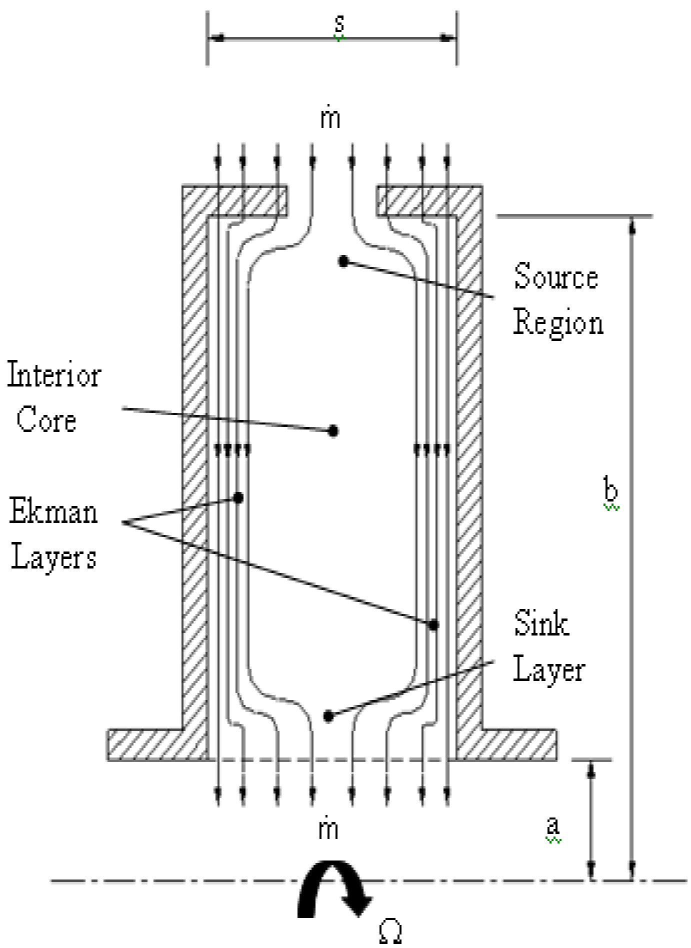

Figure 2.26: A Schematic Diagram of the Flow Structure for a Rotating Cavity with Radial Inflow and c = 1 (Owen and Rogers, 1989)

Figure 2.26 shows the flow structure for a rotating cavity with radial inflow for c = 1, while Figure 2.27 shows the flow structure for a rotating cavity with radial inflow for c <

1, with a recirculation within the source region with outflow near the discs and inflow outside the boundary layers. Firouzian et al (1985) and Firouzian (1986) all confirmed this isothermal flow structure in their flow visualisation experiments.

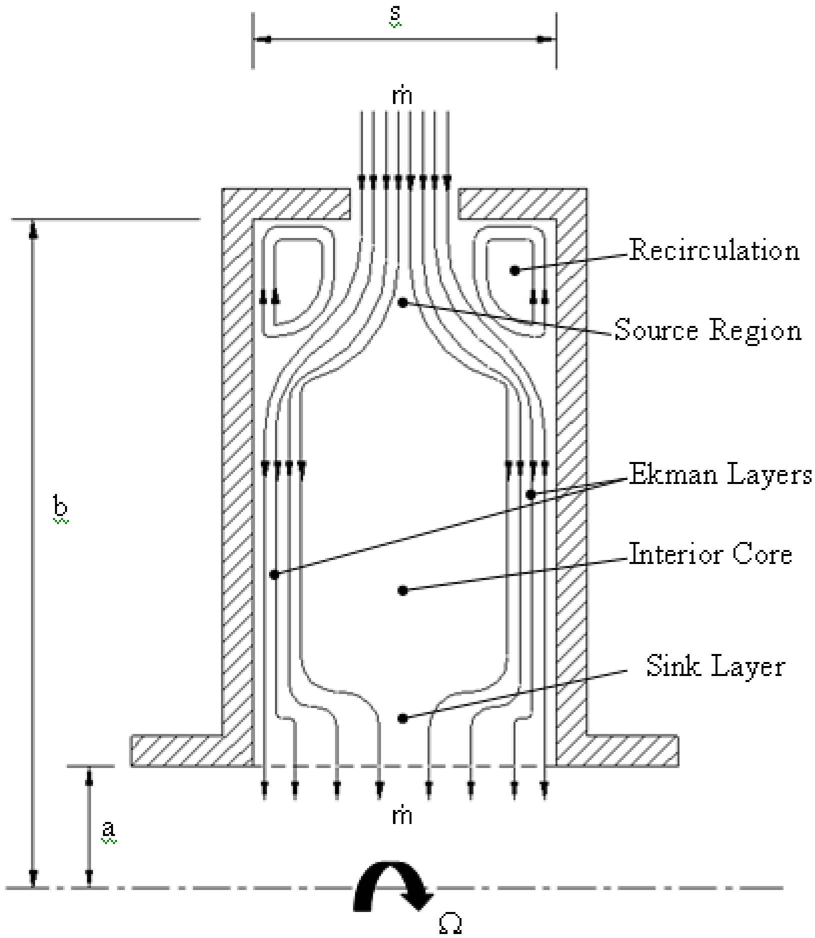

Figure 2.27: A Schematic Diagram of the Flow Structure for a Rotating Cavity with Radial Inflow and c < 1 (Owen and Rogers, 1989)

Chew et al (1989), Farthing, Chew and Owen (1991), Farthing and Owen (1991) found a large pressure drop across a cavity with radial inflow. This according to the authors can be reduced with the use of radial fins on the discs, but there are limited practical uses of radial fins in an engine due to stress limitations. The other solution is to use nozzles that have a tendency to reduce the inlet swirl ratio, c. The pressure drop across the nozzles is known to increase with decreasing c, giving a total pressure drop which is always greater than that associated with solid body rotation.

Finally, Farthing and Rogers (1987) and Farthing, Long and Rogers (1991) presented heat transfer measurements from discs with cobs, for $c \approx 1$ and with an increasing temperature profile. They found that in the presence of an inviscid core, the Nusselt number increases (with decreasing radius) in the source region, the same as in the case of radial outflow where the maximum value, Nu_{max} is reached close to the edge of the source region and subsequently begins to decrease. In general, Nu_{max} increases with both C_w and $Re_{\phi,b}$. Finally, Firouzian (1986) obtained Nusselt numbers wherein was evident a 'double-hump' characteristic due to the recirculation in the source region for plane discs and $c \approx 0.59$.

2.8 The Rotating Cavity with Axial Throughflow

A rotating cavity with an axial throughflow of air can be used to model the flow that occurs between adjacent co-rotating compressors discs inside a gas turbine engine where the cooling air flows through the centre of a stack of compressor discs. The cavity is formed by two adjacent discs of inner radius a and outer radius b, separated by an axial distance s and bounded at the periphery by a cylindrical shroud.

2.8.1 The Isothermal Cavity

For isothermal conditions, where all the surfaces are at the same temperature as the fluid, vortex breakdown in the central jet of air can result in nonaxisymmetric flow inside the cavity. If the discs are at different temperatures, nonaxisymmetric flow predominates.

Pincombe (1983) and Farthing et al. (1992a) carried out a study on the flow structure in an isothermal axial throughflow for various geometric configurations using flow visualization and velocity measurement. They noticed that under certain conditions, axi-symmetric and non-axisymmetric vortex breakdown can occur depending on the value of the following dimensionless groups such as gap ratio, G, rotational Reynolds number $Re_{\text{Ø}}$, axial Reynolds number Re_z and the Rossby number, Ro.

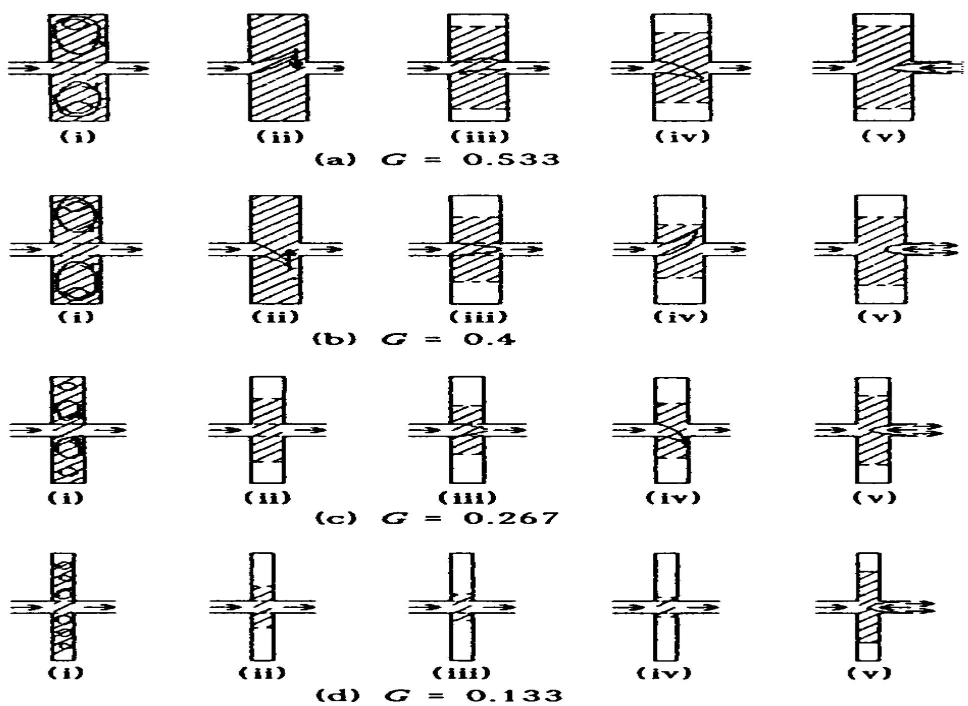

Figure 2.28: Visual Impressions of Smoke Patterns for an Isothermal Rotating Cavity with an Axial Throughflow of Air (Farthing et al. 1992a)

The interaction of the throughflow of air with the cavity air was found to generate one or more toroidal vortices in the cavity with nearly no penetration of the throughflow into the cavity.

The characteristic flow schematics for the case of throughflow of air with no rotation of the cavity for different values of G are shown in Figure 2.28. The values of G used are 0.533, 0.4, 0.267 and 0.133. The study was under taken for the following Ro values ∞, 25, 4, 2 and 1 representing case i, ii, iii, iv and v respectively as shown in Figure 2.28. They observed that for a stationary cavity with Ro = ∞ and G = 0.4 or 0.533, a dominant toroidal vortex was formed inside the cavity. For G = 0.267, two counter-rotating vortices were noticed and for G= 0.133, three counter-rotating vortices were noticed. The observed that the central throughflow was also affected by rotational speed and that axial jet of air passing through the centre of the cavity was sometimes deflected from the axis of rotation as it flowed out. They came to a conclusion that axi-symmetric and non axi-symmetric vortex breakdown could occur in rotating cavity such as isothermal cavity. As the rotational speed was increased four regimes of vortex breakdown were identified. Figure 2.29 shows the four regimes (Ia, IIa, Ib and IIb) of vortex breakdown for G = 0.533.

Farthing et al. observed that for turbulent flow, there was no discernible signs of influence on the vortex and the central jet with rotational speed for values of Rossby number higher than 100 with G=0.533.

For Mode la with $21 \leq Ro \leq 100$, they observed the occurrence non axi-symmetric vortex breakdown where the jet of air gets diverted into the cavity as illustrated in case a (ii) of Figure 2.28.

For Mode lla with 2.6 ≤ Ro ≤ 21, as the rotational speed increased, the jet would become axi-symmetric again but with intermittent oscillations as illustrated in case a (iii) of Figure 2.28.

For Mode lb with 1.5 ≤ Ro ≤ 2.6 showed a "flickering flame" appearance of the central jet with intermittent excursions into the cavity as illustrated in case a (iv) of Figure 2.28.

For Rossby values below Ro=1.5, the flow turned axi-symmetric again and signs of reversed flow at the downstream edge of the jet was noticed as illustrated in case a (v) of Figure 2.28.

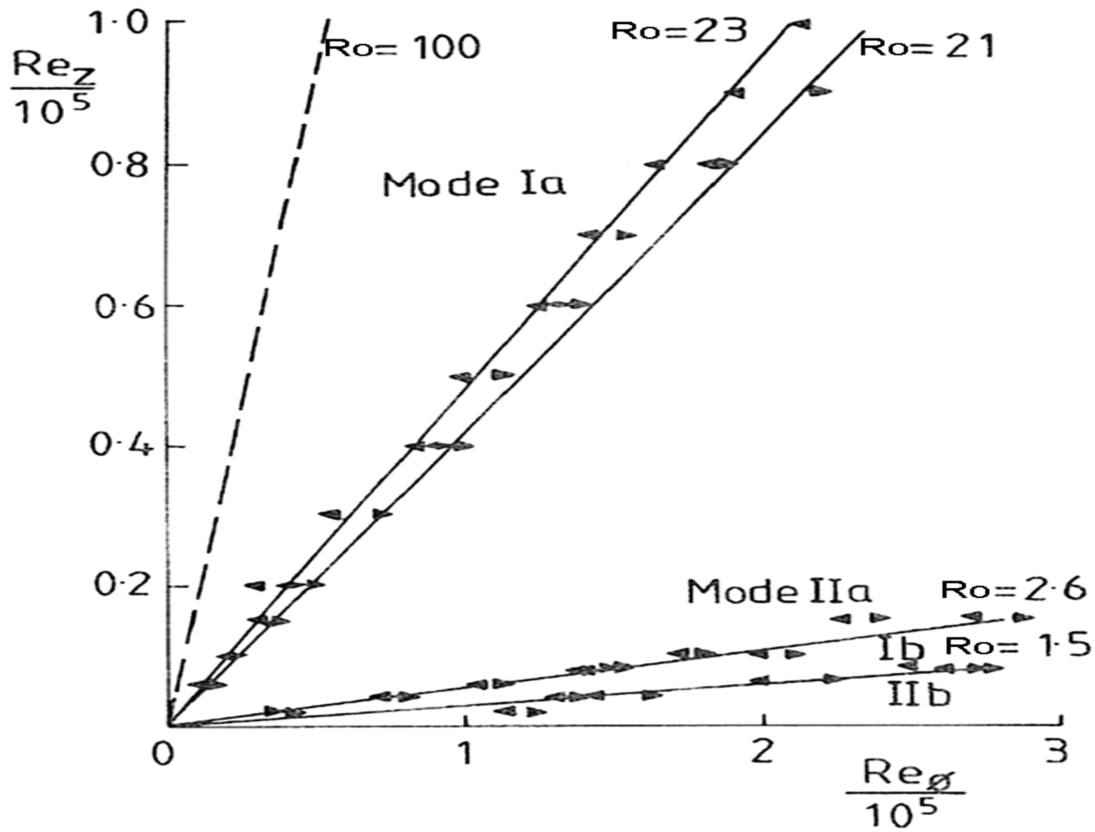

Figure 2.29: Variation of Regimes of Vortex Breakdown with an Axial Throughflow of Air in an Isothermal Rotating Cavity: G = 0.533 (Farthing et al. 1992a)

2.8.2 Fluid Flow: the Heated Cavity

Farthing et al. (1992a) carried out flow visualization and LDA studies inside a rotating cavity with an axial throughflow for case where the discs could be heated independently to produce temperature distributions that could increase, decrease or remain approximately constant with increasing radius. The shroud in this study was unheated and for same temperature distribution on both discs. They observed that for all temperature distributions, that the flow inside the cavity was seen to be non axi-symmetric.

They observed that the throughflow enter the cavity in a “radial arm” and was then separated to create a pair of circulation regions. These pair of the circulation regions is the forward or cyclonic (low pressure) region which rotate in the same direction as the discs and the rearward or anticyclonic (high pressure) region that rotate in the opposite direction. These two regions are, however, separated by a ‘dead’ zone. A boundary layer was noticed to flow radially inwards on the discs inside this region. These observations are illustrated in Figure 2.30.

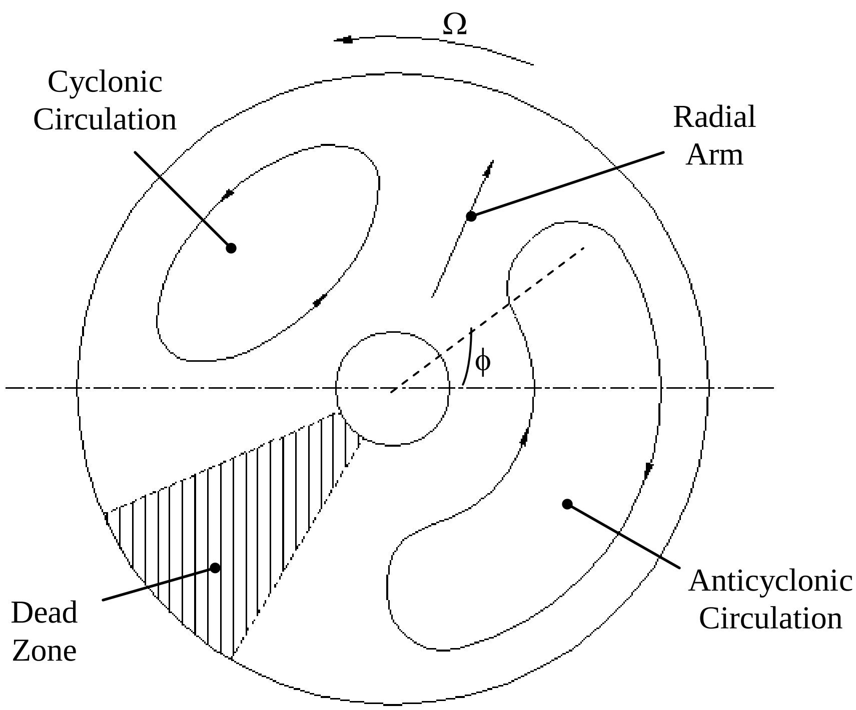

Figure 2.30: Schematic Diagram of the Flow Structure in a Heated Rotating Cavity with an Axial Throughflow of Cooling Air (Farthing et al. 1992a)

The flow structure was found to rotate at speed ω, which depend on the gap ratio, temperature change and the Rossby number. The speed was in the order of $0.9 < \omega / \Omega < 1$ where Ω is the angular speed of the discs. The vortex breakdown was observed for Ro ≈ 2. This had the effect of returning the flow in the core towards solid body rotation as Ro decreased.

Farthing (1988) performs a flow visualizations study for a case where both the shroud and the discs are heated and observed multiples radial arms with separations regions. However, when the discs were heated to a temperature of about 40°C greater than the shroud temperature, the flows return to a single radial arm.

Long and Tucker (1994a) carried out a 3D laminar unsteady computation and they observed that the results of their computations were in good agreement with the results of Farthing et al. (1992a). They observed that the predicted flow structure depends on the radial disc surface temperature distribution, and that the number of recirculation regions appeared to increase as the radial location of the maximum disc surface temperature moved radially outwards.

2.9 Summary for literature review

The literature relevant to tip clearance control between the rotating blade tip and the stationary casing in an axial flow compressor has been reviewed. This was preceded by axial compressor and compressor clearance overview. Although more data were available for aerodynamic desensitization of the tip flow, there was little information directly applicable for the actual tip clearance control between the rotating blade tip and the stationary casing in an axial flow compressor. A large body of information relevant to the actual tip clearance control were available in the patents. The tip control systems were group into two major groups namely active and passive clearance control scheme. Qualitative indications of the effect of heat transfer and fluid flow in a rotating cavity such as found in the high pressure compressor cavity relevant to tip clearance control has also been reviewed. This previous research has provided the basis for the understanding of the complex phenomena occurring inside these cavities. The free disc was used to demonstrate the flow structure that is experience when the disc inside the high pressure compressor is subjected to centrifugal acceleration. The radial outflow or inflow gave an inside of the four different regions that is experience when the cavity is superimposed with this type of flow. For a rotating cavity with axial throughflow, heating the discs or the shroud also generates rotationally-induced buoyancy forces that can destabilise the air inside the cavity. The heat transfer and fluid flow reviewed highlighted nature of flow inside the cavities similar to those found in the high pressure compressor in real engine. Heat transfer coefficient correlations relevant to this study and used in the boundary conditions in the multiple cavity rig model were presented. The results from the review of clearance control methods, patents, flow and heat transfer inside a rotating cavity would be employed in the study of tip clearance control in engine representative H.P. compressor drum operating at engine non-dimensional conditions.

Many insights into tip clearance control schemes are available in literatures such as gap height measurement, coolant injection, winglets, squealer tips and platform extension. Other studies entailed using the combinations of velocity, pressure, and flow visualization to determine the characteristics of the flow both within the tip clearance and within the blade passage but gaps in knowledge remain. From the review of works by other authors, there is still need to understand tip clearance effects by actually controlling the tip gap during engine operation using the following schemes.

1 Heat transfer coefficient scheme
2 Time constant reduction scheme
3 Radial inflow application scheme

This present study will utilise the effect of increasing heat transfer coefficient, disc time constant reduction and radial inflow injection into the drum cavity to reduce the tip gap during engine operations. This would decrease the time constant of the drum by increasing the heat transfer coefficient of the drum thereby causing the drum to heat up faster hence narrowing down the large gap that existed at the beginning of engine transient operation between the casing and the blade. This would cause a reduction in the cruise clearance and a reduction in of clearance at surge point and hence reductions in the overall specific fuel consumption giving rise to higher engine efficiency.

Chapter 3

Finite Element Analysis Program SC03 Model

3.1 Introduction

In this chapter a brief description of the test rig assembly as modelled using the finite element analysis solver (SC03) is presented with a detailed description of SCO3 and its procedure. General descriptions of the test rig configurations are given in Section 3.2, while details of the finite element analysis solver (SC03) used are provided in Sections 3.3 through to 3.14.

3.2 General Description of Rig

The experimental rig used in the present study follows several generations of rotating cavity rigs that have been used in the TFMRC at the University of Sussex over the years. More precisely, the experimental rig used has four rotating cavities; it is referred to as a 'multiple cavity rig' (MCR) and is pictured in Figure 3.1. The multiple cavity rig (MCR) represents the internal set-up of a high pressure compressor where the rotor and inner shaft of the rig were scaled down from a Rolls Royce Trent aero-engine to a ratio of 0.7:1. The rig is to simulate the internal air system flows within a High Pressure (HP) compressor where air, extracted from the Intermediate Pressure (IP) compressor and predestined for the Low Pressure (LP) turbine discs and seals, flows axially through the annular passage between the HP compressor discs bores and the enclosed IP drive shaft.

The rig was designed to be not only representative of typical current engine geometry but also able to run as close as possible to typical non-dimensional operating conditions. The present test facility was purposely modified and built to satisfy the objective of this study.

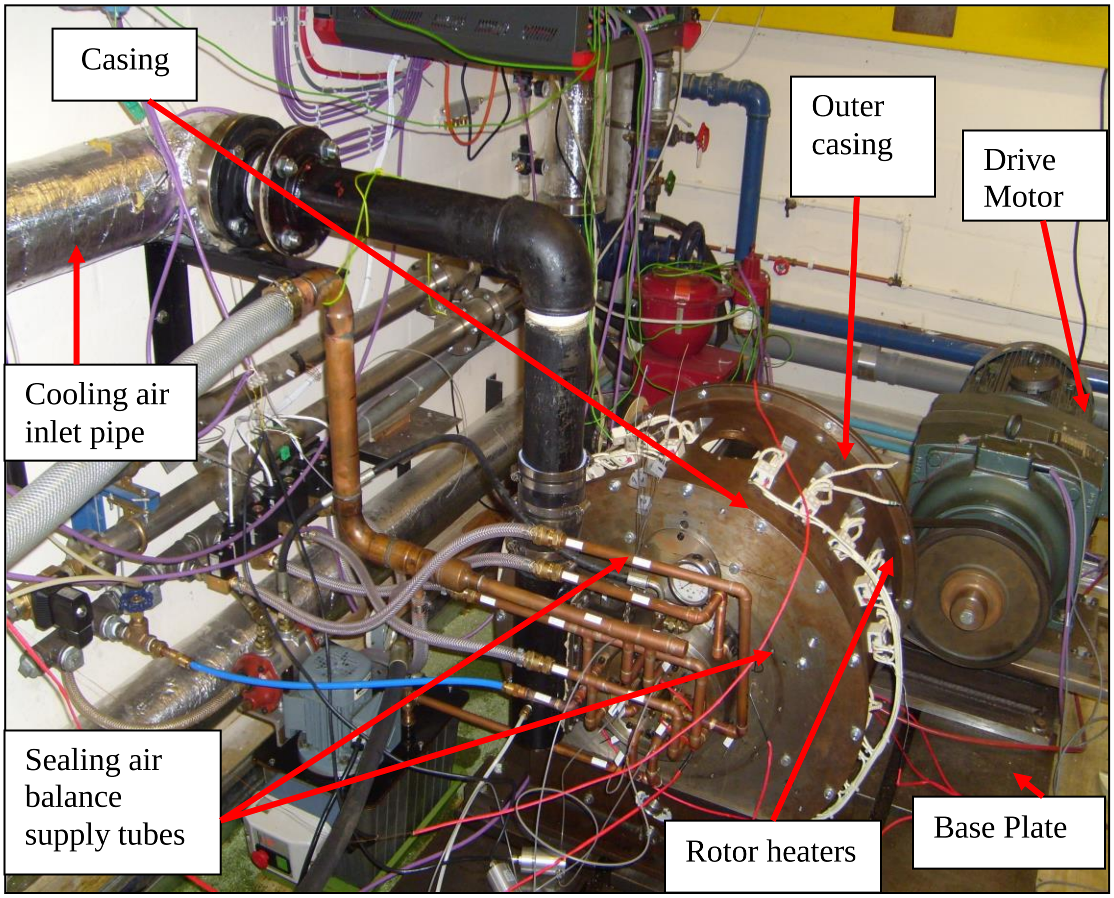

Figure 3.1: A Photograph of the Multiple Cavity Rig in the Laboratory

A disc stack geometrically similar to a real engine is featured, forming the internal cavities, and a shaft is represented at the inner radius, although it is stationary. Compressed air flows through the annulus gap between disc bore and shaft as the cooling air would be inside a real high pressure compressor. The rotor is made of titanium 318 with an outer diameter of 491.3 mm and forms four cylindrical cavities with an inner radius a = 70.1 mm, an outer radius b = 220.0 mm (a/b = 0.32), and a disc spacing s = 42.9 mm (G = s/b = 0.195). The non-rotating inner shaft has an outer radius r_s = 52.0 mm ($\Delta r = a - r_s$ = 18.1 mm).

The major measurement section of the rig comprises a rotating disc of b = 220.0 mm housed in a pressurised casing. The disc is driven by means of a 18.5 kW AC electric motor. The transmission system comprises a gearbox, couplings, and a device to measure driveshaft torque. The present rig was modified to study the effect of compressor disc flow, cavity heat transfer, and radial inflow on temperature distribution on the disc in the cavity. The main structural modifications are the installation of a new 60 channel telemetry system, machining of the radial inflow supply channel through the rotor into the cavity and the use of Insulfrax as an insulator in the both ends of the rotor as shown in Figure 3.2.

The rotor assembly is housed within a mild steel, non-pressurised casing and supported by a high-precision grease-lubricated ball bearing on the upstream side and an oil-lubricated cylindrical roller bearing on the downstream side. An alternating current motor was used to rotate the rotor by means of a TASC Unit driving a poly-vee belt and the operating speeds achieved were varied up to 7500 rev/min. The cooling air enters the rotor through a circumferential array of 6 × ∅25 mm holes in the rotor endplate. On the back of these holes is a thin perforated plate known as a diffuser plate that creates a uniform velocity profile at the inlet to the rotor. For a detailed description of the multiple cavity rig the reader is referred to Alexiou (2000), Long and Childs (2007), Long Miché and Childs (2007) and Miché (2008).

The radial inflow was directed through the ducts from the upstream section of the rig through 32 holes on the endplate of the rotor through the 16 holes into cavity 4 of the rig as shown in Figure 3.2.

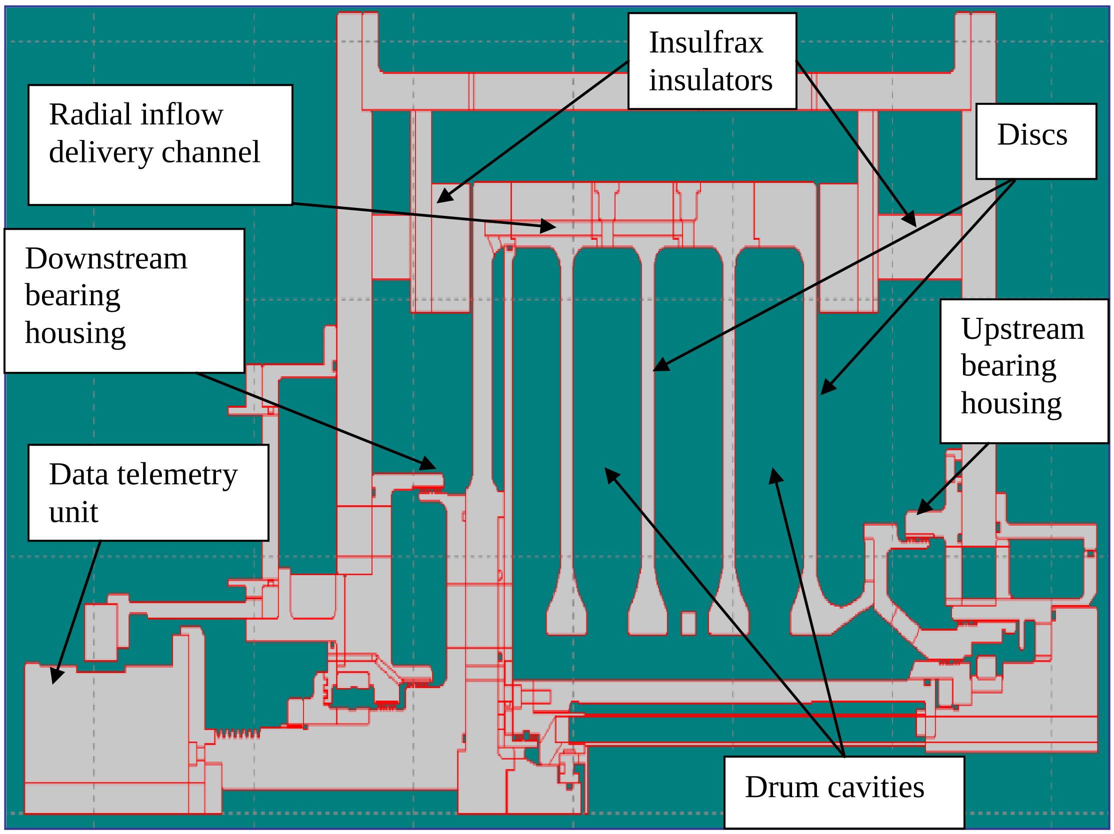

Figure 3.2: Multiple Cavity Rig Model and the main modifications

Hot mainstream annulus flow is simulated using air heaters. Two heater systems were used. There are radiant heaters for the rotor and an additional heater for the radial inflow supply. The outer drum also positions the 24 kW radiant heater array. The heaters are driven from a three-phase power controller, which is connected to the central control system. The compressor drum was machined to allow for the installation of the 79 rotating frame thermocouple on the rotor and holes for supply and delivery of the radial inflow into the cavity as shown in Figure 3.3. Figure 3.3 shows the multiple cavity rig rotor assembly and model points (mp) locations at which the surface temperatures on the rotor disc were measured.

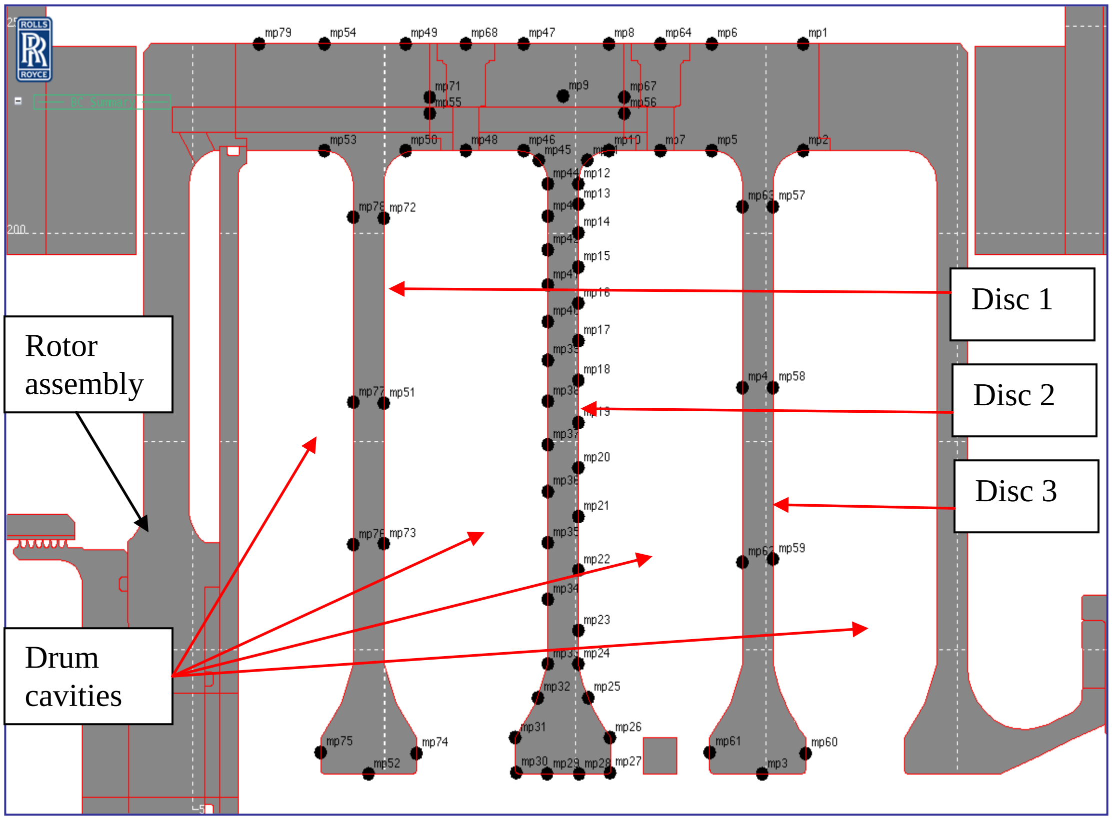

Figure 3.3: Rotor of the multiple cavity rig with instrumentation points

In all, 79 thermocouples were located and defined in the model as reference locations on the rotor disc for the measurement of the surface temperature as shown in Figure 3.3. The thermocouples relating to the heat transfer of disc 1 were located on the disc's surface for temperature measurement upstream at model points (mp) 72, 51, and 73 and downstream as 76, 77, and 78. Those thermocouples relating to the heat transfer of disc 2 were the surface thermocouples' measurements upstream at model points 12 -23 and downstream as 34 - 44. Those thermocouples relating to the heat transfer of disc 3 were the surface thermocouples' measurements upstream at model points 57, 58, and 59 and downstream as 62, 4, and 63. The shroud heat transfer of cavity 2 was obtained by the use of the measurement of surface thermocouples at model points 68 and 48, while the surface thermocouples at model point 7 provided the data necessary to originate the heat transfer characteristics of the shroud in cavity 3. The heat transfer of the cob regions was obtained by the use of the measurement of surface thermocouples at model points 75, 52and 74 for disc 1, model points 24 - 33 for disc 2, and model points 61, 3 and 60 for disc . However, in this study, concentration was in cavity 3. Table 3.1 shows all axial and radial positions (model points 1-79) of the rotor thermocouples used for temperature measurement as modelled in Figure 3.3.

Model points	**Axial Position (mm)**	**Radial Position (mm)**
1	109.6810	245.65
2	109.6810	220.00
3	98.9410	70.10
4	93.7606	163.00
5	85.7610	220.00
6	85.7610	245.65
7	72.3110	220.00
8	58.8610	245.65
9	46.8610	233.12
10	58.8610	220.00
11	53.1808	217.66
12	50.8606	212.00
13	50.8606	207.15
14	50.8606	200.22
15	50.8606	191.96
16	50.8606	183.33
17	50.8606	174.27
18	50.8606	164.72
19	50.8606	154.58

Table 3.1: Location of Rotor thermocouples according to Figure 3.3

Model points	Axial Position (mm)	Radial Position (mm)
20	50.8606	143.72
21	50.8606	131.98
22	50.8606	119.08
23	50.8606	104.60
24	50.8606	96.55
25	53.4626	88.38
26	54.4086	78.83
27	59.1206	70.39
28	51.0406	70.10
29	42.6806	70.10
30	34.6006	70.39
31	34.3106	78.83
32	40.2616	88.38
33	42.8606	96.55
34	42.8606	112.07
35	42.8606	125.69
36	42.8606	137.97
37	42.8606	149.25
38	42.8606	159.73
39	42.8606	169.56
40	42.8606	178.86
41	42.8606	187.69
42	42.8606	196.13
43	42.8606	204.22
44	42.8606	212.00
45	40.5106	217.66
46	36.5510	220.00
47	36.5510	245.65
48	21.4110	220.00
49	5.6910	245.65
50	5.6910	220.00
51	-3.942965E-02	163.00
52	-4.03943	70.10
53	-15.589	220.00
54	-15.589	245.65
55	9.5310	228.94
56	60.441	228.94
57	101.7610	206.50
58	101.7610	163.00

Table 3.1 (Continued): Location of Rotor thermocouples according to Figure 3.3

Model points	Axial Position (mm)	Radial Position (mm)
59	101.7610	121.75
60	110.3110	75.00
61	85.2106	75.25
62	93.7606	121.00
63	93.7606	206.50
64	72.3000	245.65
65	72.3110	220.00
66	72.3110	220.00
67	62.8606	232.83
68	21.4106	245.650
69	21.4110	220.00
70	21.4110	220.00
71	11.9606	232.83
72	-3.942965E-02	203.75
73	-3.942965E-02	125.50
74	8.51057	75.00
75	-16.5894	75.25
76	-8.03943	125.25
77	-8.03943	159.50
78	-8.03943	204.00
79	-32.6694	245.65

Table 3.1 (Continued): Location of Rotor thermocouples according to Figure 3.3

3.2.1 Rig Capabilities

Before the commencement of the rig modification, a set of intended operating parameters were set having been obtained from the Trent 1000 aero-engine. The parameters used in the rig and modelled in the 2D modelling of the rig were expected to be within the range given in Table 3.2.

Parameter	Symbol	Idle conditions	Max. take-off conditions
Bore mass flow	$\dot{m}_{bore}$	0.23 kg/s	1.35 kg/s
Bore temperature	T_{bore}	291K	381K
Bore pressure	P_{bore}	2.8 x 10^5 Pa	5.5 x 10^5 Pa
Rotor speed	N	3000 rev/min	8000 rev/min
Radial inflow temperature	T_{radial}	350 K	469 K

Table 3.2: Parameters used for the Investigation in the test rig

The corresponding range of non-dimensionless parameters for the cavity of the rig and their relationship with normal engine operating conditions during idle, maximum take-off, and cruise are given in Table 3.3. The MCR conditions were matched to the non-dimensionless parameters shown in Table 3.3.

Parameter	Symbol	Idle conditions	Max. take-off conditions
Axial Reynolds number	Re_z	1.88 x 10^5	8.75 x 10^5
Rotational Reynolds number	$Re_{\emptyset}$	3.1 x 10^6	1.0 x 10^7
Shroud Grashof number	Gr_{shaft}	5.4 x 10^{11}	6.4 x 10^{12}

Table 3.3: Non-dimensional Parameters for Trent 1000 compressor

3.3 Finite Element Analysis Program (SC03)

This section describes the features of the program relevant to the models presented in this thesis. SC03 is a finite element analysis program developed by Rolls-Royce plc. SC03 is the Rolls-Royce approved numerical in-house solution method program for all classes of heat transfer problems. There are several analysis performed using SCO3 including thermal analysis, structural analysis and thermo-mechanical analysis. The thermo-mechanical analysis is presented in details in Section 3.3.1.

The SC03 code use a finite element (FE) approach to solve the solid conduction, with 1D boundary conditions. The conduction of the heat transfer problems are handled automatically in SCO3. The SCO3 analysis process involves geometric definition, boundary condition definitions, boundary condition inputs, input checking, model running, output checking and processing. An axisymmetric model has been produced for the multiple cavity rig using the SC03. Three-dimensional modelling and analysis are also possible within SC03. The SC03 model was used primarily for simulating the test facility and predicting its behaviour at different operating conditions.

When a model is created for the first time in SCO3, it is essential to have a database file *(filename.db)* to store all the data. It is also necessary to specify a number of default values (default material, rotational speed, thickness, temperature, etc.) before running the program for the first time. However, these default values can be redefined at a later stage, where necessary. The geometry should be created in a CAD system and then supplied to SCO3 by importing it into the program in an IGES format because the drawing facilities within the SCO3 software are quite limited. The geometry needs to be checked to confirm its consistency before the chaining process. The chaining process is performed if there are no errors in the geometry. This process is essential before the application of the boundary conditions. After the chaining process, the geometry can then be meshed. This is followed by other processes such as definition of area properties in the domains. These properties are speed, material, thickness and the assigning of a local thickness property to modelled non-axisymmetric feature. The next stage in this modelling is the application of the structural and thermal boundary conditions. In the absence of test data from rig or engine runs the thermal boundary conditions are chosen based on a good judgement of the geometric and physical case. In order to restrain rigid body motion, in an axisymmetric model, a normal restraint should be used to apply the prescribed displacements. All the information on geometry, area properties, boundary conditions, is stored in the database file. Any other data required for multi-time point analyses data such as time varying speeds, temperatures, are held in the Basic Design Data, BDD, file (*filename.bdd)*. The type of analysis is then specified and initiated such as thermal, structural, linear, non-linear, thermo-mechanical analysis. The calculated results are written automatically in the results file (*filename.res*) while the output from several places in the program such as boundary conditions is contained in the general output file. A confirmation of the successful completion of the analysis is given, at the end of each run. In the event of any errors, this can be traced from the diagnostics file.

The results for temperatures, stresses and displacements can be presented on the screen as colour filled or line contours while a time varying display of any transient results can be viewed graphically. A time point can be specified to plot the results at a given time from a transient run. The program allows for a time plot for up to 10 user specified points.

The modelling of the MCR was supervised by Dr. Nick Atkins, the models had never previously been used by the group and the starting point of the modelling was the modification of the existing rig drawing to suit the present study. This required the inclusion of the radial inflow supply channel and introduction of insulator called insufrax using a computer aided design (CAD) package AutoCAD followed by exporting the modified diagram into the SC03 and a further modification where necessary in SC03. Detailed explanations of the various functions and terms used in SC03 are presented in Sections 3.4–3.13. This section describes the features of the program applicable to the model presented in this thesis. SC03 analysis are presented which consist of geometry definition, mesh generation, cycle definition, domain properties definition, boundary condition definition and input checking, model running, and output checking and processing. The discussion on the decision process of deciding on the boundary conditions and the boundary condition relation to the model is also presented.

3.3.1 Thermo-mechanical analysis

Thermo-mechanical analysis is performed in SCO3 to provide thermal and displacement data for any gas turbine engine component or assembly. This analysis involves both thermal and structural analysis. Thermo-mechanical analysis includes temperature analysis and displacement analysis. Thermo-mechanical analyses are used in the prediction of component temperatures, component stresses, analysis of engine movement, deflections of axisymmetric or plane structures, and clearance optimisation. Hence, before commencing a thermo-mechanical analysis, the type of analysis to be performed must be considered. Best practice, as followed here, is to agree this with the customer, based on the accuracy requirement for the calculations and the time scales. In a thermo-mechanical analysis, a 2D axisymmetric analysis is performed if the geometry, loading and resultant displacements are assumed to be axisymmetric. A 2D axisymmetric analysis could also be performed if some of the components with 3D features in the geometry and the effect on displacements are approximated in 2D for example for aerofoils and the intercase region. Two types of analysis can be performed in SCO3 namely linear or non-linear. But a linear analysis is the conventional (default) analysis that is performed in SCO3 during which the Geometric Non-linearity (GNL) is turned off. However, non-linearly analysis can be performed if requested as this would bring about additional structural iterations whereby the change in the centre of mass is reflected, thus changing the applied moment. The linear analysis is computationally simpler' since a linear analysis is performed for each time point to give a better first approximation of displacements/stresses.

The thermo-mechanical model should be validated against both transient and steady state temperature and displacement data over a test cycle for example a square cycle which is used in this study. Thermo-mechanics process therefore describes the way in which temperature and displacement analyses should be performed to provide thermal and displacement data for any gas turbine engine component or assembly. The description of temperature analysis and displacement analysis are presented in Section 3.3.1.1 and 3.3.1.2 respectively.

3.3.1.1 Temperature analysis

Finite element analysis is the recommended method for temperature predictions. However, for very simple problems theoretical displacement analysis is suitable. Temperature analysis involves a numerical solution method for heat transfer problems. The heat transfer process is the study of the processes by which energy, in the form of heat, is transferred from one medium to another where the driving potential is a difference in temperature. The amount of thermal energy E contained in a body is proportional to its temperature, and to the amount of mass (m) of the body. The relationship between the change in thermal energy E, associated change in temperature T and the mass of the body is given as:

$$\Delta E = mc\Delta T \tag{3.1}$$

Where, c is the constant of proportionality called the specific heat capacity, which has the unit of J/kg K.

Heat, can be introduced into a gas at constant pressure and constant volume. Hence in equation 3.1, for a perfect gas, at constant pressure c is the specific heat capacity at constant pressure is denoted c_p , where E is the enthalpy H. While at constant volume c is the specific heat capacity at constant pressure is denoted c_v , where E is the internal energy U. T is the static temperature which indicates the level of energy possessed by the substance. The temperature of the moving fluid is measured by a stationary thermocouple embedded in the model as shown in Figure 3.3 as model point (MP) mp1 to mp79. The measurement of the temperature of the fluid takes effect when the fluid is brought to rest.

The kinetic energy is converted to internal energy as the fluid comes to rest. This conversion will always occur at the stationary solid boundary according to the no slip condition. This will cause an increase in the local internal energy hence the local static temperature will rise to a temperature known as stagnation temperature. The stagnation temperature is given as:

$$T_{stag} \approx T + \frac{v^2}{2c_p} \qquad \textbf{(3.2)}$$

Due to the effect of increase in local internal energy on local static temperature, the term total energy of the free stream divided by the specific heat capacity due to pressure $\dfrac{T + \frac{v^2}{2}}{C_p}$ in Equation 3.2 is called the total temperature T_0. Hence the total temperature T_0 is given in Equation 3.3 and that T_0 can be considered as being equal to T_{stag}.

$$T_0 = T + \frac{v^2}{2c_p} \qquad \textbf{(3.3)}$$

The modes of heat transfer are conduction, convection and radiation. A combination of these modes may occur at any one time in practice or in some cases a single mode may be dominant and control the flow process. Conduction and convection are both important in the majority of gas turbine problems with radiation being significant in specific cases such as combustor problems, turbine casings and engine shutdown conditions.

3.3.1.1.1 Conduction

This is the mode of heat transfer in a solid material that occurs due to a temperature difference between different parts of the material. However, it may also occur in liquids and gases. Conduction is governed by expression known as the Fourier's law and it is mathematically presented for 1-dimensional heat flow in x direction as:

$$Q_x = -kA\frac{dT}{dx} \tag{3.4}$$

where Q_x = heat flow rate per unit area in x-direction (mW/mm^2K)

k = thermal conductivity $(mW/mm.K)$

$\frac{dT}{dx}$ = temperature gradient in x-direction

The gradient must be negative (-ve) resulting from the convention of defining a positive heat flow in the direction of a negative temperature gradient.

The conduction heat flux, q is given as:

$$q_x = \frac{Q_x}{A} - k\frac{dT}{dx} \qquad (W/m^2) \tag{3.5}$$

In the simple case of steady state heat conduction through a wall, where thermal conductivity k is constant, and Fourier equation can be integrated to give:

$$Q = \frac{-kA(T_2 - T_1)}{\Delta x} \tag{3.6}$$

Where Δx = the distance in the x-direction

A = cross-sectional area

However, the term $\frac{\Delta x}{kA}$ is known as the thermal resistance R_{th}

3.3.1.1.2 Convection

Convection is the mode of heat transfer at a solid boundary. Convection occurs due to bulk motion of fluid. When a moving fluid encounters a solid surface, heat is convected either from it or to it, depending on the sign of the surface to fluid temperature difference (Long, 1999). The general equation of convective heat flow is given as:

$$Q = hA\left(T_m - T_f\right) \tag{3.7}$$

where:

h = heat transfer coefficient $\left(W/m^2K\right)$

A = area of heat flow $\left(m^2\right)$

T_m = surface metal temperature (K)

T_f = bulk fluid temperature (K)

The convective heat flux, q is given as:

$$q = h\left(T_m - T_f\right) \qquad \left(W/m^2\right) \tag{3.8}$$

The convection mode of heat transfer is sub-divided into two different types namely free or natural convection and forced convection. Free or natural convection occurs between a solid and a fluid undisturbed by other forces except by a temperature difference present between the two. This temperature difference creates density variation which results in the fluid motion. In free convection, the fluid motion that occurs is due wholly to the natural buoyancy forces arising from a changing density of the fluid in the surrounding area of the surface. Hence, for rotating flow problems buoyancy forces depend on the rotational speed and local radius. In free convection, the heat transfer coefficient will increase the force of the buoyancy-induced motion, which would in turn increase the temperature difference that causes it. Hence, in free convection, the heat transfer coefficients also depend on the scale of the surface to fluid temperature difference. In forced convection, the fluid may be forced by some external mean such as pump and fan. This occurs where there is a major applied motion of the fluid in relation to the source or sink of heat. It may also involve separation of flow from surfaces or a phase change of the fluid. Natural and forced convection are classified according to both laminar and turbulent flow. The extent of heat convection is influenced by many factors. These factors are the characteristics of the fluid flow, the thermal conductivity of fluid, the shape and magnitude of the fluid and the solid boundary.

Convection problems are complex and can be modelled using dimensional analysis and empirical methods based on the concept of the heat transfer coefficient. Values of heat transfer coefficient can be derived from measurements for any particular geometry, flow condition and set of fluid physical properties, following which functional relationships may then be developed from dimensional analysis. The non –dimensional parameters used in heat transfer coefficient correlations in SCO3 are Reynolds number Re which characterises the fluid flow, Nusselt number Nu which characterizes the heat transfer, Prandtl number Pr that reflects fluid properties and Grashof number Gr that characterises buoyancy driven flows or natural convection. Details of the correlation used in SCO3 are presented in Section 3.9.

The main task in a finite element temperature analysis is therefore in the calculation and specification of convective boundary conditions. The boundary condition types available within SC03 are thermal streams, Thermal ducts, thermal voids, convecting zone, prescribed temperatures, external and internal radiation which are presented in details in Section 3.7. The accurate calculation and representative specification of thermal boundary condition equations is vital to the formation of a quality finite element model. In all cases the boundary condition equations must be put together to enable calculation by the SCO3 program at any engine condition. The automatic analysis system is used to process the results from the cycle runs. The results are usually presented in the form of temperature versus time graphs or contour plots. In temperature analysis, two conditions are performed; there are steady state and transient conditions.

Furthermore, in thermal analysis, attention is given to the conservation of mass and the conservation of energy. These conservations are very important in the modelling of flow through thermal stream boundary conditions. For the conservation mass, it means that, for the steady state system, the mass flow entering the system must equal the mass flow leaving the system. While for the conservation of energy, it means that, for the steady state system, the energy entering the system must equal the energy leaving the system.

3.3.1.1.2 Radiation

This is a mode of heat transfer where there is an exchange of heat between bodies without the presence of any intervening medium. Hence, radiation is an energy transfer which is transmitted most freely in a vacuum. At the temperatures above absolute zero, all matter emit radiation in the form of electromagnetic waves of various wavelengths. At this temperature, electrons in the molecules of the material at the surface of a component will vibrate thereby emitting radiation energy. The amount of radiation energy emitted will depends on the absolute temperature. A typical example is the everyday experience of our body being warmed by the sun, with approximately $1.5x10^{11}m$ of empty space separating it from the earth (Long, 1999). The heat transfer by radiation from an object at an absolute temperature, with a body of surface area A is given Stefan-Boltzmann law as:

$$Q = \sigma A T^4{}_1 \qquad (watts) \tag{3.9}$$

The radiation boundary conditions used in SCO3 program are internal and external radiation which are presented in details in Section 3.7.7 and 3.7.8 along with the black body radiation.

3.3.1.2 Displacement analysis

Finite element analysis is the recommended method for displacement predictions. However, for very simple problems theoretical displacement analysis is suitable. Displacement analysis is used for displacement predictions. The thermal boundary conditions have a significant impact on the final displacements due to thermal growth, temperature effect on material properties and fluid pressure defined in the thermal boundary conditions. There are a number of effects that contribute to the total displacement in a typical engine application. These are thermal expansion, centrifugal growth, pressure growth and tensile strain.

Displacement analyses in SCO3 can be used in the calculation of axisymmetric closure from the finite element model. Predominantly in compressors, these displacements could be characterised using time constants. These closures include the effects of rotor centrifugal loads (CF), rotor thermal expansion, rotor deflections due to pressure loads, casing pressure dilation and casing thermal expansion. Structural loads are very important in displacement analysis as such consideration must be made to the definition of loading on the model. One of such loads is the centrifugal load that is automatically calculated by SC03 by appropriately specifying the rotational speeds for each component. Additionally, the pressures defined within the thermal boundary conditions in the model of thermo-mechanical process, will apply pressure loading to the structure. The thermal strains will also be accounted for and the geometry reference temperature should be set to the as-built temperature which as a default value $20^{o}C$. However, to suit the ambient day temperature for a particular cycle, this default value should not be changed. The displacement analysis is performed on two main conditions which are steady state and transient conditions. Steady state conditions describe engine conditions where displacements do not change with time, meaning that components have reached their thermal and structural equilibrium state. While transient conditions, illustrate conditions where displacements are changing with time, moreover, a transient analysis may also include steady state conditions. The displacement analysis results will usually be presented as a function of time over a full engine cycle.

Displacements analyses are computed to support the design process for a number of reasons. These are fuel efficiency, surge margin, failure cases, integrity and life. Compressor tip clearances must be minimised to reduce leakage paths in the main gas path and the release of abraidable lining material must also be minimised to avoid increase tip clearances as both will lead to higher fuel consumption hence lower fuel efficiency. As previously mentioned, minimizing the release of abraidable lining material will reduce tip clearances and the reduction in compressor tip clearances will prevent surge occurrence. The clearances of titanium components should be controlled as excessive rubbing of these components can result in titanium fires leading to cases of component failure. Integrity and Life of engine components can be improved through axial and circumferential gapping of many components such as tips, shroud segment and blade platforms, to avoid excessive stresses or fouling during the relative movement between components during a mission. Also, bearing interference fits and running clearances must be controlled to avoid loss of interference which can cause localised wear or vibrations.

3.4 Geometry

To start a model set-up in SC03, geometric data are imported either by means of an Initial Graphics Exchange Specification (IGES) file as a set of unconnected curves created using a computer aided design (CAD) package or using the drawing facilities accessible within the SC03 program.

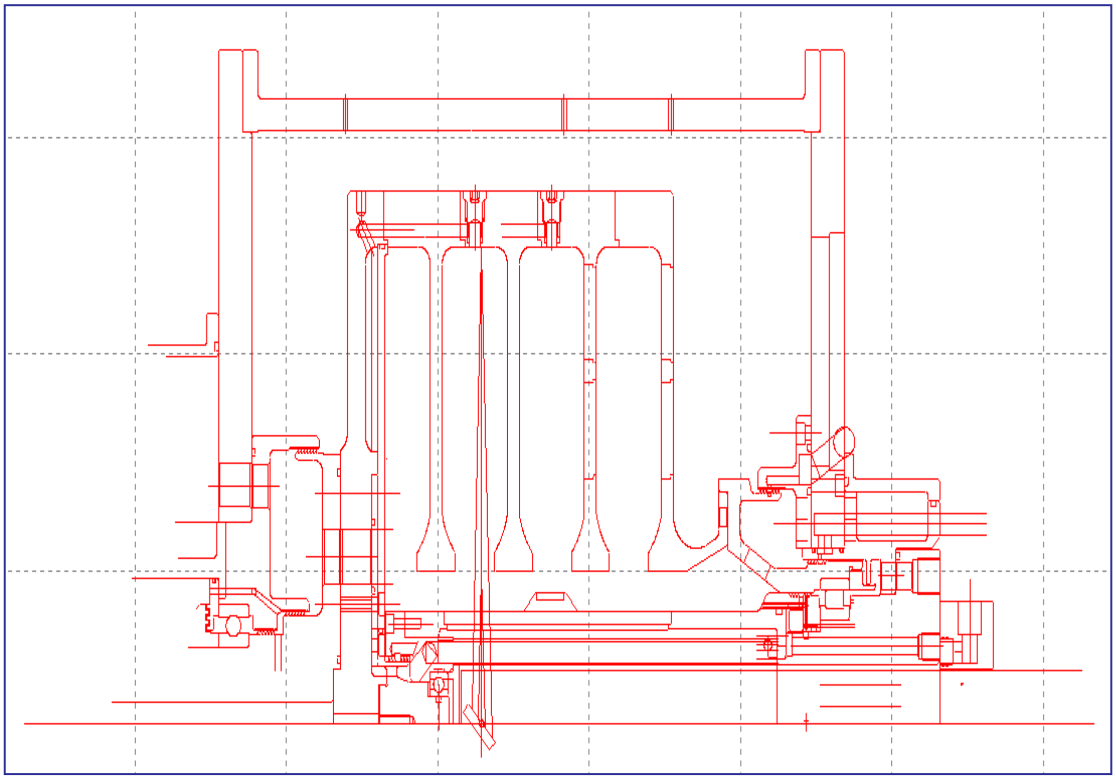

Figure 3.4: Multiple cavity rig model geometry imported by means of IGES into SC03 program

However, a Standard for the Exchange of Product (STEP) model data file can also be used. Figure 3.4 shows the geometry data imported by means of IGES into SC03 program.

When the data has been successfully imported, the geometry edges, geometry surfaces, and solid faces will be visible. For complex geometries, it advisable to use the CAD package because drawing facilities within the SC03 program are limited. After importing the model from CAD as an IGES file into the SC03, the model is saved into the SC03 program with a specific name that ends with ‘.pm’ (physical model). This is identified as a .pm file before a clean-up activity is performed using the inbuilt design facilities.

The geometry is checked for its consistency with the original drawing to correct any distortion and not to unintentionally alter the geometry from the original design target. All parts of the geometry are examined for unacceptable inconsistencies such as gaps, folds, or duplicate entities; these are marked "x" unconnected and a warning message with square red sign at the point of the unconnected lines is given in each case as shown in Figure 3.5. If there are no errors then the geometry is chained to connect lines or entities together and to determine splitting entities. When the geometry has been chained successfully, the model is ready for further operation within the SC03.

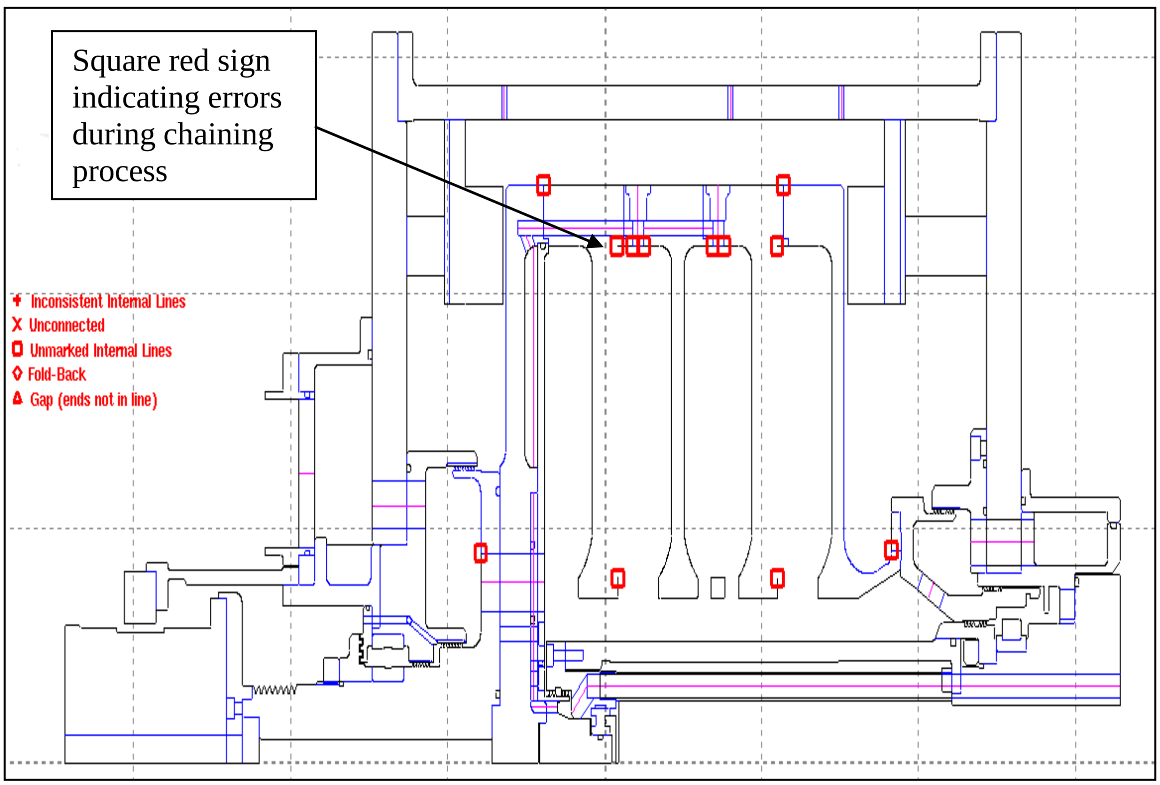

Figure 3.5: MCR model showing Errors in the model during chaining process

Hole centrelines must also be defined where necessary before chaining the geometry to determine which lines are connected to each other. This is necessary in order to apply the boundary conditions. Chaining is the process of connecting lines or entities to each other to form a model. Internal lines should be marked for lines having material on both sides of the component and these lines will immediately turn blue in colour. The lines that have air or some other fluid on one side are known as the external lines. Both the 2D and the 3D geometry analysis tools are accessible in the Model Analysis Control Panel. This includes meshing, domain definitions, application of thermal boundary conditions, definition of engine cycle, running of SC03, and output processing of the result.

3.5 Meshing

When the clean-up of the geometry is complete, the geometry can then be meshed. The choice of mesh has profound effect on the accuracy, convergence, and speed of the solution. Meshing is the breaking up of a physical domain such as a 2D domain in 2D geometry and 3D domain in 3D geometry into simpler subdomains called the elements. The shape of these elements depends on whether the model is 2D or 3D. SC03 has an inbuilt automatic mesh generator that generates the mesh automatically when the analysis is run, and this is accessible in the Mesh Analysis Control Panel. The program uses an automatic mesh generator of quadratic six-node triangular elements in 2D and ten-node tetrahedral elements in 3D. In the case of the 2-D MCR baseline model, a six-node triangular element was generated in 0.690967sec, with a total of 10007 elements and 22504 nodes. The major steps completed by SC03 during automatic meshing are geometry recognition, node generation and surface triangulation. The element density is controlled by the triangle distortion ratio, which has a default value of 4 in SC03. Figure 3.6 shows a multiple cavity rig model meshed with six-node triangular elements in 2D.

Other form of meshing can be employed, including adaptive meshing and the use of external meshes. The element density is controlled by the triangle distortion ratio, which has a default value of 4 in SC03. If the mesh fails, the analysis during mesh generation will stop and a mark ‘x’ is shown where the geometry has a problem and that is then fixed and remeshed, and in some cases the mesh is refined for greater accuracy. This is good practice for complex models and where there is doubt in the geometry, to ensure that the meshing is acceptable.

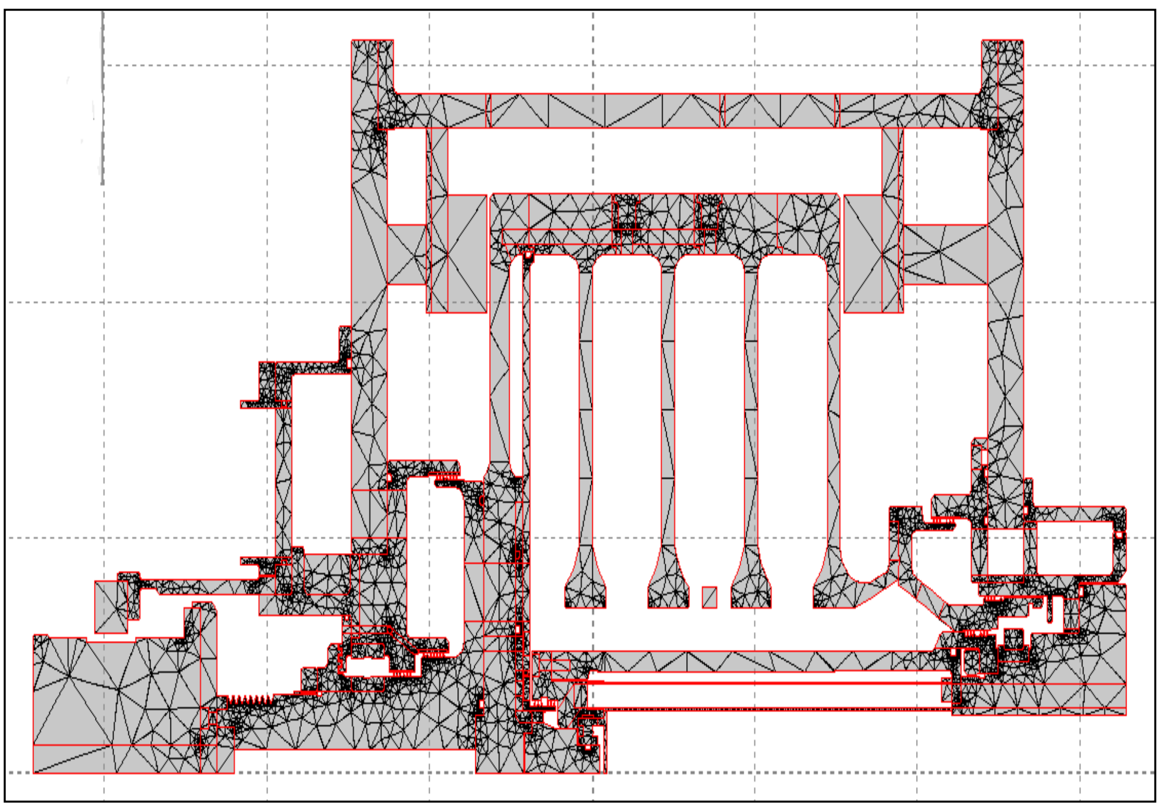

Figure 3.6: The geometry of the multiple cavity rig model meshed with six-node triangular elements in 2D

3.6 Domain Definitions

Each component within an SC03 model is defined by a separate solid domain which utilises material properties appropriate to that component. The domain definition involves the use of a Domain Control Analysis Panel to input the required material type, which is accessed from the ‘Commit’ file that stores all the material types in SC03. New material can be read into the SC03 from other sources if needed as a .mat file (‘filename.mat’) and the material names are 3–4 character codes, while the thermal and structural material properties (Young’s modulus, thermal conductivity, specific heat capacity, Poisson’s ratio, density, and coefficient of expansion) must be defined in the material file.

Other relevant properties in the domain control panel are: rotational speed relating to the cycle and domain type such as 3D, axisymmetric, plane stress, or plane strain, which are applied to regions known as sub-domains bounded by internal or external geometry lines. The local speed property of a component defines closed regions with speed that is different from the default speed in the SC03. Appropriate rotational speeds must be defined within the Domain Control Panel because many heat transfer correlations require the local rotational speed for analysis. For the multiple cavity rig, where the rotor speed is a time-varying parameter, all the casings are defined as having a local speed of 0. In the MCR SC03 model, titanium (TFF) is used for the HPC disc, C1023 (QAB) for the casing and CMV (AEF) is used for the shaft.

A non-axisymmetric element known as non-hoop can be modelled by assigning a local thickness property to the closed region defining this element, therefore identifying the area to which load, pressure, and heat flux are applied. The thickness property is used to represent 3D features in 2D axisymmetric models and the thickness expression can only be used by SC03 if plane stress which is not axisymmetric is chosen as the domain type. The holes property is used to describe a closed region with a circumferential row of circular holes and the effective local element thickness is determined assuming that the area is axisymmetric. Thickness in SC03 is defined as the amount of material at a given circumference. For n holes on a pitch circle diameter (see Figure 3.7). The Uniform thickness can be calculated as follows:

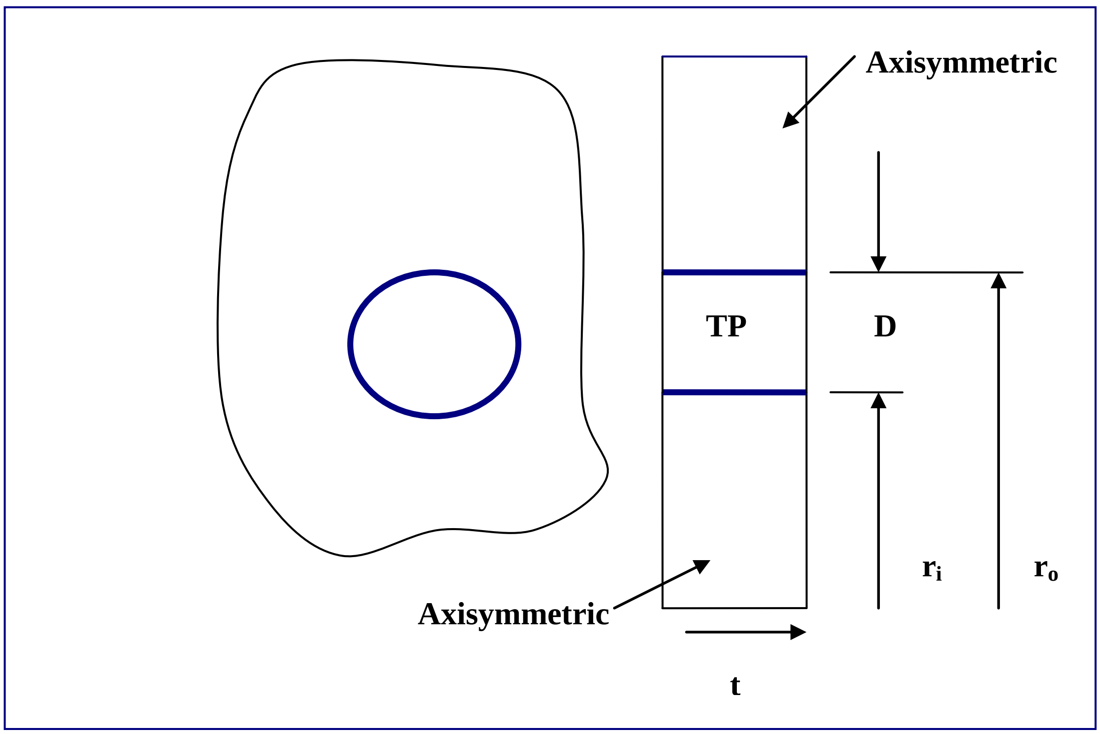

Figure 3.7: Thickness property definition on a pitch circle diameter

Diameter of holes, $D_{holes} = r_0 - r_i$ **(3.10)**

Pitch circle radius, $r_m = \dfrac{(r_0 + r_i)}{2}$ **(3.11)**

The actual volume of n holes, $V_{act} = \left(\dfrac{\pi D^2}{4}\right) \cdot t \cdot n$ **(3.12)**

The swept volume between r_0 and r_i, $V_{swept} = \pi\left(r_0^{\ 2} - r_i^{\ 2}\right) \cdot t$ **(3.13)**

The fraction of air, $X_{air} = \dfrac{V_{act}}{V_{swept}}$ **(3.14)**

The fraction of material, $X_{mat} = 1 - X_{air}$ **(3.15)**

Thickness property, $TP = X_{mat}.2.\pi.r_m$ **(3.16)**

wherer t = thickness of hole

Other domain properties include displaying of domain numbers, domain initial temperature specification, which can be a user expression such as dbtemp = 293.15K or could be a database parameter (bdd) such as TAMB, an equivalent of the ambient temperature, and thermal and structural loads. For details on the practice on thickness property, readers are referred to Rolls-Royce plc (2004).

3.7 Thermal Boundary Conditions

The selection of boundary conditions and the associated correlations used to define the heat transfer coefficient between the solid and fluid domains is essential for an accurate representation of the temperature distribution within the solid domain. However this is not an easy task as the analyst will rely more upon experience and personal judgements in the choice of the appropriate boundary type and correlation from among those available in SC03 in line with the analysis. The chosen boundary conditions are applied to any portion of the fluid-to-solid boundary within the model, and any boundary without a specific boundary condition is modelled as an adiabatic surface. The boundary conditions within the SC03 program are Prescribed Temperature, Convecting Zones (CZ), Thermal Voids (VO), Thermal Streams (ST), Thermal Ducts (DU), External Radiation (ER) and Internal Radiation (IR). Sections 3.7.1 to 3.7.9 provide an overview of the boundary conditions available in SC03 and those used in the SC03 model shown in Figure 3.8. For more details on boundary conditions the reader is referred to Alexiou (2000) and Illingworth (2006).

In the multiple cavity rig model used in this research as shown in Figure 3.8, the outer surface of the casing was modelled with convecting zones for the reason that the rig would be operated in a room with continuous ventilation. Convecting zones, with a high heat transfer coefficient, were used to model the heating of the outer surface of the rotor, with jets of hot air through the ducts. In all the boundary conditions, air was used as the fluid. The heat transfer coefficients and the temperature rise due to the frictional heating of air (windage) were calculated using inbuilt correlations contained within the program.

External radiation from the casing to the room was also considered in the model. Streams and ducts with a rotating free disc correlation as heat transfer coefficient were applied at the cobs of the discs and the shaft with a windage heat pick up term. The cavities were modelled as voids where natural convection from a vertical plate is assumed. The natural convection was modelled using the natural convection correlations. The natural convection correlations associated with plate and cylinder known as natural convection correlations for upper surface of plates (NUS) and natural convection correlation for vertical plates or cylinder (NVP) were used as the heat transfer coefficient for voids modelling in the cavities and the length of the plate was used as an argument. According to the flow visualisation and heat transfer work of Farthing et al. (1992a and b), the Grashof number was defined using the centripetal acceleration, $\Omega^2 r$, and the radial distance from the shroud, $y = b - r$. A stream was fed to each void as a power input. The temperature output from the voids in each cavity was mixed with the temperature of the axial throughflow, at the exit from each cavity.

Ducts were used to simulate the flow of the air through the rotating and non-rotating holes in the rig. They were used to model the flow through all ducts and holes. Ducts are used also to model the radial inflow through the ducts into the cavity. The forced convection correlation known as MNUN was used as the heat transfer coefficient for ducts modelling. The flow area, length and mean hydraulic diameter of the duct were employed as arguments. The pressure, temperature and mass flow rate of the cooling air and the radial inflow air at the inlet to the rig were defined as time-varying parameters to allow for transient analyses. Using the supplied inlet cooling air temperature as the starting point, the temperature output from one boundary condition was used as the temperature input to the next boundary condition. In the case of radial inflow, the temperature output from one boundary condition was also used as the temperature input to the next one. Mixing the temperatures from streams or ducts was possible. The inlet pressure was used as air pressure in the boundary condition while the mass flow rate was used in the boundary conditions. The temperature, pressure and mass flow rate of the cooling air was supply into model cavity via a bore flow inlet in the upstream into the rig through duct 1 (DU1).

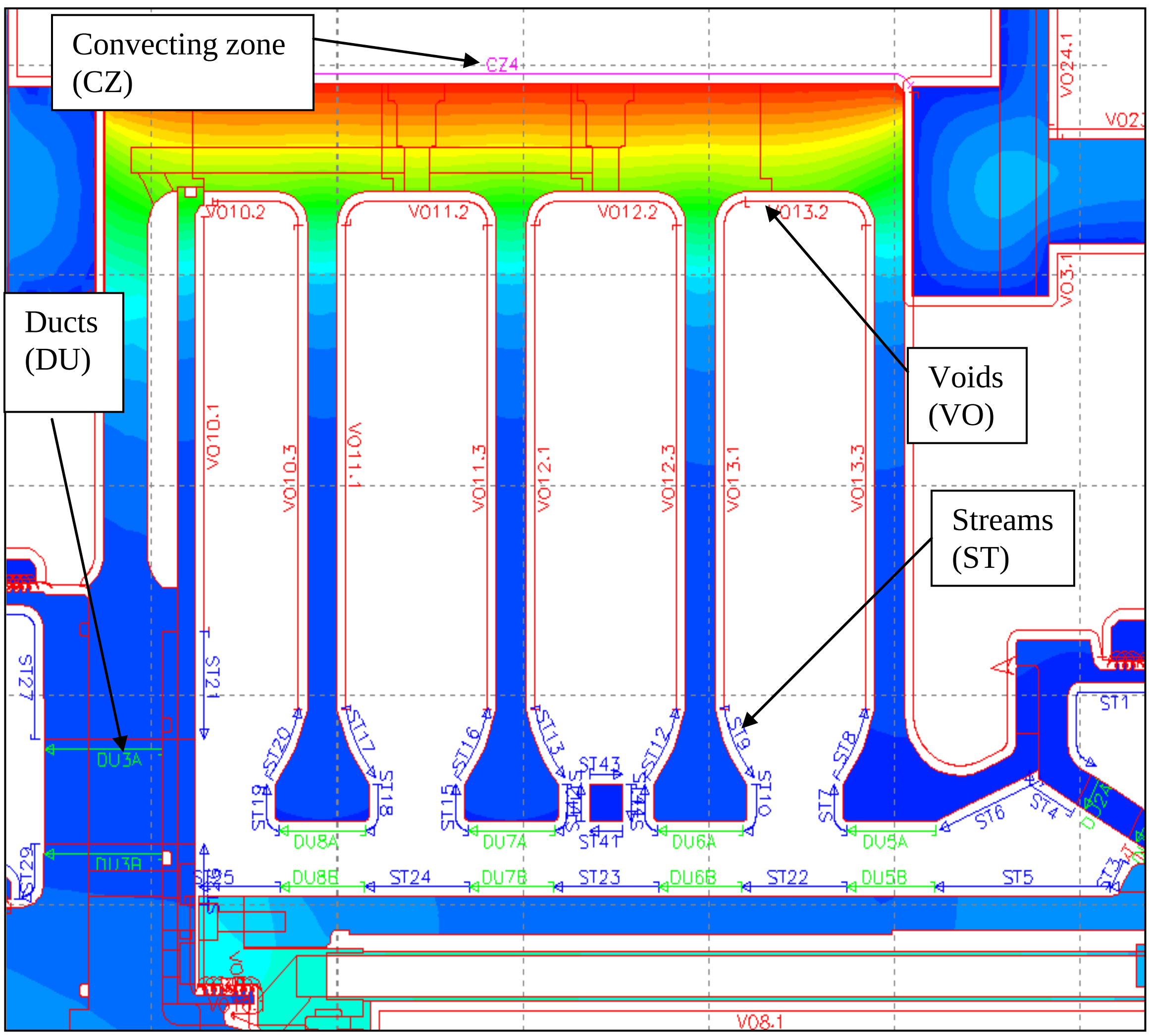

Figure 3.8: SC03 model of the Multiple Cavity Rig (MCR) with boundary conditions

3.7.1 Prescribed Temperature

A prescribed temperature boundary is used to described a boundary in which a known temperature or temperature distribution is applied to a portion of the boundary. A single expression for surface temperature is supplied, although a fixed value or a valid SC03 expression or graph can also be used. At the beginning of the analysis the prescribed temperature must match the initial domain temperature. However, problems may be encountered when two prescribed temperature boundary conditions apply at a single point. If this occurs, then the temperatures at that point must match or be within a suitable, pre-determined tolerance of 2^{o}C. This is always the source of large temperature errors in regions local to prescribed temperature boundary conditions. To avoid these errors, the best practice is to model a prescribed temperature using a convecting zone with a very high heat transfer coefficient as in the case of the rotor surface in Figure 3.8. This will cause the metal temperature to be equal to the fluid temperature.

3.7.2 Convecting Zone (CZ)

Convecting zone boundary conditions are used where the fluid temperature distribution is known and the temperature used may be a single value or may vary in space and time. In this model, convecting zones are modelled around the outer surface of the casing and the outer surface of the rotor as shown in Figure 3.8. The convecting zones are regions where the neighbouring fluid regions have an infinite heat capacity such that the fluid temperature specified in that region will not change in spite of the degree of the resulting heat transfer between the fluid and the component. Four parameters are required to define a convecting zone boundary condition: fluid type, fluid temperature, fluid pressure, and heat transfer coefficient. The fluid type is commonly air but could be another fluid defined by the user such as oil. The fluid temperature (K) applied may be a single value or may vary as a function in space and time. The fluid pressure is used in the heat transfer coefficient correlation calculation where necessary and for the determination of the pressure load in a thermo-mechanical analysis. The heat transfer coefficient may be a predetermined value or expression in SC03. The SC03 database holds a large number of approved inbuilt heat transfer correlations that calculate the heat transfer coefficient and these are discussed in Section 3.9. Variation of the heat transfer coefficient will vary the heat flux in the system. The heat flux from a convecting zone is calculated from Equation 3.17, where A is the surface area, h is the heat transfer coefficient, T_f is the fluid temperature, and T_s is the surface temperature.

$$Q = hA\left(T_f - T_s\right) \qquad \textbf{(3.17)}$$

3.7.3 Thermal Void (VO)

A thermal void is used to depict portions of the boundary in a model with negligible heat capacity. In the multiple cavity rig model used in this study, the cavities were modelled with voids where natural convection from a vertical and upper surface of plate or cylinder is assumed as shown in Figure 3.8. It was used for the baseline model (model without radial inflow). A thermal void has properties that are almost the exact opposite of convecting zone properties. This is so because the convecting zone is a region of infinite heat capacity while a thermal void is a region of negligible heat capacity. A thermal void has a single temperature, meaning that it represents a region with uniform temperature and is at instantaneous equilibrium with its surroundings. The thermal void can consequently be used to transfer heat across an air cavity and by equating the net heat flow into it to zero; the temperature of the fluid can then be derived. The void can be controlled by two heat sources such as convection from the surrounding walls and an additional power term from a mass flow into the void if present.

The instantaneous equilibrium implied by thermal voids indicates that there is no net heat flux into the void, as shown in Equation 3.18.

$$\int h(T_s - T_f)dA + Q_{in} = 0 \tag{3.18}$$

where: Q_{in} = the amount of heat input into the void from external sources such as the thermal stream or duct defined in the power input field in the void panel.

A is the surface area, T_s is the components temperature, and T_f is the void temperature.

Hence the uniform temperature in the void is defined as:

$$T_f = \frac{\int hT_s dA + Q_{in}}{\int hdA} \tag{3.19}$$

The amount of heat input into the void is given as:

$$Q_{in} = W\left[\int_0^T C_p dT_{stream} - \int_0^T C_p dT_f\right] \tag{3.20}$$

In cases where the changes in temperature are small, the C_p term is ignored, giving the heat input into the void as:

$$Q_{in} = WC_p\left(T_{stream} - T_f\right) \quad \textbf{(3.21)}$$

where: W = stream mass flow rate (Mg/s)

3.7.4 Thermal Stream (ST)

Thermal streams are the most frequently used thermal boundary condition in SC03. They are used to define the heat transfer at boundaries where there is a known, finite flow of fluid along their length. A thermal stream has a finite heat capacity and has the ability to absorb energy from one place on the surface and transport it to another. In the model shown in Figure 3.8, streams were applied at the cobs of the discs and the shaft with a windage heat pick up term and were also used to direct axial throughflow into the rig cavity. In a thermal stream, the inlet air temperature is defined at the start of the analysis and the variation in fluid temperature is calculated along the boundary due to the effect of convection, the heat capacity of the stream, and any additional heating brought in by windage. Transient variation in component fluid temperatures is possible with appropriate choice of heat transfer coefficients and flow system properties. The arrangement of the two points defined by the thermal streams' boundary gives the direction of the flow and they are capable of being linked and mixed together. In general, thermal streams are used effectively in SC03 to model the flow of air, heat exchange, and heat pick-up throughout engine internal cooling air systems. Six parameters are required to illustrate these boundary conditions in SC03: fluid type, mass flow rate, pressure, temperature, the heat and temperature pick-ups, and the convective heat transfer coefficient. An enthalpy balance is used to calculate the mixed temperature where two or more streams mix together to produce a combined temperature at the inlet to another stream as shown in Equation 3.22.

$$W_1 \int_{T_1}^{T_m} C_p T dT + W_2 \int_{T_2}^{T_m} C_p T dT = 0 \qquad \textbf{(3.22)}$$

3.7.5 Thermal Ducts

A thermal duct is comparable to a thermal stream except that two portions of the boundary are defined between which the flow occurs and is used where a flow between components is separated by only a small space or flow occurs through holes within a component. Thermal ducts are used to signify turbulent flow in small confined passages where there is a possibility of heat exchange between the surfaces due to turbulent mixing. As shown in Figure 3.8, ducts were used to model the flow through all ducts and holes and were used also to model the radial inflow through the ducts into the cavity space. The same parameters as in a stream are required in the duct definition, and include fluid type, mass flow rate, pressure, temperature, the heat and temperature pick-ups, and the convective heat transfer coefficient. The arrangement of the two corresponding points defined by the ducts boundary gives the direction of the flow, and there can be an exchange of energy between the two surfaces and conveyed through the duct flow.

3.7.6 External Radiation

In SC03, the external radiation boundary condition is used to describe a part of the boundary having a specified emissivity which can convey radiation and obtain it from a remote source that is not clearly modelled or is not part of the model but has a known temperature. The external radiation was applied on the outside casing of the model. External radiation is used if one or more components are not specified in the model. The remote temperature identifies the temperature through which the radiation is exchanged, while the emissivity is used to describe the proportion of black body radiation that can be emitted. The Stefan Boltzmann equation is employed to calculate the heat flux as follows:

$$q = \varepsilon\sigma\left(T_R{}^4 - T_s{}^4\right) \qquad \textbf{(3.23)}$$

where σ = Stefan Boltzmann constant = 5.6687×10^{-9} W/m^2 K^4

T_R = temperature of radiator (K)

T_s= temperature of surroundings (K)

ε = emissivity (=1 for ideal radiator)

The effective radiation heat transfer coefficient is applied using the expression:

$$h_{rad} = \left\{\sigma\left(T_R + T_S\right)\left(T_R{}^2 + T_S{}^2\right)\right\} \qquad \textbf{(3.24)}$$

3.7.7 Internal Radiation

The internal radiation heat transfer boundary condition is used to describe portions of the boundary which are able to transmit radiation and receive it from themselves and each other. The view factors are calculated automatically. This type of radiation is applied by indicating the boundaries and their emissivity. Internal radiation was applied on the surface of the rotor. Internal radiation is important in cases where the convective heat transfer coefficient is relatively low or in cases where there are relatively high surface temperatures such as turbine casings. It is also vital where there are large temperatures differences between the surface and the surroundings. Internal radiation heat flux is given by the equation:

$$Q_{Grey} = \xi_{1-2} A_1 \sigma \left(T_1^{\,4} - T_2^{\,4} \right) \qquad \textbf{(3.25)}$$

where: Q_{Grey} = heat flow rate from a grey body

ξ_{1-2} = grey body view factor, which is given as:

$$\xi_{1-2} = \frac{1}{\left(\frac{1-\varepsilon_1}{\varepsilon_1}\right) + \frac{1}{F_{1-2}} \frac{A_1}{A_2} \left(\frac{1-\varepsilon_2}{\varepsilon_2}\right)} \qquad \textbf{(3.26)}$$

3.8 Boundary condition inputs

The input parameters for boundary conditions are fluid type, mass flow, fluid temperature, absolute and relative temperature, fluid pressure, temperature and heat pick-up and heat transfer correlations. The selection of boundary conditions, its input and the associated correlations used to define the heat transfer coefficient between the solid and fluid domain is essential to an accurate representation of the temperature distribution within the solid domain.

3.8.1 Fluid Type

The working fluid is pure (i.e. dry) air. The automatic analysis program SC03 handles the calculation of the properties of air such as temperature, density, specific heat capacity, thermal conductivity, kinematic viscosity, dynamic viscosity, and the Prandtl number.

Sutherland's law is use to compute the dynamic viscosity. Sutherland's law expresses the relation between the dynamic viscosity and the absolute temperature of an ideal gas. It is given as,

$$\mu = \frac{C_1 T^{3/2}}{T+S} \qquad \textbf{(3.27)}$$

Where for air $C_1 = 1.458\text{X}10^{-6}\, kg/ms\sqrt{K}$

T is in Kelvin and $S = 110.4\text{K}$

3.8.2 Mass Flow

Mass flow terms in SC03 are defined in order to characterise the fluid flow over a boundary of the finite element model. The main function of the mass flow in component temperature prediction is to define the heat capacity of the fluid flow with the help of the specific heat. The main flows in SC03 are the main engine annulus flow, turbine rim gas ingestion, and entrainment flow.

3.8.3 Fluid Temperature

Fluid temperatures are usually defined at the initial point of a flow system analysis, while the succeeding fluid temperature distributions in the system are calculated automatically by the analysis program depending on the boundary conditions used. In an engine, the main annulus fluid temperature may be specified based on two engine performance parameters such as the inlet (upstream) temperature and the exit (downstream) temperature, as shown in Equation 3.28.

$$\mathrm{X} = \frac{T - T_1}{T_2 - T_1} \tag{3.28}$$

The Equation can be rearranged to give the equation for fluid temperature as:

$$T = T_1 + \mathrm{X}(T_2 - T_1) \tag{3.29}$$

Where:

X = scaling constant

T = known fluid temperature

T_1 = inlet or upstream temperature

T_2 = exit or downstream temperature

3.8.4 Absolute and Relative Temperature

Absolute and relative temperatures are vital in the thermal modelling of the interdisc cavity such as that found in the MCR model. The reason being that they are used to convert temperature when moving from a stationary to rotating component (or vice versa). In SC03, absolute total temperature is used for stationary parts which are nozzle guide vane (NGV), casings and stators. The relative total temperature is used for rotating parts such as rotor discs and blades.

The temperature at the surface of the rotating component is given as:

$$T_{rel} = T + \frac{V^2{}_{rel}}{2C_p} \qquad \textbf{(3.30)}$$

The temperature of the stationary component surface is given as:

$$T_{abs} = T + \frac{V^2{}_{abs}}{2C_p} \qquad \textbf{(3.31)}$$

Equation 3.30 and Equation 3.31 can be combined to give:

$$T_{rel} = T_{abs} - \frac{V^2{}_{abs}}{2C_p} + \frac{V^2{}_{rel}}{2C_p} \qquad \textbf{(3.32)}$$

where:

T = static temperature

V_{rel} = relative fluid velocity

V_{abs} = absolute velocity

3.8.5 Fluid Pressure

Fluid pressures are defined in thermal boundary conditions for the evaluation of fluid density, and in the application of a pressure load at the surface in thermo-mechanical analysis involving a combined temperature and displacement analysis. In SC03, the recommended accuracy for fluid pressures for all thermal boundary conditions is $\pm$5Pa.

3.8.6 Temperature and Heat Pick-up

This is the frictional heating of air in a system .The heat pick up (HPU) due to a change in radius in a rotating system is calculated using SC03 in a built windage correlation known as the VORX correlation. The arguments used are rotational speed, angle of surface relative to axis and perimeter to be specified. In SC03, VORX (N) correlation is used when it is applied to an edge while VORX (N, Alpha, Perimeter) correlation is used when it is applied to a face.

HPU= VORX (N, A, P) **(3.33)**

Where:

N = rotational speed (rad/s)

A_a = A= Alpha = half cone angle (rad)

Perimeter = wetted perimeter normal to the angle alpha

For details on temperature and heat pick-up, the reader is referred to Chew, 1988.

3.9 Heat Transfer Correlations

A wide-ranging correlation has been developed to aid in the estimation of convective heat transfer coefficients for a range of cases, such as natural convection, and forced convection for internal and external flow. SC03 has inbuilt empirical correlations which are capable of automatically calculating all heat transfer coefficients. The accuracy and validity of the model will depend on the correct choice of correlation, and the related correction factors used in any modelling process. The empirical heat transfer correlations used in this modelling and their flow regimes are:

- Natural Convection – Plate and Cylinder
- Forced Convection – Rotating Flow
- Forced Convection – Ducts and Plates

The SC03 command, flow pattern, operational range, application area and the non-dimensional quantities associated with each heat transfer correlation are presented in Section 3.9.1 – 3.9.3

3.9.1 Natural Convection – Plate and Cylinder

The natural convection correlations associated with plate and cylinder known as NUS and NVP were used for voids modelling in the cavity and other parts of the MCR model. For details on natural correlation from natural convection from upper surfaces of hot horizontal plates and lower surfaces of cool horizontal plates (NUS) and natural convection from vertical plates or cylinder (NVP), the reader is referred to McAdams (1958) and Fishenden & Saunders (1950). Table 3.4 shows SC03 correlations for natural convection for plates and cylinder with area of application and the non-dimensional parameter used which is called the Rayleigh number (Ra). Rayleigh number is given as:

$$Ra = \Pr . Gr \tag{3.34}$$

SC03 Command	Flow Pattern	Correlation	Range
nus(L)	Upper Surface of Hot Plates & Lower surface of Cool Plates	h = 0.54 $Ra^{0.25}$ k/L h = 0.14 $Ra^{0.33}$ k/L	$Ra \leq 2 \times 10^7$ $Ra > 2 \times 10^7$
nvp(L)	Vertical Plate or Cylinder	h = 0.59 $Ra^{0.25}$ k/L h = 0.129 $Ra^{0.33}$ k/L	$10^4 < Ra \leq 10^9$ $Ra > 10^9$

Table 3.4: SC03 correlations for natural convection for plates and cylinder

3.9.2 Forced Convection for Rotating Flow

The forced convection correlation in SC03 for rotating flow are turbulent free disc (fdf and frd), laminar free disc (fdlam and frlamd), general free disc (fdgen and frgend), general rotating flow (genrot) and rotating drum (drum). Table 3.5 shows SC03 correlations for the forced convection for rotating flow. The forced convection correlation for rotating flow known as FRGEND (NH) was used for streams modelling in the cavity of model with radial inflow, around the disc cob and other parts that stream are used in the MCR model. FRGEND (NH) will perform during both laminar and turbulent conditions. Details information for forced convection correlation for rotating flow can be found in Dorfman, L. A. (1963), Northrop, A. & Owen, J. M., (1988a), Dennis, R. W., Newstead, C. & Ede, A. J. (1970) and Cobb, E. C. & O A Saunders, O. A. (1956).

SC03 Command	Flow Pattern	Correlation	Range
fdgen & frgend(NH)	General Free Disc	$h = 0.616Re^{0.5}\ Pr^{1/3}$ k/r $h = 0.0267Re^{0.8}\ Pr^{0.6}$ k/r	$Re \leq 2.4x10^5$ $Re > 3.0x10^5$

Table 3.5: SC03 correlations for forced convection for rotating flow

3.9.3 Forced Convection for Ducts and Plates

The forced convection correlations which are related to duct are the non-rotating duct (fcd and mfcd), flat plate (fcp, frp and mfrp) and forced convection in a duct (nun and mnun). Table 3.6 shows SC03 correlations for forced convection in a duct for laminar flow based on Sieder and Tate correlation and Table 3.7 shows SC03 correlations for forced convection in a duct turbulent flow based on Nunner heat transfer correlation.

SC03 Command	Flow Pattern	Correlation	Range
MNUN (AREA,DH DLENGTH , W)	Duct	$Nu_{FD} = 1.86\left[\frac{\mathrm{Re}.\mathrm{Pr}.D_h}{L}\right]^{1/3}.\left[\frac{\mu}{\mu_w}\right]^{0.14}$	Re<2100

Table 3.6: SC03 correlations for Forced Convection for Duct for Laminar flow

SC03 Command	Flow Pattern	Correlation	Range
MNUN (AREA,DH DLENGTH , W)	Duct	$Nu = \frac{\lambda \mathrm{Pr}.\mathrm{Re}}{8.\left[1+1.5.\mathrm{Pr}^{-1/6}.\mathrm{Re}^{-1/8}\left[\frac{\lambda \mathrm{Pr}}{\lambda_0}-1\right]\right]}$	$2300<Re<8x10^5$

Table 3.7: SC03 correlations for Forced Convection for Duct for Turbulent flow

The NUN (AREA, DH, DLENGTH, ROUGH) and MNUN (AREA, DH, DLENGTH, ROUGH, W) correlations are employed to calculate heat transfer coefficients for forced convection in a duct. The forced convection correlation known as MNUN was used for ducts modelling in the MCR model. The heat transfer coefficient can be found using the hydraulic diameter of the duct as the characteristic dimension.

3.10 Definition of Cycle

The cycle describes the analysis to be performed in any SC03 program and this consists of a ramp and a set of conditions which are accessed by the ramp. SC03 identifies a series of distinct time points called the ‘ramp points’ in any cycle. The environmental parameters such as temperature and the cycle running speed are specified at each ramp point before any analysis is performed. These parameters are said to vary linearly between two successive distinct time points as shown in Figure 3.9.

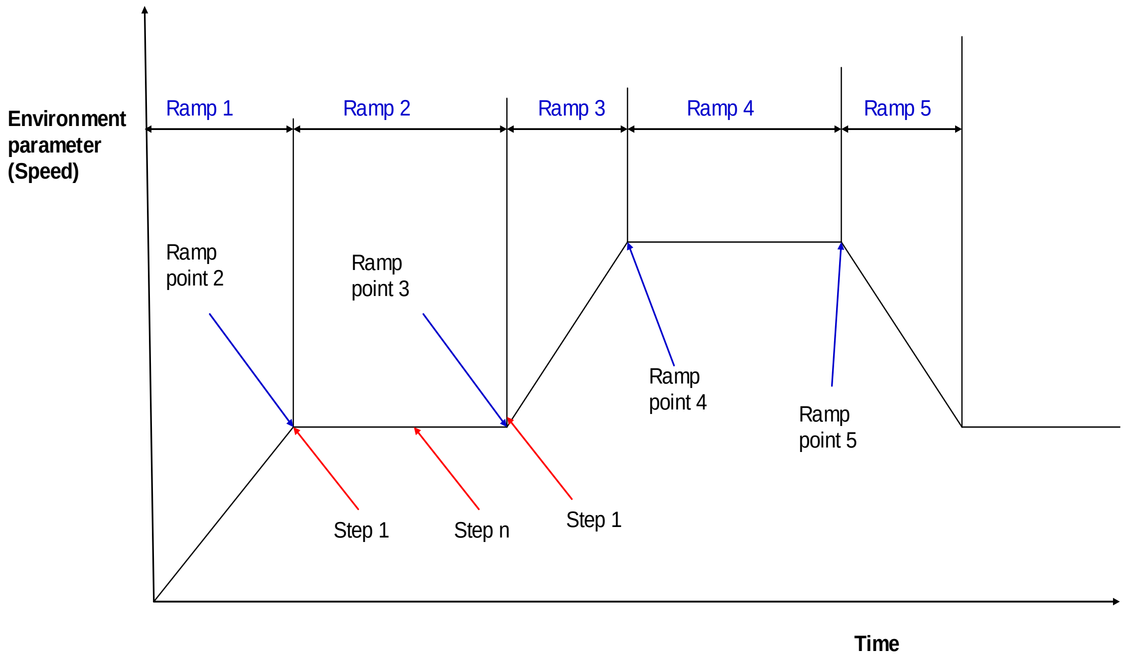

Figure 3.9: Cycle definition

In the SC03 model, the first ramp point is called ramp point 1 with a time point at t = 0 seconds and a rotational speed of 1 rad/s with uniform temperature. The second ramp point describes the idle conditions in the cycles, which normally occurs at the time point of 60 seconds, while the next ramp point, which specifies the engine running cycle (the acceleration to maximum take off), and takes place from say 1000 seconds to 2000 seconds depending on the analysis. In most cases, transient temperatures are required for a number of cycles. Engine cycles include the square cycle, flight cycle, certification cycle, running-in handling cycle, hot-reslam cycle, altitude relight cycle, and performance and type test cycle. In this thesis, attention is paid to the square cycle as this was the cycle that was run and used to produce the results.

3.10.1 Square Cycle

This is a simple design point engine cycle consisting of start, stabilisation at idle, acceleration to maximum, stabilisation at maximum take-off (MTO), deceleration to idle, and stabilisation at idle. It gives a basic understanding of temperature, displacement, and clearance response in the cycle. This is the first cycle that is run in any FEA to verify model behaviour. Figure 3.10 shows a typical engine square cycle with speed in revolution per minute (rpm) against time in seconds indicating points of maximum take off (MTO) and stabilisation at idle (stab. Idle) in the cycle.

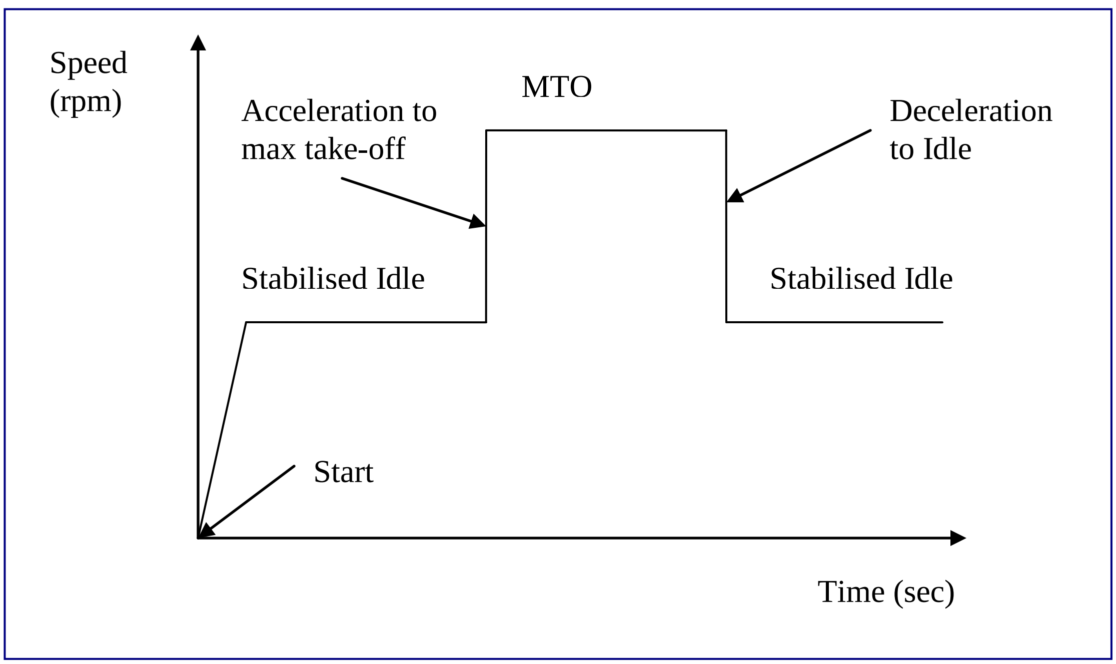

Figure 3.10: A typical engine square cycle with speed in revolutions per minute against time in seconds

The square cycle is used to study the effect of potential clearance in displacement analysis and it also provides data for the scaling calculation that is employed to investigate clearances at other engine conditions. Details of compressor clearance analysis are presented in Chapter 5.

3.11 Model Running

Model running is performed after the validation of all boundary conditions and the engine cycle to achieve the best result. The models are generally run on a local computer or on computer servers. The runs may be interactive running or batch submission and can be run as steady state analysis or transient analysis.

This analysis type can be accessed and controlled in the global control panel in SC03 and one type of analysis is performed for every run. The analysis run command is used to request an analysis on the current local computer, and when it is selected an initial output results file panel will appear prompting for the name of the result file to which the results of the model run will be saved automatically in the SC03 as a .fem file. If the input is verified as successful, a confirmation panel is given which summarises the type and accuracy of the analyses to be performed. The accuracy depends on the user predetermined values for the analysis. These are the run time, speed, bore temperature, bore pressure, the bore mass flow and the engine cycle used.

At the end of all analytical runs, SC03 will give an indication of whether the analysis was successful or not with a dialogue box saying ‘ok’ or ‘failed’, and if the analysis was successful then the results are stored as contours or graphical data such as key values. Generally, a summary of the progress of the analysis is given in the SC03 output window.

3.12 Output Processing

SC03 uses an automatic analysis system to process the results from a cycle run. The results are usually processed and presented in four different ways such as contour plots, ‘get values’, time plots, and user-defined graphs. This is after a thorough model check of fluid type for boundary conditions other than air only, mass flows, fluid temperatures, fluid pressures, heat transfer coefficients, and material type.

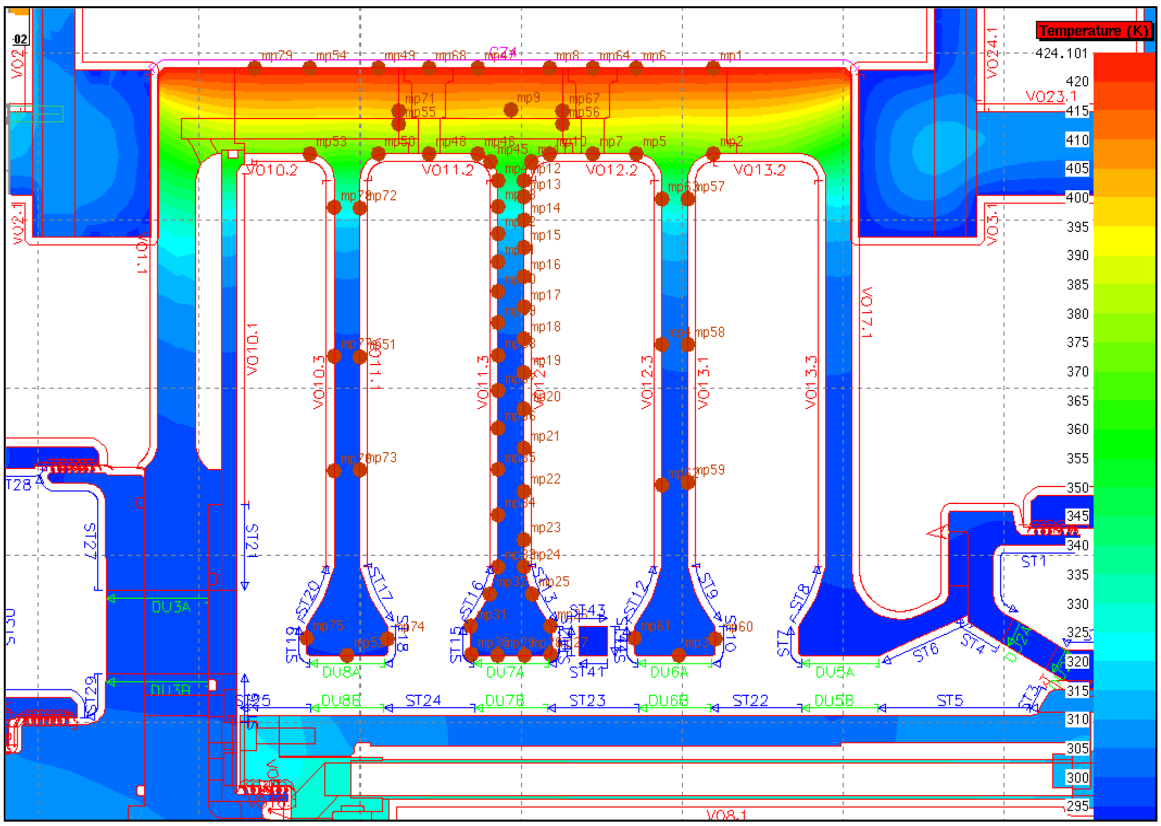

Figure 3.11: Temperature contour plots with a maximum rotational speed of 8000rpm, maximum take-off temperature of 381K, maximum take-off mass flow rate of 1.35kg/s and maximum take-off pressure of 5.5x10^{5}Pa

The contour plots provide a qualitative understanding of the predicted temperature, stress, and distribution in and around a component. Figure 3.11 shows the temperature contour plots of the multiple cavity rig model while Figure 3.12 shows the circumferential (hoop) stress contour plots of the multiple cavity rig model with a maximum speed of 8000rpm, maximum take-off temperature of 381K, maximum take-off mass flow rate of 1.35kg/s and maximum take-off pressure of 5.5×10^5Pa.

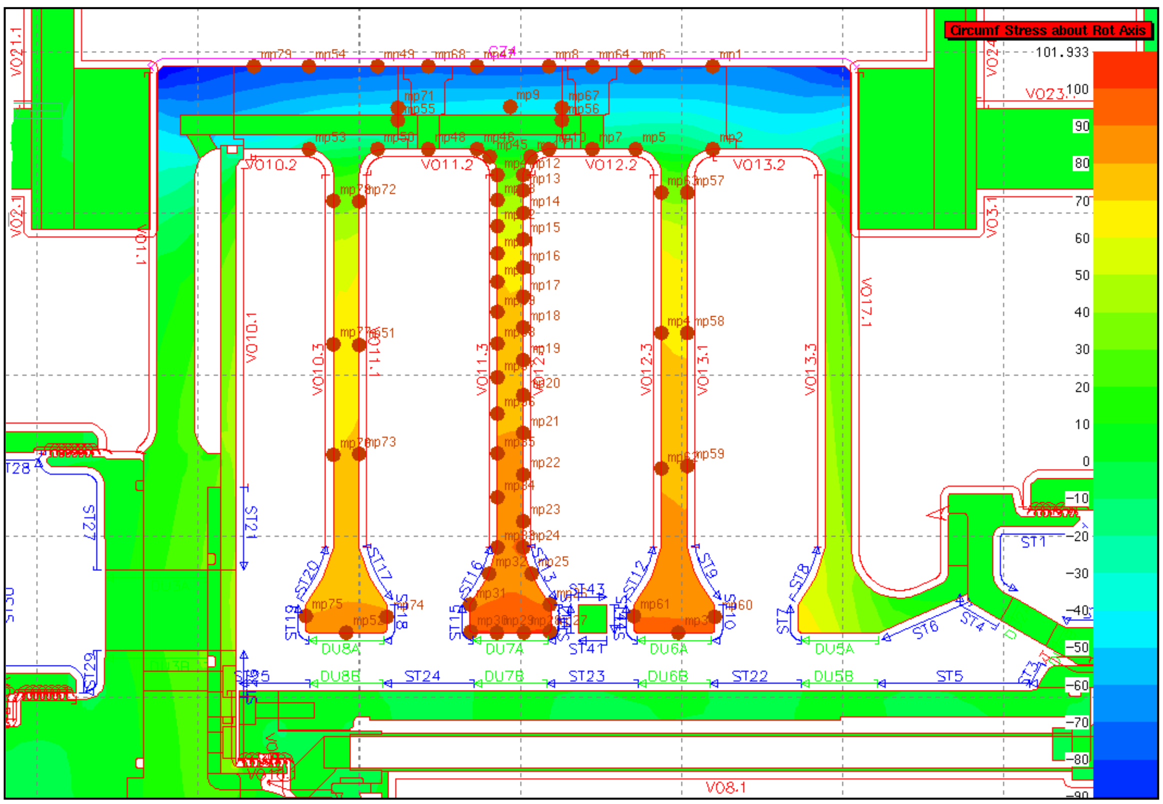

Figure 3.12: Circumferential stress contour plots with a maximum speed of 8000rpm, maximum take-off temperature of 381K, maximum take-off mass flow rate of 1.35kg/s and maximum take-off pressure of 5.5×10^5Pa

For the determination of the absolute value at a point on the model, the 'get values' result type is used, which has the capability to determine the value at a specific point on the model at specific times during the analysis cycle and whose values are at the nearest mesh node as shown in Figure 3.13.

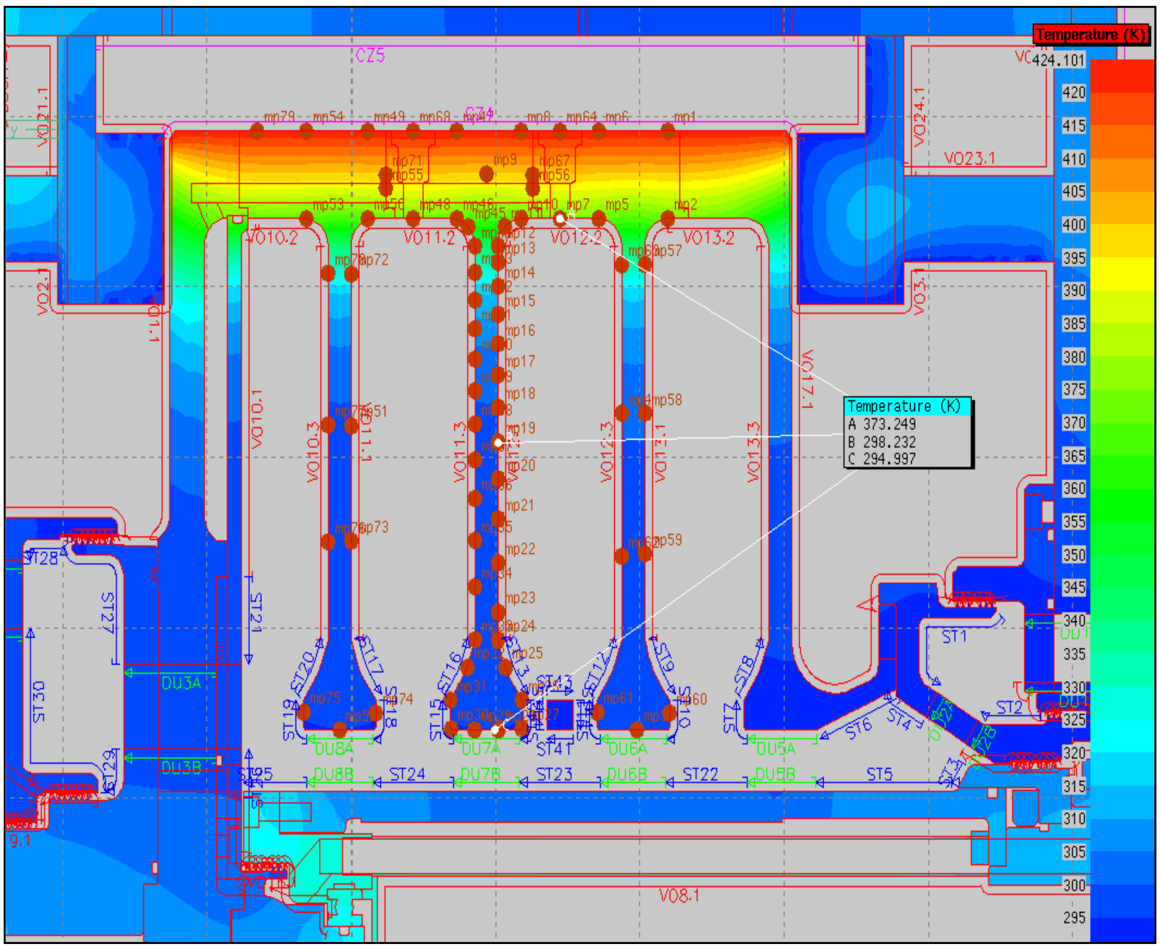

Figure 3.13: Get values result plot

Other ways of presenting the analysis results are through time plots, which are capable of generating a graph of the result at a specific point on the model for the complete analysis cycle, as shown in Figure 3.14. User-defined graphs, enable results values to be combined with each other or with external data such as engine measurements by defining the points at which results are to be graphed using ‘reference points’ and using the graph layout panel to manipulate the plot variables depending on the desired result. Another way of presenting results is the user-defined result technique; this is in the form of metal temperature or displacement difference between two points in the model. Details results of the multiple cavity rig modelling are presented in Chapter 7.

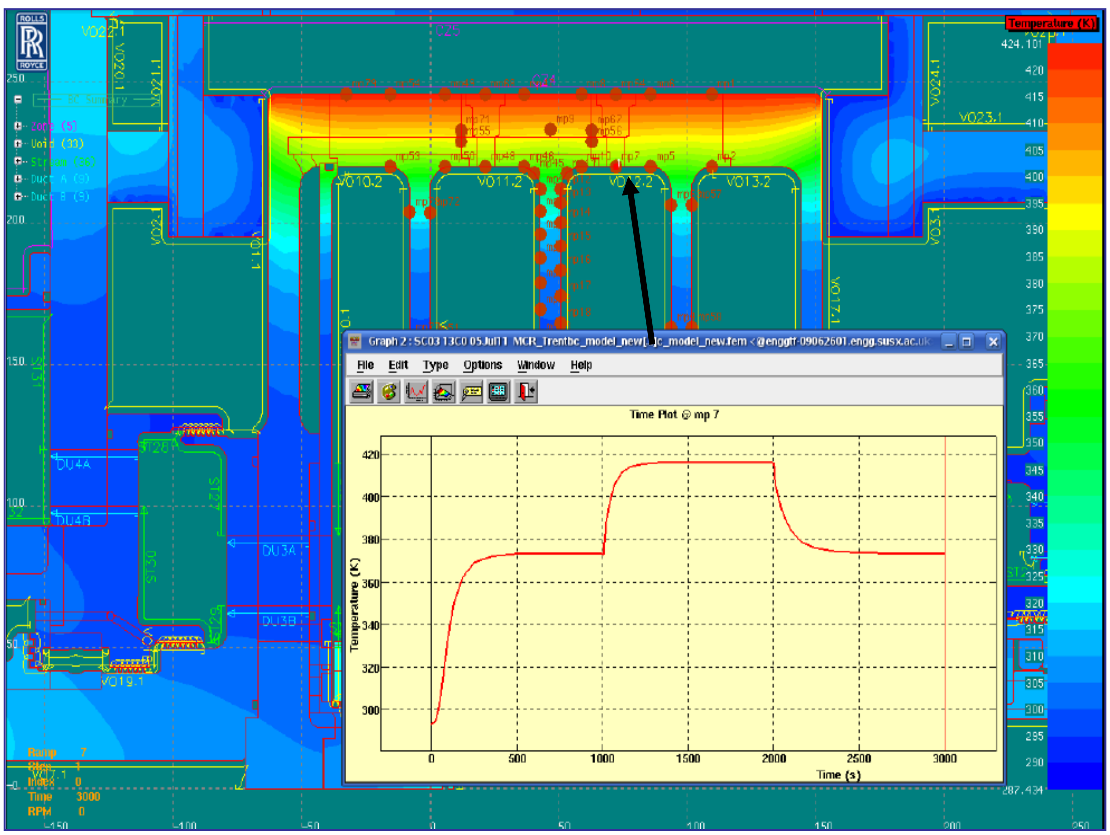

Figure 3.14: Time plot at model point 7

3.13 Thermal Matching

Thermal matching is the process in which the finite element thermo-mechanical model is calibrated against the real engine experimental data. The SC03 model is run for a user defined engine operating cycle as mentioned in Section 3.10. At the start of any matching process, a thermo-mechanical model of the component, the experimental test data from the cycle, and a .bdd file representing the cycle run by the test engine are required. For the matching process to be successful, considerable amounts of man hours and expertise are required for appropriate selection of the boundary condition to be used at a specific boundary and accurate choice of boundary inputs such as the heat transfer correlation. Details of the thermal matching of the 2D modelling of the multiple cavity rig model with the lumped parameter method and the experimental data of the rig are presented in Chapter 7.

3.14 Summary

This Chapter describes the test facility used to investigate the tip clearance control concepts using radial inflow in the cavity of an H.P. compressor. A test rig has been developed to support the work of this study. The rig was representative of real engine geometry and was capable of running at typical non-dimensional operating conditions. The non-dimensional parameters are presented in Table 3.3. This Chapter also provides information on the finite element program used for the modelling which is known as SC03. A full thermo-mechanical model was built using the SC03, to verify the reliability of the rig.

CHAPTER 4

4.1 1-D MODELLING

This chapter focuses on the lumped parameter method used in the development of the concept for tip clearance control. The 1-D modelling was used to validate the SC03 model. This is a matching exercise where the finite element thermo-mechanical model results are calibrated against the lumped parameter results. The analysis makes use of a heat transfer and fluid flow based lumped parameter spreadsheet in combination with a full axisymetric thermo-mechanical finite element High Pressure Compressor (HPC) casing and drum model. The HPC models are used to investigate the effect of various parameters on the closure behaviour of the various HPC stages. The effect of heat transfer coefficient, cavity mass flow, coefficient of thermal expansion of material, temperature, pressure ratio and time constant on the closure characteristics of HPC was quantified.

The most promising concept quantified, which is the focus of this study was to increase the heat transfer coefficient of the drum leading to a reduction in the time constant of the drum. It is established in Chapter 5 that by introducing the radial inflow into the drum cavity, the heat transfer coefficient increased was further enhance therefore a further reduction on the time constant of the drum. The software packages used are SC03, Matlab and Microsoft Excel.

In this Chapter, the validation of the lumped model with data from SC03 model setup was examined. This include a brief description of the Lumped mass parameter method, mathematical model setup of model and the approach used for matching simulation results from SC03 with Lumped model data. The validation result from Stage 3 simulation and Lumped model is presented.

4.2 Lumped-Mass Parameter Method

In this section, consideration is given to the transient analysis of a body in which the temperature is assumed to be constant at any point within and on the surface of the body at a given instant of point. It is assumed that the temperature of the whole body changes uniformly with time. Such an analysis is called a lumped mass parameter method. The lumped parameter scheme divides a thermal system into a number of distinct lumps and assumes that the temperature difference inside each lump is negligible. It is a simple and approximate procedure in which no spatial variation in temperature is allowed. The change in temperature in such a system varies only with respect to time. It is therefore obvious that the lumped heat capacity is limited to small sized bodies or high thermal conductivity material as the case with rotor/blade of axial compressor in a gas turbine engine. The lumped transient analysis in heat transfer implies that a mass has insignificant internal resistance to heat transfer and is used when a material has relatively low thermal resistance relative to the external thermal resistance.

It is important to note that the transient response of a system to heat transfer process is critical in aerospace industry. A good example is the heating up of gas turbine compressors during transient operation as they are brought up to speed during take-off. The discs that carry the blades are thick and take a long time to heat up or come to temperature, while the casing is thin thus heat up or comes to temperature rapidly. During this process, the casing expands away from the blade tips, occasionally sufficient to cause serious difficulties with aerodynamic performance of the engine. This may even lead to a phenomenon called surge and may result in increased consumption of aviation fuel. The different expansion by both the casing and the rotor blade resulting from the variation in temperature with time during the various engines operating cycle such as acceleration and deceleration gives rise to different time constants which is a feature of the lumped system analysis.

4.3 The Lumped Parameter Concepts for compressor clearance control

Time constants are a feature of the lumped system analysis for thermal systems. This is employed when objects cool or warm uniformly under the influence of convective cooling or warming as the case in this study during acceleration and deceleration. Time constant is the time required for a physical quantity to rise from zero to $1-\frac{1}{e}$ which is equivalent to 63.2% of its final steady value when it varies with time (t) as $1-e^{-kt}$. And it is also the time required for a physical quantity to fall to $\frac{1}{e}$ which equivalent to 36.8% of its initial value when it varies with time (t) as e^{-kt}.

Considering a thermal system when an object cools or warm uniformly under the influence of convective cooling or warming, the heat transfer from the body to the ambient at a given time is proportional to the temperature difference between the body and the ambient. Figure 4.1 shows a solid lumped model for thermal analysis.

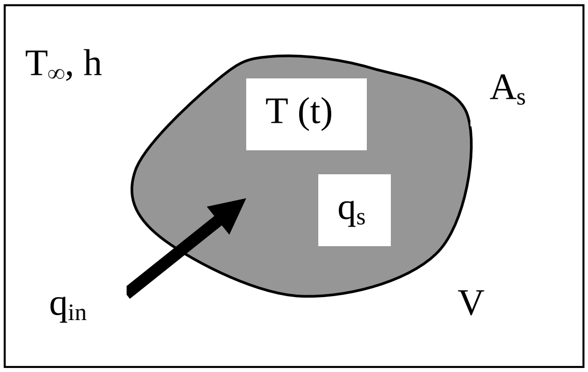

Figure 4.1: A solid lumped model

From Figure 4.1:

Net rate of heat transfer into the solid = $hA_s(T_\infty - T)$ (4.1)

Rate of increase of internal energy of the solid = $\rho C_p V \dfrac{dT}{dt}$ (4.2)

Therefore equating Equation 4.1 and 4.2 it gives:

Net rate of heat transfer into the solid = Rate of increase of internal energy of the solid

$$hA_s(T_\infty - T) = \rho C_p V \frac{dT}{dt} \tag{4.3}$$

From Equation 4.3, an expression can be obtained for the temperature of the solid as a function of time assuming h and T_∞ are constant as follows:

$$T(t) = T_\infty + (T_0 - T_\infty)e^{\frac{-hA_s}{\rho C_p V}.t} \tag{4.4}$$

If $\dfrac{-hA_s}{\rho C_p V} = \dfrac{1}{\tau}$, Equation 4.4 becomes,

$$T(t) = T_\infty + (T_0 - T_\infty)e^{\frac{-t_s}{\tau}} \tag{4.5}$$

The time needed to heat a solid from the initial temperature T_0 will be given as:

$$t = \frac{\rho C_p V}{hA_s} = \ln\left(\frac{T_\infty - T_0}{T_\infty - T}\right) \qquad (4.6)$$

The time constant is given as:

$$\tau = \frac{\rho C_p V}{hA_s} \qquad (4.7)$$

Time constant is the ratio of thermal capacitance to convection thermal resistance and this indicate that the lower the time constant, the faster the solid is heated. It also shows that the greater the masses (ρV) and heat capacities (C_p), the slower the changes in temperature while the larger the surface areas (A_s) and better heat transfer (h), the faster the temperature changes in the solid.

where:

h =heat transfer coefficient, (W/ (m^2K))

A_s = is the surface area, (m^2)

T (t) = body temperature at time t, (K)

T_0 = the constant ambient temperature, (K)

ρ = density, kg/m^3

Cp = specific heat ($Jkg^{-1}K^{-1}$) and

V = the body volume, (m^3)

The lumped capacitance method is generally said to be valid if the dimensionless Biot number is less than 1, that is $(Bi < 1)$.

Biot Number, $Bi = \frac{hL_c}{k}$ (4.8)

But characteristic length $L_c = \frac{V}{A_s}$ (4.9)

It should be observed that $\frac{V}{A_s}$ represents a characteristic dimension of the body. The Biot number represents a ratio between conduction resistances within the body to convection resistance at the surface of the hot body as described in Equation 4.10 as:

$$Bi = \frac{\left(\frac{L_c}{KA_s}\right)}{\left(\frac{1}{hA}\right)} \tag{4.10}$$

where:

k = thermal conductivity of the solid**,** (W/ (m.K))

For details on time constants and lumped system analysis for thermal systems, the reader is referred to White (1984), Kreith and Bohn (1993), Lewis et al. (2004) and Incropera et al. (2007).

In summary, the lumped-mass capacity method shows that if the mass, volume and the area of the solid are constant, that increasing the heat transfer coefficient of the body will results in the reduction of the time constant and that decreasing the heat transfer coefficient of the body will results in the increased of the time constant. The aim of the study is to decrease the time constant of the drum by increasing the heat transfer coefficient of the systems thereby causing the drum to heat up faster hence narrowing down the large gap that existed at the beginning of engine transient operation between the casing and the blade. This would cause a reduction in the cruise clearance and a reduction in of clearance at surge point and hence reductions in the overall specific fuel consumption giving rise to higher engine efficiency.

4.3.1 Mathematical Models

A mathematical 1-D model was created in MATLAB to determine the effect of the various parameters on tip clearance in axial compressor with the relevant equation encoded into the Matlab program for the analysis. Figure 4.2 shows a flow diagram of the mathematical model employ in this study. The flow diagram model setup employed in this study starts with the environmental parameters (time vectors, temperatures and speed) setup which produces the square cycle for the analysis as shown in Figure 4.3. Upon successful completion of the environmental parameters setup, casing and drum displacements calculations setup are performed. This is followed by the generation of data for drum and casing total thermal growth as shown in Figure 4.7 and Figure 4.8 respectively. If data are not successfully generated as indicated in the diagram with a 'No' sign, the process is refined and repeated while the 'Yes' sign indicated successful generation of data and a continuation of the next process. The next process is to perform the closure behaviour setup follow by the generation of the closure behaviour data.

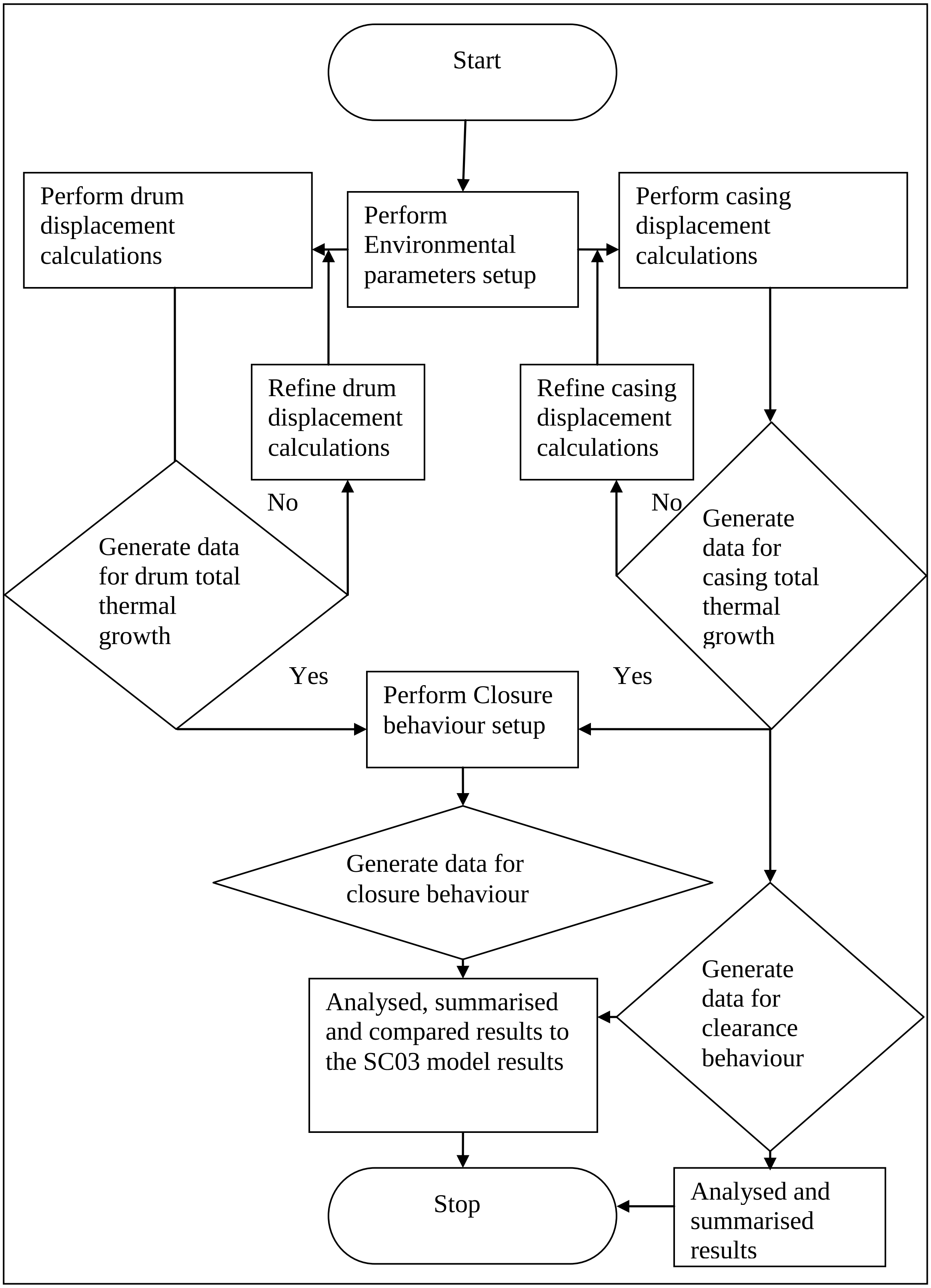

Figure 4.2: Flow diagram of the mathematical model

Upon successful generation of the closure characteristics data, the results are analysed, summarised and compared to the SC03 model results as shown in Figure 4.11. The next process is to perform the clearance behaviour setup followed by the generation of the clearance behaviour data. Detail descriptions of the setups are presented in section 4.4 through to section 4.6.

Before a lumped parameter model is set up for tip closure analysis, it is necessary to run a SC03 rotor and casing models through a calibration square cycle.

As described in Section 3.8.1, the square cycle models the various phases during engine operation consisting of start, stabilization at idle, acceleration to maximum take off (MTO), stabilization at maximum take off (MTO), deceleration to idle and stabilization at idle. The environmental parameters used for the 1D modelling for the lumped parameter analysis are presented in Table 4.1.

Parameters	Idle	MTO	Cruise
Speed (RPM)	8,467.17	12,359.24	12,016.72
Inlet temperature (T26)	350.86	599.61	582.21
Outlet temperature T30	516.13	909.12	876.20

Table 4.1: Environmental parameters used for the 1D modeling for the lumped parameter analysis

In this analysis, an extended square cycle is used which includes the cruise phase. Figure 4.3 shows the variation of speed with time in the so called extended Square cycle with indication of the idle, maximum take off (MTO) and cruise phases in the cycle. At the start, the engine was allowed to reach a thermal steady state with no external power applied, at a rotor speed of 8467.17 rpm representing the stabilised low power or idle engine condition. After 2000 seconds, the power was switched on and the speed of the rotor was gradually increased to 12,359.24 rpm representing engine acceleration to maximum take over condition. The engine was then allowed to reach a new thermal steady state representing the stabilised high power engine condition at 4000s.

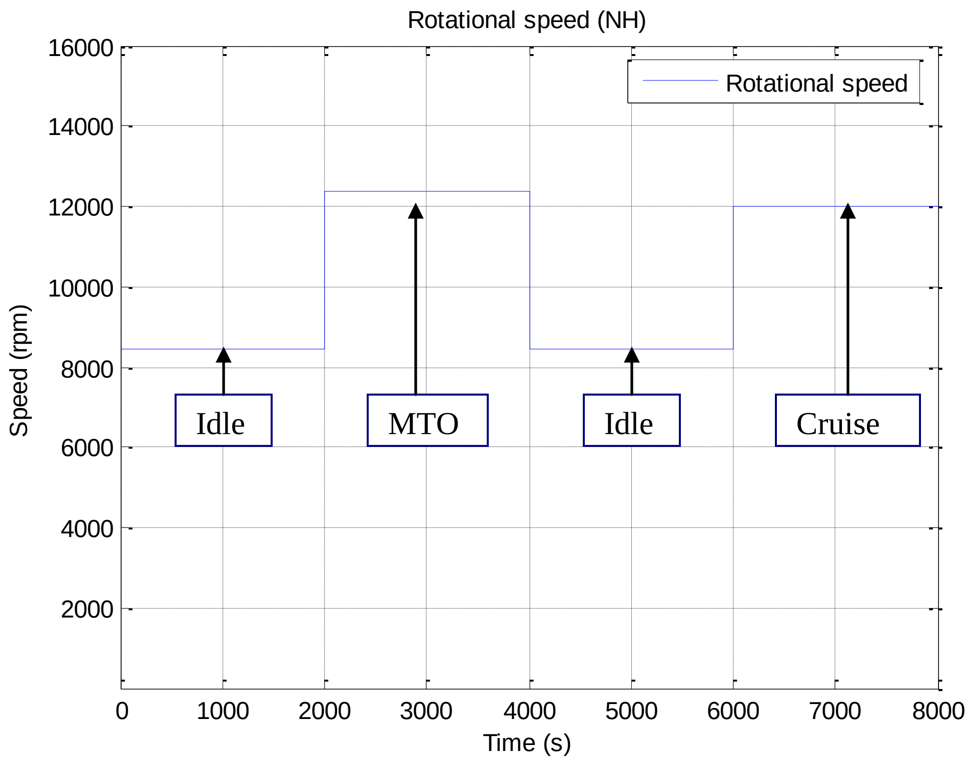

Figure 4.3: The variation of speed with time in the so called extended Square cycle with indication of the Idle and maximum take off (MTO) phases in the cycle with rotational idle speed of 8,467.17 rpm and maximum take off speed of 12,359.24 rpm.

The power was then switched off and the rotor speed reduced to 8,467.17 rpm, thus simulating an engine deceleration which started at 2460 s. Then the final steady state was reached at 6000s and the data were recorded. The power was again switched on the speed of the rotor was gradually increased to 12,016.72 rpm representing an engine acceleration to cruise condition. The engine was then allowed to reach a new thermal steady state representing the stabilised cruise engine condition at 8000s.

From the SC03 analyses, the rotor and casing growths and responses rates are extracted. The results are use as the baseline for setting up of the mathematical model for the lumped parameter method for the study of the effect of various parameters on the closure characteristics of each stage in a HP compressor. . Figure 4.4 shows a typical closure plot where the closure characteristic is plotted against time during engine transient operation in the so called extended Square cycle.

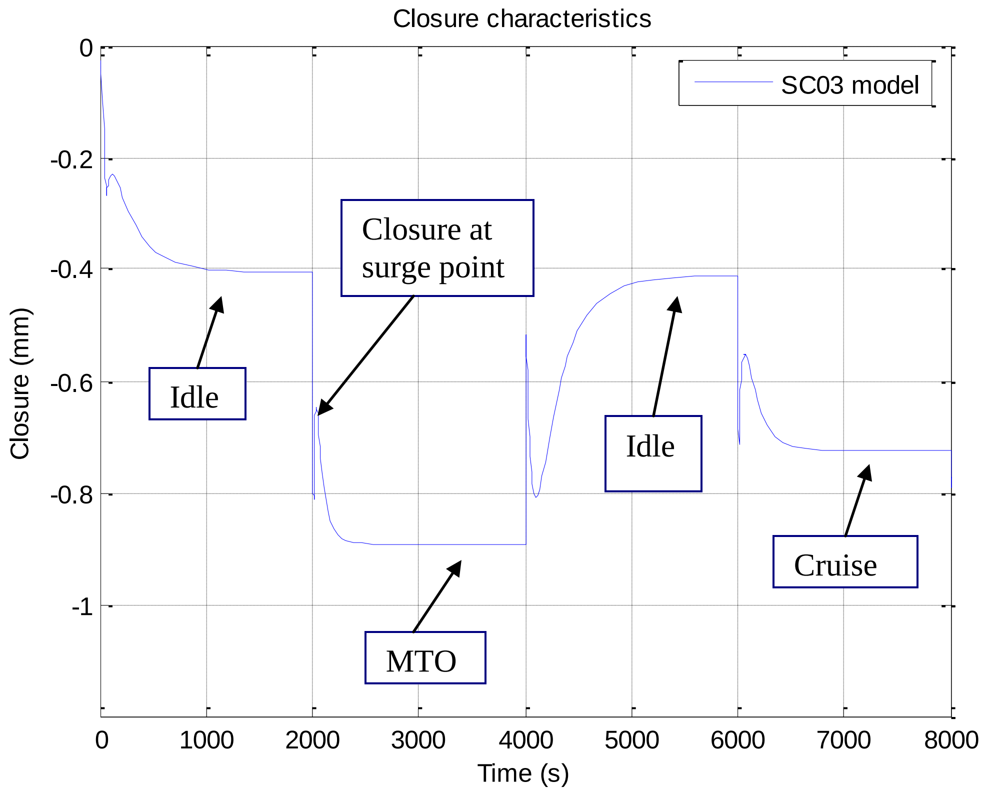

Figure 4.4: A typical closure plot showing the variation of closure characteristic time during engine transient operation in the so called Extended Square cycle.

Two basic analyses are employed in a square cycle to determine the compressor clearance during engine transients specifically the closure and the clearance analyses. The displacement of casing relative to rotor displacement is called Closure.

For a given cycle, the clearance depends on casing displacement relative to the rotor displacement, and the cold build clearance (CBC). The policy governing the clearance control scheme depends on the engine designer or manufacturer. In Rolls Royce Plc, this is achieved by using a sensible cold build clearance (CBC). Some of the definitions used by Rolls Royce Plc as guiding principle on clearance control scheme were given in Section 2.1.3

4.4 The basic layout of the mathematical model for compressor control

The parameters used in the mathematical model include environmental, stage and materials parameters. The environmental parameters are use for temperature and speed set up in the model while the stage and material parameters are use to determine the centrifugal growth of the drum and for the thermal growths calculations in the model. The mathematical model is split into 4 main Sections namely; environmental parameters, the input data, the calculation and the results sections.

4.4.1 The environmental parameters

The environmental parameters for real engine models 524 and Trent 1000 used in commercial aircraft are discussed in details in the sections. The environmental parameters are use for temperature and speed set up in the mathematical model. The environmental parameters include the followings:

1. Compressor (Spool) speed in revolution per minute;
2. Fluid Temperatures in Kelvin and
3. Cold build reference temperature.

1) Compressor (Spool) speed

This is the rotational speed of the rotor with respect to time at any instance during the engine various operations which includes speed at Idle, speed at maximum take off (MTO) and speed at cruise conditions. Compressor (Spool) speed is in revolution per minute (rpm) but in SC03 is identified as NH in radian per seconds.

$$NH(rpm) = \frac{(rpm)}{60} * 2\pi(rad/s) \qquad \textbf{(4.11)}$$

2) **Fluid Temperature**

The fluid temperatures vital to this study include the bore temperature and the main temperature specified for Idle, maximum take off and cruise conditions. Fluid temperatures are generally defined at the starting point of a flow system only such as temperature in the main gas path (normally the main annulus). The successive fluid temperature distributions are calculated automatically by the analysis program depending on the boundary conditions defined in the system. The main annulus temperatures may be specified at two significance engine parameters namely inlet or upstream temperature (T26) and outlet or downstream temperature (T30). Figure 4.5 shows the different entering and exit points in a gas turbine engine. In terms of compressor, the entering point is at the upstream indicated as 26 and the exit is downstream indicated as 30, hence, the entering or upstream temperature is called T26 and exit or downstream temperature is called T30.

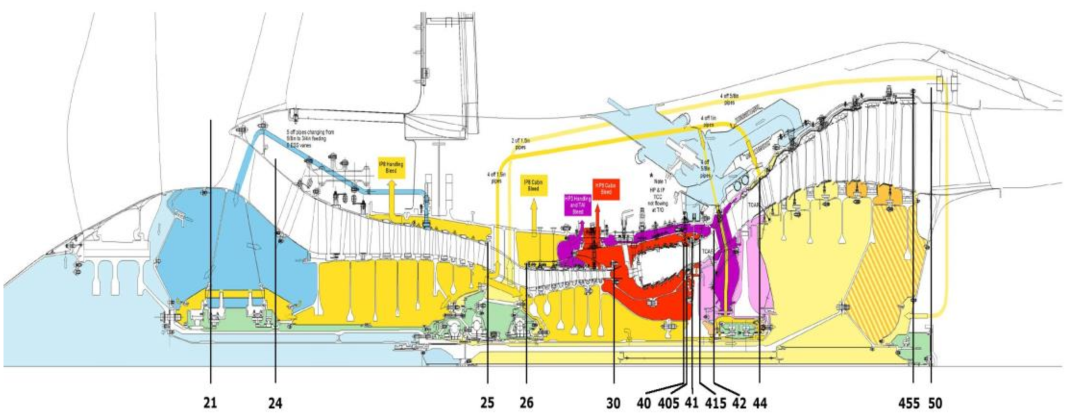

Figure 4.5: Different entering and exit points in a gas turbine engine. For compressor, the entering point is at the upstream indicated as 26 and the exit is downstream indicated as 30 (courtesy Rolls Royce Plc).

The fluid stage temperatures in gas turbine engine for example Model 524 and Trent 1000 is classified according to the point in the square cycle (Idle, MTO or Cruise). The fluid temperature is scaled on two main annulus parameters T26 and T30 as shown in Equations 4.12 and 4.13.

The measurement of temperature are taken at those points (T26 and T30) and recorded as T26 Idle, T26 MTO, T26 Cruise, T30 Idle, T30 MTO and T30 Cruise. These are used in the analysis of the closure in the cycle and hence to calculate the clearance throughout engine operating cycle.

$$k = \frac{T - T26}{T30 - T26} \qquad \textbf{(4.12)}$$

The Equation can be rearranged to give the equation for fluid temperature as:

$$T = T26 + k(T30 - T26) \qquad \textbf{(4.13)}$$

Where:

k = scaling constant

T = known fluid temperature

T26 = inlet or upstream temperature

T30 = exit or downstream temperature

3) Cold build reference temperature

The cold build reference temperature is the designer fixed temperature which is usually an ambient temperature at 293K.

4.4.2 The input data

This section contains all the stage parameters for drum and casing of the HP compressor used in the mathematical model. These are the time constants of casing and drum at idle, acceleration, deceleration and cruise. Others include x-factor of drum and casing at idle, acceleration, deceleration and cruise, and drum and casing delay. This section also contains casing and drum blade coefficient of thermal expansion for the material (α), casing and drum radii, blade length or blade height, thermal conductivity of drum and the young modulus of drum. The derivation of the stage parameters are dealt with in detail in Section 4.4.3.

4.4.3 The modelling set up

This section described how the time vector, speed and stage temperature are setup in the model. It also includes the equations employed for the calculation of the disc, casing and blade thermal growths for a particular point in the extended square cycle. The centrifugal growth of the drum, variable coefficient of thermal expansion for the drum, drum and casing displacements are also dealt with in this section. Finally the closure behaviour at each stage is obtained by the differences between the casing displacement and the drum displacement. For details on the mathematical model, the reader is referred to Anderson (1997).

4.4.3. 1 Time vector

The time vector setup involves modelling the process through different time step namely start up, first idle, stabilisation idle, maximum take off, stabilisation at max-take off, cruise and finally Idle. The total range of time that is required for the analyses to be completed is between 0 seconds and 10,000 seconds for full calibrations in Trent 1000 engine models and is encoded into the model as t = 1:10000. The times step includes:

- t0 = 0; engine start-up

- t1 = 2000; stabilised idle
- t2 = 4000; stabilised max take-off
- t3 = 6000; stabilised idle

4.4.3. 2 Speed setup

The speed setup involves the modelling of the speed with respect to time as the engine moves from idle position accelerating to maximum take off, stabilising at maximum take off, decelerating to cruise position and finally decelerating to idle position. Figure 4.6 shows the variation of rotational speed with time throughout the engine extended square cycle. The speed at various point in cycle are encoded into the model in the mathematical model using Matlab.

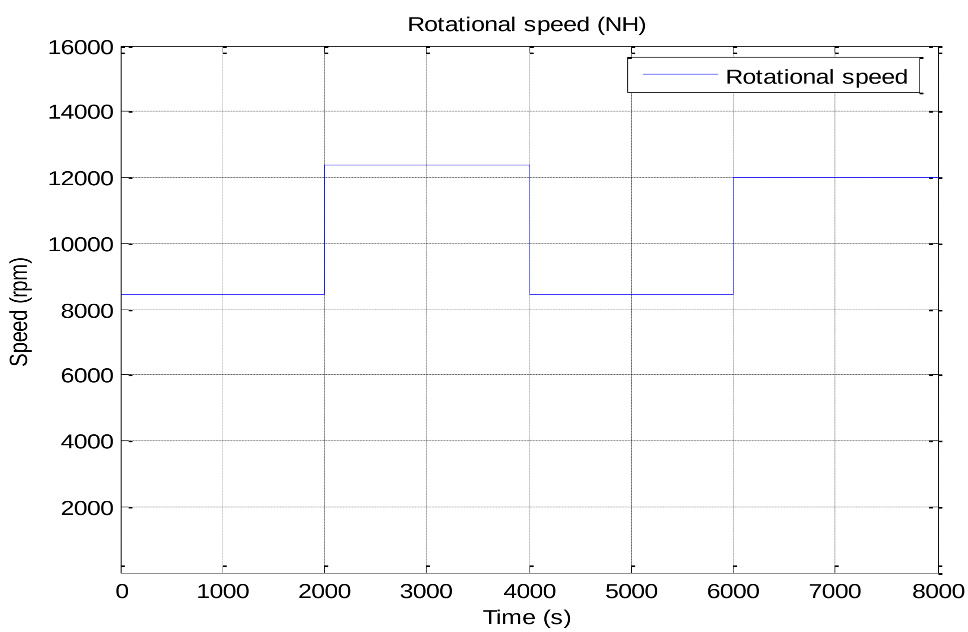

Figure 4.6: The variation of rotational speed with time in the extended square cycle with the rotational speed of approximately 8,467.17, 12,359.24, and 12, 016.72 rpm for Idle, MTO and cruise respectively over a time of 8,000 s.

4.4.3. 3 Drum displacement calculations

This involves the analysis of drum displacement during engine transient throughout the square cycle. The thermal growths of the drum have to be scaled to different conditions to allow growths to be calculated at any condition throughout any engine cycle. The scaling calculation is performed by taking into consideration the relationship between the stage temperature and drum growth given by the Equation 4.14.

$$\delta_{th} = R\alpha(T_{drum} - 288.15) \qquad \textbf{(4.14)}$$

Equation 4.14 shows that the thermal growths of the drum and stage temperature are related together with the coefficient of thermal expansion (α) for the drum material and the radius of the drum (R). If the thermal expansion of the drum (δ_{th}) at maximum take off and idle are known, the equivalent stage temperatures at idle and maximum take off can be obtained by rearranging Equation 4.14 giving the following equation.

$$T_{drum} = \frac{\delta_{th}}{R\alpha + 288.15} \qquad \textbf{(4.15)}$$

To enable the stage temperature to be calculated for any value of T26 and T30 that is at inlet and out of each stage, an "X – factor scaling equations is required which is given below.

$$X = \left(\frac{T_{drum} - T26}{T30 - T26}\right) \qquad \textbf{(4.16)}$$

Rearranging Equation 4.16, the stage temperature for any value of T26 and T30 is given as:

$$T_{drum} = T26 + X * (T30 - T26) \qquad \textbf{(4.17)}$$

4.4.3. 4 Drum centrifugal growth setup (CF growth)

The centrifugal growth (CF) of the rotor is obtained by scaling the CF growth at the square of the maximum rotation speed of the drum. This is modelled as the ratio thermal conductivity of drum to the young modulus multiply by the square of the speed. This is presented in Equation 4.18 as:

$$CF_{drum} = \frac{k_{drum}}{E} * rpm\text{^}2 \tag{4.18}$$

where:

CF_{drum} = centrifugal growth of drum

K_{drum} = thermal conductivity of drum

E= young modulus of drum

rpm = drum rotational speed in revolution per minute

4.4.3. 5 Drum steady state thermal growths

The drum steady state thermal growths are scaled and modelled from maximum thermal growth of drum using the stage temperature as presented in Equation 4.19. It is assumed that the coefficient of thermal expansion (α) for the drum material is constant.

$$\delta_{th} = \delta d_{th\max} * \left(\frac{T - 288.15}{T_{\max} - 288.15} \right) \tag{4.19}$$

Where δ_{th} = Steady state thermal growths

$\delta d_{th\max}$ = drum thermal growth at maximum take off

T = known fluid temperature

T_{max} = drum stage temperature at maximum take off

4.4.3. 6 Drum transient thermal growth

The transient thermal growth of the drum has an exponential response. The values of the stage temperature, drum time constant during acceleration and deceleration, acceleration and deceleration time and the thermal growths of drum are modelled to give the drum transient thermal growth. The governing equation for the modelling of transient thermal growth of drum is given by Equation 4.20

$$d_{tran} = 288.15 + \left(T_{stage} - 288.15\right) * \left(1 - \exp^{\frac{-\Delta t}{\tau}}\right) \qquad \textbf{(4.20)}$$

where:

d_{tran} = transient thermal growth of drum

T_{stage} = stage temperature for Idle, MTO and Cruise

Δt = change in time

τ = thermal time constant

The transient thermal growths are modelled with respect to ramp times over the complete engine cycles.

4.4.3.7 Drum displacement

The drum displacement is given by the multiplication of the drum radius, alpha and the transient thermal growth of drum. The coefficient of thermal expansion may be a variable coefficient of thermal expansion which is a function of the transient thermal growth of the drum. Equation 4.21 shows the variable drum coefficient of thermal expansion (α)

while Equation 4.22 below shows the relationship between radius, coefficient of thermal expansion (α) and the transient thermal growth of the drum to give the drum displacement. Equation 4.22 calculates the drum displacement at any point in time in the cycle.

$$\alpha d_{variable} = \alpha d * \left(d_{tran}\right) \tag{4.21}$$

$$d_{displacement} = r * \alpha d_{variable} * d_{tran} \tag{4.22}$$

where:

αd = coefficient of thermal expansion for the drum material

$\alpha d_{variable}$ = variable coefficient of thermal expansion for the drum material

d_{tran} = transient thermal growth of drum

r = drum radius

4.4.3. 8 Drum total thermal growth

The total thermal growth of the drum is obtained by the combine effect of the transient thermal growths of the drum with the drum centrifugal growth (CF). That is modelling the combine effect of Equation 4.18 and Equation 4.20. Figure 4.7 shows the variation of drum total thermal growth with time over the extended square cycle for stage 3 of Trent 1000 drum model.

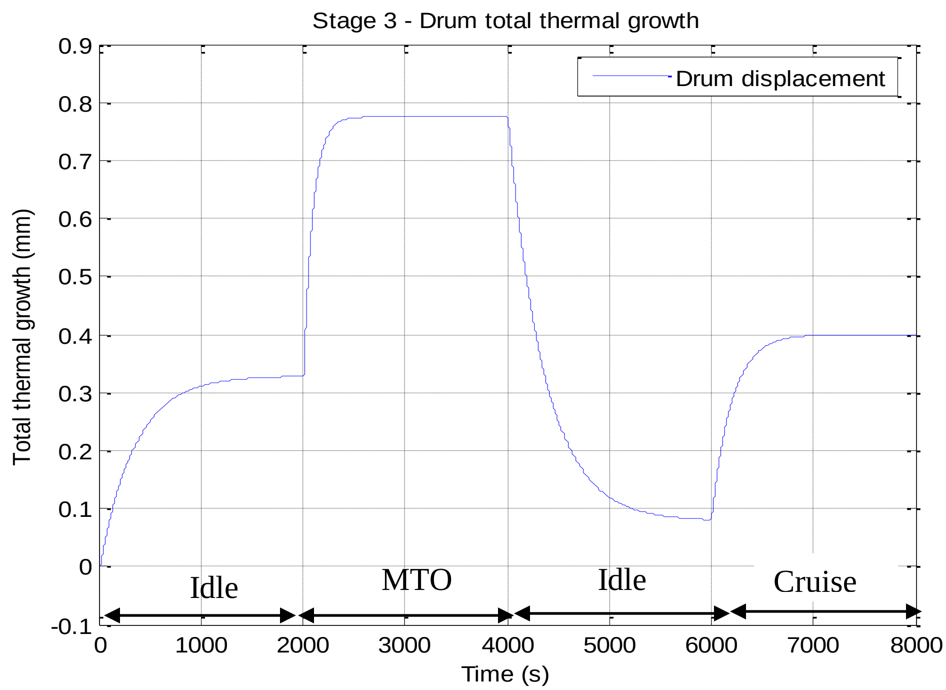

Figure 4.7: The variation of drum total thermal growth with time over the extended square cycle for stage 3 of Trent 1000 drum model.

The result gives the drum total thermal growth characteristics over the square cycle as shown in Figure 4.7.

4.4.3. 9 Casing displacement calculations

The casing deflections are due to pressure difference across the shell of the casing. The centrifugal growth (CF) of the casing is obtained by scaling the CF growth at the maximum rotation speed of the rotor to the power of 6. This is modelled as the ratio of the thermal conductivity of drum to the young modulus multiply by the sixth root of the speed. This is described by the Equation 4.23 as:

$$CF_{casing} = \frac{k_{drum}}{E} * rpm\hat{}6 \qquad \textbf{(4.23)}$$

where:

CF_{casing} = centrifugal growth of casing

K_drum = thermal conductivity of drum

E= young modulus of drum

rpm = rotor rotational speed in revolution per minute

4.4.3. 10 Casing steady state thermal growths

The casing thermal growths are scaled from maximum thermal growth of casing using the stage temperature and associated value of the coefficient of thermal expansion (α). This is given by Equation 4.24

$$\delta_{th} = \delta c_{th\max} * \left(\frac{T - 288.15}{T_{\max} - 288.15} \right) * \left(\frac{\alpha_T}{\alpha_{\max}} \right) \quad \textbf{(4.24)}$$

Where δ_{th} = Steady state thermal growths

$\delta c_{th\max}$ = casing thermal growth at maximum take off

T = know casing temperature

$T_{\max}$ = maximum casing stage temperature

α_T = value of the coefficient of thermal expansion with respect to temperature

$\alpha_{\max}$ = value of the coefficient of thermal expansion at maximum take off

4.4.3. 11 Casing transient thermal growth

The transient thermal growth of the casing has an exponential response as in the case of the drum. The values of the stage temperature, drum time constant during acceleration and deceleration, acceleration and deceleration time and the thermal growths of casing are modelled to give the casing transient thermal growth. The governing equation for the modelling of transient thermal growth is given by Equation 4.25

$$C_{tran} = 288.15 + \left(T_{stage} - 288.15\right) * \left(1 - \exp^{\frac{-\Delta t}{\tau}}\right) \qquad \textbf{(4.25)}$$

where:

C_{tran} = transient thermal growth of casing

T_{stage} = stage temperature for Idle, MTO and Cruise

Δt = change in time

τ = thermal time constant

The transient thermal growths are modelled with respect to ramp times over the complete engine cycles.

4.4.3. 12 Casing displacement

The casing displacement is given by the multiplication of the casing coefficient of thermal expansion with the transient thermal growth of casing. The coefficient of thermal expansion may be a variable coefficient of thermal expansion which is a function of the transient thermal growth of the casing. Equation 4.26 shows the link between the casing coefficient of thermal expansion (α) and the transient thermal growth of the casing to give the casing displacement. Equation 4.26 calculates the casing displacement at any point in time in the cycle.

$$C_{displacement} = \alpha_{casing} * C_{tran} \tag{4.26}$$

where:

α_{casing} = coefficient of thermal expansion of casing

C_{tran} = transient thermal growth of casing

4.4.3. 13 Casing total thermal growth

The total thermal growth of the casing is obtained by the combine effect of the casing centrifugal growth (CF) with the transient thermal growths of the casing. That is modelling the combine effect of Equation 4.23 and Equation 4.25. The result gives the casing total thermal growth characteristic over the square cycle as shown in Figure 4.8. Figure 4.8 shows the variation of casing total thermal growth with time over the extended square cycle for stage 3 of Trent 1000 casing model.

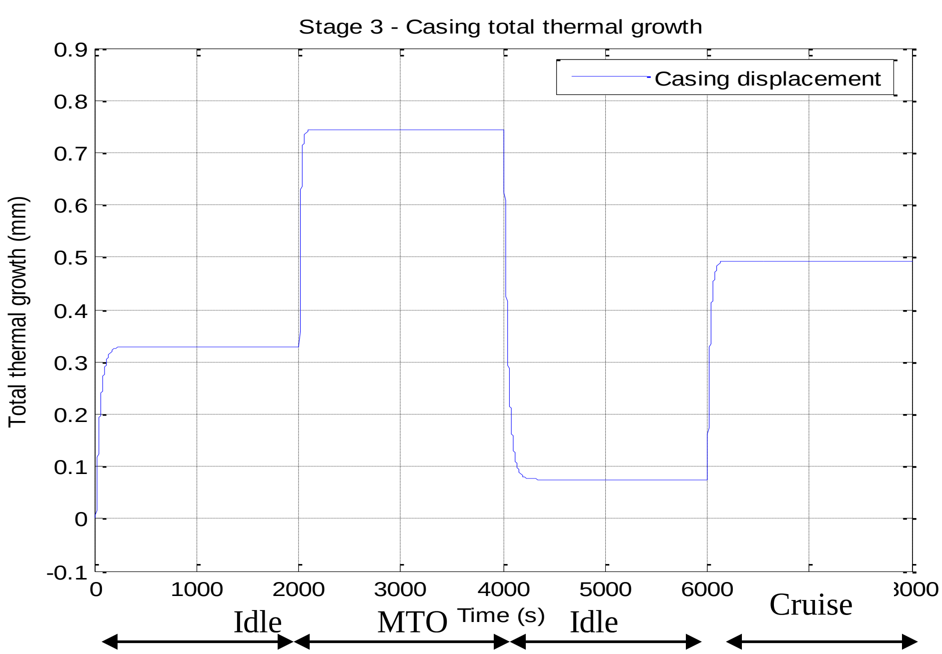

Figure 4.8: The variation of casing total thermal growth with time over the extended square cycle for stage 3 of Trent 1000 casing model.

4.5 The closure behaviour

In this section, the lumped parameter closure behaviour of stage 3 is presented while codes for other stages are presented in appendix 4. This closure behaviour involves the modelling of all the effects associated with Equation 4.14 – Equation 4.26.

Figure 4.9 shows the variation of total thermal growth of casing and drum with time over the extended square cycle for stage 3 of Trent 1000 casing and drum models. This shows casing movement relative to drum movement during engine transient over the extended square cycle.

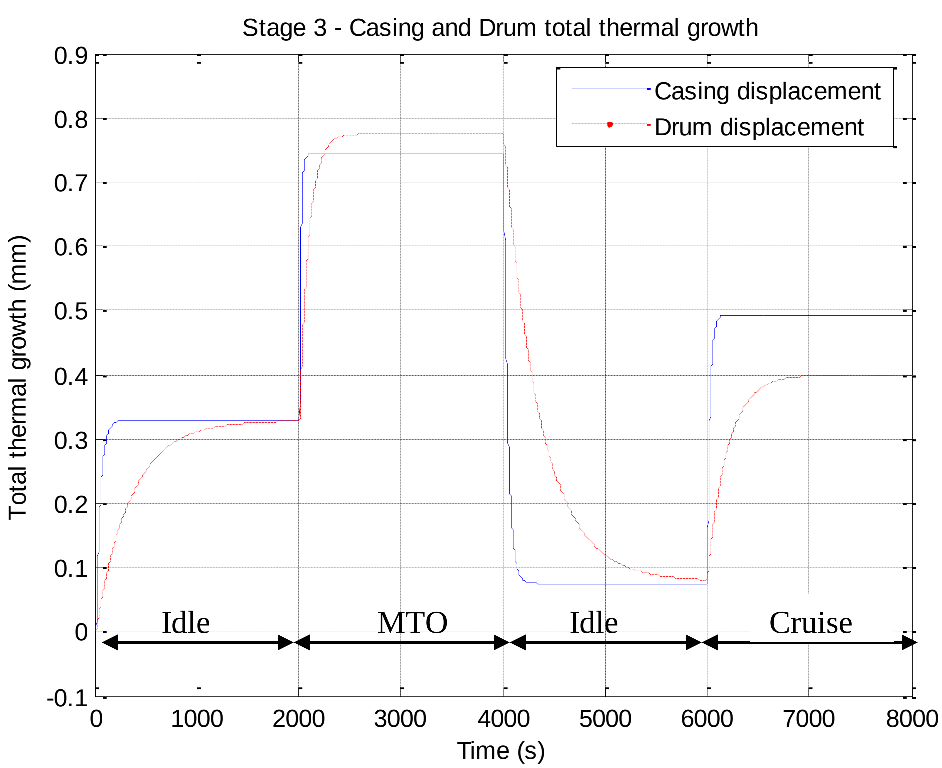

Figure 4.9: The variation of total thermal growth of casing and drum with time over the extended square cycle for stage 3 of Trent 1000 casing and drum models

The closure behaviour of each stage is given by the relative expansion of the casing to the expansion of the drum. When the casing displacement is subtracted from the drum displacement at any point in the cycle, the results is called the closure as shown in Figure 4.10. Figure 4.10 shows the variation of Lumped model closure with time over the extended square cycle for stage 3 of Trent 1000 casing and drum models.

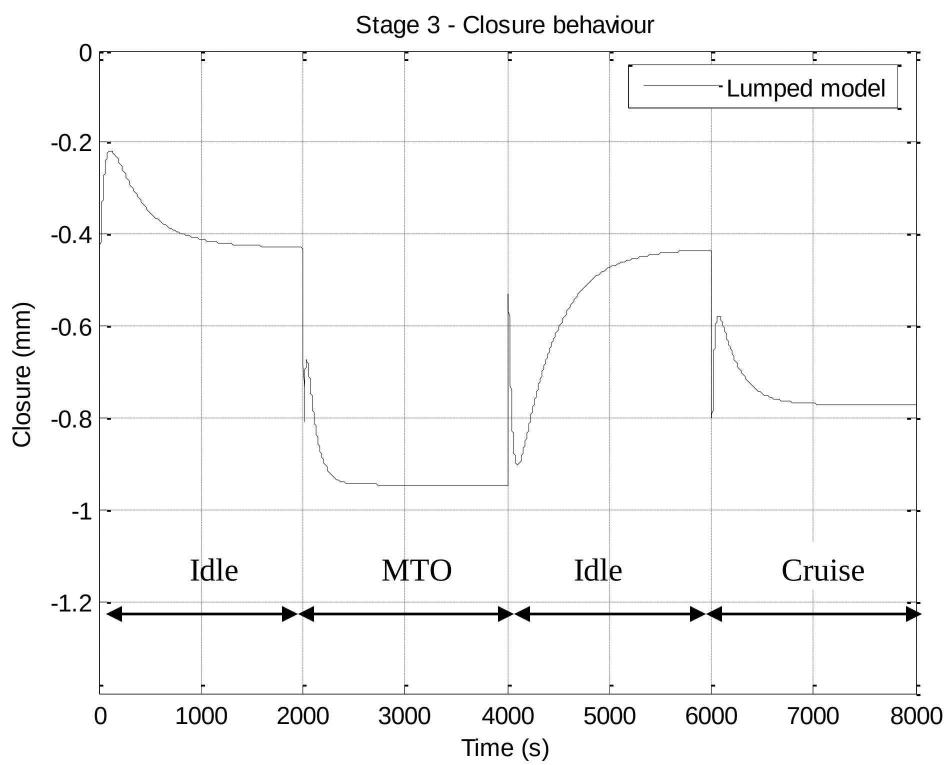

Figure 4.10: The variation of Lumped model closure with time over the extended square cycle for stage 3 of Trent 1000 casing and drum models

4.6 Thermal matching of the Lumped and SC03 models

This involved the matching of the result from the lumped model with the results of the SC03 model. If the matched well then it is assume that the validation of the SC03 is correct. Further matching is done between the lumped model, SC03 model and the results obtained from the multiple cavity rig. Figure 4.11 shows matching of the Lumped model closure with SC03 closure over the extended square cycle for stage 3 of Trent 1000 casing and drum models.

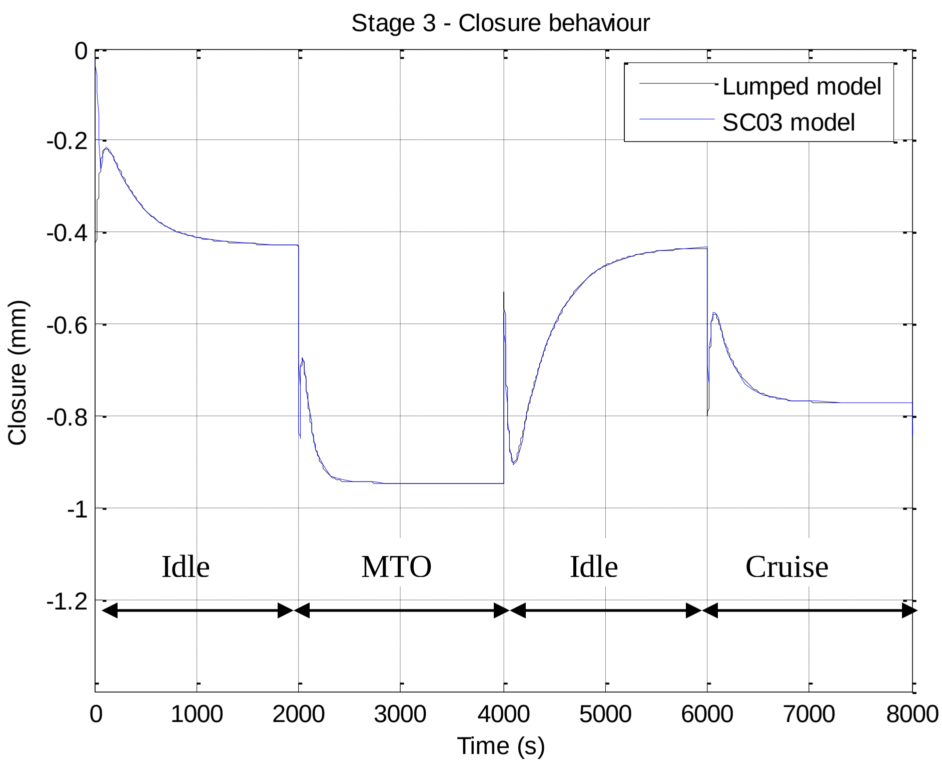

Figure 4.11: The Lumped model closure matched with SC03 closure over the extended square cycle for stage 3 of Trent 1000 casing and drum models.

As shown in Figure 4.11, the 1-D model (Lumped parameter analysis) closure is in very good agreement with the prediction of 2-D model from the SC03 over the extended square cycle for stage 3. This is confirmed by the matching profile of SC03 2-D model closure variation over time with the Lumped parameter model closure for the entire cycle. During engine transient, there are no discrepancies during acceleration, deceleration and cruise operation of both models, hence the time constant and closure data at any point in the cycle in both models are the same.

4.7 Summary

This chapter has reported on the 1D modelling of the of tip clearance control concepts using the lumped parameter method. The lumped parameter data was calibrated against the SC03 HP compressor drum and casing models simulation. The result of stage 3 is presented.

An extended square cycle with the rotational speed of 8,467.17, 12,359.24, and 12, 016.72 rpm for Idle, MTO and Cruise respectively over a time of 8,000s was used. Inlet temperature (T26) of 350.86, 599.61 and 582.21 for Idle, MTO and cruise respectively and exit temperature (T30) of 516.13, 909.12 and 876.20 for Idle, MTO and cruise respectively were modelled in the lumped model.

The variation of total thermal growth of casing and drum with time over the extended square cycle for stages 3 Trent 1000 casing and drum models were studied. This variation gives the closure characteristics of the system during engine transient. The Lumped parameter model closure was matched with SC03 closure over the extended square cycle for stages 3 of Trent 1000 casing and drum models. The overall result of the matching process shows that the results of the lumped model are in good agreement with the results (time constant and closure data) of the SC03 model. Evidence can be seen in the matching profiles of the two models as shown in Figure 4.11.

Chapter 5

Sensitivity analysis using HP compressor drum and casing models of RB211-524 and Trent 1000 engine

5.1 Sensitivity analysis

Based on the choice of a passive clearance control scheme involving the control of the disc and casing thermal response, a sensitivity analysis was carried out. This was to determine the quantitative effect of various parameters on the closure behaviour of the various high-pressure compressor stages, hence the overall effect on clearance. These parameters are heat transfer coefficient, cavity mass flow, radial inflow, coefficient of thermal expansion of material and time constants. The effects of these parameters are analysed using the drum and casing models of the RB211-524 model and Trent 1000 engine.

It is important to define the following as they will be encounter throughout this thesis:

- Heat transfer coefficient
- Cavity mass flow
- Compressor pressure ratio
- Time constants
- Coefficient of thermal expansion of material

- **Heat transfer coefficient:** This is the proportionality coefficient between the heat flux and the temperature difference. It is used in calculating the heat transfer by convection or phase transition between a fluid and a solid. It is also often calculated from the Nusselt number which is a dimensionless number as given in Equation 2.11. The heat transfer coefficient has SI units in watts per squared meter kelvin.

$$h = \frac{Q}{A\Delta T} \quad \mathrm{W/\,(m^2K)} \qquad \textbf{(5.1)}$$

The relevant heat transfer coefficient correlations used in the modelling of flow in RB211-524 G/H-T HPC engine model and Trent 1000 are presented in Equations 5.6 through to 5.11.

- **Cavity mass flow rate:** This is mass flow rate of air that flow through the cavity. Its unit is kilogram per second in SI units.

$$\dot{m} = \rho v A \qquad \mathrm{kg/s} \qquad \textbf{(5.2)}$$

- **Pressure ratio (PR):** This is the ratio of the air total outlet pressure to the air total inlet pressure. It is usually greater than 1. In compressor, several stages are used to produce a high compressor pressure ratio (CPR) with each stage producing a small pressure increase. If the exiting pressure is p2 and the entering pressure is p1, then PR is given in Equation 5.3.

$$PR = \frac{p_2}{p_1} \qquad \textbf{(5.3)}$$

- **Time constant:** This is the time required for the system to response to reach 63.2% during acceleration from Idle to maximum take-off and the time required for the system fall or decay to 36.8% during deceleration from maximum take-off to Idle. The equation for time constant is given in Equation 5.8.

- **Coefficient of Thermal Expansion of material:** It is a measure of the change in length of a material in response to a change in temperature. Materials expand as temperature increase and contract as temperatures decrease. The change in length of the material is therefore proportional to change in temperature. Hence, materials expand in response to heating and contract on cooling. It is denoted with a symbol α.

The sensitivity analysis is based on the lumped parameter concept for tip clearance control which was presented in detail in Chapter 4. The concept postulate that if the mass, volume and the area of the solid are constant, that increasing (decreasing) the heat transfer coefficient of the body will results in the reduction (increase) of the time constant.

The intent of this study is to decrease the time constant of the drum by increasing the relevant heat transfer coefficients. This will cause the compressor drum to heat up faster hence narrowing down the large gap that existed at the beginning of engine transient operation between the casing and the blade. This would effect a reduction in the cruise clearance and a reduction in clearance at first acceleration (max take off) and hence reductions in the overall specific fuel consumption giving rise to higher engine efficiency. The variation of closure with time over a square cycle of stage 1 HP compressor for RB211-524 engine was presented in Figure 2.5. The values of the parameters used in RB211-524 for this first analysis are presented in Table 5.1.

Parameters	Description	Value	Units
T26 Idle	Inlet fluid temperature at idle	331.20	K
T26 MTO	Inlet fluid temperature at MTO	544.3	K
T30 Idle	Outlet fluid temperature at idle	456.30	K
T30 MTO	Outlet fluid temperature at MTO	851.6	K
P26 Idle	Inlet pressure at idle	21.30	Psi
P26 MTO	Inlet pressure at MTO	108.6	Psi
P30 Idle	Outlet pressure at idle	56.95	Psi
P30 MTO	Outlet pressure at MTO	505.5	Psi
NH Idle	Speed at idle	6473.4	rev/min
NH MTO	Speed at MTO	10096.7	rev/min
α	Coefficient expansion of drum	9.87E-06	

Table 5.1: The engine parameters and environmental parameters and their values used in RB211-524 for this analysis

The effect of time constants and coefficient of thermal expansion of material were studied using RB211-524 and their results are presented in Figures 5.1 through to 5.8. The effect of heat transfer coefficient and the drum time constant on the closure behaviour of stage 3 of a Trent 1000 engine compressor drum and casing model is presented in Section 5.4. The corresponding finite element model is illustrated in Figures 5.13. The effect of radial inflow on the closure behaviour of stage 3 and hence its impact on tip clearance is presented in Section 5.5. The study used a simplified lumped-parameter spreadsheet model in conjunction with a full axisymmetric thermo-mechanical finite-element high-pressure compressor drum and casing model. The first parametric study used a one-dimensional spreadsheet in conjunction with the result from the SC03 model of a RB211-524 Roll-Royce engine. The second study was carried out on a much more recent engine model, an axisymmetric Trent 1000 drum and casing model supplied by Roll-Royce plc. The results of the sensitivity analysis are presented in Sections 5.3, 5.4 and 5.5.

5.2 Basic principle for tip clearance control analysis

It is considered useful at this point in time to formally define the terms Square Cycle, Full Hot Re-Slam, Cold Build Clearance, Closure and Clearance as they will be referred to frequently throughout this thesis.

- **Square cycle:** This is a simple design point engine cycle consisting of start, stabilisation at idle, acceleration to maximum, stabilisation at maximum take-off (MTO), deceleration to idle, and stabilisation at idle. It gives a basic understanding of temperature, displacement, and clearance response in the cycle.
- **Full hot re-slam closure:** This is the worst case after deceleration when it is required to accelerate back to MTO conditions. It is the minimum clearance point after deceleration from maximum take-off (MTO) when the engine power is low during deceleration. It is added to the tightest point in the cycle beyond stabilised maximum take-off point to calculate the cold build clearance in the cycle. It is the parameter that sets the clearance.

- **Cold build clearance (CBC):** At the start of an engine, both casing and blade are stationary and have a specific clearance between them known as cold build clearance (CBC). This is the manufacturer design gap. They are two ways to calculate the cold build clearance in any given square cycle as given in Equation 5.4 and 5.5.

$$\delta_{CBC} = \frac{\delta_{FHR}}{2} + \delta_{MAX} \quad \textbf{(5.4)}$$

$$\delta_{CBC} = \frac{\delta_{FHR} + \delta_{MAX}}{2} \quad \textbf{(5.5)}$$

- **Closure:** Compressor closure is the displacement of the casing relative to rotor displacement in a compressor.

$$\delta_{close} = \delta_{c} - \delta_{r} \quad \textbf{(5.6)}$$

- **Clearance:** This is the addition of the cold build clearance to closure in a square cycle.

$$\delta = \delta_{CBC} + \delta_{close} \quad \textbf{(5.7)}$$

The method for controlling tip clearance indicates that for a given square cycle, tip clearance depends on:

- Casing displacement
- Rotor displacement

Two essential analyses are performed to determine the compressor clearance during transients over a square cycle, namely:

- The closure analysis
- The clearance analysis

In the clearance control analysis, a positive y-axis on the graph represents clearance plots while a negative y-axis represents closure plots. In the clearance graph, the point zero on the graph represents the touching of blade and casing while negative number indicates the rubbing between the blade and the casing.

The sensitivity study presented in Section 5.3, 5.4 and 5.5 will give an inside on how to control the above complex behaviour in HP compressor during transient operation.

5.3 Sensitivity results with RB211-524 HPC engine models

A sensitivity analysis was performed with RB211-524 HP compressor engine models to quantify the effect of disc heat transfer coefficient increased (decrease) on disc time constant at the tip of the rotor. The overall impact on compressor clearance was also studied. Another analysis carried out using the models was the effect of material selection on the compressor clearance during transient operation.

5.3.1 Time constant study

The RB211-524 G/H-T HPC engine model and spreadsheet were used to study the effect of the time constant on the rotor and casing closure characteristics, and the results are presented graphically in Figures 5.1 through to 5.5. The time constant study was undertaken assuming the disc or casing section behaves as a lumped mass.

Assuming a lumped mass approximation, the time constant (τ) is represented by Equation 5.8.

Time constant, $\tau = \frac{mC}{hA}$ **(5.8)**

Figure 5.2 shows the rotor thermal growth characteristics for stage 1 of the RB211-524 aero engine model; with the effect of a change in a 30 percent reduction and 30 percent increase in the rotor time constant during engine transient operation. This value was suggested by the industrial partner. The SCO3 model uses inbuilt heat transfer coefficient correlations and the correlations were given in Chapter 3. The relevant heat transfer coefficient correlations used are the natural convection from upper surfaces of hot horizontal plates and lower surfaces of cool horizontal plates given in Equations 5.9 and 5.10, natural convection from a vertical plate or cylinder are given in Equation 5.11 and 5.12 and forced convection from a free disc with laminar or turbulent flow are used as shown in Equations 5.13 and 5.14.

$h = 0.54\ Ra^{0.25}\ k/L \qquad Ra \leq 2 \times 10^7$ **(5.9)**

$h = 0.14\ Ra^{0.33}\ k/L \qquad Ra > 2 \times 10^7$ **(5.10)**

$h = 0.59\ Ra^{0.25}\ k/L \qquad 10^4 < Ra \leq 10^9$ **(5.11)**

$h = 0.129\ Ra^{0.33}\ k/L \qquad Ra > 10^9$ **(5.12)**

$h = 0.616 Re^{0.5}\ Pr^{1/3}\ k/r \qquad Re \leq 2.4 \times 10^5$ **(5.13)**

$h = 0.0267 Re^{0.8}\ Pr^{0.6}\ k/r \qquad Re > 3.0 \times 10^5$ **(5.14)**

Figure 5.1 shows a more rapid response from the rotor during engine accelerations and a more rapid shrinkage during engine decelerations when the time constant is reduced by 30%. However, a slower response from the rotor during engine accelerations and decelerations respectively is observed when the time constant is increased by 30% when compared to the baseline analysis.

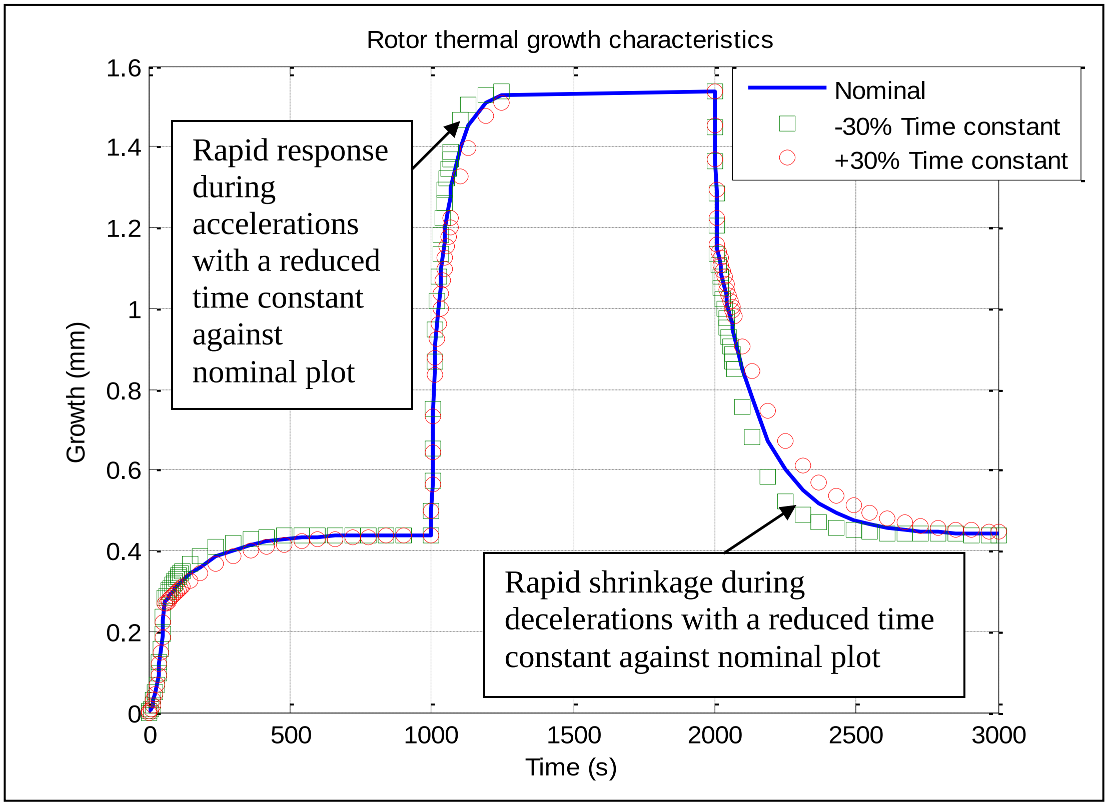

Figure 5.1: The variation of rotor tip thermal growth with time over a square cycle of stage 1 HP compressor for RB211-524 engine with (+/-30%) time constant (τ) during transient operation

The effect of this different time constant of the rotor is observed in the closure characteristics of the two schemes (+/-30% τ) as shown in Figure 5.2. The analysis shows that with a 30% reduction in time constant, there is a reduction in closure characteristics during acceleration and with an increase in closure during deceleration in comparison to the nominal case. But with a 30% increase in time constant, an increase in closure characteristics can be observed during acceleration and decrease in closure during deceleration.

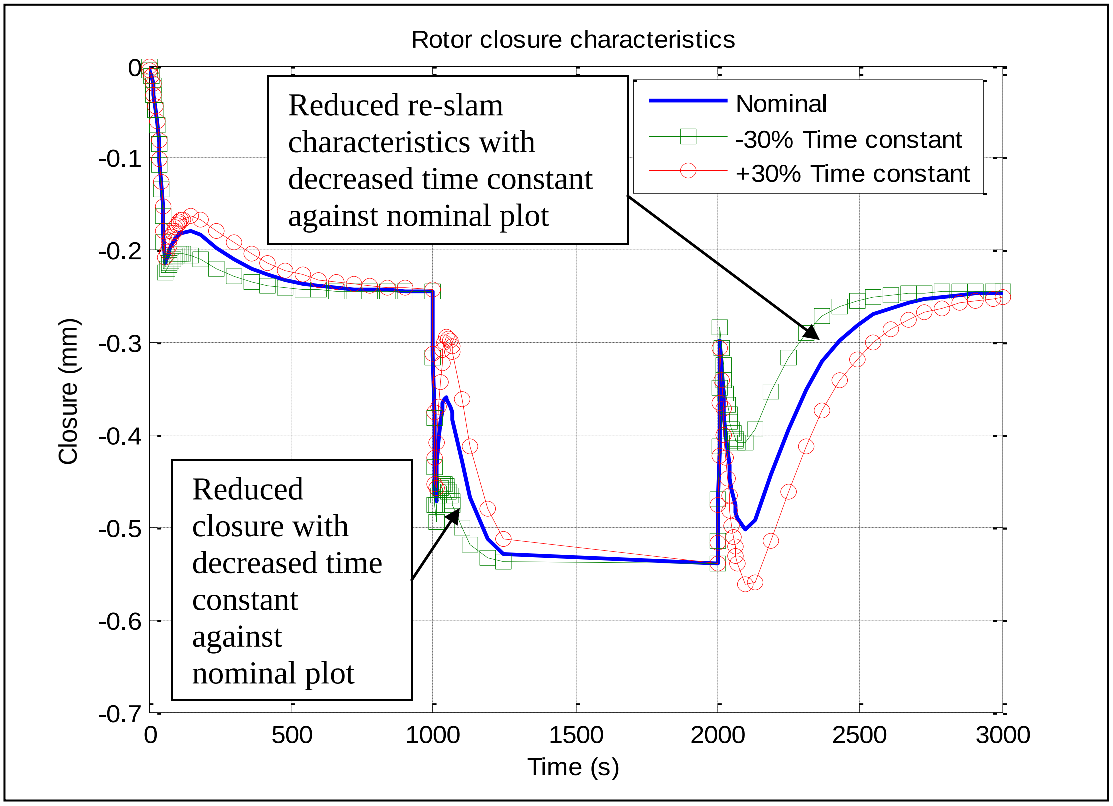

Figure 5.2: The variation of rotor closure characteristics with time over a square cycle for stage 1 of the RB211-524 aero engine model with the effect of (+/- 30%) time constant (τ) during transient operation

The effects of these two schemes (+/-30% time constant) are converted into clearance characteristics of the rotor in the cycle during transient operation by applying the clearance control Equation 5.7. When the cold build clearance is added to the closures in the cycle, the results obtained are the overall clearances in the cycle as shown in Figure 5.3. The overall result calculated against the baseline model are summarised in Table 5.2.

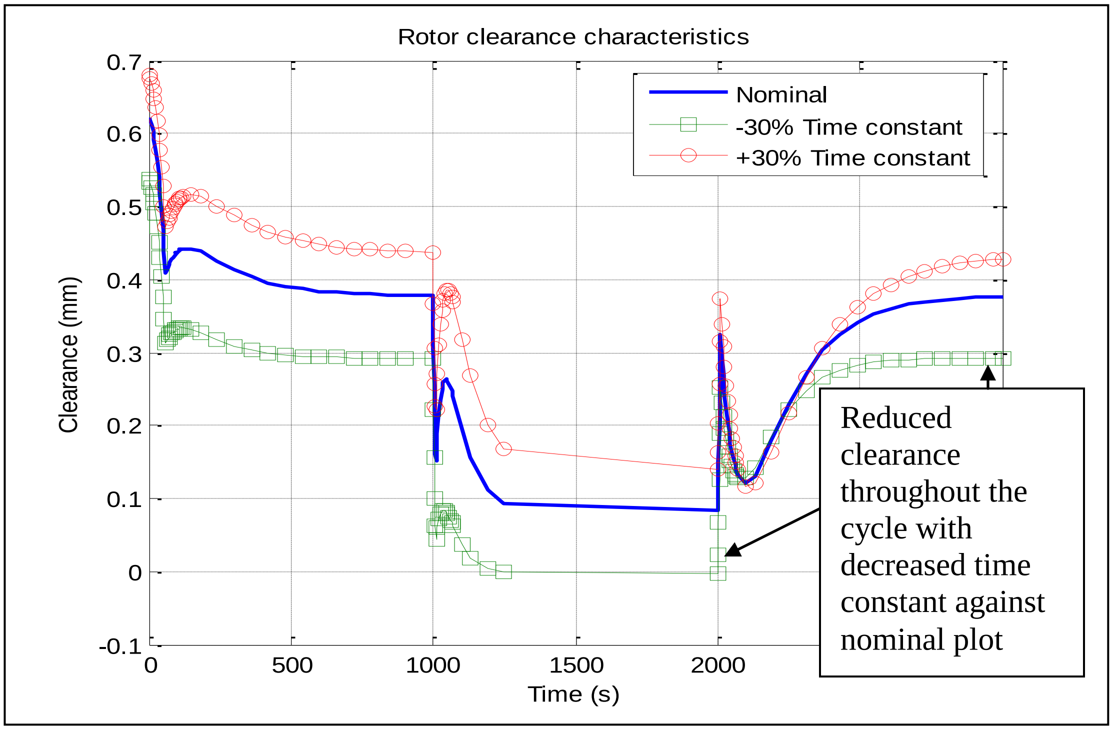

Figure 5.3: The variation of rotor clearance characteristics with time over a square cycle for stage 1 of the RB211-524 aero engine model with the effect of (+/- 30%) time constant (τ) during transient operation

Conditions	**Worst case acceleration**	**Stabilised MTO**	**Stabilised Idle**
With -30% τ	0.181mm reduction in clearance	0.086mm reduction in clearance	0.084mm reduction in clearance
With +30% τ	0.122mm increase in clearance	0.057mm increase in clearance	0.052mm increase in clearance

Table 5.2: Result summary of RB211-524 aero engine rotor model clearance analysis with the effect of (+/- 30%) time constant (τ) during transient operation

Finally, the disc time constants are found to depend on the heat transfer coefficient of the disc. An increase in the heat transfer coefficient reduces the disc time constant. Hence, increasing the thermal response of the high pressure compressor (HPC) drum will reduce the reslam characteristic at t = 2100 s of the drum, therefore reducing the cold build clearance (CBC) and hence the reduction in clearance. The point, at which the clearance is ‘0’, indicates the touching of the casing and the blade during the transient operation.

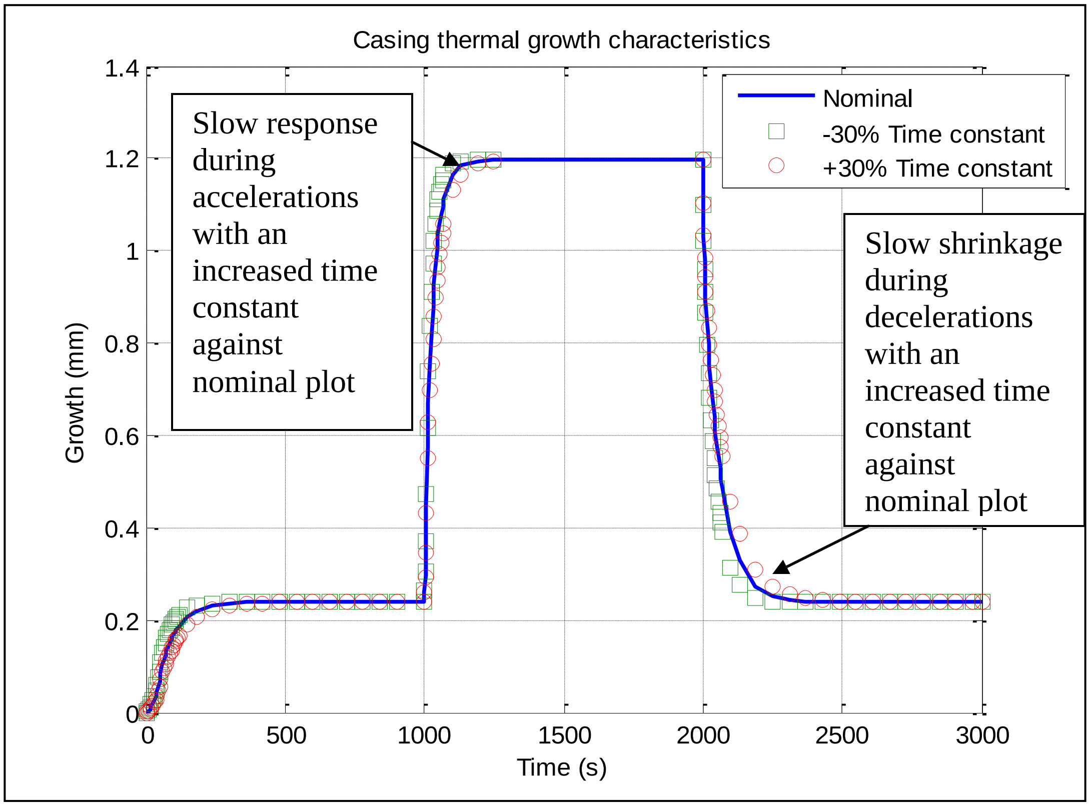

Figure 5.4: The variation of casing thermal growth characteristics with time over a square cycle for stage 1 of the RB211-524 aero engine model with the effect of (+/-30%) time constant (τ) during transient operation

Figure 5.4 shows the casing thermal growth characteristics for stage 1 of the RB211-524 aero engine model with the effect of a change in a 30 percent reduction and a 30 percent increase in casing time constant during transient operation.

Using the nominal case as a baseline, there are differences in the casing thermal growth for the two schemes (+/-30%) which are caused by an increase or decrease in the time constant. Figure 5.4 shows that with 30% reduction in time constant, there is a more rapid thermal response of the casing during engine accelerations and a more rapid thermal shrinkage during engine decelerations. A slower response of casing during engine accelerations and decelerations respectively are obtained with a 30% increase in time constant.

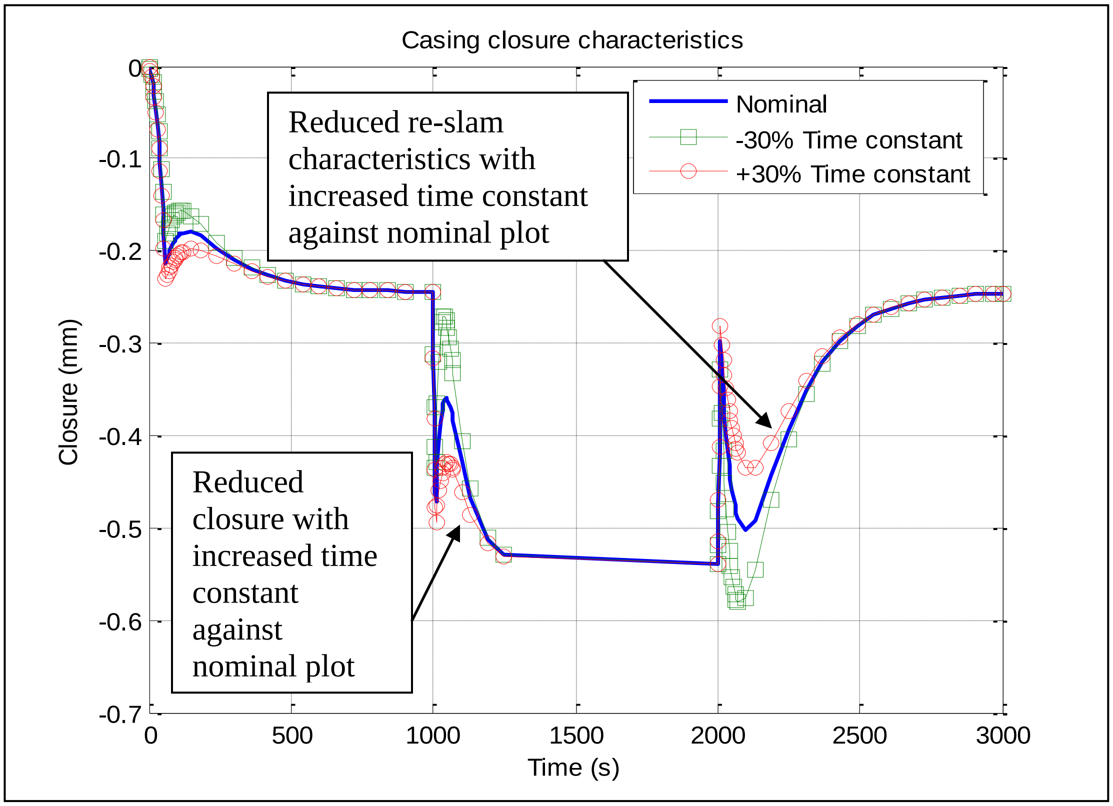

Figure 5.5: The variation of casing closure characteristics with time over a square cycle for stage 1 of the RB211-524 aero engine model with the effect of (+/- 30%) time constant (τ) during transient operation

The effect of this different time constant of the casing is observed in the closure characteristics of the two schemes (+/-30% time constant) as shown in Figure 5.5. When compared to the nominal case, the analysis shows that with a 30% increase in time constant there is a reduction in closure characteristics during acceleration and an increase in closure during deceleration. But with a 30% reduction in time constant, an increase in closure characteristics can be observed during acceleration and decrease in closure during deceleration.

The effects of these two schemes (+/-30% time constant) are converted into clearance characteristics of the casing in the cycle during engine transient operation by applying the clearance control Equation 5.7. When the cold build clearance is added to the closures in the cycle, the results obtained are the overall clearances in the cycle as shown in Figure 5.6. The overall result calculated against the baseline model are summarise in Table 5.3.

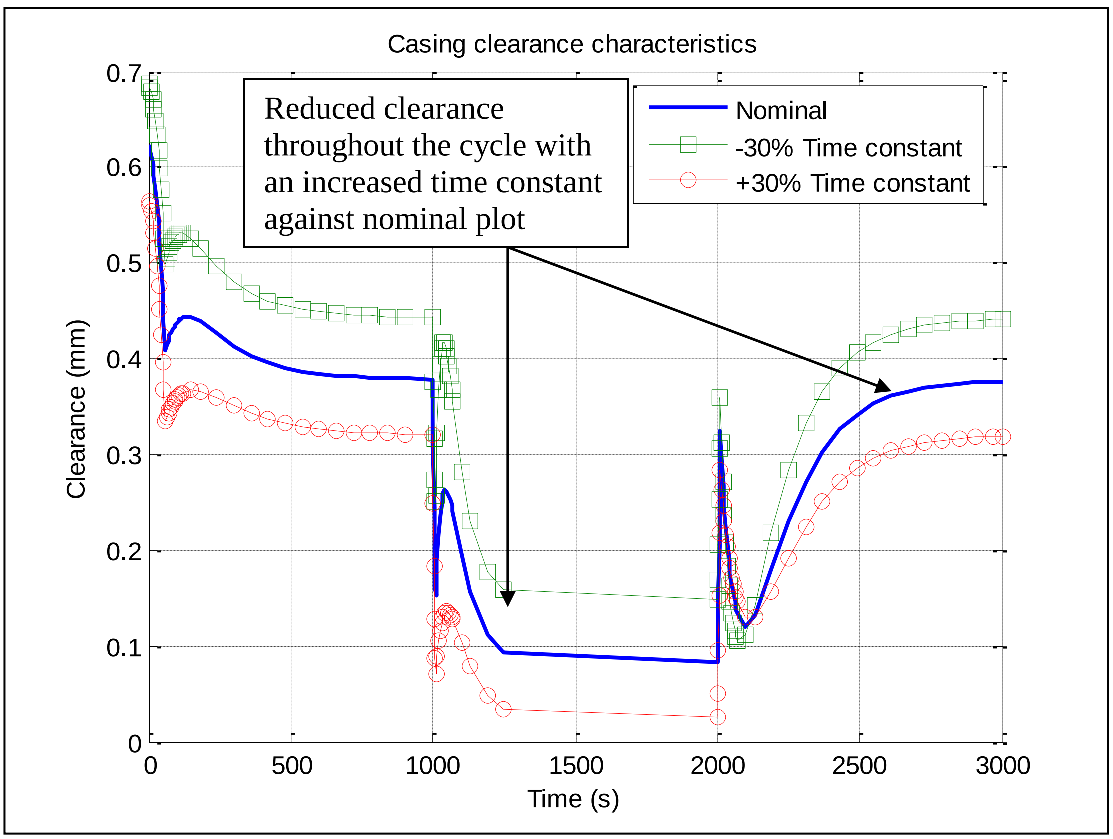

Figure 5.6: The variation of casing clearance characteristics with time over a square cycle for stage 1 of the RB211-524 aero engine model with the effect of (+/- 30%) time constant (τ) during transient operation

Conditions	Worst case acceleration	Stabilised MTO	Stabilised Idle
With -30% τ	0.149mm increased in clearance	0.065mm increased in clearance	0.065mm increased in clearance
With +30% τ	0.128mm reduction in clearance	0.058mm reduction in clearance	0.058mm reduction in clearance

Table 5.3: Result summary of RB211-524 aero engine casing model clearance analysis with the effect of (+/- 30%) time constant (τ) during transient operation

From the time constant (τ) analysis for compressor clearance for RB211-524 rotor and casing models, it is concluded that decreasing the time constant of the rotor and increasing the time constant of the casing reduces the clearances in the compressor. This will give a better tip clearance in the engine during transient operations.

5.3.2 Effect of material selection on compressor clearance

The choice of component materials with appropriate thermal expansion coefficients (α) can also be used to control blade tip clearance. This analysis will examine the effect changing the material has on the temperature and movement of the rotor blade relative to the casing in an RB211-524 G/H-T HP compressor engine model; and hence the overall impact on compressor clearance. In an aircraft engine, different materials are used for different components depending on their strength, fatigue life, temperature limits, etc. For example, titanium alloys are used in aircraft components such as rotor blades due their excellent strength-to-weight ratio, high corrosion resistance, high crack resistance, fatigue resistance and capability to endure high temperatures. In this analysis, two materials designated as TBB with α =9.347E-06 and QMP with α =1.48E-05 both titanium alloy (which have different thermal expansion coefficients) are used as material for an HP compressor rotor blades for the study. The choice of the two materials was based on their regular used by the industrial partner in their engines and as such the need for verification to ascertain the best in term of tip gap control during engine transient.

The basic rotor blade model of the RB211-524 G/H-T HP compressor engine consists of TBB for stages 1 and 2 of the rotor blade, while QMP was used for stages 3 to 6. In this analysis, a computation of stage 1 rotor blade thermal growth and tip clearance was performed with TBB, and a second analysis was carried out by replacing the TBB with QMP to compare the effect each material has on tip clearance during transient operations over an engine square cycle.

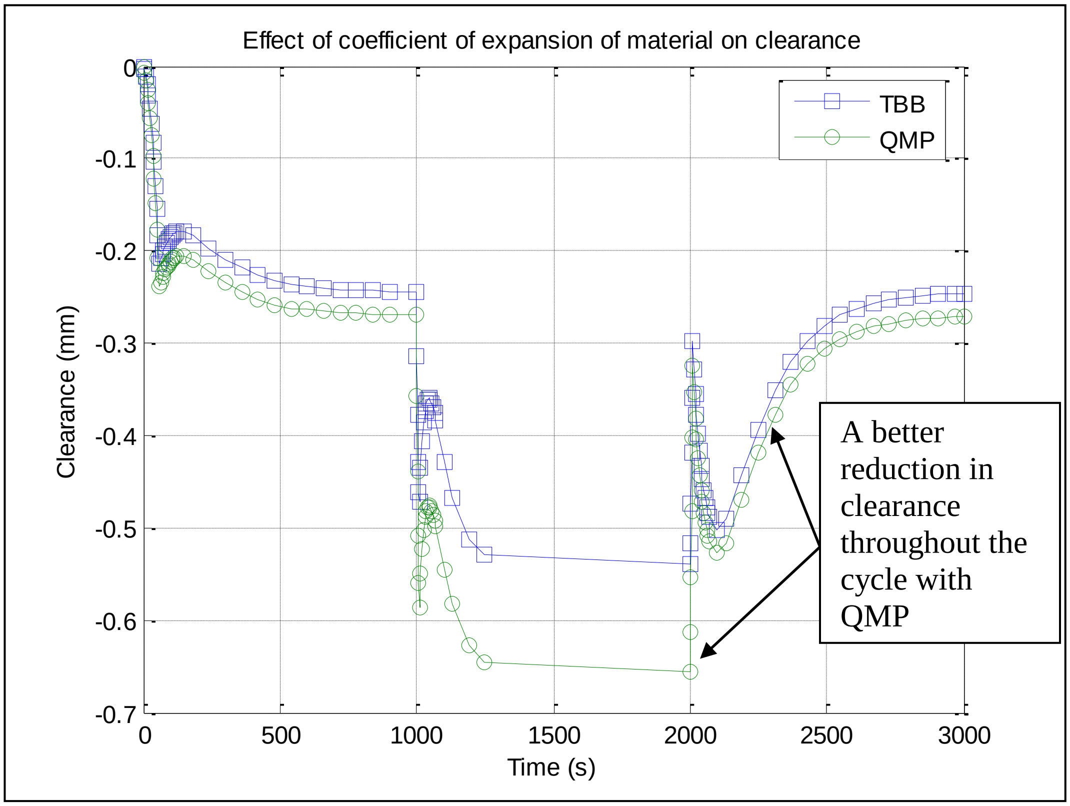

Figure 5.7: **The variation of tip clearance with time over a square cycle for the basic model with material TBB and the modified rotor blade design model with material QMP for stage 1 HP compressor of RB211-524 engine**

The result of the analysis is presented in Figure 5.7. Figure 5.7 shows tip clearance as a function of time for the basic model TBB and the modified rotor design model QMP. The material selection analysis results show that QMP, with a higher thermal expansion coefficient gives a reduced tip clearance compared to TBB. Hence the reason for using the material with a higher thermal expansion coefficient in the rotor blade of the last stages of the HP compressor so as to withstand the high thermal stress and complex flow behaviours.

5.4 Sensitivity study with Trent 1000 engine models

The sensitivity results are presented in the form of closure and clearance graphs. The effect of an increase in heat transfer on the drum time constant and the impact on compressor clearance for all stages in a Trent 1000 engine is presented, and radial inflow analysis carried out on stage 3 only.

SC03 modelling setup for Trent 1000 engine consists of the following: Models used are Trent 1000 drum model and Trent 1000 casing model. The Cycle data used is Square cycle with bottom of loop cruise and test bed equivalent cruise. Model boundary conditions used for each disc have Streams modelled around the disc cob and Voids are used in the interdisc cavity. Figure 5.8 shows the Trent 1000 casing model with blades and casing support structures while the six stage Trent 1000 drum model showing the six discs and cavities is shown in Figure 5.9.

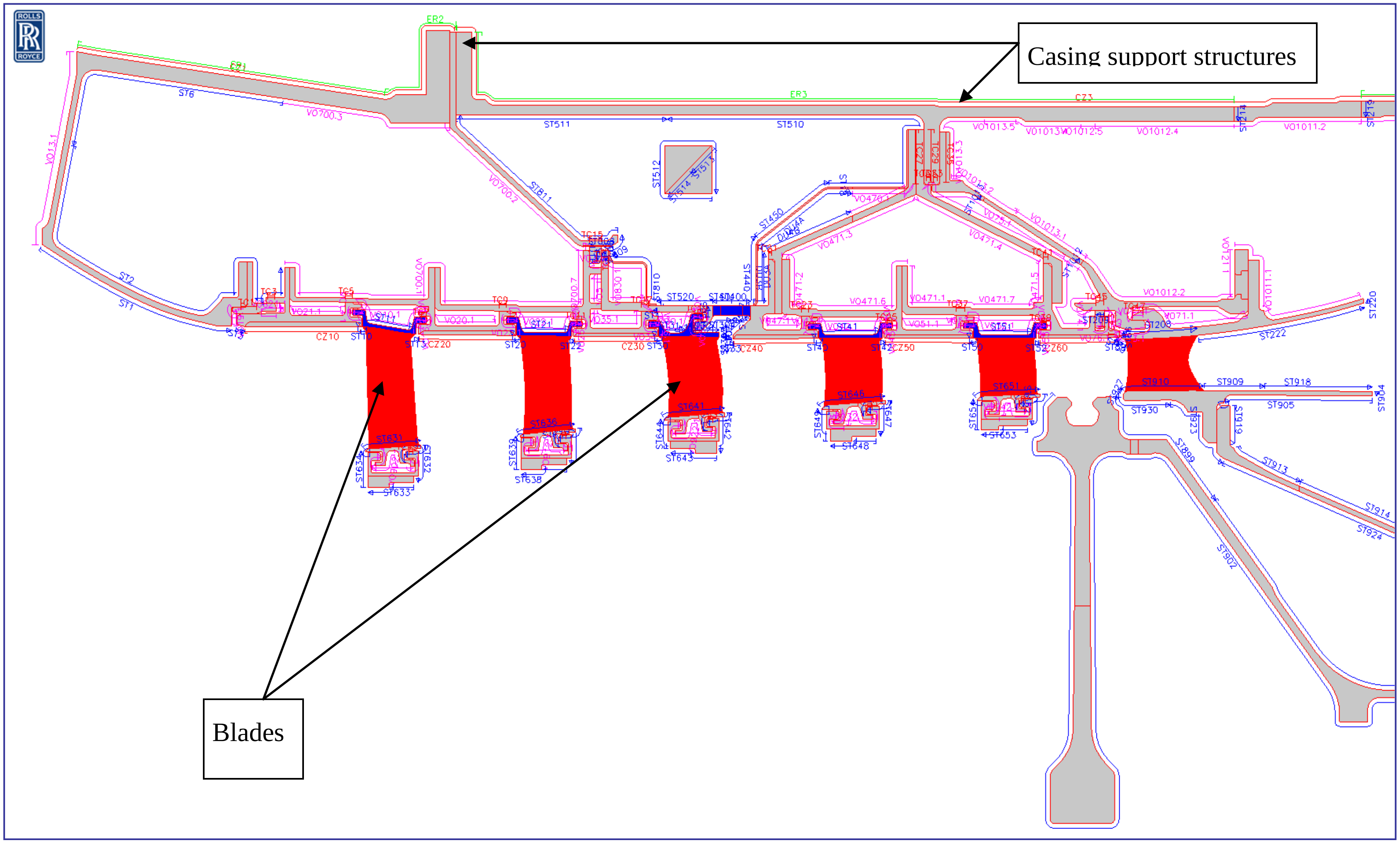

Figure 5.8: A finite element model of the Trent 1000 HPC casing model showing blades and casing support structures

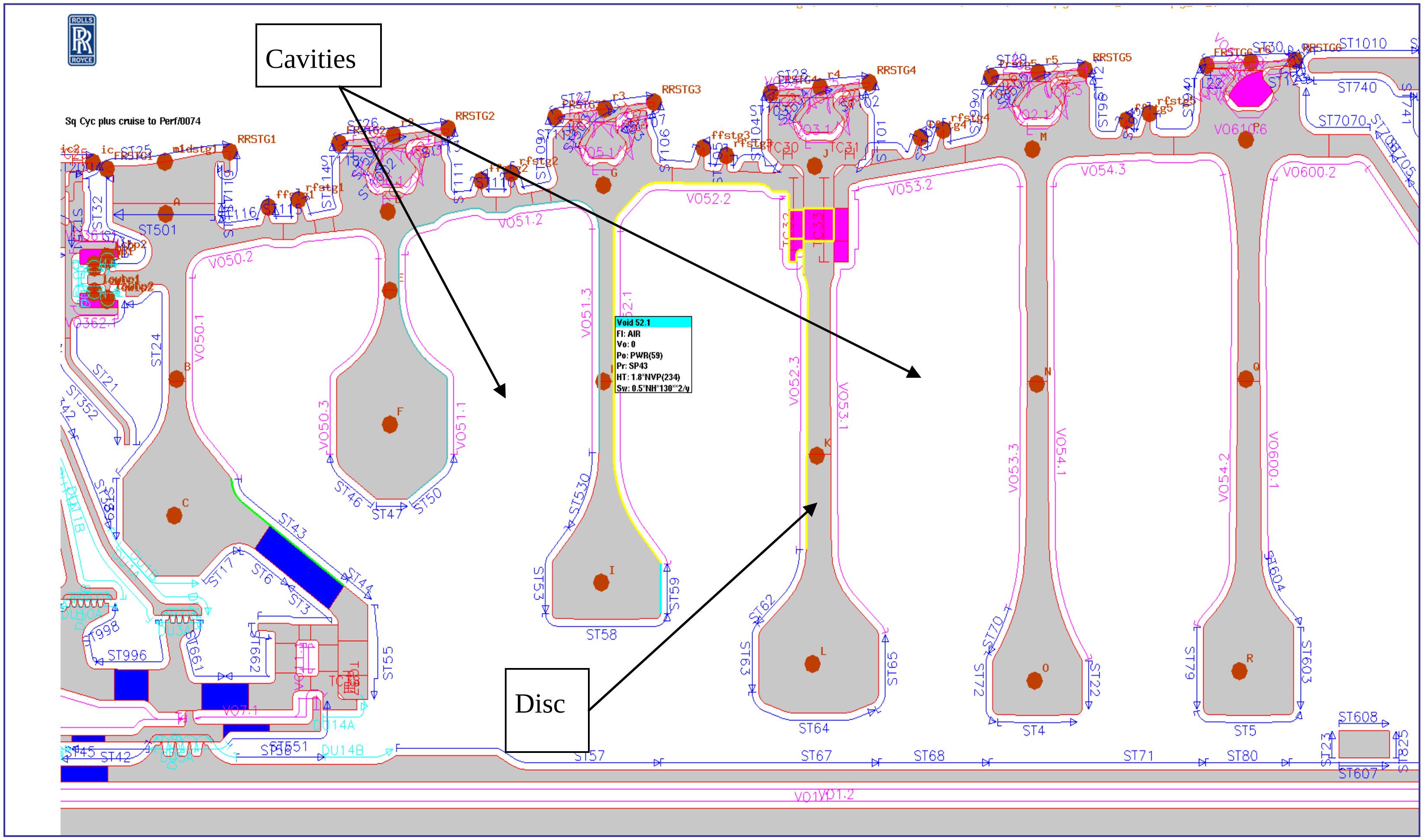

Figure 5.9: A finite element model of the Trent 1000 HPC drum model with six discs and cavities

Three model reference points are specified on each disc of each stage at the disc rim, mid disc and disc cob using alphabet (A-R) for temperature and displacement measurement. The model reference point, the description of the model position on each stage and their coordinates are given in Table 5.4. The results of the analysis are presented in Section 5.4.1.

Model Point	Position	Stage	Axial Position (mm)	Radial Position (mm)
A	Disc rim	1	-42.5833	225.781
B	Mid disc	1	-39.2174	180.584
C	Disc cob	1	-39.8744	143.141
D	Disc rim	2	25.1591	226.567
E	Mid disc	2	25.816	204.89
F	Disc cob	2	25.816	168.147
G	Disc rim	3	90.6494	233.793
H	Mid disc	3	90.8494	179.927
I	Disc cob	3	90.1925	124.747
J	Disc rim	4	155.226	239.049
K	Mid disc	4	155.883	159.563
L	Disc cob	4	154.569	102.413
M	Disc rim	5	221.573	243.647
N	Mid disc	5	222.887	179.27
O	Disc cob	5	222.23	97.8143
P	Disc rim	6	286.606	246.274
Q	Mid disc	6	286.606	180.584
R	Disc cob	6	284.636	100.442

Table 5.4: Model reference points with their coordinates for the six stages of the Trent 1000 HPC drum

The Trent 1000 drum consists of six stages, with two adjacent discs forming the cavity of each stage. The nominal model boundary conditions supplied have streams around the disc cob on each disc and voids in the cavity.

The study was performed by increasing the heat transfer coefficient in the cavity of the drum by a heat transfer coefficient enhancement factor of 1, 2, 4, 6 and 8. The heat transfer coefficients were obtained from the natural convection from upper surfaces of hot horizontal plates and lower surfaces of cool horizontal plates, natural convection from a vertical plate or cylinder and forced convection from a free disc with laminar or turbulent flow. These correlations were given in Equation 5.9 through to Equation 5.14. Three reference points were specified on each disc at various coordinates, from where the temperatures and displacements were measured. Average heat transfer coefficient is used to show the clearance reduction trends in terms of disc time constant.

5.4.1 Sensitivity analysis results of Trent 1000 models

The results of the analysis performed using the Trent 1000 drum and casing models are presented for the six stages in the form of:

- Contour plots
- Temperature vs. time graph
- Blade tip thermal growth graph
- Time constant reduction graph
- Closure characteristics graph
- Clearance characteristics graph

The analysis was carried out by increasing the heat transfer coefficient with an increased factor of 2, 4, 6 and 8. The stages in the model were run separately at first, and all stages of the model were then subsequently run together to check for consistency. When both results were compared; it was found that the two runs were in good agreement with each other, showing consistency in the model. The engine parameters used are presented in Tables 5.5 for stage 3. Engine parameters and results for stages 1, 2, 4, 5 and 6 are presented as appendix 5.

Parameters	Description	Value	Units
T26 Idle	Inlet fluid temperature at idle	350.859	K
T26 MTO	Inlet fluid temperature at MTO	599.61	K
T26 Cruise	Inlet fluid temperature at cruise	582.206	K
T30 Idle	Outlet fluid temperature at idle	516.13	K
T30 MTO	Outlet fluid temperature at MTO	909.119	K
T30 Cruise	Outlet fluid temperature at cruise	876.20	K
RPM Idle	Idle speed	8461.76	Rad/s
RPM MTO	MTO speed	12351.37	Rad/s
RPM Cruise	Cruise speed	12009.07	Rad/s
Drum alpha		9.87E-6	
Casing alpha		0.99E-6	
Thermal conductivity		659	W/(K.m)
Radius		358.7	mm
Blade height		36.0	mm
Young modulus E		110E9	N/m^2

Table 5.5: The engine parameters and environmental parameters for stage 3

Figure 5.10 shows the temperature contour plots of the Trent 1000 drum model with a highest temperature of 935.6 K and with an ambient temperature of 288.15 K. The temperature distribution on each disc is analysed at disc rim, mid disc and disc cob of each stage. For stage 3 this is indicated by the disc model points G, H and I respectively.

Figure 5.11 shows blade thermal growth as a function of time over the square cycle. The growth characteristics were obtained by increasing the inbuilt heat transfer coefficient in the drum cavity and around the disc cob by a factor of 2, 4, 6 and 8. As shown in Figure 5.11, there is a fast response time constant of the blade during acceleration and rapid contraction during deceleration as the heat transfer coefficient is increased. The proof can be seen in the zoom sections of acceleration and deceleration of Figure 5.11. There is evidence of a reduced cruise clearance as would be shown in clearance plots of Figure 5.16.

Figure 5.10: Temperature contour plots of the Trent 1000 drum baseline model without radial inflow with a highest temperature of 935.6 K and with an ambient temperature of 288.15 K for the six stages

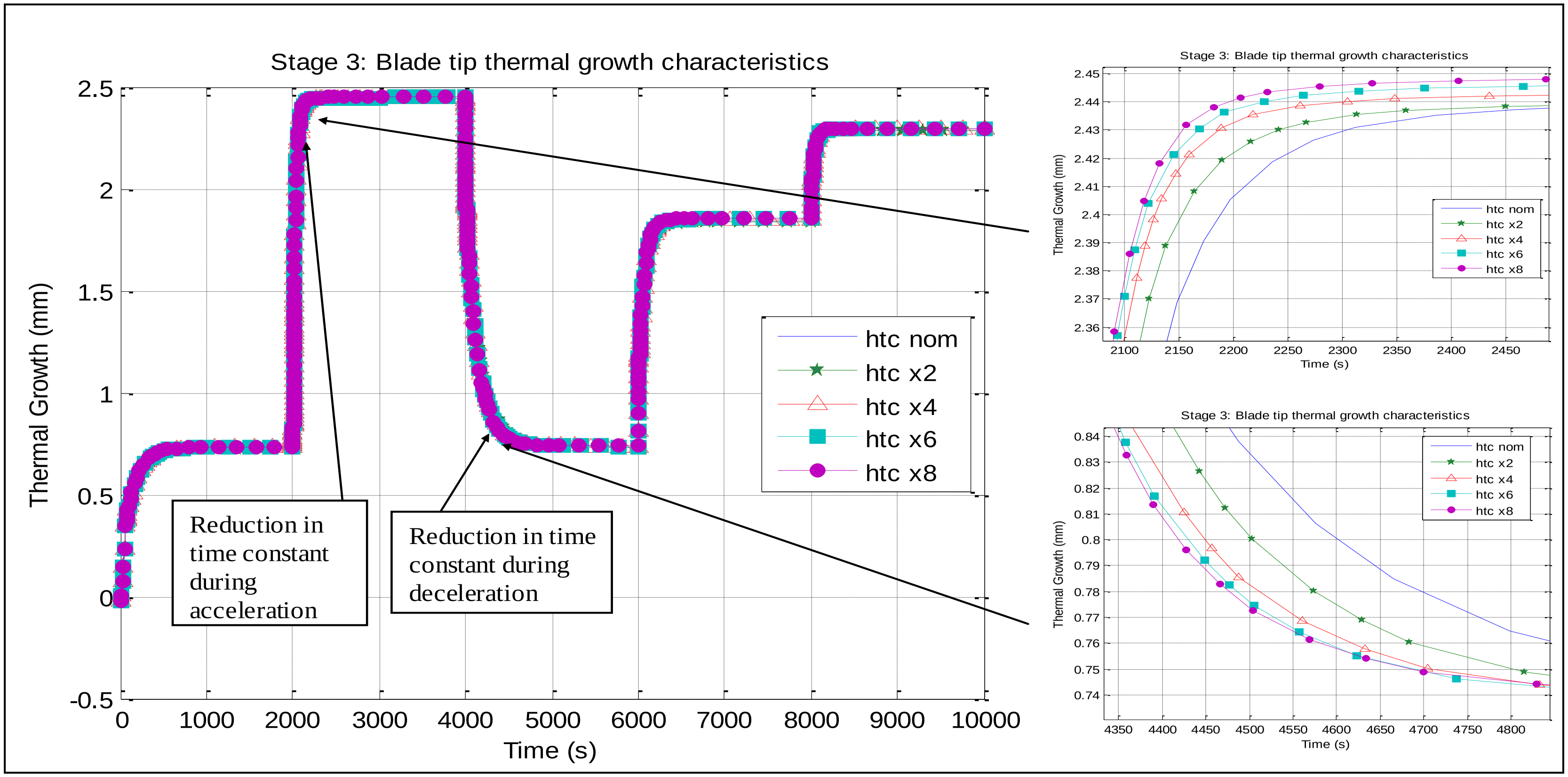

Figure 5.11: The variation of rotor blade tip thermal growth with time over the square cycle for the Trent 1000 HP compressor stage 3 drum and casing models showing the effect of heat transfer coefficient increase on rotor blade tip time constant (τ) without radial inflow. The Figures on the right, top and bottom are the zoom-in sections of acceleration and deceleration section during engine transient

The slopes of the line represent the rate at which the time constant is changing due to heat transfer enhancement; hence the slopes are a measure of the rate of heat transfer. Continuous increase of the heat transfer coefficient will not guarantee a continuous time constant reduction because as time goes on, the rate of heat transfer decreases making the slopes of the lines less steep with more gently sloped. This is the diminishing effect of heat transfer coefficient and this can be improved further by the introduction of radial inflow into the cavity to further enhance the heat transfer.

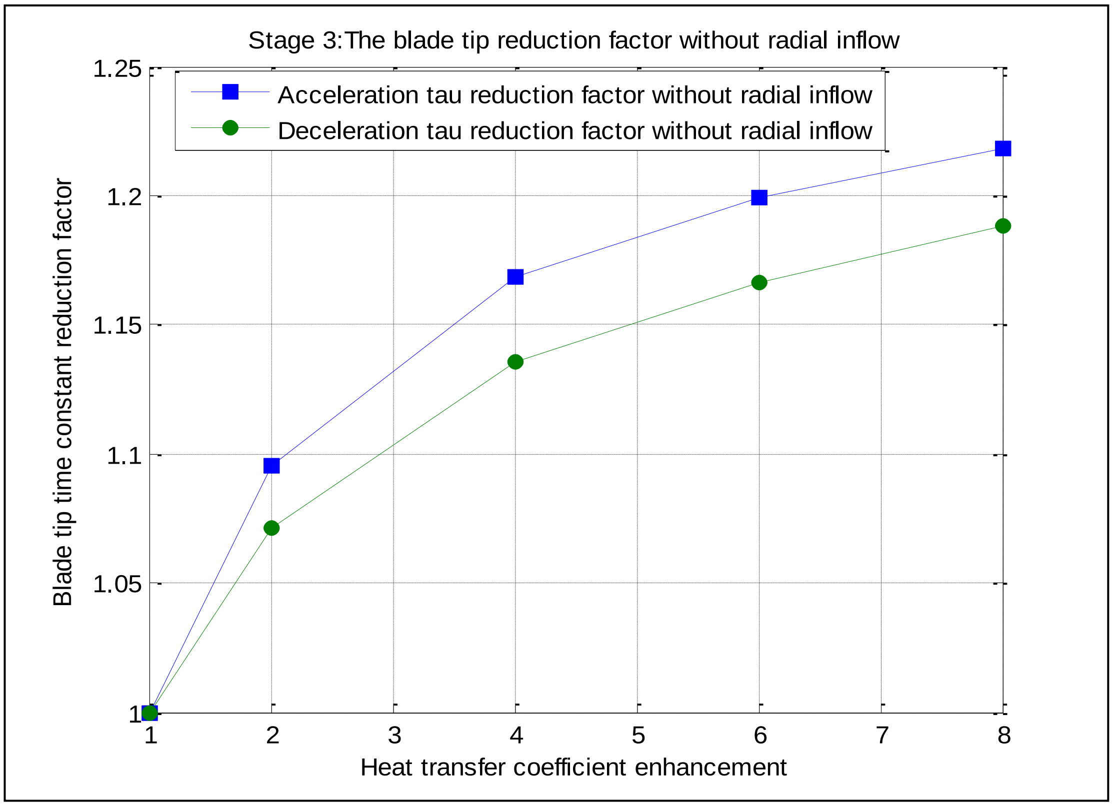

Figure 5.12: The variation of blade tip time constant reduction factor with heat transfer coefficient during acceleration from "Idle to MTO" and deceleration from "MTO to Idle" over a square cycle for the Trent 1000 HP compressor stage 3 drum and casing models without radial inflow

Figure 5.12 shows the variation of blade tip time constant reduction factor with heat transfer coefficient during engine transient operation.

As discussed in section 5.3.1, it follows from equation (5.8), that by increasing the heat transfer coefficient in the drum cavity, the drum time constant is reduced; hence a higher blade tip time constant reduction factor due to the fast thermal response of the drum.

Figure 5.13 shows the variation of drum time constant reduction factor with heat transfer coefficient during engine transient operation. By increasing the heat transfer coefficient in the drum cavity, the time constant reduction factor is higher for the disc cob than the mid disc and the disc rim due to centrifugal acceleration and a finite flow of fluid around the disc cob region. The disc rim gives a lower time constant as it tends to cool quicker than the mid disc and the disc cob due to the flow over it by secondary airflow, used to cool some components of the engine.

The nominal (baseline) data is obtained from the analysis run with the SC03 in built heat transfer coefficient. The nominal (baseline) closure data are -0.40667mm for stabilised idle at 2000s, -0.6485mm for worst case acceleration, -0.89425mm for stabilised maximum take off (MTO) at 4000s, -0.41176mm for stabilised idle at 6000s and -0.72626mm for stabilised cruise closure.

The nominal clearance data are 0.591462mm for stabilised idle at 2000s, 0.349631mm for worst case acceleration, 0.103885mm for stabilised maximum take off (MTO) at 4000s, 0.586374mm for stabilised idle at 6000s and 0.271867mm for stabilised cruise clearance. Other data can be assessed from appendix 5.1 through to 5.5.

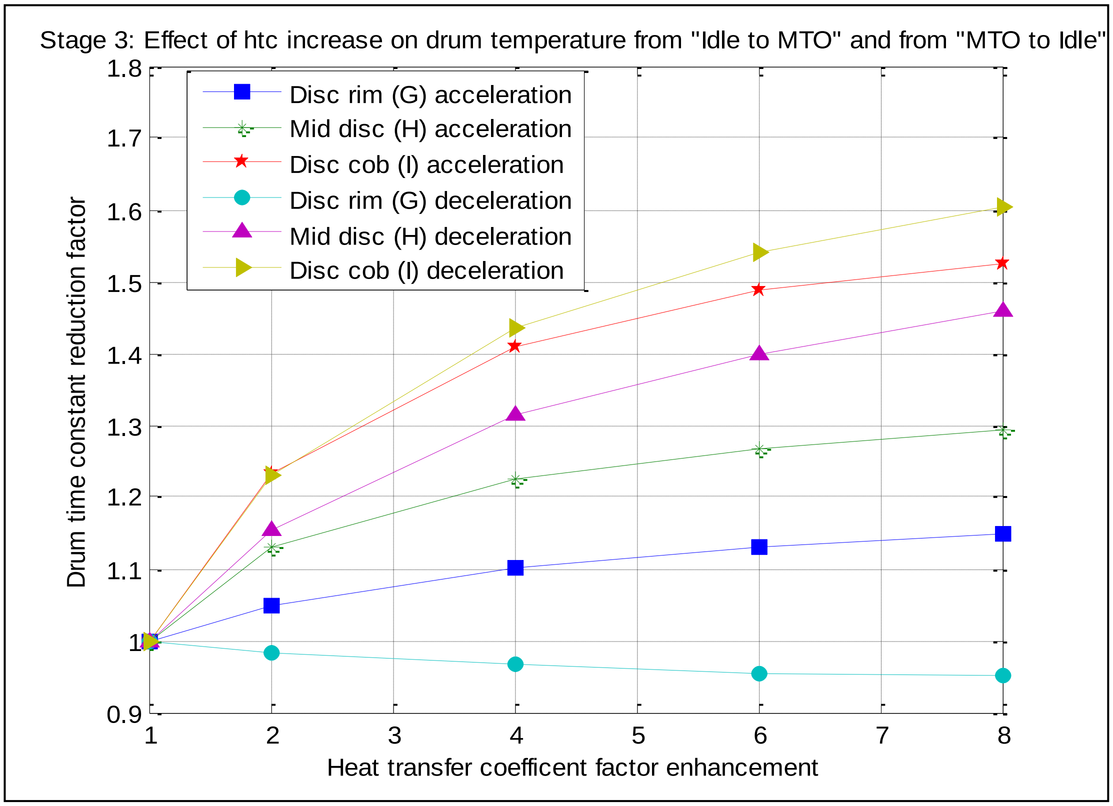

Figure 5.13: The variation of drum time constant reduction factor with heat transfer coefficient for temperature during acceleration from "Idle to MTO" and deceleration from "MTO to Idle" over a square cycle for the Trent 1000 HP compressor stage 3 drum and casing models at disc rim, mid disc and disc cob without radial inflow

Figure 5.14 shows the variation of drum time constant reduction factor with heat transfer coefficient during transient operation. As the heat transfer coefficient in the drum cavity is increased, the time constant reduction factor is higher for the disc cob and the mid disc than the disc rim due to thermal expansion and centrifugal acceleration; hence higher deflections. The disc rim gives a lower deflection due to the engine architecture around the rim region, which does not permit easy movement, making it rigid. The overall benefit of the reduction in the temperature and the displacement time constant of the drum are illustrated in the closure and clearance characteristics plots in Figures 5.14 and 5.15 respectively.

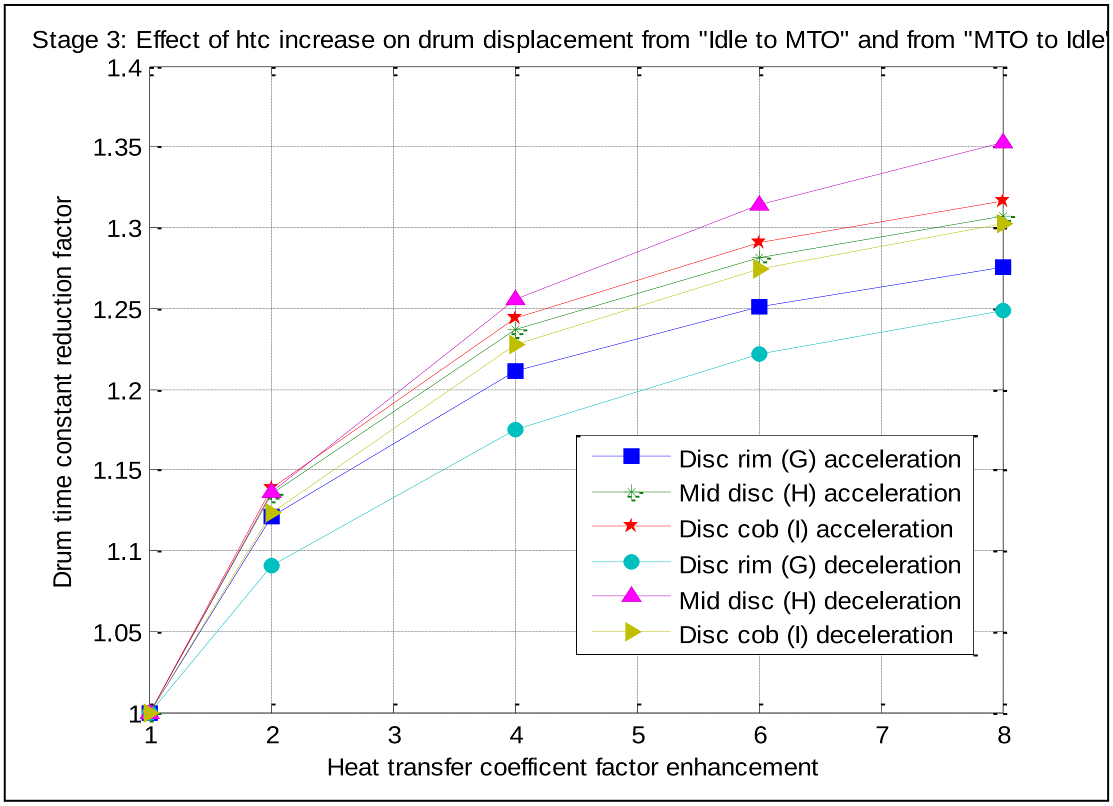

Figure 5.14: The variation of drum time constant reduction factor with heat transfer coefficient for displacement during acceleration from "Idle to MTO" and deceleration from "MTO to Idle" over a square cycle for the Trent 1000 HP compressor stage 3 drum and casing models at disc rim, mid disc and disc cob without radial inflow

Figure 5.15 shows closure as a function of time over the square cycle for the Trent 1000 stage three engine compressor drum and casing models. The casing is heated during transient periods to increase its diameter relative to the blade tip; resulting in a reduction in the tip closure. As the heat transfer coefficient is increased, the gap between the casing and the blade tip keeps reducing due to thermal expansion of the casing and the centrifugal acceleration associated with the drum. The closure plots show approximately 7%, 13%,15% and 17% reductions in closure at worst case acceleration (max take off overshoot), and 0.4 %, 1.3 %, 2% and 2.5% reductions in closure at stabilised cruise for heat transfer coefficient increases of 2, 4, 6 and 8 respectively from the baseline plot as shown in Table 5.6. Table 5.6 illustrates the closure reduction factor as a percentage of the nominal gap between the rotor blade tip and the casing for stage 3 baseline model (without radial inflow).

Stage 3 closures as percentage (%) increase or decrease of the nominal gap for baseline model (without radial inflow)					
htc increase factor	Stabilised Idle	Worst case acceleration	Stabilised MTO	Stabilised Idle	Stabilised cruise
Nominal	n/a	n/a	n/a	n/a	n/a
2	-0.2	7.0	0.0	0.0	0.4
4	-0.6	12.8	0.4	0.4	1.3
6	-1.1	15.3	0.8	0.7	2.0
8	-1.4	17.0	1.0	1.1	2.5

Table 5.6: Stage 3 closures as percentage (%) increase or decrease of the nominal gap for baseline model (without radial inflow)

The small percentage reduction in closure shows a significant effect on blade tip clearance as illustrated in Figure 5.16. The closure characteristics for the baseline (nominal) case, heat transfer coefficient increase factor (htc) of 2 and 8 are presented for clarity.

Increasing the heat transfer coefficient with a factor of 8, the stage 3 closure will be reduced the closure at worst case acceleration by 17% and 25% at stabilised cruise respectively. The small percentage reduction in closure here will show a significant effect on clearance when added to the cold build clearance (CBC).

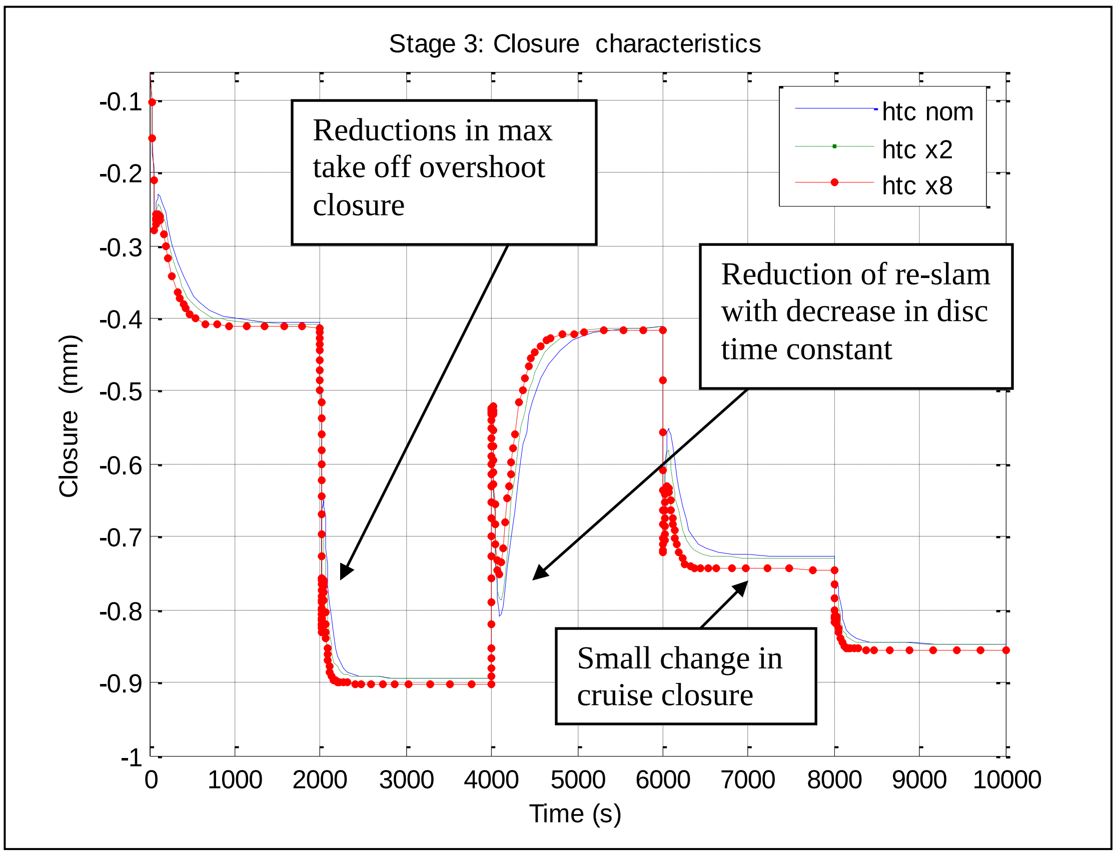

Figure 5.15: The variation of closure with time over the square cycle for the Trent 1000 HP compressor stage 3 drum and casing models as a function of heat transfer coefficient without radial inflow

Figure 5.16 shows the variation of clearance with time over the square cycle for the Trent 1000 HP compressor stage 3 drum and casing model. The casing is heated during transient periods to increase its diameter relative to the blade tip; resulting in a reduction in the cold tip clearance and consequently providing a steady state running clearance. The small percentage reduction in closure shows a significant effect on blade tip clearance with approximately 20%, 35%, 43% and 47% reductions in clearance at worst case acceleration (max take off overshoot), and 10 %, 18 %, 24% and 27% reductions in clearance at stabilised cruise for heat transfer coefficient increases of 2, 4, 6 and 8 respectively from the baseline plot, as shown in Table 5.7. Table 5.7 illustrates the clearance reduction factor as a percentage of the nominal gap between the rotor blade tip and the casing for stage 3 baseline model (without radial inflow).

Stage 3 clearances as percentage (%) reduction of the nominal gap for baseline model (without radial inflow)					
htc increase factor	Stabilised Idle	Worst case acceleration	Stabilised MTO	Stabilised Idle	Stabilised cruise
Nominal	n/a	n/a	n/a	n/a	n/a
2	4.0	19.3	22.0	4.0	9.4
4	7.1	35.0	42.0	7.0	18.1
6	9.1	43.0	54.0	9.0	24.0
8	10.1	47.0	61.0	10.0	27.0

Table 5.7: Stage 3 clearances as percentage (%) of the nominal gap for baseline model (without radial inflow)

The analysis shows an overall reduction in tip clearance throughout the engine cycle with an increase in the heat transfer coefficient due to reduction in reslam characteristics; hence a reduction in drum time constant.

In conclusion, a better tip clearance control can be achieved by reducing the high pressure compressor (HPC) drum time constant. The drum time constant can be reduced by introducing a factor to the inbuilt heat transfer coefficient of the drum to enhance heat transfer in the cavity. Increasing the thermal response of the high pressure compressor (HPC) drum will reduce the reslam characteristics of the drum, therefore reducing the cold build clearance (CBC) and hence the reduction in cruise clearance.

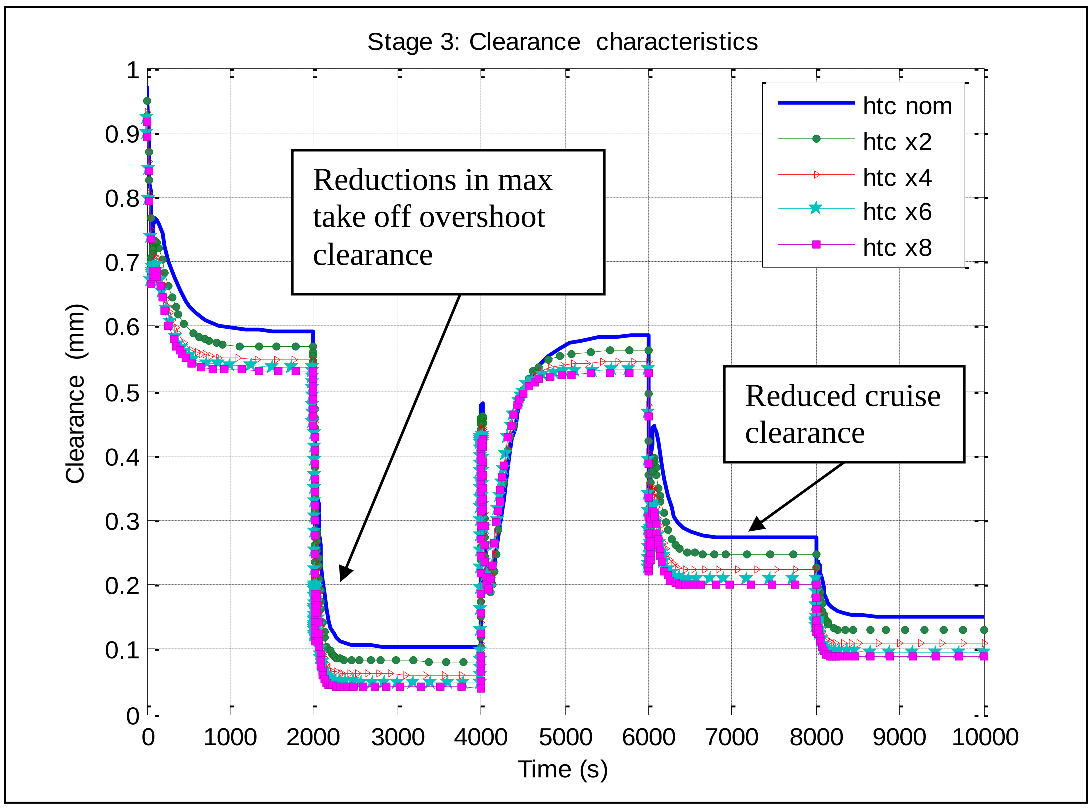

Figure 5.16: The variation of clearance with time over the square cycle for the Trent 1000 HP compressor stage 3 drum and casing model as a function of heat transfer coefficient without radial inflow

Other methods that could be to enhance heat transfer are the use of radial inflow in the cavity, the used of plain fin surfaces to increase the effective heat transfer surface, increasing the heat transfer coefficient without appreciably changing heat transfer area by using the used of wavy or corrugated channels to provide mixing, and the use of interrupted fins to increase both the heat transfer coefficient and the heat transfer area Stone (1996).

A further reduction in clearance can be achieved by introducing radial inflow into the drum cavity to further increase the disc heat transfer coefficient in the cavity; hence a further reduction in disc drum time constant. The result of a further reduction due to the introduction of radial inflow is presented in Section 5.5

5.5 Radial inflow analysis

Radial inflow is the bleed air from the compressor core flow which is ducted into the drum cavity to improve heat transfer in the cavity. The introduction of the radial inflow into the drum cavity will increase the heat transfer coefficient in the cavity; hence a reduction in drum time constant. By introducing radial inflow into the cavity, a further increase of the heat transfer coefficient of the disc is achieved and hence a further reduction in the disc time constant. The speedy thermal response of the drum during transient, caused by the radial inflow in the cavity, results in the reduction of the tip clearance between the rotating blade and the stationary casing in the HP compressor; hence a better tip clearance control.

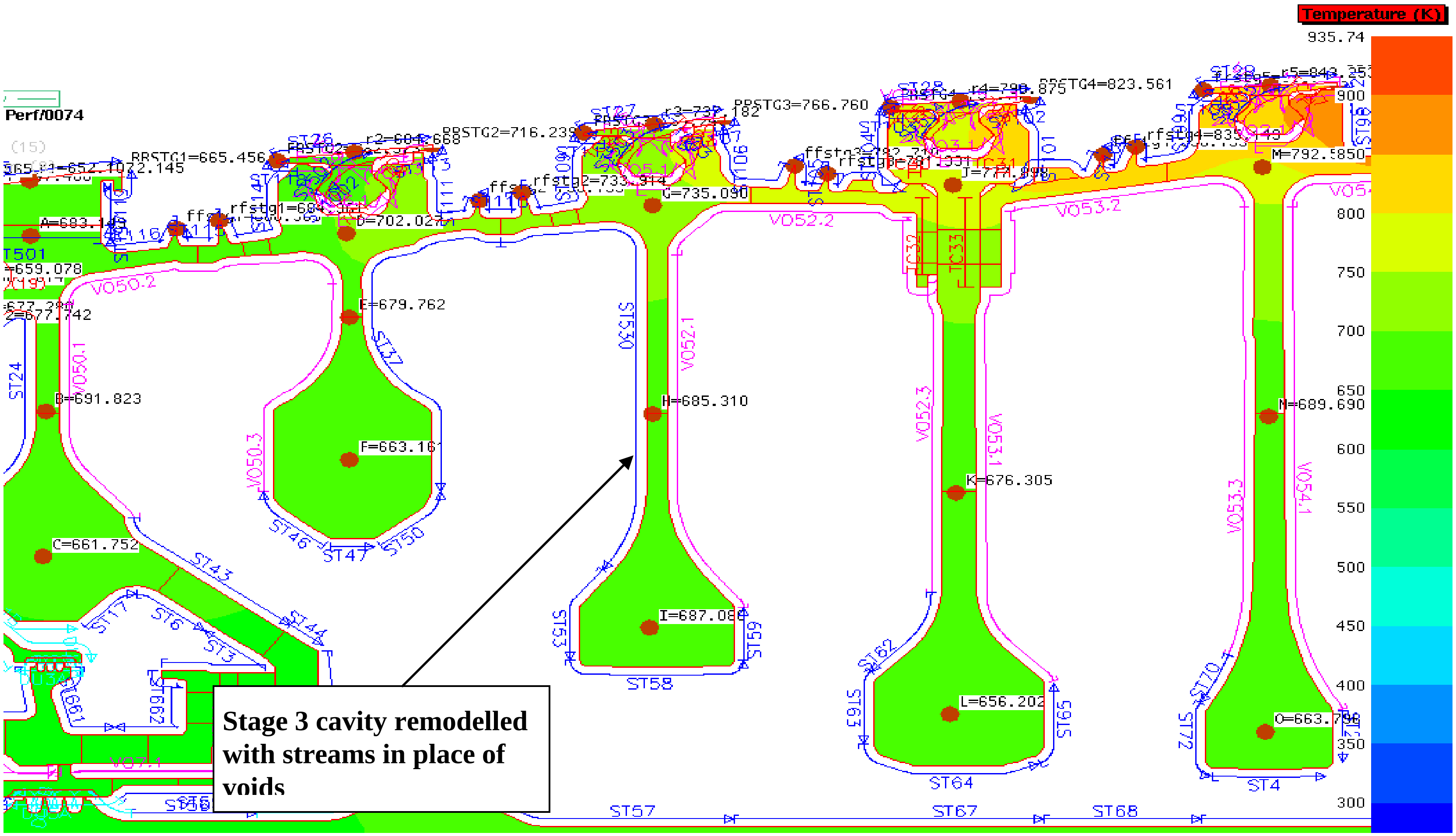

Figure 5.17: Stage 3 Trent 1000 HP compressor drum cavity model remodelled with streams in place of the voids with radial inflow

The drum cavity of stage 3 was remodelled to allow for a finite flow of fluid in the cavity. This was performed by replacing the voids in the cavity with streams, and a radial inflow of fluid was supplied and ducted into the cavity as shown in Figure 5.17. Stage 3 was used since it has approximately the same geometry dimension as the MCR that is used to demonstrate a proof of the concept. The first analysis was carried out by increasing the heat transfer coefficient with an increased factor of 2, 4, 6 and 8.

The second analysis was based on the pre-test computational fluid dynamics (CFD) results carried out in Thermo-Fluid Mechanics Research Centre (TFMRC) by Dr. Atkins as part of the wider NEWAC research project, which show that if approximately 6% of bore mass flow is introduced into the drum cavity with a heat transfer of 150 W/m^{2}k, it is capable of reducing the stabilised cruise clearance by approximately 30%. Figure 5.17 shows the stage 3 Trent 1000 HP compressor drum cavity model remodelled with streams in place of the voids. 6% of the bore mass flow was introduced into the cavity as radial inflow to increase the heat transfer in the drum cavity.

Figure 5.18 shows the variation of blade thermal growth with time over the square cycle for a model with radial inflow. The growth characteristics were obtained by introducing a radial inflow of 6% bore mass flow into the drum cavity, and analysis was performed in the same way as in Section 5.4.1.

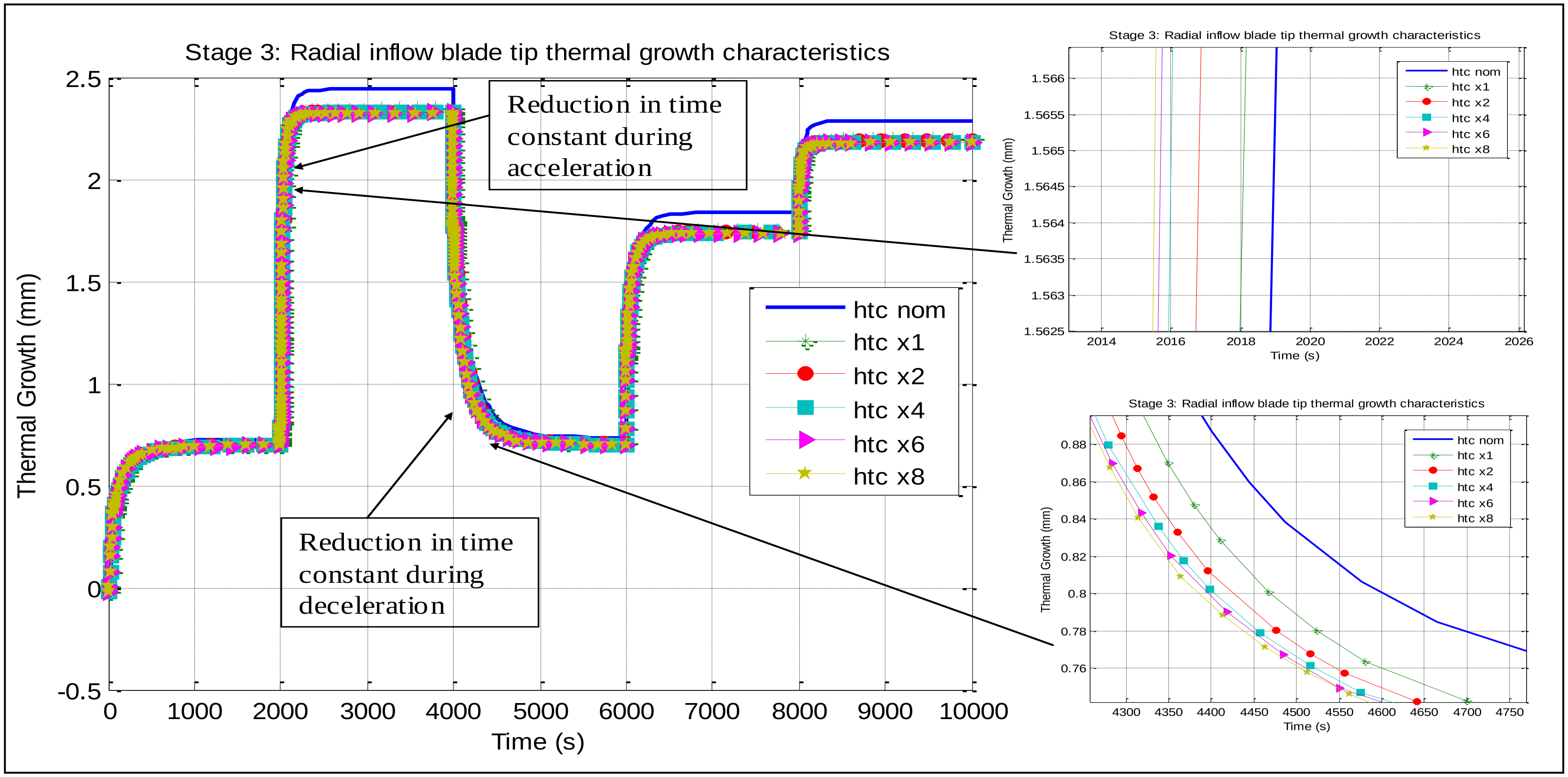

Figure 5.18: The variation of rotor blade thermal growth with time over the square cycle for the Trent 1000 HP compressor stage 3 drum and casing models with radial inflow showing effect of heat transfer coefficient increase on blade tip time constant (τ) with radial inflow. The Figures on the right, top and bottom are the zoom-in sections of acceleration and deceleration section during engine transient

In Figure 5.18, there is a further fast response time constant of the blade during acceleration and a further contraction during deceleration due to introduction of radial inflow into the drum cavity. The evidence can be seen in the zoom sections of acceleration and deceleration of Figure 5.11. The confirmation of the response time can be seen in the comparison of blade tip reduction factor for model with and without radial inflow of Figure 5.19. This resulted in an increased heat transfer in the cavity and hence a further reduction in closure characteristics throughout the cycle, with a significant effect on cruise, as would be shown in the cruise clearance plots.

Figure 5.19 shows the variation of blade tip time constant reduction factor with heat transfer coefficient during engine transient operation. The introduction of radial inflow introduction into the cavity further increased heat transfer in the drum cavity; hence a further reduction in drum time constant. This gave a higher blade tip time constant reduction factor due to a further fast thermal response of the drum, resulting from more mass flow, high fluid temperature, high thermal expansion and centrifugal acceleration associated with the disc in the cavity.

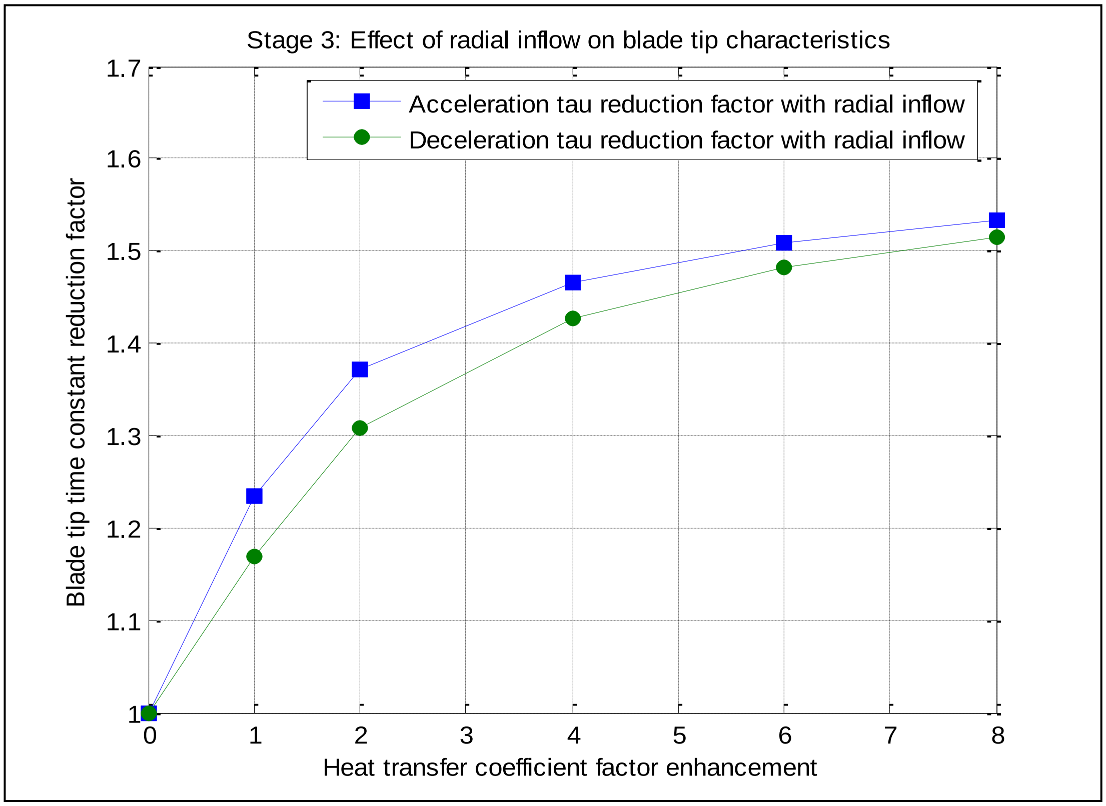

Figure 5.19: The variation of blade tip time constant reduction factor with heat transfer coefficient during acceleration from "Idle to MTO" and deceleration from "MTO to Idle" over a square cycle for the Trent 1000 HP compressor stage 3 drum and casing models with radial inflow

Figure 5.20 shows blade tip time reduction factor comparison plots for the model without radial inflow and the model with radial inflow. The result shows that the model with radial inflow has a higher time constant reduction factor. This gave a reduced clearance throughout the engine cycle when compared to the model without radial inflow; and hence a better reduction in tip clearance than the model without radial inflow as shown in Figure 5.24.

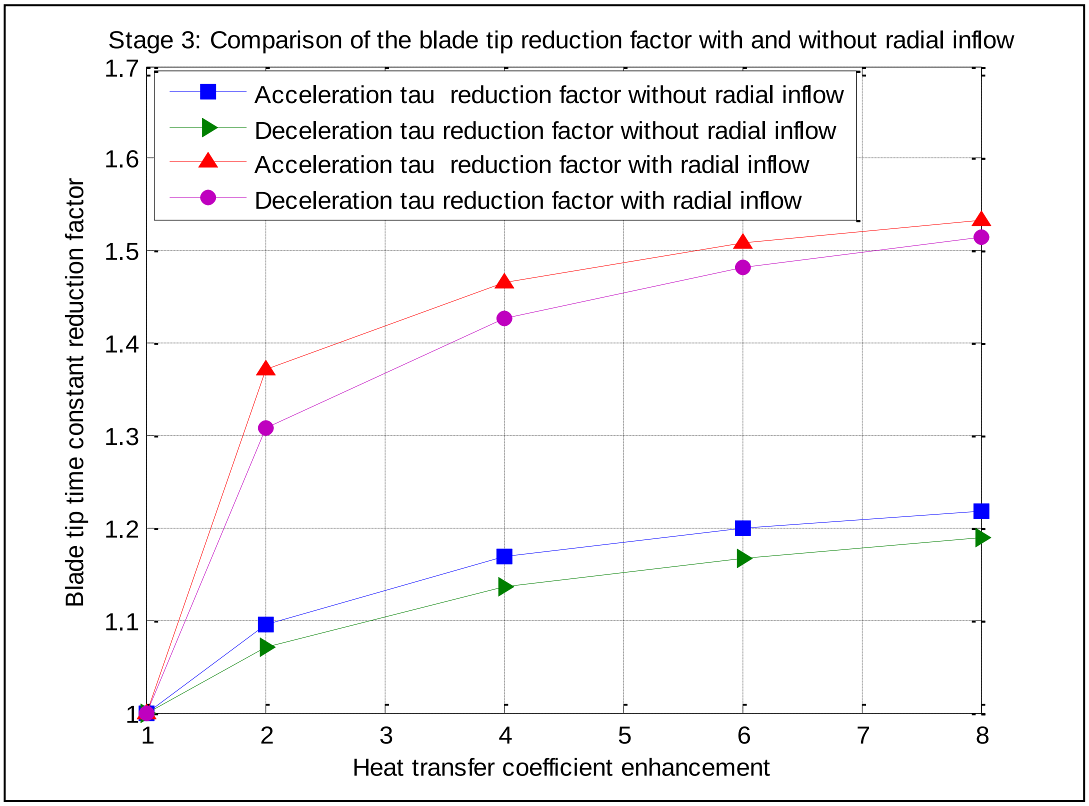

Figure 5.20: The rotor blade tip time constant reduction factor comparison during acceleration from "Idle to MTO" and deceleration from "MTO to Idle" over a square cycle for the Trent 1000 HP compressor stage 3 drum and casing models for the model without radial inflow and the model with radial inflow

Figure 5.21 shows the variation of drum time constant reduction factor with heat transfer coefficient during engine transient operation with radial inflow. By introducing radial inflow into the drum cavity, the heat transfer coefficient in the drum cavity is further increased, giving rise to a higher time constant reduction factor at the disc cob than at the mid disc and the disc rim due to centrifugal acceleration and more circulation of flow around the disc cob region. The disc rim gives a lower time constant because it tend to cool quicker than the mid disc and the disc cob due to the flow over it by secondary airflow, used to cool some components of the engine.

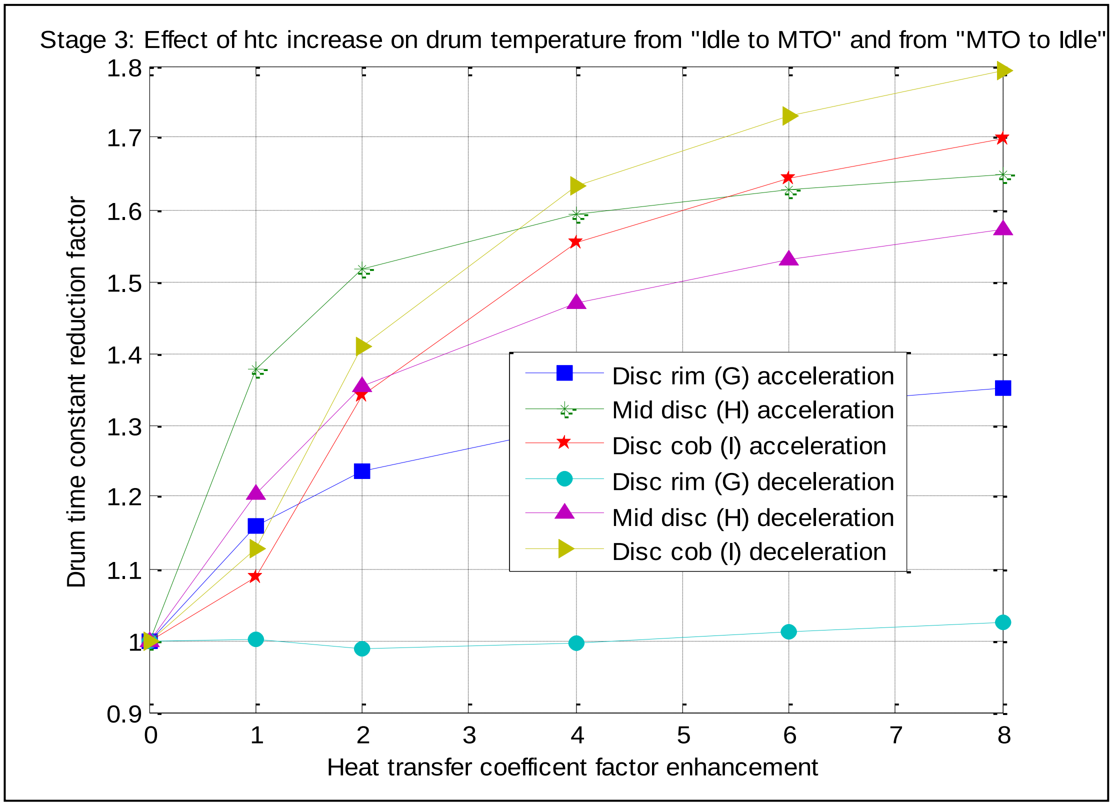

Figure 5.21: The variation of drum time constant reduction factor with heat transfer coefficient for temperature during acceleration from "Idle to MTO" and deceleration from "MTO to Idle" over a square cycle for the Trent 1000 HP compressor stage 3 drum and casing models at disc rim, mid disc and disc cob with radial inflow

Figure 5.22 shows the variation of drum time constant reduction factor with heat transfer coefficient during engine transient operation with radial inflow. As the heat transfer coefficient in the drum cavity is increased, the time constant reduction factor for the model with radial inflow becomes higher and higher for the disc cob and the mid disc than for the disc rim, due to thermal expansion, centrifugal acceleration and more circulation of flow around the disc cob region; hence the higher deflections when compared to the model without radial inflow. The disc rim gives a lower deflection due to the engine architecture around the rim region which does not permit easy movement, making it rigid. The overall benefit of the reduction in temperature and the displacement time constant of the drum with radial inflow is illustrated in the closure and clearance characteristics plots in Figures 5.23 and 5.24 respectively.

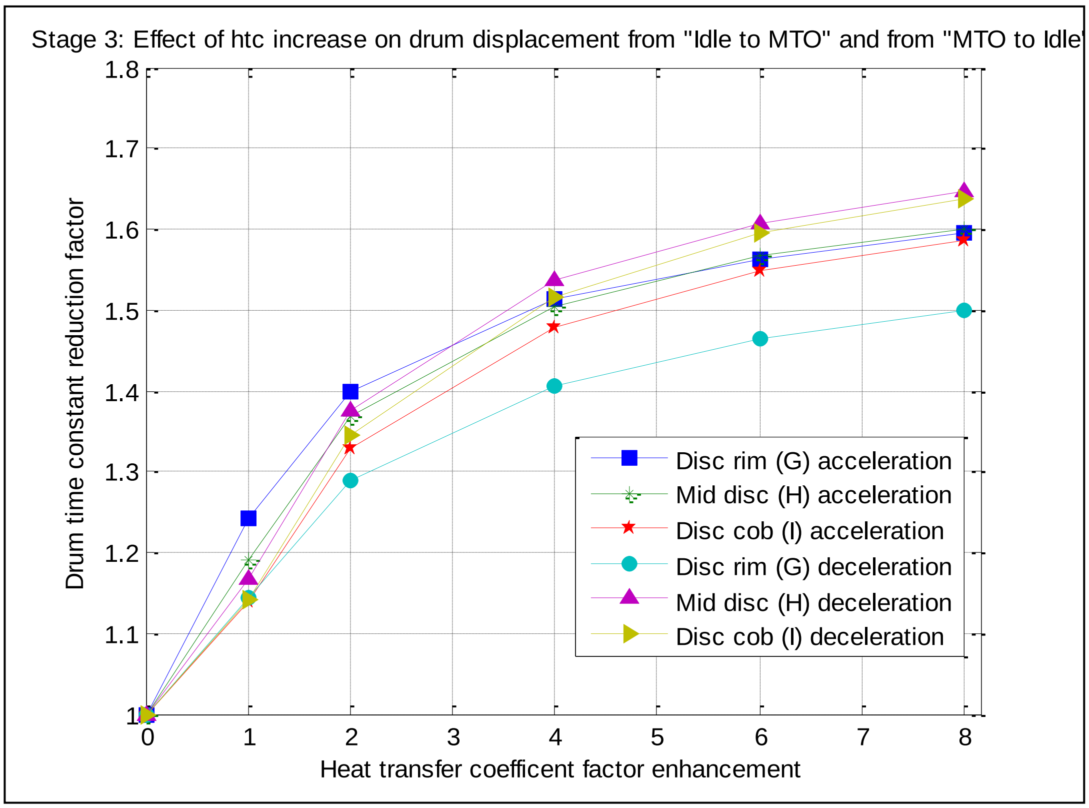

Figure 5.22: The variation of drum time constant reduction factor with heat transfer coefficient for displacement during acceleration from “Idle to MTO” and deceleration from “MTO to Idle” over a square cycle for the Trent 1000 HP compressor stage 3 drum and casing models at disc rim, mid disc and disc cob with radial inflow

Figure 5.23 shows closure as a function of time over the square cycle for the Trent 1000 stage 3 engine compressor drum and casing models with radial inflow. The casing is heated during transient periods to increase its diameter relative to the blade tip, resulting in a reduction in the tip closure. With the introduction of radial inflow into the drum cavity, the heat transfer coefficient is further increased giving rise to reduced reslam characteristics with a large cruise closure.

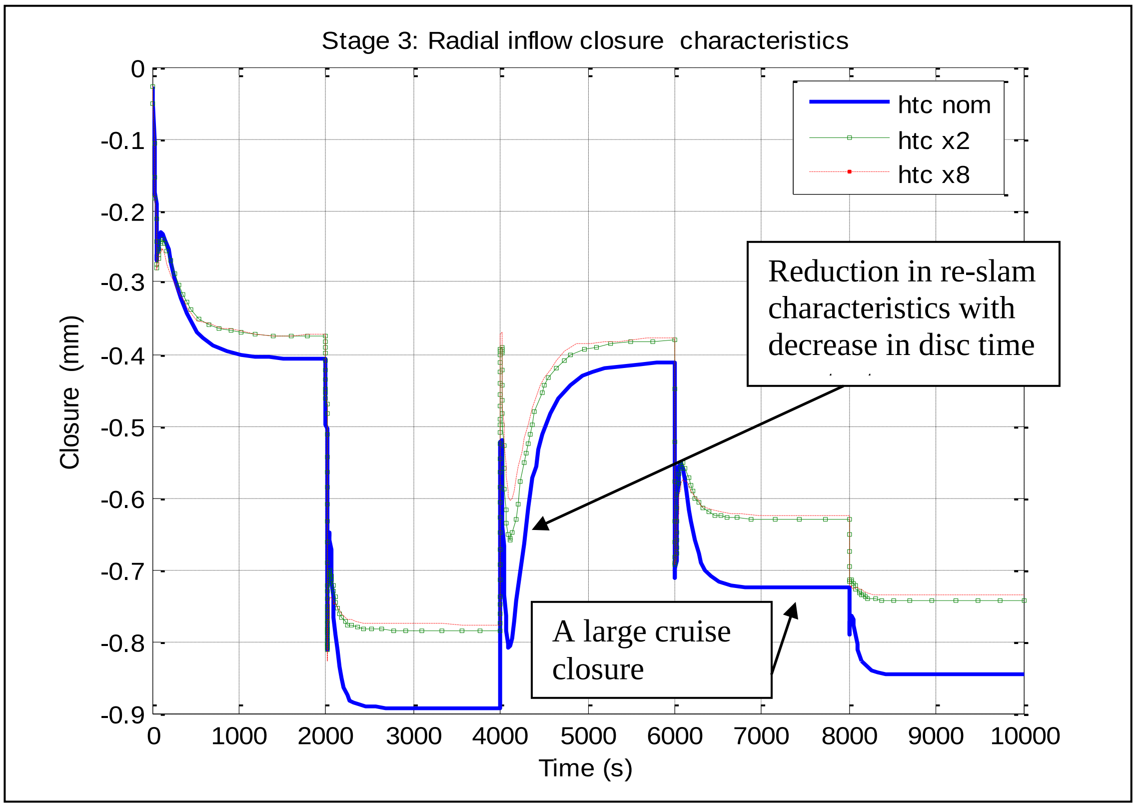

Figure 5.23: The variation of closure with time over the square cycle for the Trent 1000 HP compressor stage 3 drum and casing models as a function of heat transfer coefficient with radial inflow

Table 5.8 shows Stage 3 closures as percentage (%) increase or decrease of the nominal gap for model with radial inflow.

Stage 3 closures as percentage (%) the nominal gap for model with radial inflow					
htc increase factor	Stabilised Idle	Worst case acceleration	Stabilised MTO	Stabilised Idle	Stabilised cruise
Nominal	n/a	n/a	n/a	n/a	n/a
1	7.02	-2.35	11.00	6.80	11.87
2	7.65	-8.26	12.10	7.41	13.07
4	8.12	-12.08	12.77	8.00	13.70
6	8.40	-13.40	13.01	8.26	13.92
8	8.45	-13.97	13.14	8.52	14.00

Table 5.8: Stage 3 closures as percentage (%) increase or decrease of the nominal gap for model with radial inflow

The closure plots show approximately 2% 8%, 12%,13% and 14% decrease in closure at worst case acceleration (max take off overshoot), and 12%, 13 %, 14%, 14% and 14% increase in closure at stabilised cruise for the heat transfer coefficient increases of 1, 2, 4, 6 and 8 respectively from the baseline data. The large percentage increase in closure at stabilised cruise shows a significant effect on blade tip clearance, as illustrated in Figure 5.24. Table 5.9 illustrates clearance reduction factor as percentage of the nominal gap between the rotor blade tip and the casing for stage 3 with radial inflow.

Stage 3 clearances as percentage (%) reduction of the nominal gap for model with radial inflow					
htc increase factor	Stabilised Idle	Worst case acceleration (Max take off overshoot)	Stabilised max take off (MTO)	Stabilised Idle	Stabilised cruise
Nominal	n/a	n/a	n/a	n/a	n/a
1	12	33	3	13	6
2	19	56	32	19	17
4	23	70	51	23	25
6	25	77	63	25	30
8	26	80	70	26	33

Table 5.9: Stage 3 clearances as percentage (%) of the nominal gap for model with radial inflow

Figure 5.24 shows clearance as a function of time over the square cycle for the Trent 1000 HP compressor stage 3 drum and casing model. The casing is heated during transient periods to increase its diameter relative to the blade tip, resulting in a reduction in the cold tip clearance and consequently providing a steady state running clearance. The small percentage increase in closure shows a significant effect on blade tip clearance with approximately 33%, 56%, 70%, 77% and 80% reductions in clearance at worst case acceleration (max take off overshoot), and 6%, 17 %, 25 %, 30% and 33% reductions in clearance at stabilised cruise for heat transfer coefficient increases of 1, 2, 4, 6 and 8 respectively from the baseline plot, as shown in Table 5.6 and represented graphically in Figure 5.25 and Figure 5.26 respectively. The nominal clearance data can be

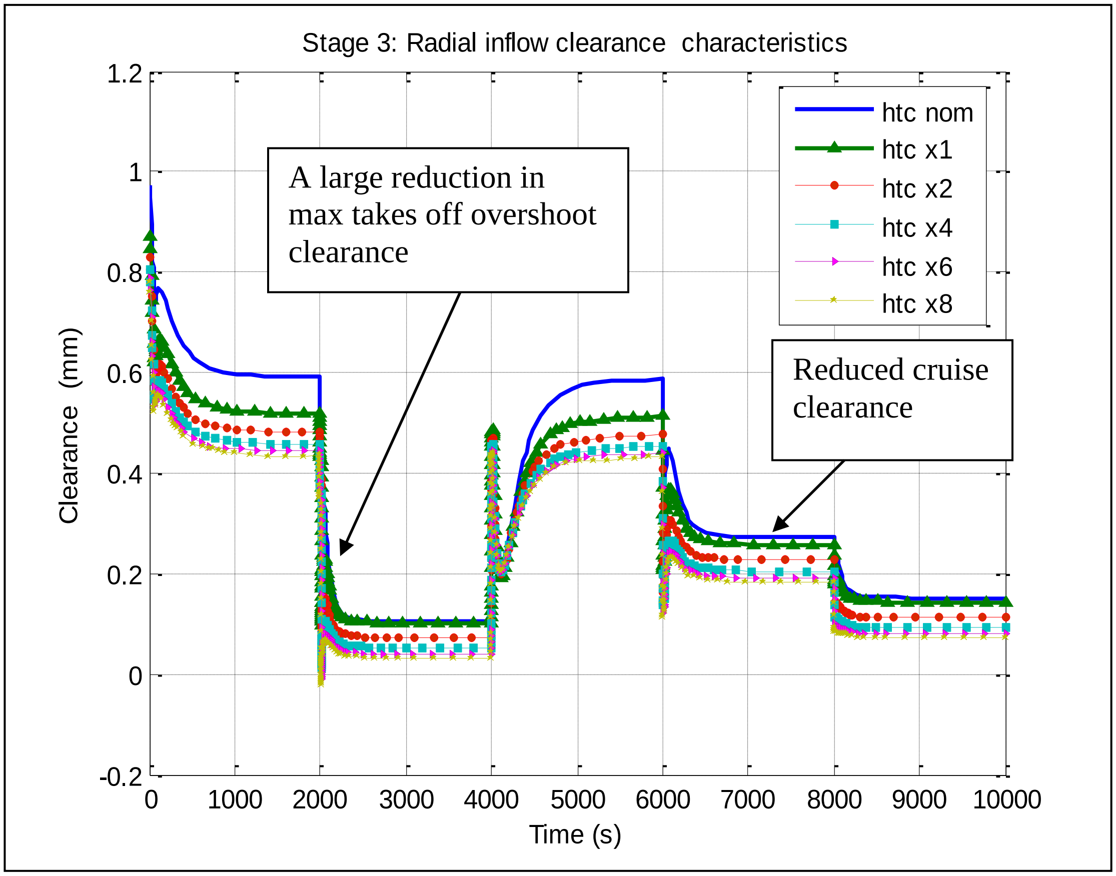

Figure 5.24: The variation of clearance with time over the square cycle for the Trent 1000 HP compressor stage 3 drum and casing model as a function of heat transfer coefficient with radial inflow

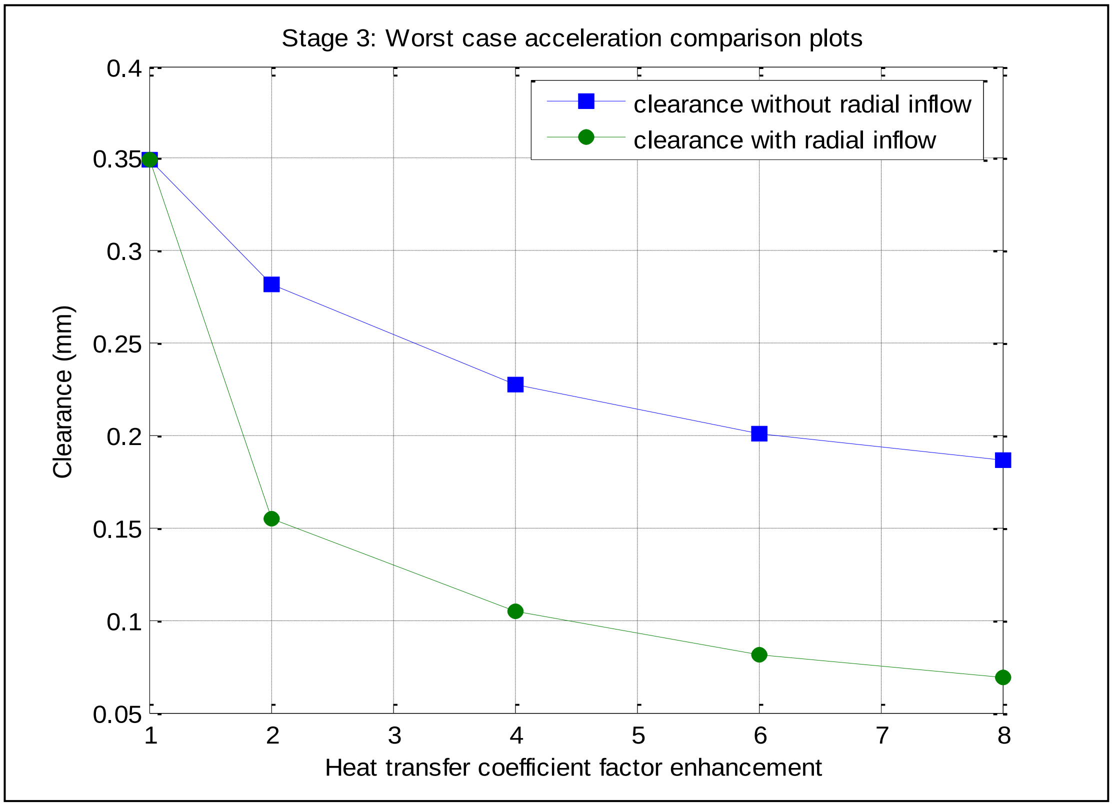

Figure 5.25: The comparison of the worst case acceleration clearance for Trent 1000 HP compressor stage 3 drum and casing model as a function of heat transfer coefficient with radial inflow and without radial inflow

The overall effect of reduction at worst case acceleration as shown in Figure 5.26 is the reduction in surge occurrence during engine transient.

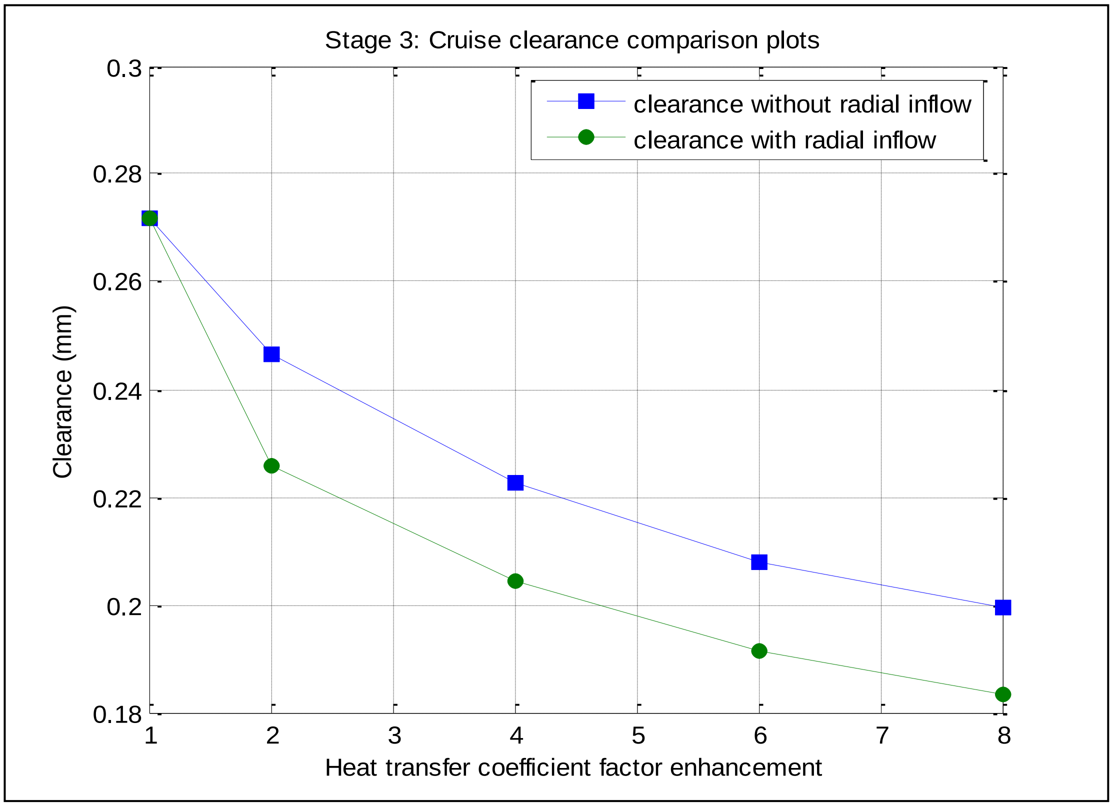

Figure 5.26: The comparison of stabilised cruise clearance for Trent 1000 HP compressor stage 3 drum and casing model as a function of heat transfer coefficient with radial inflow and without radial inflow

The results of the sensitivity analysis and its benefit are summarised using Figure 5.27, Figure 5.28 and Figure 5.29. Figure 5.27 shows the clearance comparison plots for the model without radial inflow and the model with radial inflow for the nominal case. The result shows that the model with radial inflow has a reduced clearance at worst case acceleration (maximum take off overshoot) and stabilised cruise clearance. It also indicates that there is a reduction throughout the engine cycle when compared to the model without radial inflow. At worst case acceleration, the model with radial inflow is capable reducing tip approximately 56% calculated against the baseline data. Figure 5.28

shows the zoom section of the worst case clearance comparison plots for the models without radial inflow and the model with radial inflow for the nominal case.

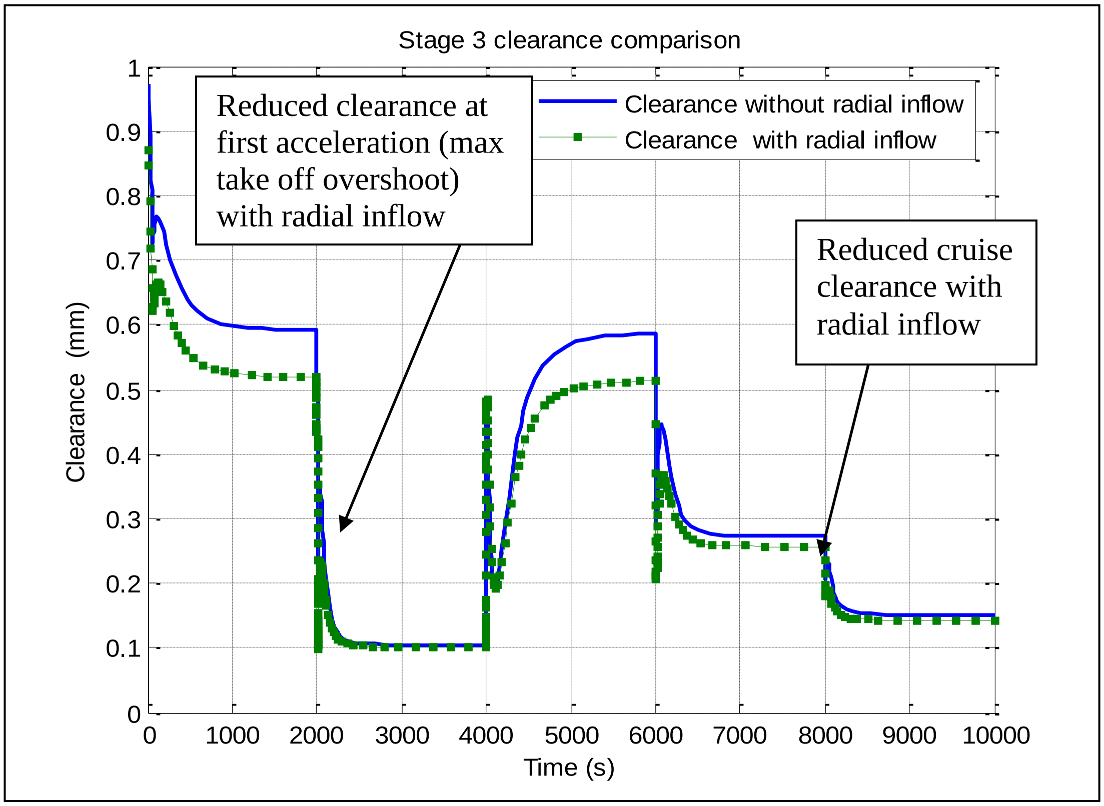

Figure 5.27: The comparison of clearance for the Trent 1000 HP compressor stage 3 drum and casing models for model without radial inflow and the model with radial inflow for the nominal case

Figure 5.29 shows the cruise clearance comparison plots for the model without radial inflow and the model with radial inflow for the nominal case. The result shows that the model with radial inflow has a reduced clearance at stabilised cruise throughout the engine cycle when compared to the model without radial inflow. At cruise clearance, the model with radial inflow is capable reducing tip by approximately 17% calculated against the baseline data. Figure 5.29 shows the zoom section of the stabilised clearance comparison plots for the models without radial inflow and the model with radial inflow for the nominal case.

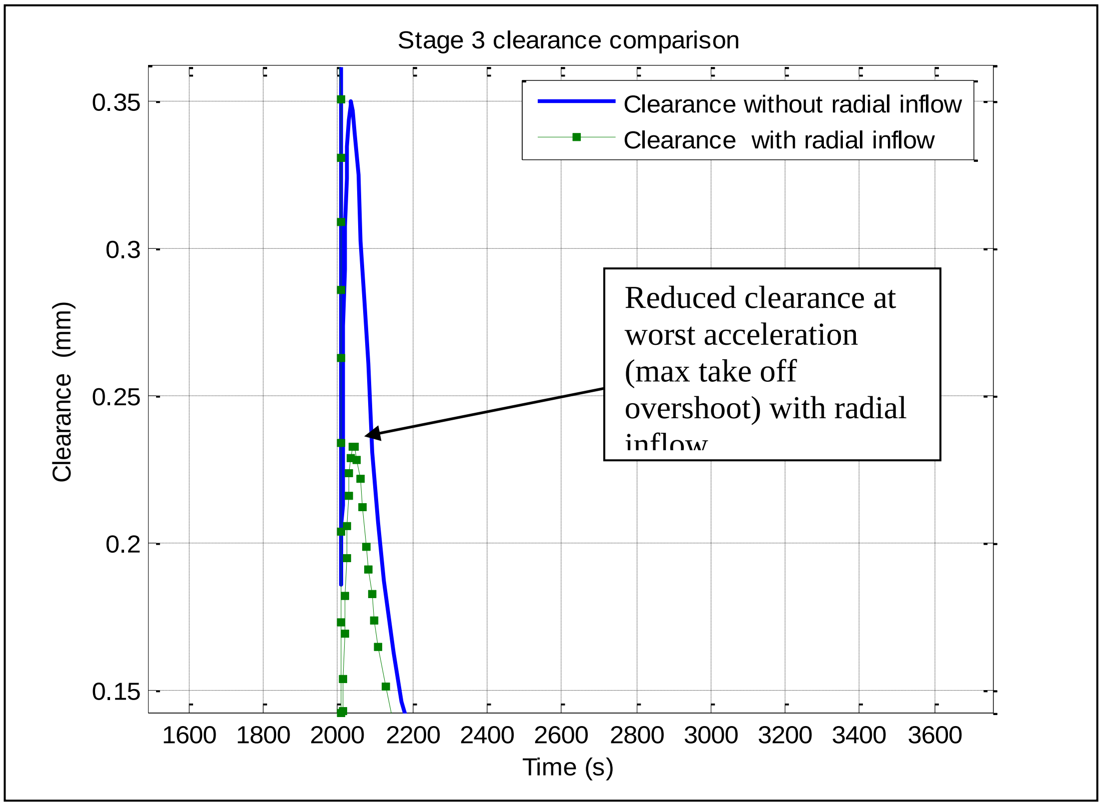

Figure 5.28: The zoom section of the worst case acceleration clearance comparison plots for the models without radial inflow and the model with radial inflow for the nominal case

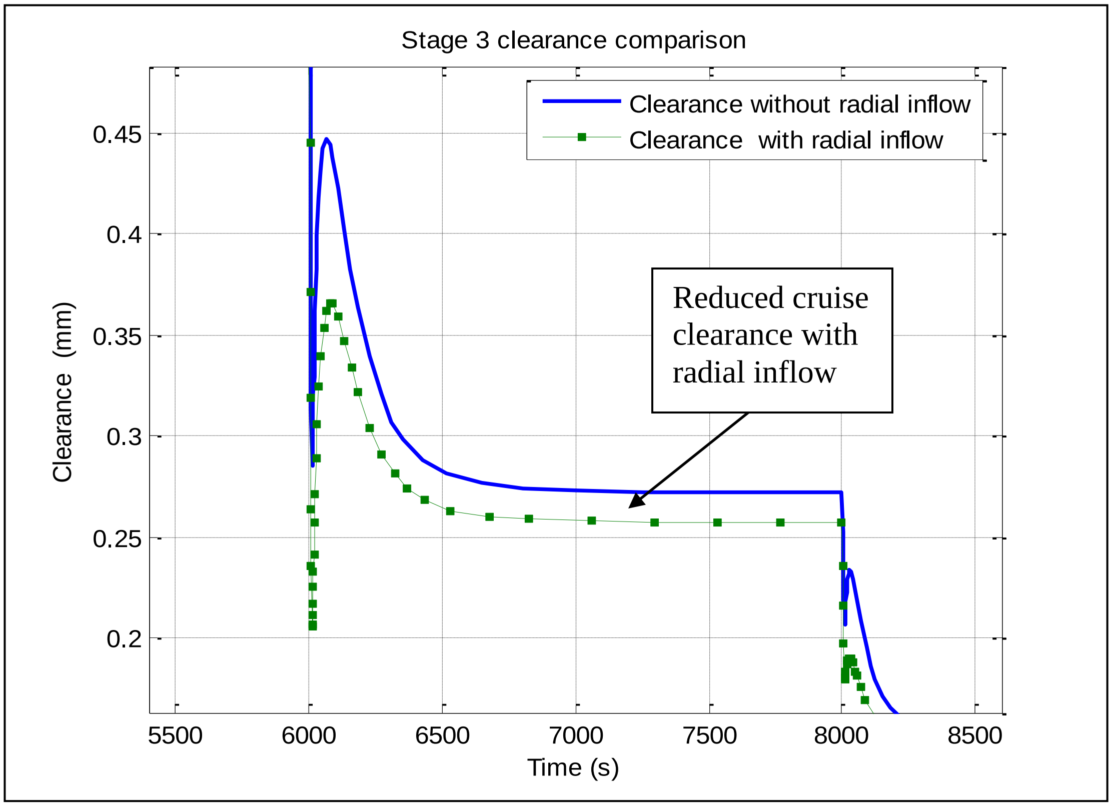

Figure 5.29: The zoom section of the stabilised cruise clearance comparison plots for the model without radial inflow and the model with radial inflow for the nominal case

The overall result shows that an increase in heat transfer coefficient in the cavity would increase the thermal response of the high pressure compressor (HPC) drum and this will reduce the reslam characteristics of the drum, hence the reduction in cruise clearance throughout the engine cycle for all the six stages. However, the reduction is small but can be enhanced with the introduction of radial inflow into the cavity of the drum to improve the heat transfer in the cavity. Figure 5.30 shows the stabilised cruise clearance reduction characteristics against heat transfer coefficient increase factor for all of the six stages.

The overall effect of reduction in cruise clearance for all the six stages is the improvement in engine efficiency, reduction in the specific fuel consumption (sfc) and hence reduction in the overall cost of operation of the engine by its operator.

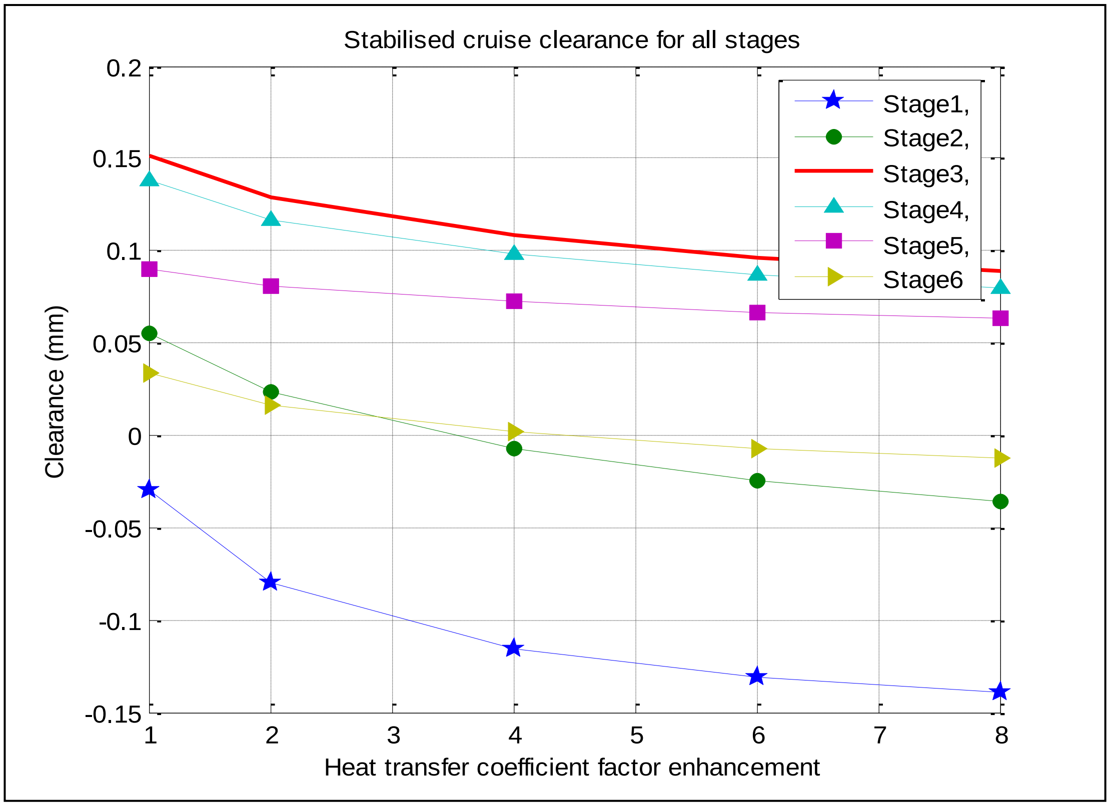

Figure 5.30: Stabilised cruise clearance against heat transfer coefficient increase factor for all of the six stages

5.5.1 Radial inflow analysis based on Pre-test CFD result

The Trent 1000 drum model was remodelled with streams instead of voids as illustrated in Section 5.5, with modification in the value of the heat transfer coefficient used. The inbuilt heat transfer coefficient in the cavity was replaced with specific heat transfer coefficient values of 50W/ (m^2K), 100 W/ (m^2K) and 150W/ (m^2K). Table 5.10 illustrates the clearance reduction factor as a percentage of the nominal gap between the rotor blade tip and the casing with specific heat transfer coefficient of values of 50W/ (m^2K), 100 W/ (m^2K) and 150W/ (m^2K). The heat transfer coefficient values were based on a pre-test computational fluid dynamic analysis (CFD) carried out as part of the wider NEWAC programme by Dr. Nick Atkins which shows that approximately 30% reduction in cruise clearance can be obtained using 6% radial inflow with an associated heat transfer coefficient of 150 W/ (m^2K). The nominal stabilised clearance used is 0.271867mm.

Clearance reduction (% of nominal gap) with specific heat transfer coefficient					
htc in cavity (streams)	Stab. IDLE	Worst case acceleration	Stab. MTO	Stab ILDE	Stab. cruise
Nominal	n/a	n/a	n/a	n/a	n/a
50	-3.9	-10.2	45.6	-4.3	13.4
100	-2.3	-4.2	58.4	-2.7	18.2
150	-1.3	0.4	66.7	-1.7	21.1

Table 5.10: Clearance reduction factor as percentage (%) of the nominal gap with specific heat transfer coefficient (50W/ (m^2K), 100W/ (m^2K) and 150 W/ (m^2K))

Figure 5.31 shows radial inflow closure as a function of time over the square cycle for the Trent 1000 HP compressor stage 3 drum and casing models with specific values of heat transfer coefficient of 50W/(m^2K), 100W/(m^2K) and 150 W/(m^2K). The analysis shows a reduction in reslam characteristics with the various heat transfer coefficient when compared to the baseline plot.

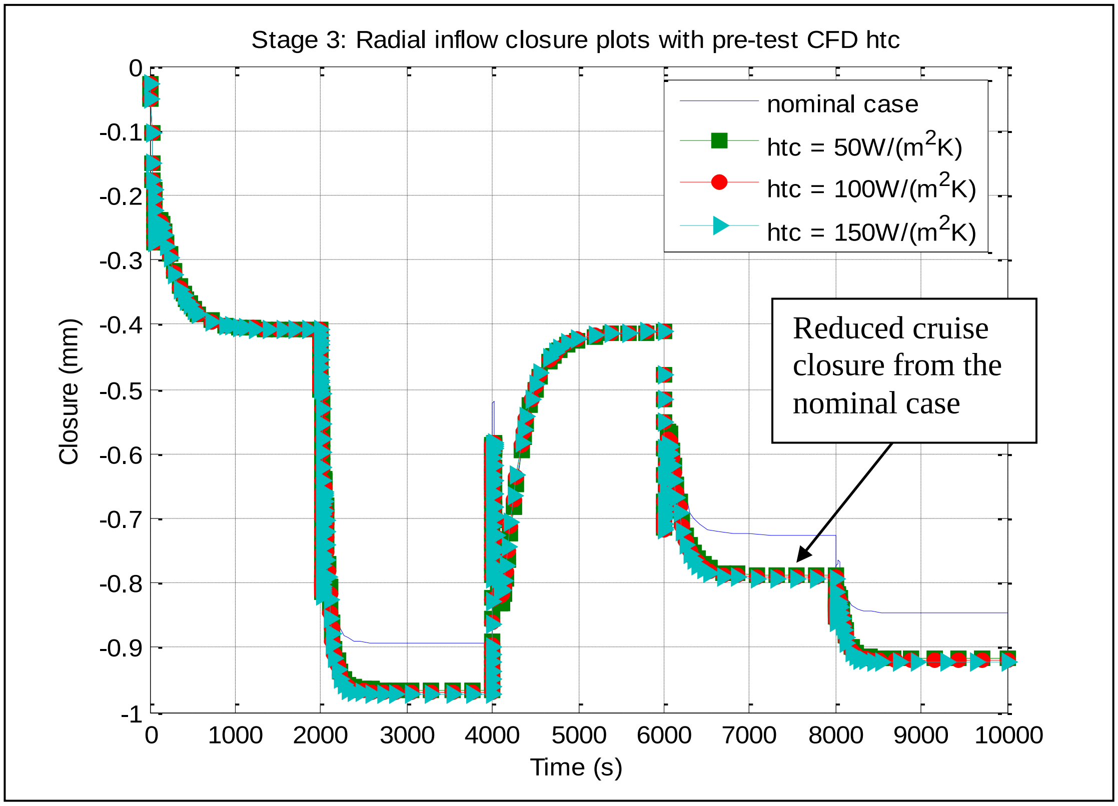

Figure 5.31: The variation of closure with time over the square cycle for the Trent 1000 HP compressor stage 3 drum and casing models as a function of specific heat transfer coefficient (50W/ (m^2K), 100W/ (m^2K) and 150 W/ (m^2K)) with radial inflow

The benefit of the reduction in reslam characteristics to the clearance is illustrated in the clearance plot of Figure 5.32. Figure 5.32 shows radial inflow clearance as a function of time over the square cycle for the Trent 1000 HP compressor stage 3 drum and casing models, with specific values of heat transfer coefficient. The results of the analysis indicate that it is possible to reduce the baseline cruise clearance by approximately 13%, 18% and 21% using heat transfer coefficients of 50W/(m^2K), 100W/(m^2K) and 150

W/(m^{2}K) respectively. The 21% reduction in cruise clearance with 150 W/(m^{2}K) is in good agreement with the pre-test CFD result of approximately 30% reduction in cruise clearance with 6% radial inflow with 150 W/(m^{2}K).

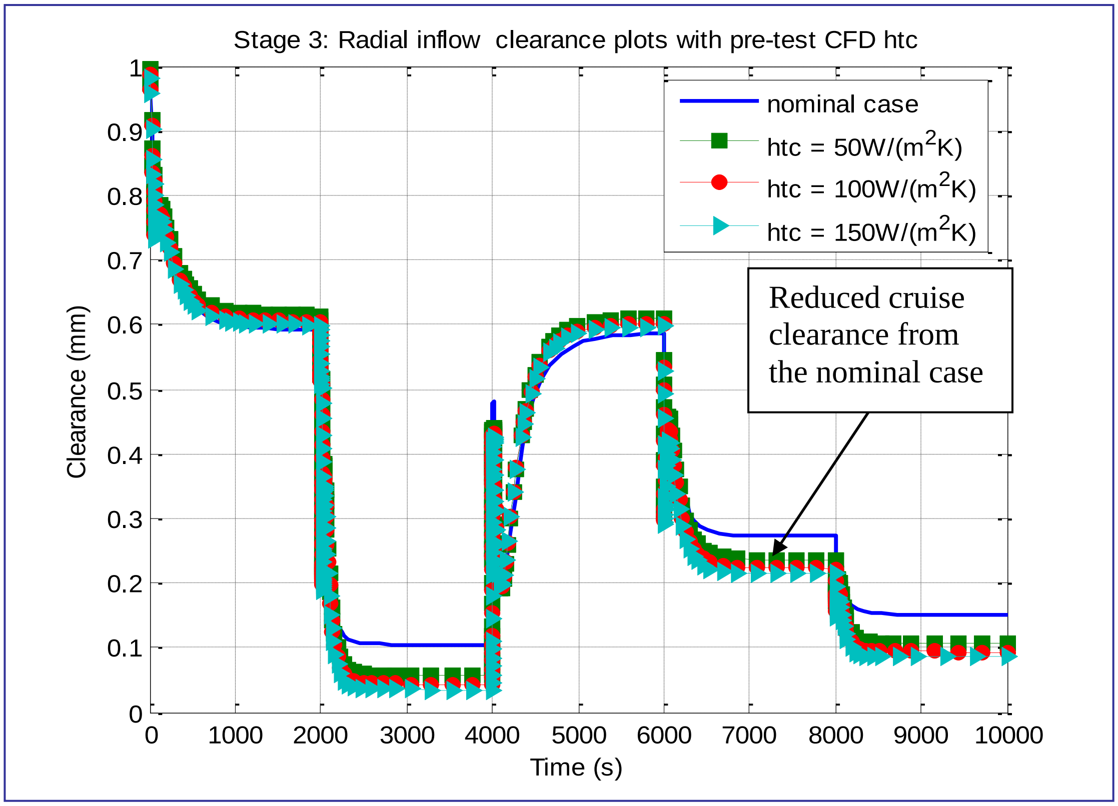

Figure 5.32: The variation of clearance with time over the square cycle for the Trent 1000 HP compressor stage 3 drum and casing models as a function of specific heat transfer coefficient (50W/ (m^{2}K), 100W/ (m^{2}K) and 150 W/ (m^{2}K)) with radial inflow

5.6: Summary

This chapter has reported on the sensitivity study of the of tip clearance control concepts using drum and casing models of two engines. These are RB211-524 and Trent 1000 models. The disc time constants are found to depend on the heat transfer coefficient of the disc. An increase in the heat transfer coefficient reduces the disc time constant. A reduction of the time constant for the rotor and an increase of the time constant for the casing is better for clearance and this is possible by increasing the heat transfer coefficients (htc) in the system.

The time constant analysis for the RB211-524 drum and casing model shows that a reduction in the rotor time constant reduces the re-slam characteristics. This will result in a reduced clearance throughout the cycle and vice versa. An increase in the casing time constant also reduces the re-slam characteristics giving rise to reduced clearance throughout the cycle and vice versa. Hence, a proper closure and clearance, requires the reduction in drum time constant with an increase in casing time constant.

The sensitivity study for Trent 1000 engine shows that, with 6% radial inflow, there are potential reductions of stabilised cruise clearance and clearance at worst case acceleration (max take-off) when compare to the baseline model. The blade tip time constant reduction analysis comparison between the model without radial inflow and the model with radial inflow shows a higher time constant reduction for the model with radial Inflow, and hence abetter compressor clearance control.

The overall results show significant enhancement with radial inflow on tip clearance. With 6% radial inflow, the clearance at worst case acceleration (max take off overshoot) is reduced by approximately 33%, 56%, 70%, 77% and 80%. The clearance at stabilised cruise is reduced at 6%, 17 %, 25 %, 30% and 33%. The above results are for heat transfer coefficient increases factors of 1, 2, 4, 6 and 8 respectively calculated against the baseline clearance.

In the case with heat transfer coefficient, (50W/ (m2K), 100W/ (m2K) and 150 W/ (m2K)), the results of the analysis indicate that it is possible to reduce the baseline cruise clearance by approximately 13%, 18% and 21% respectively.

Finally, an increase in the heat transfer coefficient will reduce the time constant of the drum. This will reduce the reslam characteristics in the cycle, hence, a proper clearance throughout the cycle during transient operation.

Chapter 6

Multiple Cavity Rig (MCR) Model Validation

Validation is a process of verifying that a model is a correct representation of the process or system for which it is proposed. Validation is achieved if the predictions from the model are in good agreement with the experimental observations or mathematical model. It is performed by evaluating the predicted and measured temperatures to make certain that the thermal behaviour of the model reproduces the measured characteristics at transient and steady state conditions. Validation is often performed by comparing the values of parameters of the model with values obtainable independently from other methods, such as, a mathematical model or an experimental method. When the data obtained from the experiment or mathematical model matches those from the SC03 model, the validation is said to be accurate and the model is confirmed.

According to Monico and Chew (1993), in some cases, it may be possible that the modelling assumptions used may not accurately represent some of the physical processes; as such, a mathematical method would be preferable for use in the matching process. In this analysis, a lumped parameter method was used for the validation. In this project, the parametric predicted results from the SC03 model of the MCR are compared with lumped parameter results. The Grid Independence study is presented in section 6.2. In section 6.3 the SC03 model data are validated against the lump parameter result while the validation of SC03 data against the experimental results is presented section 6.4. The summaries drawn from the validation exercise are presented in section 6.5.

6.1 Thermal matching

The matching exercise is the process whereby the finite element thermo-mechanical model is calibrated against the engine measurements or a mathematical model. The requirements for the matching exercise are the thermo-mechanical model of the MCR with disc 2 upstream predicted data from the square cycle, the lumped parameter model results of the cycle and the results of the cycle run of the test rig. The experimental results are compared to the SC03 model predictions in Section 6.4.

The SC03 models produced provide transient thermal simulations which are run to user-defined operating cycles. The SC03 program computes the internal temperature distribution of the rig components using the transient, variable property, heat conduction equation with appropriate thermal boundary conditions to account for the convective and radiative heat transfers. The convective boundary conditions are modelled by specifying flow distribution, local air temperatures, and heat transfer coefficients based on Nusselt number correlations.

To calibrate the finite element thermal model against measured engine test data, heat transfer coefficients in the thermal boundary conditions are adjusted until the acceptable accuracy is reached (± 5K for transient and ± 2K for steady state). This adjustment involves varying of the coefficients for the heat transfer coefficient expressions. This would vary the heat transfer coefficient, and hence produce a change in the heat transfer predicted by the model at that point leading to variation in the temperature at that point. This may also affect the steady state temperature, the local metal transient response and the heat pickup along the boundary condition. This would lead to the predicted temperatures by the thermal model matching the measured data, giving similar temperature and time constant profiles of both the computed and experimental data

To calibrate the finite element thermal model against lump parameter data, the lump parameter data are presented graphically and compared with the model results, which are presented as graphical data items. The required temperature accuracy during thermal matching, according to Rolls Royce standard, is given in Table 6.1. However, the temperature accuracy used in this matching is ± 5K for transient and ± 2K for steady state.

Type of measurement	Accuracy required
Transient	± 15K
Steady state	± 5K

Table 6.1: The require temperature accuracy for thermal matching

6.2 Grid Independence study

In SCO3 finite element programme, mesh is generated automatically when the analysis is run. The program uses an automatic mesh generator of quadratic, six-node triangular elements. The element density is controlled by the triangle distortion ratio, which has a default value of 4. For both steady state and transient cycles, the thermal accuracy was set to 2°C. A converged solution was produced after four (4) refinements with a time of 0.690967s during transient operation. The final mesh had 10007 elements and 22504 nodes. An example of grid independent is shown in the plotting of the transient temperature result for model point MP7. Figure 6.1 shows a transient plot of the third (3^{rd}) and fourth (4^{th}) refinement meshes solutions for model point MP7. This indicates that there was no change in the results of metal temperature at MP7 for both meshes during engine transient as such the results was independent of grid. The total elements and nodes for the third (3rd) and fourth (4th) refinement are given in Table 6.2.

SN	Properties	Third (3rd) refinement	Fourth (4th) refinement
1	Time (s)	0.631572	0.690967
2	Elements	9942	10007
3	Nodes	22475	22504

Table 6.2: The third (3rd) and fourth (4th) refinement meshes properties

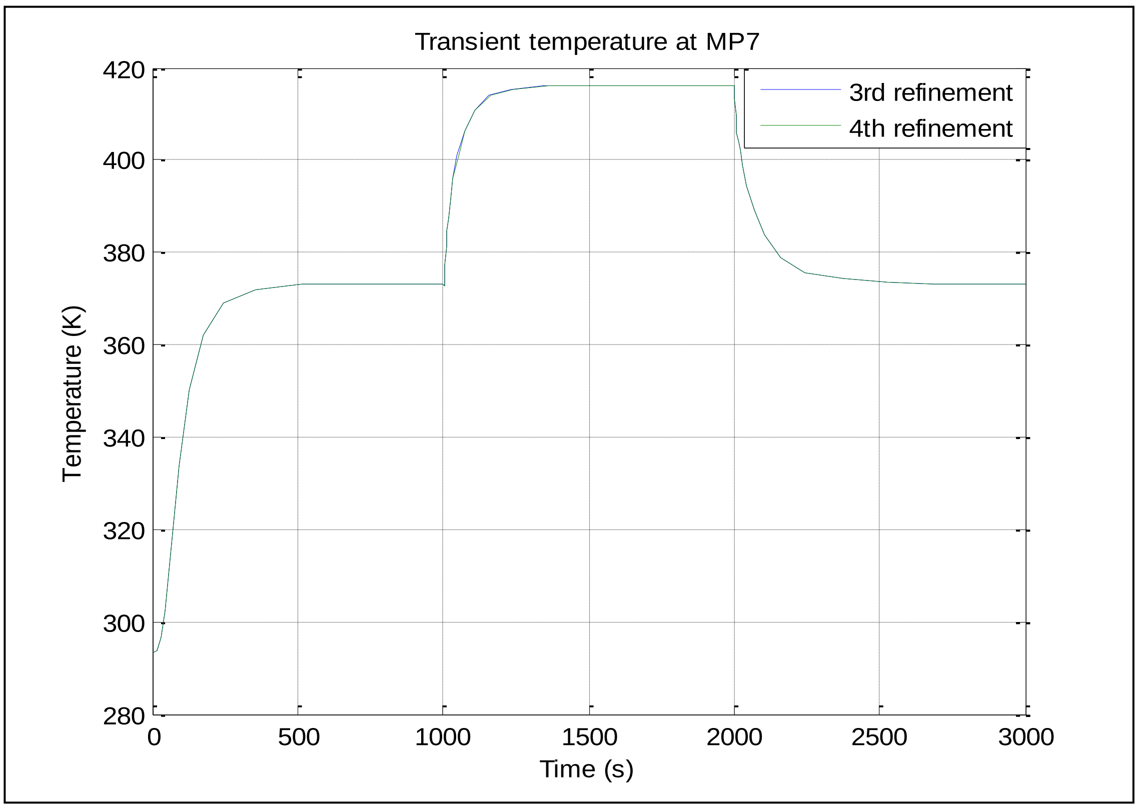

Figure 6.1: A transient plots of the third (3rd) and fourth (4th) refinement meshes solutions for model point MP7

6.3 Validation of SC03 data against the lumped parameter model

In this section, the finite element thermo-mechanical models are calibrated against the lumped parameter models. The predicted temperature profiles of both SC03 baseline and 6% radial inflow models are matched with those of the lumped model data to show similarity of the profiles within an acceptable accuracy. The validations are performed at model points MP12, MP18, MP22, and MP28 on disc 2 upstream in cavity 3. Section 6.3.1 describes the validation of baseline models (model without radial inflow) while the validation of the models with radial inflow is presented in section 6.3.2. The environmental parameters, the non-dimensional parameters, and the time history used for SC03 models are given in Chapter 5.

6.3.1 Validation of baseline models (model without radial inflow)

Figures 6.2 through to 6.5 illustrate the validation of the SC03 baseline model against the lumped model for model points MP12, MP18, MP22, and MP28. The lumped parameter mathematical model is presented in appendix 6. The validation of the SC03 baseline model against the lumped model for model point MP12 is in good agreement throughout the transient as shown in Figure 6.2. This indicates that the predicted temperature for stabilised Idle and stabilised MTO and the time constant during acceleration and deceleration at MP12 match the lumped model results.

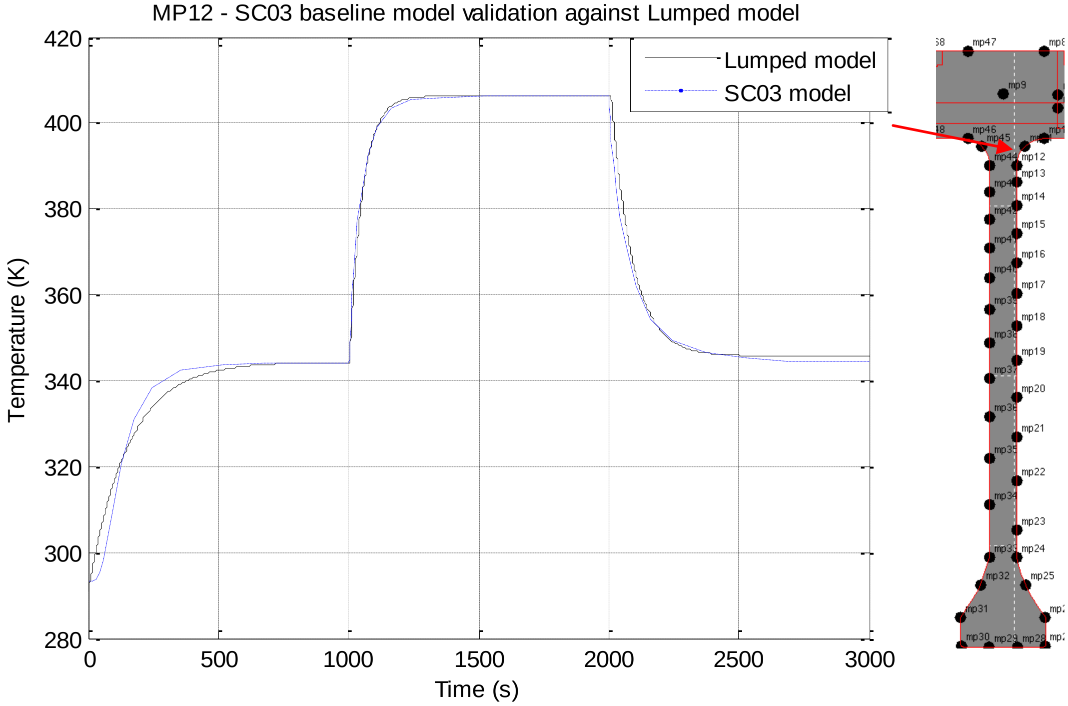

Figures 6.2: The validation of SC03 models against the lumped model for the baseline model at model points MP12

Figure 6.3 illustrates the validation of the SC03 baseline model against the lumped model for model point MP18. The comparison shows that the predicted temperature for stabilised Idle and stabilised MTO and the time constant during acceleration and deceleration at MP18 are in good agreement with the lumped model throughout the transient.

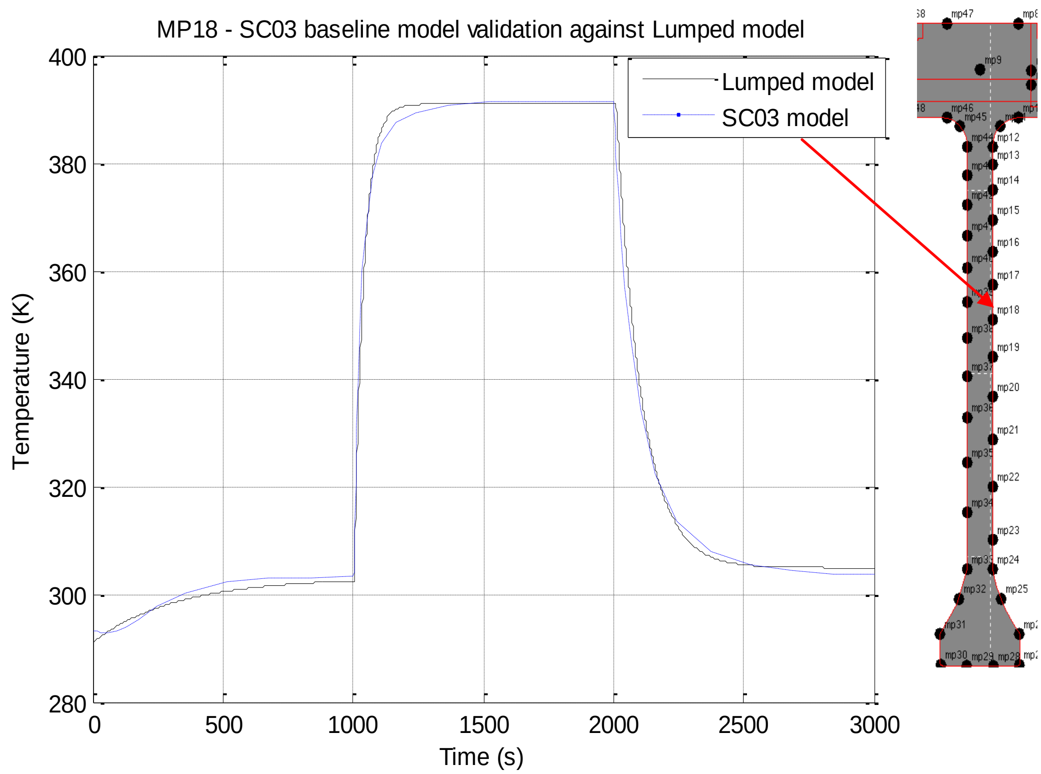

Figures 6.3: The validation of SC03 models against the lumped model for the baseline model at model points MP18

Figure 6.4 illustrates the validation of the SC03 baseline model against the lumped model for model point MP22. The evaluation proves that the predicted temperature for stabilised Idle and stabilised MTO and the time constant during acceleration and deceleration at MP22 are in good agreement with the lumped model throughout the transient.

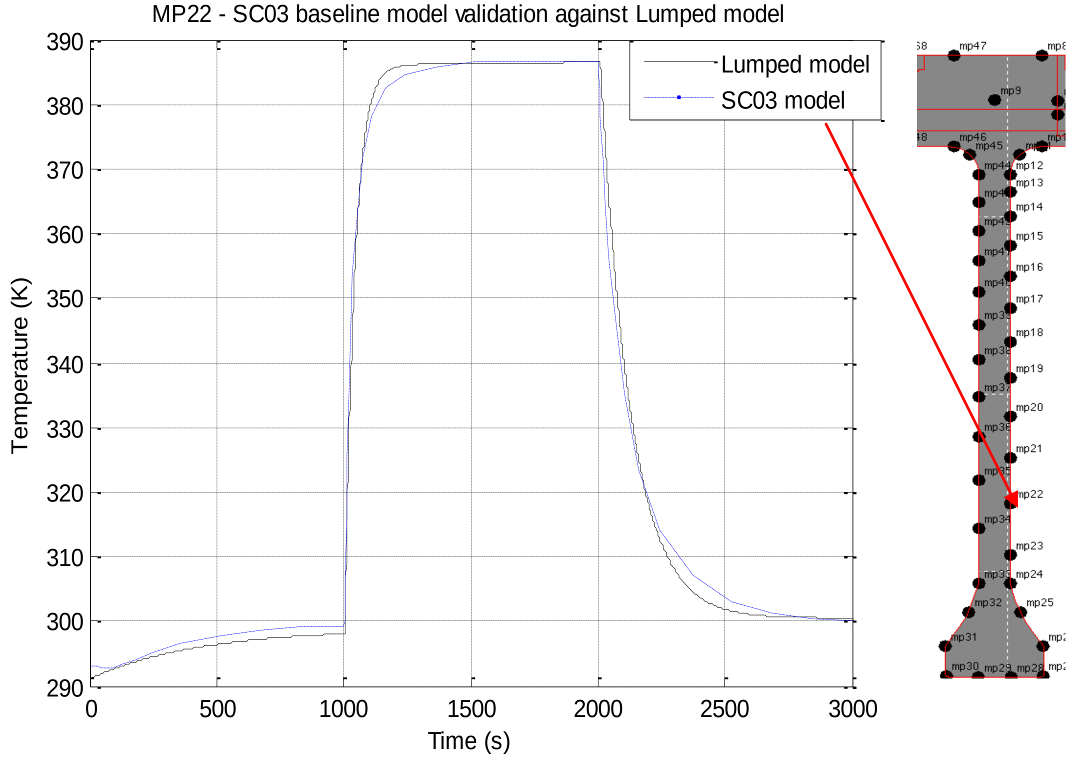

Figures 6.4: The validation of SC03 models against the lumped model for the baseline model at model points MP22

Figure 6.5 illustrates the validation of the SC03 baseline model against the lumped model for model point MP28. The assessment confirms that the predicted temperature for stabilised Idle and stabilised MTO and the time constant during acceleration and deceleration at MP28 are in good agreement with the lumped model throughout the transient.

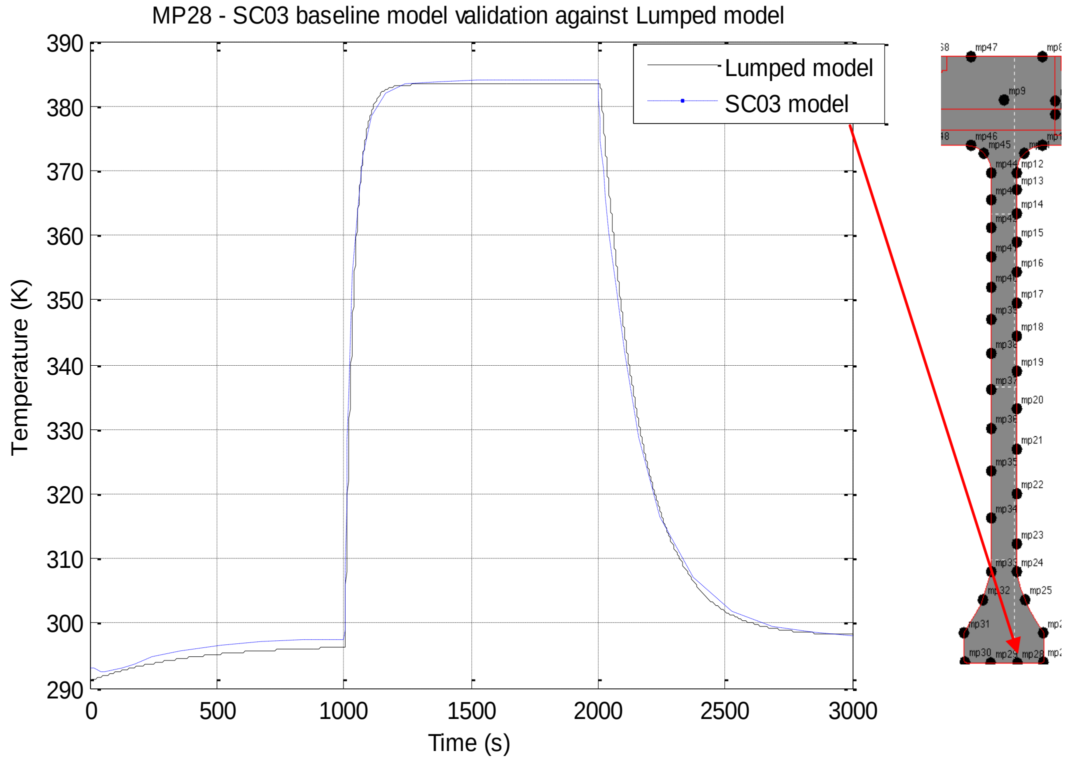

Figures 6.5: The validation of SC03 models against the lumped model for the baseline model at model points MP28

In summary, the comparison shows good agreement between the lumped parameter model and the SC03 predicted results for the baseline model at model points MP12, MP18, MP22, and MP28.

6.3.2 Validation of models with radial inflow

Figures 6.6 through to 6.9 show the validation of the SC03 model with 6% radial inflow against the lumped model for model points MP12, MP18, MP22, and MP28. The validation of the SC03 model with radial inflow against the lumped model for model point MP12 is in good agreement throughout the transient as shown in Figure 6.6. This indicates that the predicted temperature for stabilised Idle and stabilised MTO and the time constant during acceleration and deceleration at MP12 matches the lumped model results. The SC03 model slightly over-predicted temperature at max take off region (MTO) but was within the acceptable accuracy.

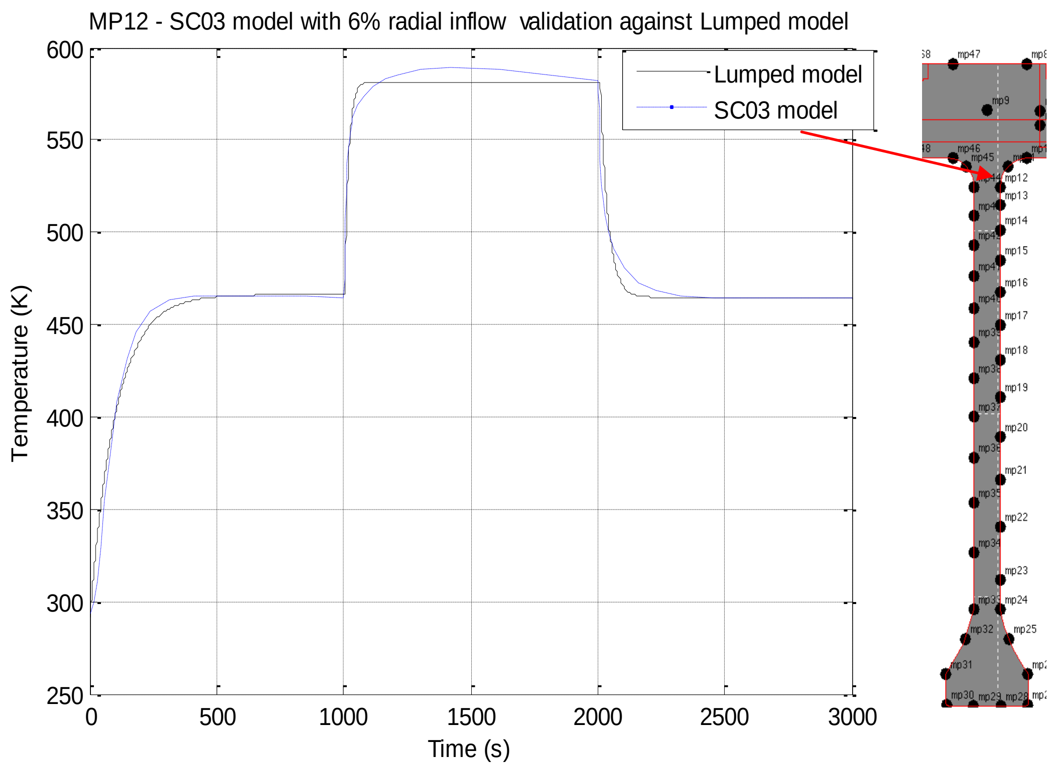

Figures 6.6: The validation of SC03 model with 6% radial inflow against the lumped model at model points MP12

Figure 6.7 illustrates the validation of the SC03 model with radial inflow against the lumped model for model point MP18. The comparison shows that the predicted temperature for stabilised Idle and stabilised MTO and the time constant during acceleration at MP18 is in good agreement with the lumped model throughout the transient. However, the SC03 slightly over-predicted the temperature at max take off (MTO) region but was within the acceptable accuracy.

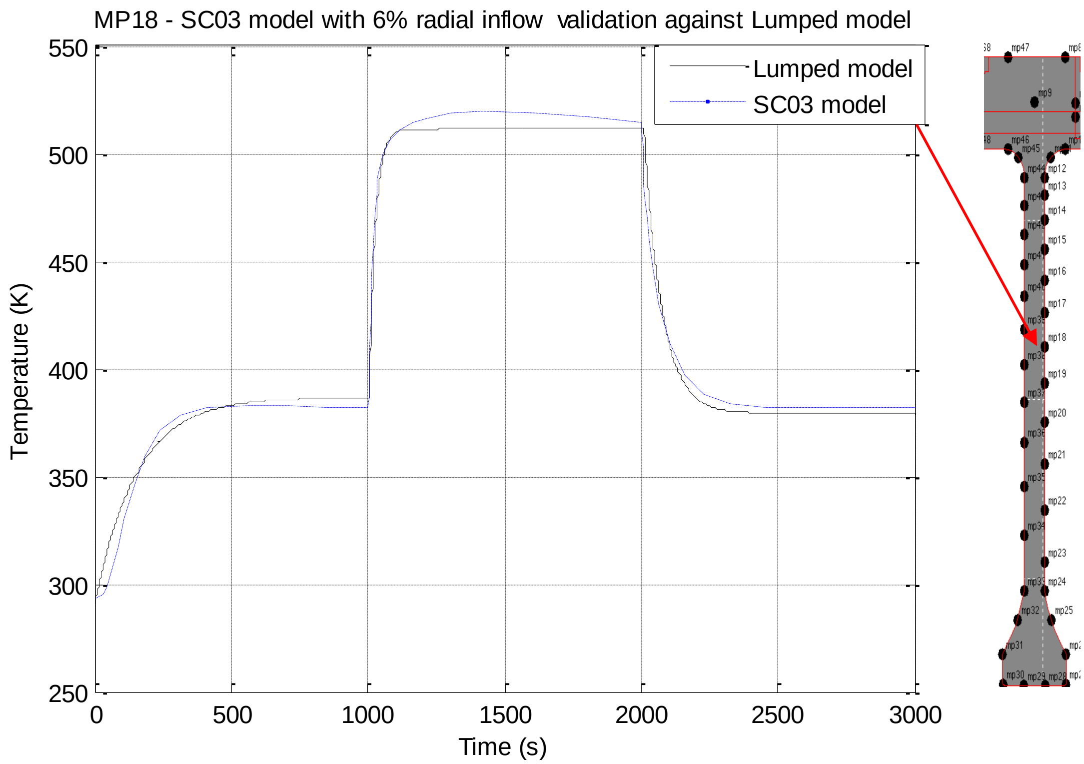

Figures 6.7: The validation of SC03 model with 6% radial inflow against the lumped model at model points MP18

Figure 6.8 illustrates the validation of the SC03 model with radial inflow against the lumped model for model point MP22. The assessment confirms that the predicted temperature for stabilised Idle and stabilised MTO and the time constant during acceleration and deceleration at MP22 is in good agreement with the lumped model throughout the transient. But with a very slight over-prediction of the temperature at max take off (MTO) region but again was within the acceptable accuracy.

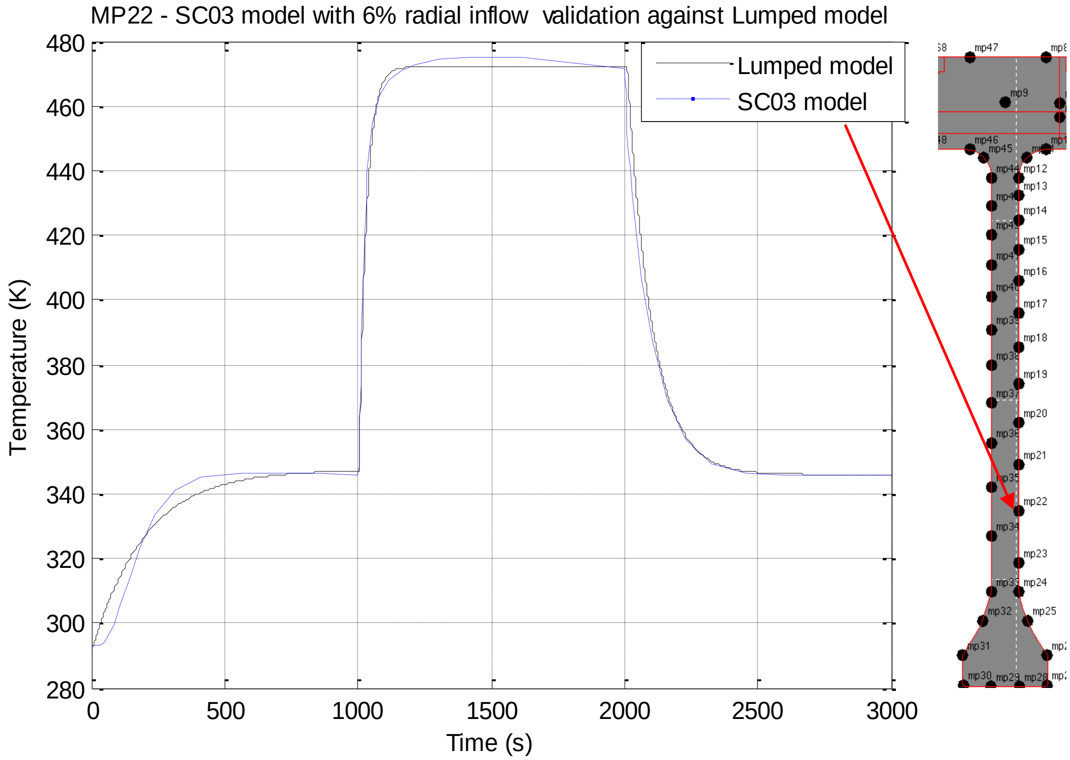

Figures 6.8: The validation of SC03 model with 6% radial inflow against the lumped model at model points MP22

Figure 6.9 illustrates the validation of the SC03 model with radial inflow against the lumped model for model point MP28. The assessment confirms that the predicted temperature for stabilised Idle and stabilised MTO and the time constant during acceleration and deceleration at MP28 is in good agreement with the lumped model throughout the transient.

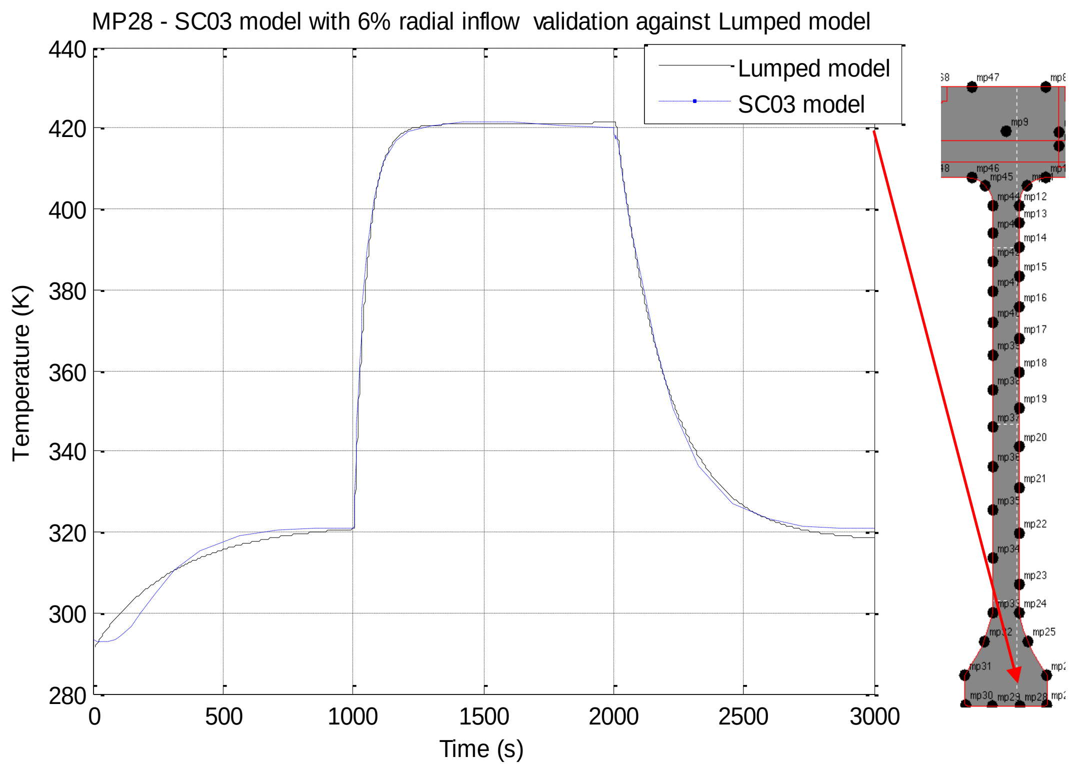

Figures 6.9: The validation of SC03 model with 6% radial inflow against the lumped model at model points MP28

In summary, the comparison shows good agreement between the lumped parameter model and the SC03 predicted results for both models with 6% radial inflow and the baseline model (without radial inflow) at model points MP12, MP18, MP22, and MP28.

6.4 Validation of SC03 data against the experimental results

In this section, the finite element thermo-mechanical model is calibrated against the engine measurements. This is performed by comparing the predicted and measured temperatures to make certain that the thermal behaviour of the model reproduces the measured characteristics at transient and steady state conditions. The predicted temperature time profiles of both SC03 baseline and radial inflow models are compared with those of the experimental data to show that they are in good agreement. The overall effects of radial inflow on disc time constant and its effect on specific areas on the multiple cavity drum are discussed. It must be highlighted that the heat transfer and the flow distribution in the disc cavities depend on environmental parameters: disc temperature distribution, rotational speed, the mass flow rate of the axial throughflow, and the radial inflow in the cavity. As stated earlier, the thermal boundary conditions are adjusted so that the predicted temperatures match the measured data, giving similar temperature and time constant profiles for both. If the correct match is not achieved, the thermal boundary conditions are modified by adjusting the multiplicative factors to the heat transfer coefficient expressions or, in some cases, by changing the flow distribution. This would modify the mass flow passing through the required point. This would in turn vary the heat transfer coefficient, and hence produce a change in the heat transfer at that point leading to variation in the temperature at that point.

The model is then run again and the procedure repeated until a reasonable match is achieved. The match is performed for the temperatures during the transient period of the cycle.

The experiment was carried out by Dr. Nick Atkins as is part of the wider NEWAC research project using the Thermo-Fluid Mechanics Research Centre's in-house multiple cavity rig incorporating H.P. compressor bore geometry, which is approximately 1:1 scale when compared to a current Trent engine. The Rossby number was fully matched to the engine values during testing. This was accomplished by setting the Rotational

Reynolds number as close to the engine values as possible while reducing the Axial Reynolds number appropriately. In Atkins (2013) an experimental investigation was carried out into the use of radial inflow as potential for compressor clearance control and concluded that a small radial inflow bleed has substantial potential for reductions in compressor clearance at high power conditions. The study shows that the use of radial inflow reduces the time constant of high pressure compressor discs. The work suggests a significant potential in steady state cruise clearance reduction which behaves almost linearly with increased steady state disc temperatures. The study confirms that a time constant reduction factor of 2 for MTO and a factor of 1.4 for idle conditions could be obtained with a radial inflow bleed of 4% bore flow. By employing the experimental results, the closure modelling is capable of reducing the 2D axis-symmetric clearance by 50% at MTO conditions. Details of the analysis of the MCR testing can be found in Atkins (2013).

6.4.1 The matching of SC03 temperature time profiles against the experimental profiles

In this section, the finite element thermo-mechanical model is calibrated against the experimental data from Atkins (2013). The predicted temperature profiles of SC03 baseline models are compared with those of the experimental data to show the similarity of the profiles. Figures 6.10 through to 6.13 show the baseline model temperature time history profiles during engine transient for SC03 simulation and experimental analysis, for model points MP12, MP18, MP22 and MP28 respectively.

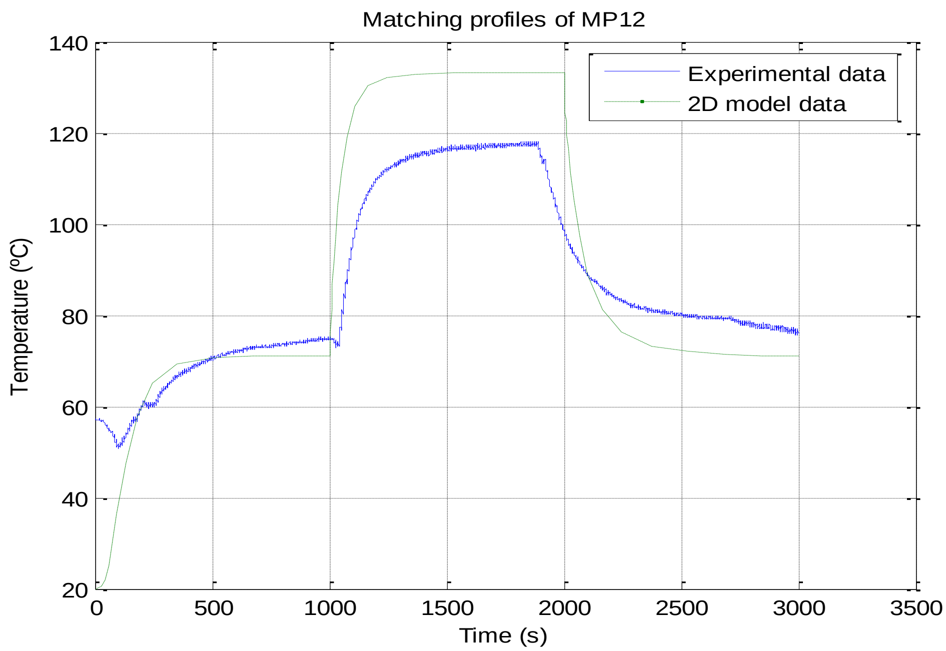

Figure 6.10: Comparison of the SCO3 and experimental temperature time profiles during engine transient for the baseline model at modal point MP12

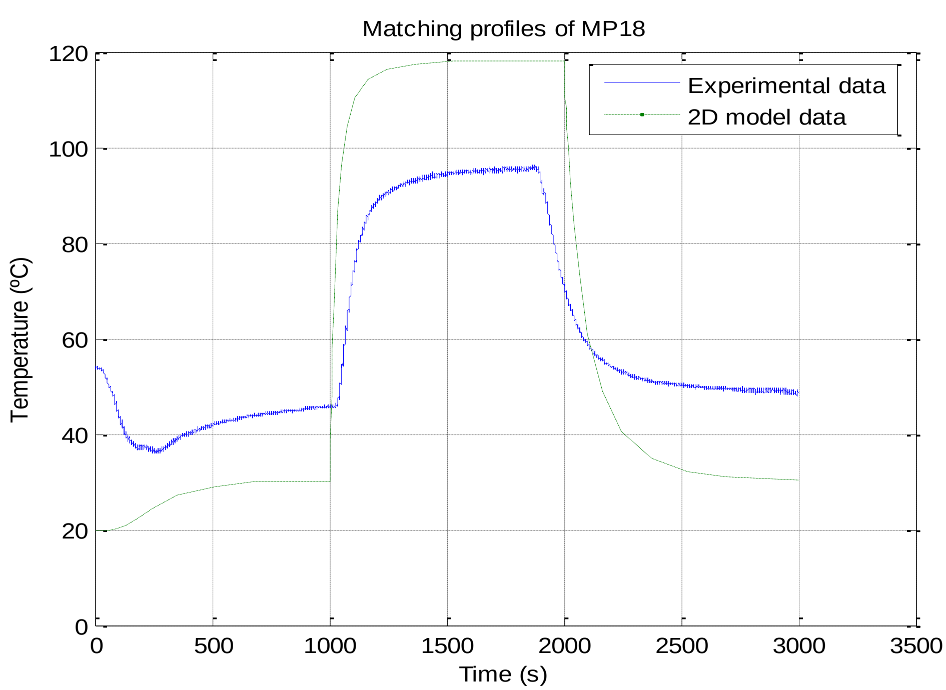

Figure 6.11: Comparison of the SCO3 and experimental temperature time profiles during engine transient for the baseline model at modal point MP18

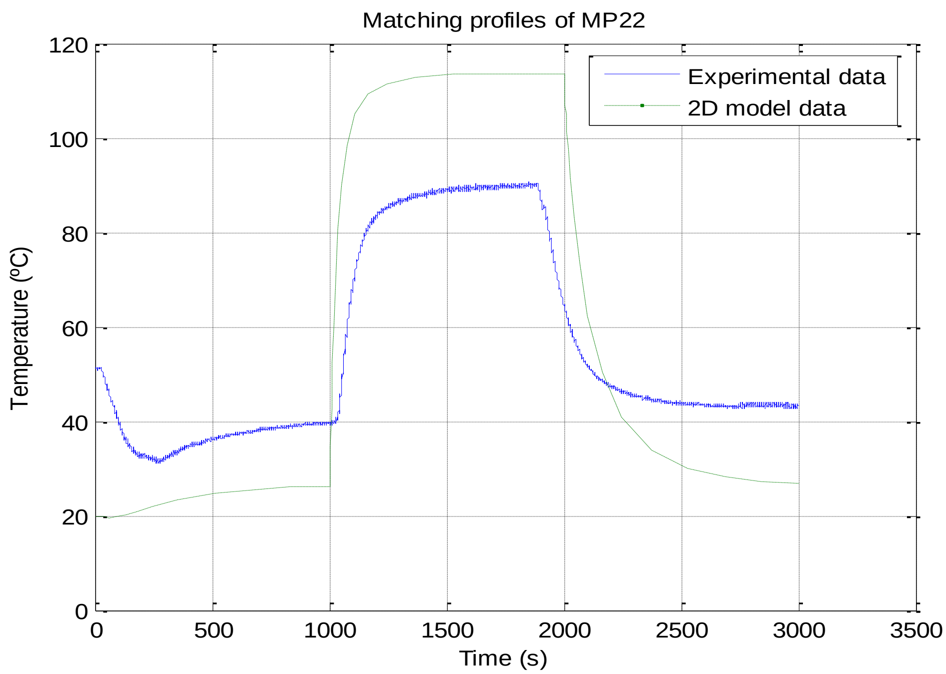

Figure 6.12: Comparison of the SCO3 and experimental temperature time profiles during engine transient for the baseline model at modal point MP22

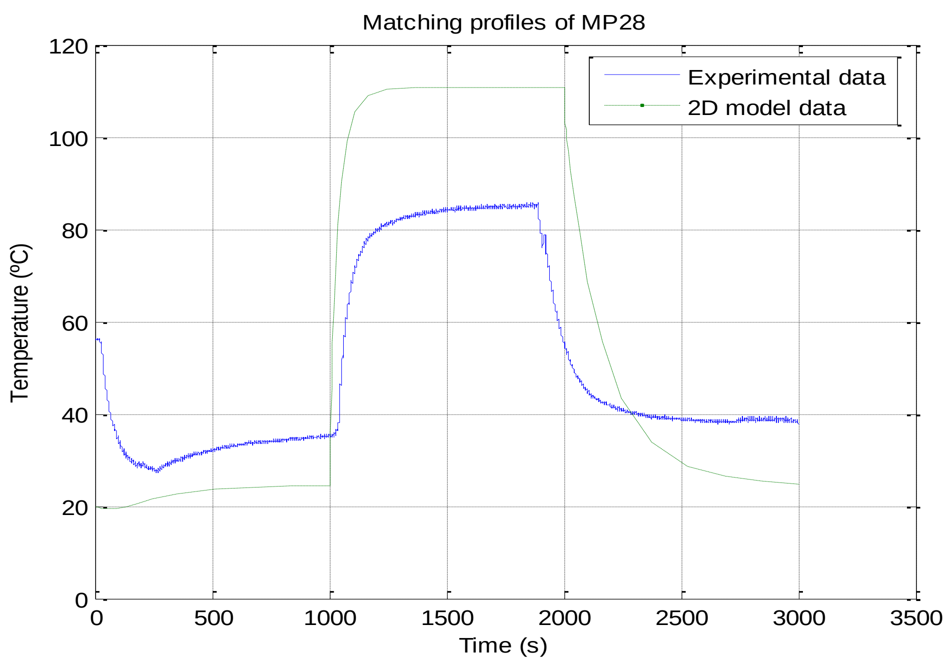

Figure 6.13: Comparison of the SCO3 and experimental temperature time profiles during engine transient for the baseline model at modal point MP28

The predicted temperature time profiles during engine transient for both the SC03 models and the experimental results are in fairly good agreement in terms of similarity in their transient profiles. However, at stabilised max take-off and deceleration regions, the agreement is not good. This discrepancy is a result of variation in the final data use for the experiments compared to the data use in the modelling of the rig. Table 6.3 shows both the experimental data and SC03 data used (the bore temperatures, inlet pressures, shroud temperatures, bore mass flow rates and rotational speed) at both idle and maximum take-off (MTO).

Parameters	Idle (Experiment)	Idle (SC03)	MTO(Experiment)	MTO (SC03)
T_{bore}	300K	291K	340K	381K
P_{inlet}	2.5 bar	2.8 bar	4.5 bar	5.5 bar
$T_{radial} \approx T_{shroud}$	370K	350K	390K	469K
Bore mass flow rate	0.2 kgs^{-1}	0.23 kgs^{-1}	0.7 kgs^{-1}	1.35 kgs^{-1}
Rotational speed	370 $rads^{-1}$	314.16 $rads^{-1}$	730 $rads^{-1}$	837.76 $rads^{-1}$

Table 6.3: Experimental and SC03 nominal test conditions

Ideally if the 2D modelling analysis was performed with the final nominal test conditions use in the experimental analysis, a good match between the SC03 data and the experimental data would be achieved. As at the time of this matching, the SC03 license had expired as such the final experimental conditions were not used in the SC03 to perform the matching. Nevertheless, the SCO3 modelling of the MCR rig study proves that a time constant reduction factor of approximately 2 for MTO and a factor of 1.5 for idle conditions could be obtained with a radial inflow bleed of 4% bore flow which is in good agreement with the experimental results by Atkins (2013).

6.5 Summary

This chapter has reported on the validation of the SC03 model data against both the lump parameter results and the experimental data.

The predicted temperature profiles and time constant data of both SC03 baseline models and 6% radial inflow models were matched with those of the lumped model data to show similarity of the profiles within an acceptable accuracy. The validations were performed at model points MP12, MP18, MP22, and MP28 on disc 2 upstream in cavity 3. The overall result of the matching process shows that the results of the lumped model are in good agreement with the results of the two MCR models (baseline model and model with 6% radial inflow). Evidence can be seen in the matching profiles of the two models as shown in Figures 6.2 through to 6.9.

Another validation was performed between SC03 models and experimental data. For the baseline case, the SCO3 predicted transient temperature time history profiles during engine transient show fairly good agreement with those of the experiment with similarity in their transient profiles. The actual level of disc time constant is in good agreement with the experimental data. However, the temperature profile appears to vary at stabilised MTO and idle due to differences with the final experimental data used.

Finally, the validation is achieved since the predictions from the SC03 models are in good agreement with the mathematical model and in reasonably good agreement with experimental results.

Chapter 7

2-Dimensional modelling of a Multiple Cavity Rig (MCR)

Finite Element Analysis (FEA) program called SC03 is used for the 2-dimensional modelling of a Multiple Cavity Rig (MCR). SC03 is a FEA program developed by Rolls-Royce plc. This program is used for thermo-mechanical analysis which includes the prediction of component temperatures, component stresses, analysis of engine movement and the deflections of axisymmetric or plane structures, as well as for clearance optimisation.

In this study, the 2-D modelling of a MCR is presented. Two models have been studied: a MCR baseline model (without radial inflow) and MCR model with radial inflow. Section 7.1 describes the non-dimensional parameters used in the MCR modelling; section 7.2 presents the MCR geometry definition while section 7.3 illustrates the modelling setup and analysis of the MCR including the cycle definition. Methodology of the analyses is discussed in this section 7.4 along with the analysis without radial inflow while radial inflow analyses are presented in section 7.5. The summary of the results is presented in section 7.6 and conclusion in section 7.7.

7.1 Non-dimensional parameters used in the Multiple Cavity Rig modelling

The non-dimensional parameters employed in the 2-D modelling of the MCR are presented in this section. The aim of the modelling is to develop a reliable thermal model suitable to validate the experimental data obtained for the MCR for tip clearance control analysis. The model will simulate the matched non-dimensional parameters. The non-dimensional quantities to be considered are rotational Reynolds number $Re_{Ø}$, axial Reynolds number Re_Z, Grashof number Gr and Rossby number Ro.

Table 7.1 provides definition of the non-dimensional parameters, and Table 7.2 identifies the values of these non-dimensional parameters used in the modelling of the MCR.

Parameters	**Symbol**	**Definition**
Axial Reynolds number	Re_z	$\mathrm{Re}_z = \dfrac{p_b W_Z \, 2(a - r_s)}{RT_b \mu_b}$
Rotational Reynolds number	$Re_{Ø}$	$\mathrm{Re}_\phi = \dfrac{p_b \Omega b^2}{RT_b \mu_b}$
Grashof number	Gr	$Gr = \dfrac{\rho^2 \Omega^2 (b(b-a))^3 \beta (T_{sh} - T_b)}{\mu^2{}_b}$
Rossby number	Ro	$Ro = \dfrac{W}{\Omega a}$

Table 7.1: Non-dimensional parameters used in the modelling of the MCR

The rotational Reynolds number $Re_{Ø}$ is the parameter that is relevant to the rotation of the cavity while the axial Reynolds number Re_z is the parameter that characterises the axial throughflow of air. The effects of the axial flow and the rotational flow can be related using the Rossby number Ro which is the ratio of the axial velocity of the tangential solid body velocity at the discs bore. The parameter that is significant to buoyancy induced flow is called Grashof number Gr. In a rotating cavity application, the expression of Grashof number based on the radial distance along the disc surface is depended on the local surface temperature and its relative centripetal acceleration by taking a height reference from the shroud Farthing et al. (1992a and b). The model is run at a rotational speed not exceeding 10,000 rpm, with a shroud temperature not exceeding 200^{0}C.

Parameter	**IDLE**	**Max take-off (MTO)**
Re_z	1.88×10^5	8.75×10^5
$Re_Ø$	3.1×10^6	1.0×10^5
Gr	5.4×10^{11}	6.4×10^{12}

Table 7.2: Trent 1000 compressor non-dimensional parameters used in the modelling of the MCR

7.2 MCR model geometry definition

The MCR is an in-house rotating cavity rig in the Thermo-Fluid Mechanics Research Centre of the University of Sussex, and has been used extensively by many researchers and authors such as Long and Childs (2007), Long Miché and Childs (2007) and Miché (2009) for flow and heat transfer studies and has provided predictions of temperature, flow features and stress analysis, as well as data for computational fluid dynamics studies. Changes have been made to the MCR, which are aimed at accurate performance of the current investigation. This are insulating the rotor endwall with Insufrax material, machining of radial inlet holes into the MCR rotor cavity and the inclusion of a telemetry unit. The latter modification will allow the flow of heated air into the cavity, which should increase the heat transfer in the cavity.

This is similar to the ducting of the radial flow of compressor air into the internal flow system of a real engine. Figure 7.1 shows the geometry cavity with radial inflow entering the cavity from the shroud and the axial throughflow entering the cavity from the bore.

The symbols $r_{s,}$ a, b and s representing shaft radius, hub radius, rotor radius and cavity width respectively. The geometrical parameters of the cavity are a shaft radius of r_s = 0.0701m, hub radius of a = 0.0802m, rotor radius of b = 0.2301m and cavity width of s = 0.048m. Based on the geometry cavity dimension, definition and modification, a multiple cavity rig model has been build for this study as shown in Figure 7.2. As stated in Chapter 3, several activities were carried out before the model is ready for any analysis such as clean up, chaining, meshing, definition of material and boundary conditions and setting the engine cycle.

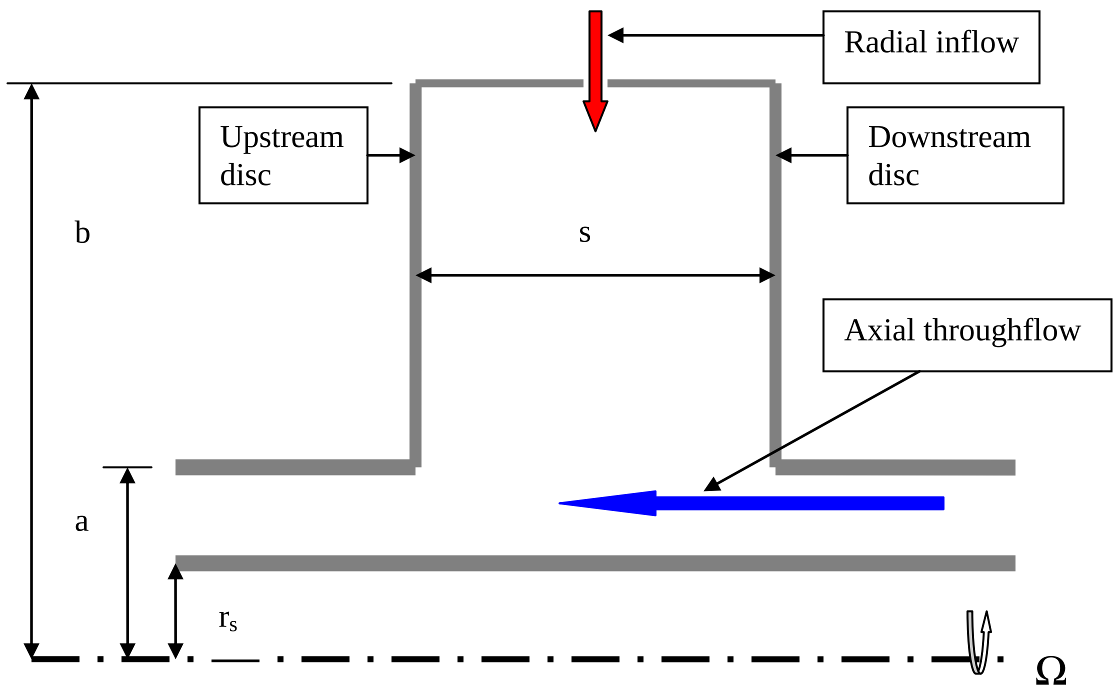

Figure 7.1: Geometry cavity definitions for the MCR

Figure 7.2 shows the multiple cavity rig model with the modifications such as machining of radial inflow channel, installation Insufrax insulator and telemetry units with rotating-with rotating-frame thermocouple location (model points) using SC03 analysis program ready for boundary conditions application and analysis. Figure 7.1 and 7.2 described the dimensions of MCR used and the modification done to the existing rig.

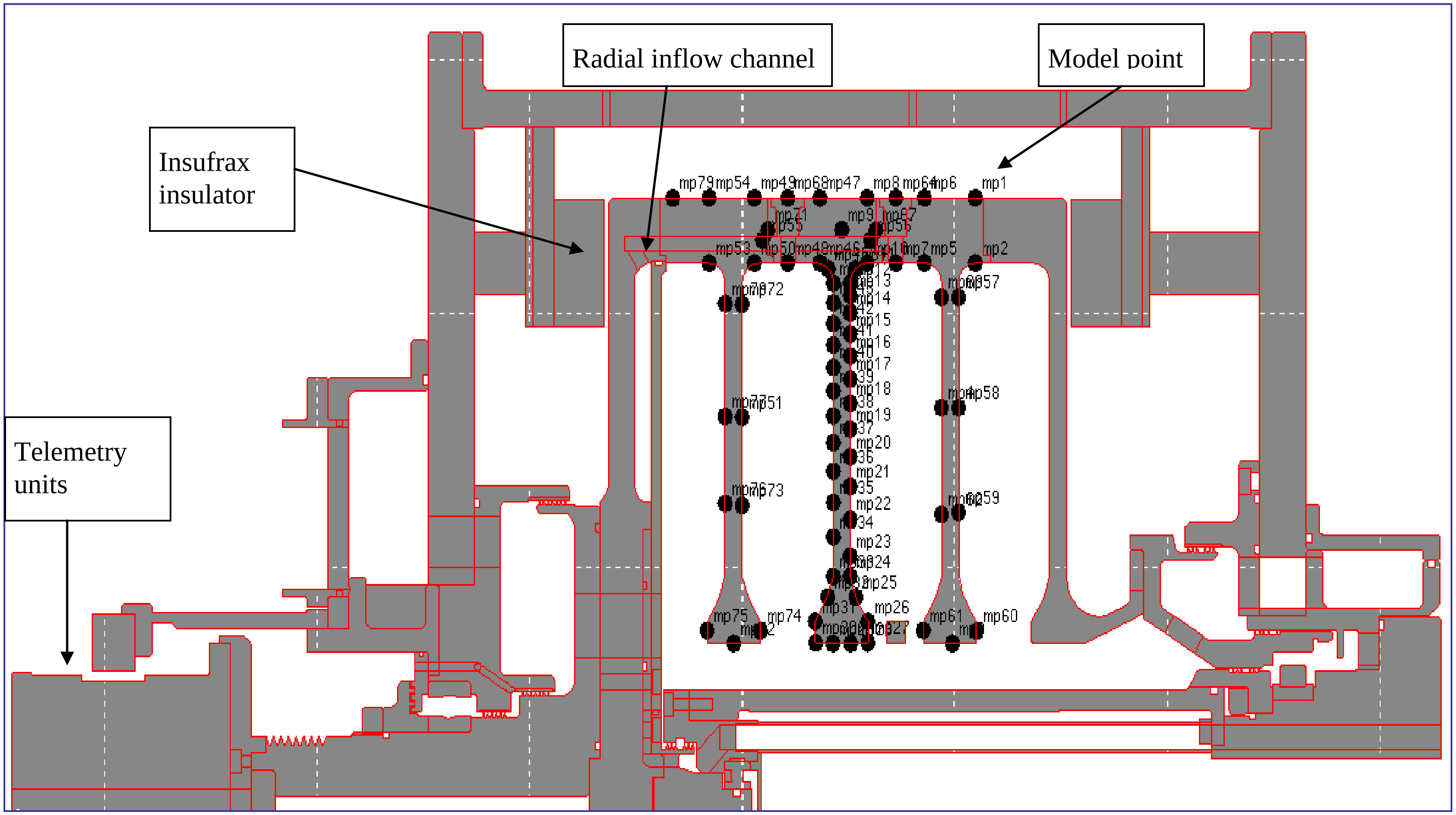

Figure 7.2: Multiple cavity rig model showing the modifications such as radial inflow channel, Insufrax insulator and telemetry units applied to the model with rotating-frame thermocouple location (model points)

7.3 Modelling setup and analysis of MCR

This section presents the modelling setup and analysis of the multiple cavity rigs (MCR) for the present study. In the modelling of the MCR, the setup included the use of two MCR models for the study. There are MCR model without radial inflow (baseline model) and MCR model with radial inflow. In the model with radial inflow, the radial inflow ducts allows the ducting of radial inflow into the cavity of the model. The cycle data used is the square cycle.

The MCR drum consists of four cavities, with two adjacent discs forming the cavity of each stage. The baseline model boundary conditions have streams around the disc cob on each disc and voids in the interdisc cavity as shown in Figure 7.3. The model consists of 154 domains. In the model, the holes property was used to declare the holes in the casing endplates and the rotor, including the holes in the perforated plate. A variable thickness property (TP) was applied to the all non-axisymmetric regions of the model, such as the radial inflow holes in the shaft and the ducts that direct inflows from the supply into the cavity. TP are also applied to channels in the downstream bearing housing. The rotor speed was defined as a time-varying parameter in the Basic Design Data (BDD) file and the default speed (NH) was used for all rotating parts. All the non-rotating parts of the rig were given a local speed, of 0. The speed of the shaft was also set as a time-varying parameter in the BDD file and the default local speed of (NI) was used in the shaft sub-domains. The rotor components of the rig are made from titanium (TFF), high tensile steel was used for the shaft and the casing was made from mild steel. The properties of the materials are given in Appendix 7.3. The oil fed roller bearing was used in the upstream side of the rig to allow for axial expansion.

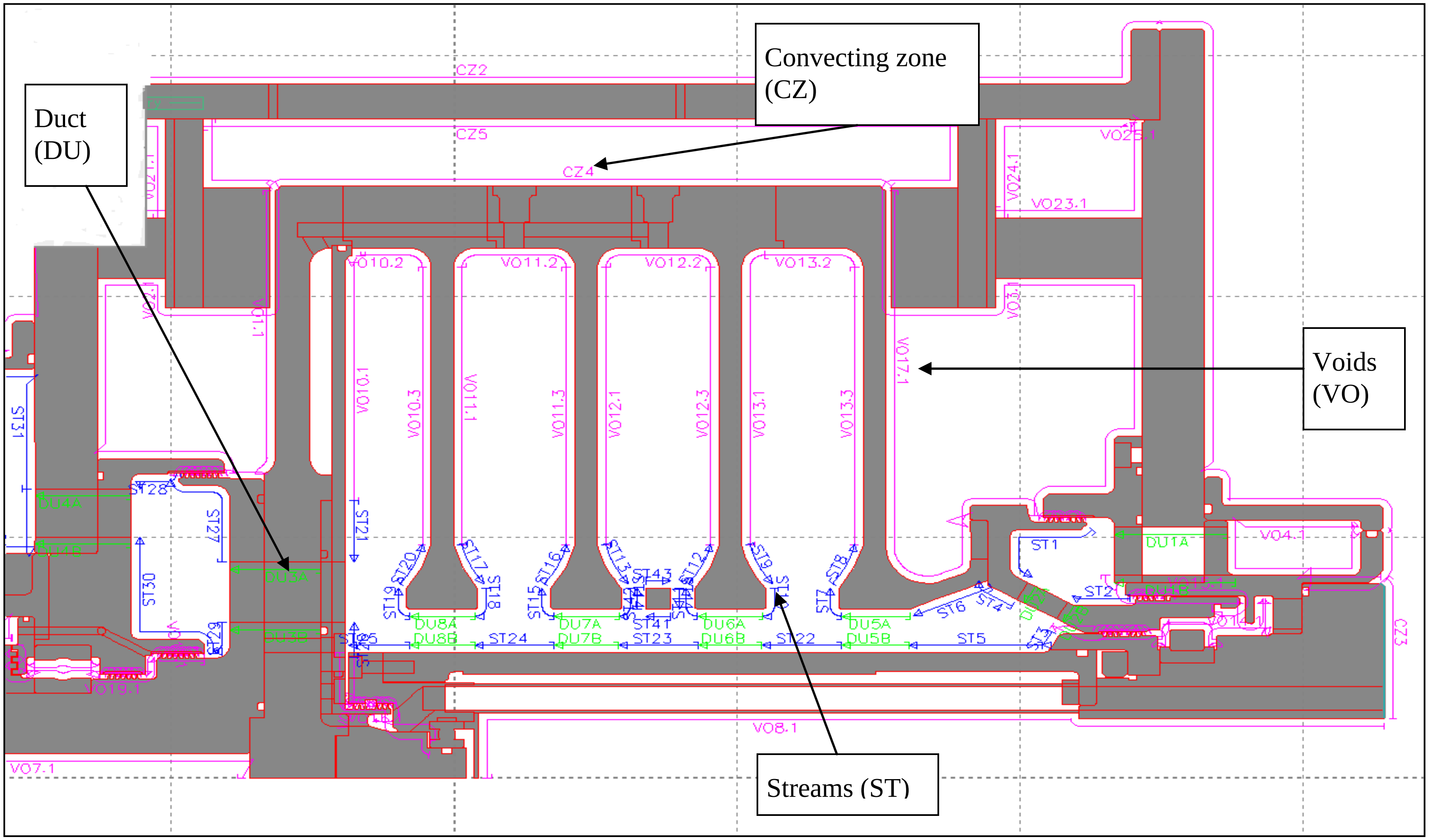

Figure 7.3: MCR model with boundary conditions applied to the model

Figure 7.3 shows MCR model with thermal boundary conditions and area of application in the model. The detailed output file is included in Appendix 7.1

The boundary conditions used in the present analysis are convecting zone (CZ), voids (VO), stream (ST) and ducts (DU). Their inputs parameters are fluid type, mass flow, fluid temperature, absolute and relative temperature, fluid pressure, temperature and heat pick-up and heat transfer correlations. The selection of boundary conditions, its input and the associated correlations used to define the heat transfer coefficient between the solid and fluid domain is essential to an accurate representation of the temperature distribution within the solid domain. These were dealt with in details in Chapter 3. The cycle definition used for the analysis in the present study is presented in Section 7.3.1. Finally, the results of the analyses are presented in Section 7.4.1 through to Section 7.5.1 for model without radial inflow (baseline model) and model with radial inflow respectively.

7.3.1 Cycle definition

The following cycle describes the analysis performed in the SC03 program, and this consists of a ramp and a set of conditions which are accessed by the ramp. The SC03 identifies a series of distinct time points called the Ramp Points of any cycle. Environmental parameters such as temperature and the cycle running speed are specified at each ramp point before any analysis is performed. These parameters are said to vary linearly between two distinct successive time points as shown in the square cycle of Figure 7.4. The time history of the analysis is presented in Table 7.3 with conditions 1, 2 and 3 representing start, idle and maximum take-off regions respectively, while the environmental parameters are shown in Table 7.4.

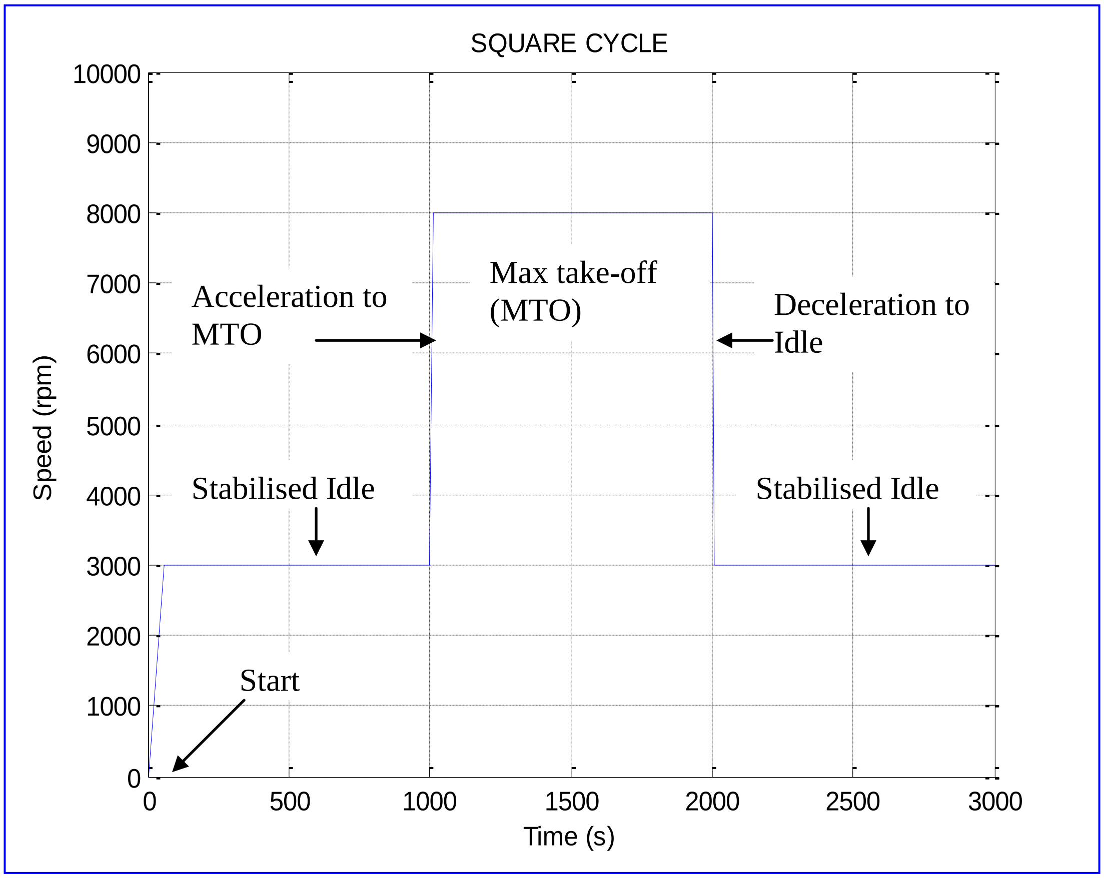

Figure 7.4: The Square cycle showing time history and speed of the analysis

Ramp	**Time (s)**	**Condition**	**Speed (rev/min)**
1	0	1	0
2	60	2	3000
3	1000	2	3000
4	1010	3	8000
5	2000	3	8000
6	2010	2	3000
7	3000	2	3000

Table 7.3: Time History for Square cycle used in the modelling of the MCR

Parameter	IDLE	Max take-off (MTO)
$\dot{m}_{bore}$	0.23 kg/s	1.35 kg/s
T_{bore}	291K	381K
$T_{o,r}$	350K	469K
p_{bore}	2.8×10^5 Pa	5.5×10^5 Pa
Shroud speed	3000 rpm	8000 rpm

Table 7.4: Environmental parameters

7.4 Methodology of the analyses

The study was performed by running the baseline model first and results obtained for the analysis. The second analysis was performed by increasing the inbuilt heat transfer coefficient in the cavity of the drum by a multiplicative factor of 2, 4, 6 and 8. Temperatures from three reference model points and one model point from the disc cob on each disc at various coordinates were used for the analysis as shown in Section 7.4.1. Average heat transfer coefficient was used to show the clearance reduction trends in terms of disc time constant.

The results of the analysis performed using the MCR drum model are presented in the form of:

- Contour plots
- Time plots
- Time constant reduction graph.

For the case without radial inflow, a simple heat transfer analysis is carried by increasing the inbuilt forced convective heat transfer coefficient in the streams around the disc cob and natural convective heat transfer coefficient in the voids in the cavity by an increased multiplicative factor of 1, 2, 4, 6 and 8. According to the relationship $\tau = \dfrac{mC}{hA}$ (see Chapter 4). An increase in the heat transfer coefficient will reduce the drum time constant.

The analysis performed was a thermo-mechanical analysis run of the model and temperature measurements were taken at the model point location on the MCR drum. The object of the analysis is to reduce disc time constant by increasing the heat transfer in the drum cavity. The time constant is the time required for a physical quantity to rise from zero to 63.2% of its final steady value or fall to 36.8% of its initial value. In this analysis, acceleration time constant is defined as the time required for the temperature to rise from the stabilised idle position at 1000s to 63.2% of its final steady value at 2000s during acceleration from Idle to maximum take-off (MTO). While deceleration time constant is defined as the time required for the temperature to fall from the stabilised maximum take-off (MTO) point at 2000s to 36.8% of its initial value at 3000s during deceleration from maximum take-off position to Idle when it varies with time.

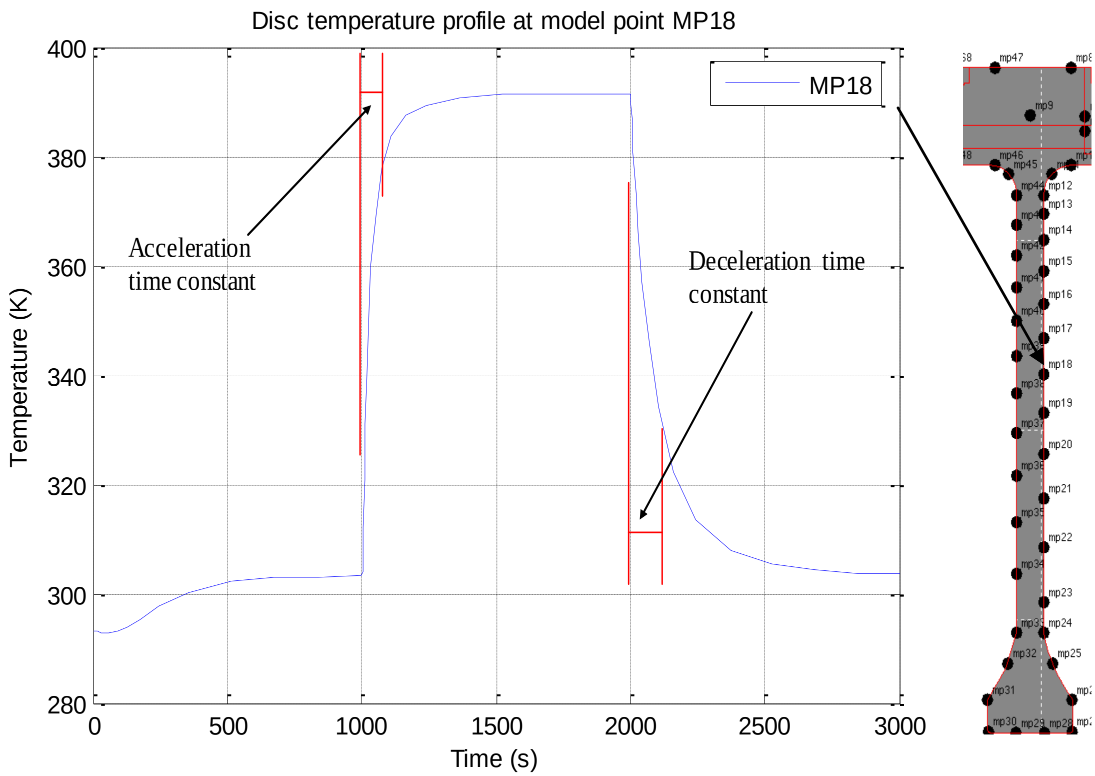

Figure 7.5: Variation of metal temperature with time at disc model point MP18 on the upstream of disc 2 in cavity 3 of the MCR for disc time constant analysis during engine transient.

Figure 7.5 shows the variation of metal temperature with time at disc model point 18 indicating the location in the graph where the acceleration and deceleration time constant are measured.

Figure 7.6 shows the temperature contour plots of the MCR drum baseline model with a bore temperature of 291K, rim temperature of 425K, idle and maximum take-off (MTO) speed of 3000rpm and 8000rpm respectively.

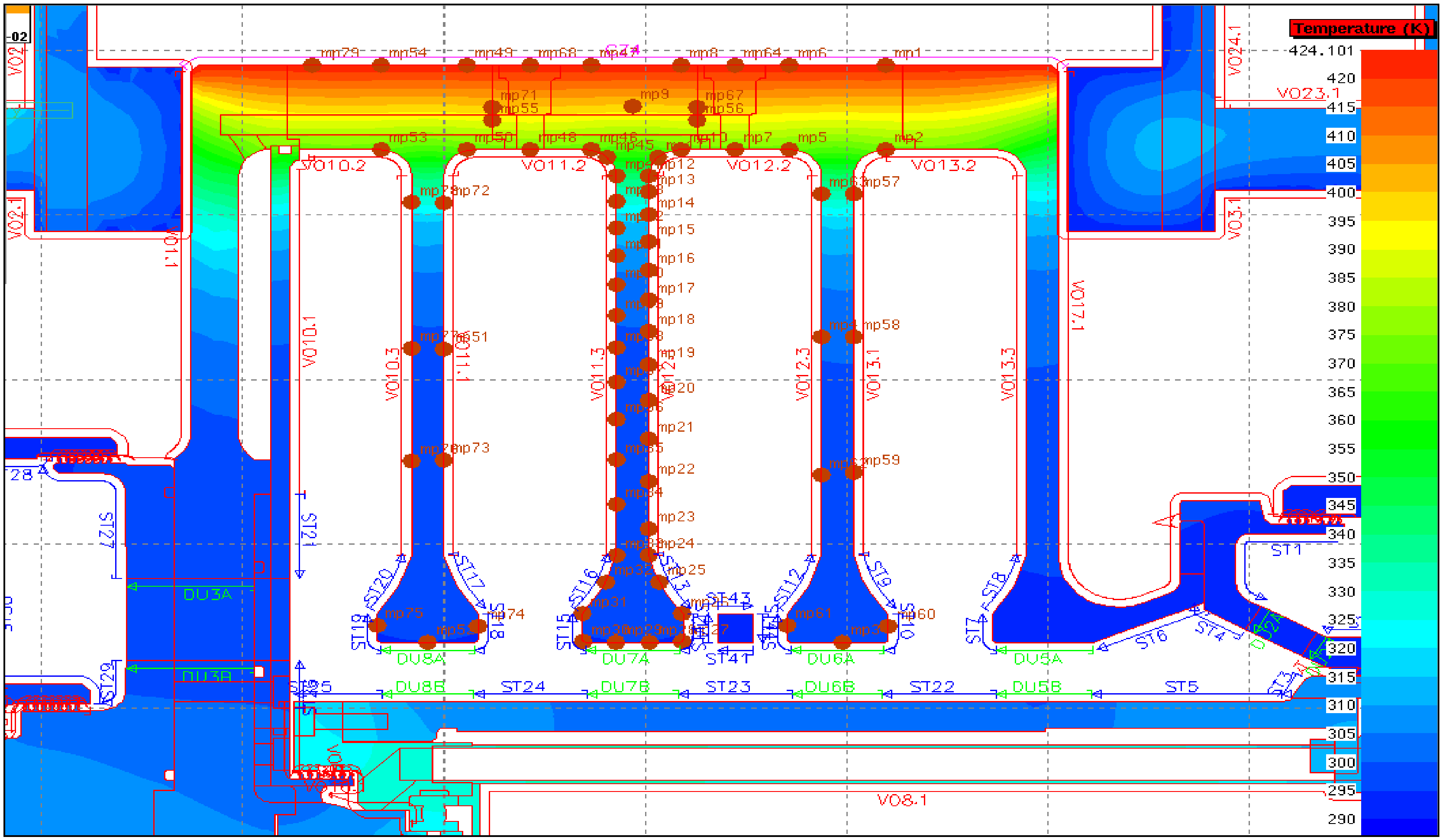

Figure 7.6: Temperature contour plots of the MCR baseline drum model with a bore temperature of 291K, rim temperature of 425K, idle and MTO speed of 3000rpm and 8000rpm respectively

The time constant analysis is performed at the top of the disc near the shroud, two positions on the disc and cob of the disc of discs 1, 2 and 3. The rotating-frame model points used for the time constant analysis are disc 2 upstream MP12, MP18 and MP22, MP28 for the disc cob, disc 2 downstream MP43, MP38 and MP35. The analyses for disc 2 upstream are presented in this section while the results for disc 2 downstream are presented as appendix 7.2.

Matlab programme was used for the post processing analysis of the results. The time constant analysis for four specified location on the upstream section of disc were obtained by evaluating the transient data using a first order model given by Equation 7.1.

$$T(t) = T_\infty + (T_0 - T_\infty)e^{\frac{-t}{\tau}} \tag{7.1}$$

where τ, is the time constant as given in Equation $\tau = \frac{mC}{hA}$ and $(T_0 - T_\infty) = \Delta T$, is the temperature change at each model point and t is time in seconds. The time constant is evaluated at the transients between the Idle and MTO during acceleration and MTO and Idle during deceleration in approximately 60 seconds. The results are presented in Sections 7.4.1 through to 7.5.1.1

7.4.1 MCR results of disc 2 upstream without radial inflow (baseline model)

The analyses for disc 2 upstream are presented in this section for model points MP12, MP18, MP22 and MP28 for the disc cob. Figure 7.7 shows the variation of rotating-frame metal temperature with time over the square cycle without radial inflow for seven model points (MP12, MP13, MP14, MP16, MP18, MP22 and MP28) on disc 2 upstream. This shows the metal temperature profiles during engine transient. The thermal growth characteristic shows different time constant during acceleration and deceleration for each model point location. This is due to differential thermal expansion of the disc and centrifugal acceleration associated with the disc in the cavity during different engine operation.

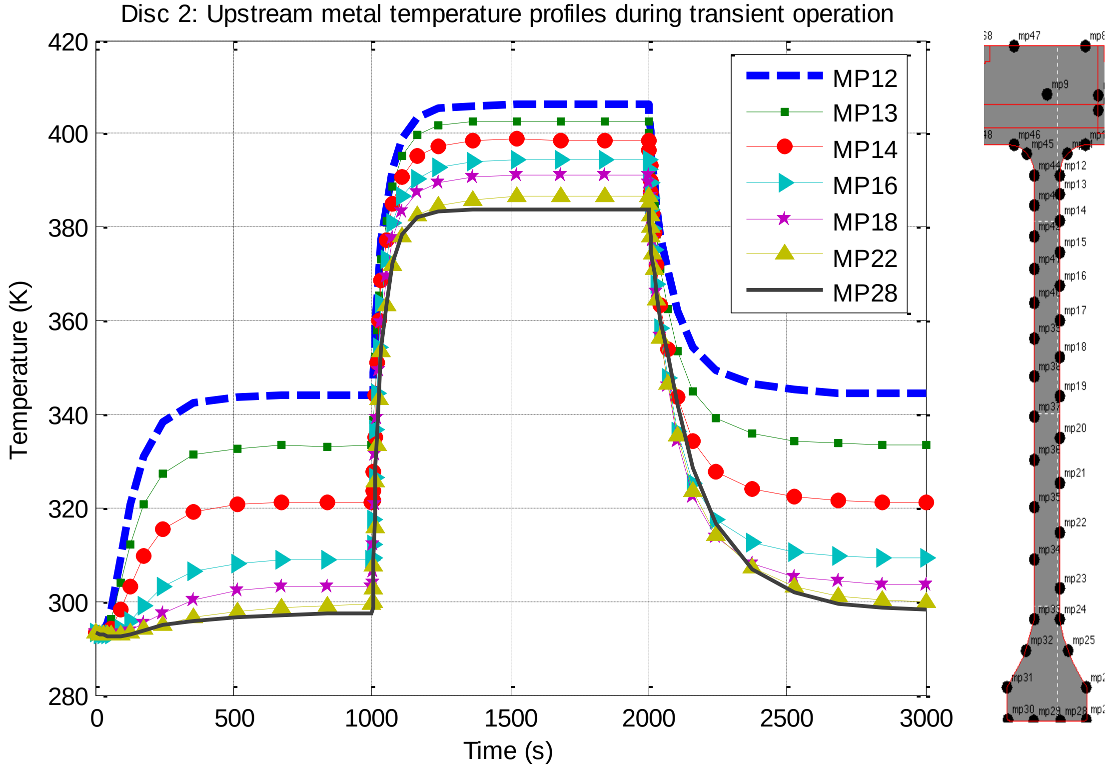

Figure 7.7: The variation of rotating-frame metal temperature with time over the square cycle without radial inflow for four model points on disc 2 upstream.

7.4.1.1 MCR results for model points MP12, MP18, MP22 and MP28

The baseline model thermal growth characteristics and time constant analysis for rotating-frame model points were obtained by increasing the heat transfer coefficient in the drum cavity and around the disc cob by a multiplicative factor of 2, 4, 6 and 8. The transient temperature profiles for the baseline (nominal) case, heat transfer coefficient increase factor (htc) of 2 and 8 are presented for clarity for MP12, MP18, MP22 and MP28. The time constant reduction factors and other results for all model points on disc 2 upstream can be assessed from individual Table in Appendix 7.4 through to 7.9.

Figure 7.8 shows the variation of temperature with time for baseline model at MP12 as a function of heat transfer coefficient. Analysis the baseline model with an increase in heat transfer coefficient in the cavity and around the disc cob would cause a reduction in disc time constant in the cavity.

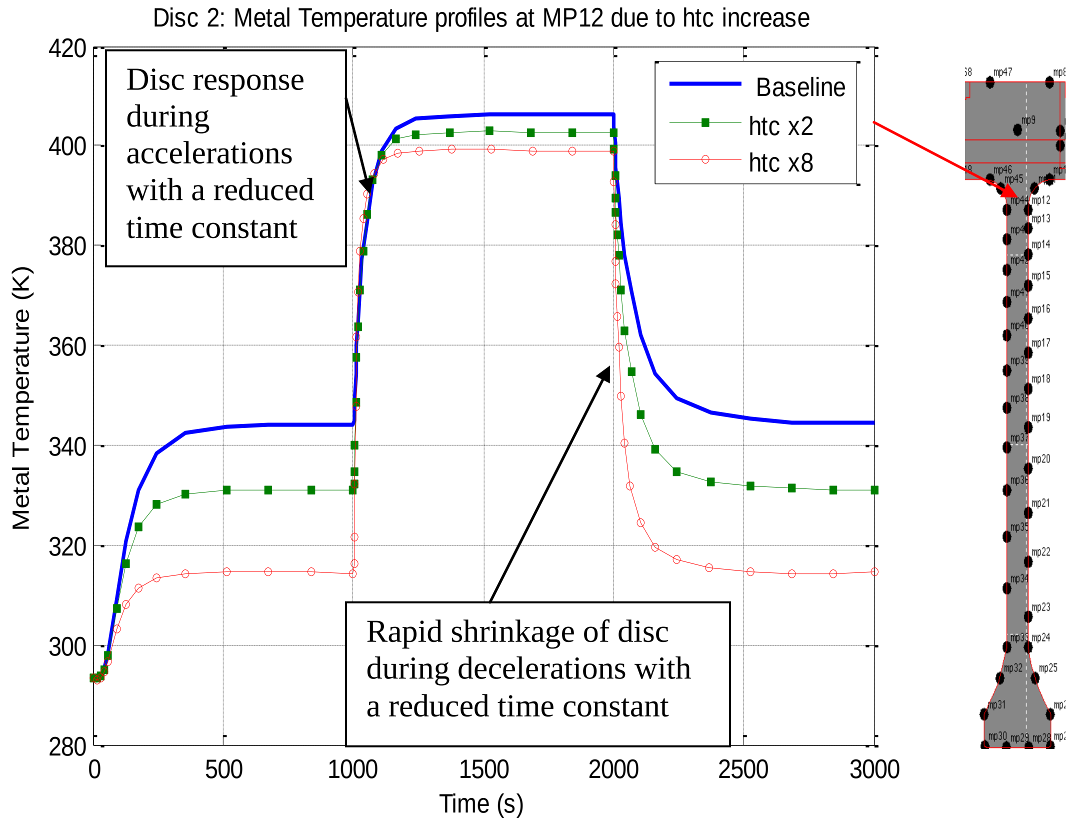

Figure 7.8: The variation of metal temperature with time for baseline model at MP12 on disc 2 upstream in cavity 3 of the MCR with increase in heat transfer coefficient during engine transient

Indication of time constant reduction from the baseline model with increase heat transfer coefficient factor is presented in Table 7.5 in the form percentage reduction and time constant reduction factor. For instance, the baseline model disc time constant at MP12 is reduced by approximately 31% during acceleration from Idle to MTO conditions and 28% during deceleration from MTO to Idle conditions with a heat transfer coefficient increased factor of 2 calculated against the baseline data.

Time constant reduction analysis for rotating-frame model point MP12						
htc increase factor	**τ_{accel} (s)**	**% reduction from baseline model**	**Time constant reduction factor**	**τ_{decel} (s)**	**% reduction from baseline model**	**Time constant reduction factor**
Baseline	48.92	0	1	81.93	0	1
2	33.60	31.33	1.46	59.35	27.56	1.38
4	23.88	51.18	2.05	44.49	45.70	1.84
6	19.87	59.38	2.46	39.28	52.05	2.09
8	18.14	62.93	2.70	36.09	55.95	2.27

Table 7.5: Time reduction analysis for rotating-frame model point MP12

During transient operation, there is a temperature change of 376.4K during acceleration from idle to max take-off and a temperature change of 358.4K during deceleration from max take-off to idle for heat transfer increase factor of 2. This gives a temperature difference of 7K and 9.6K for acceleration and deceleration when calculated against the baseline temperature change of 383.4K and 367.1K for acceleration and deceleration respectively. It is at this temperature change that the time constant is obtained. The temperature changes for all model points on disc 2 can be assessed from individual Table in Appendix 7.8 and 7.9.

Figure 7.9 shows the variation of temperature with time for baseline model at MP18 as a function of heat transfer coefficient. Increasing the heat transfer coefficient significantly reduces the disc time constant of the baseline model during both acceleration and deceleration. Evidence of the reduction is presented in Table 7.6.

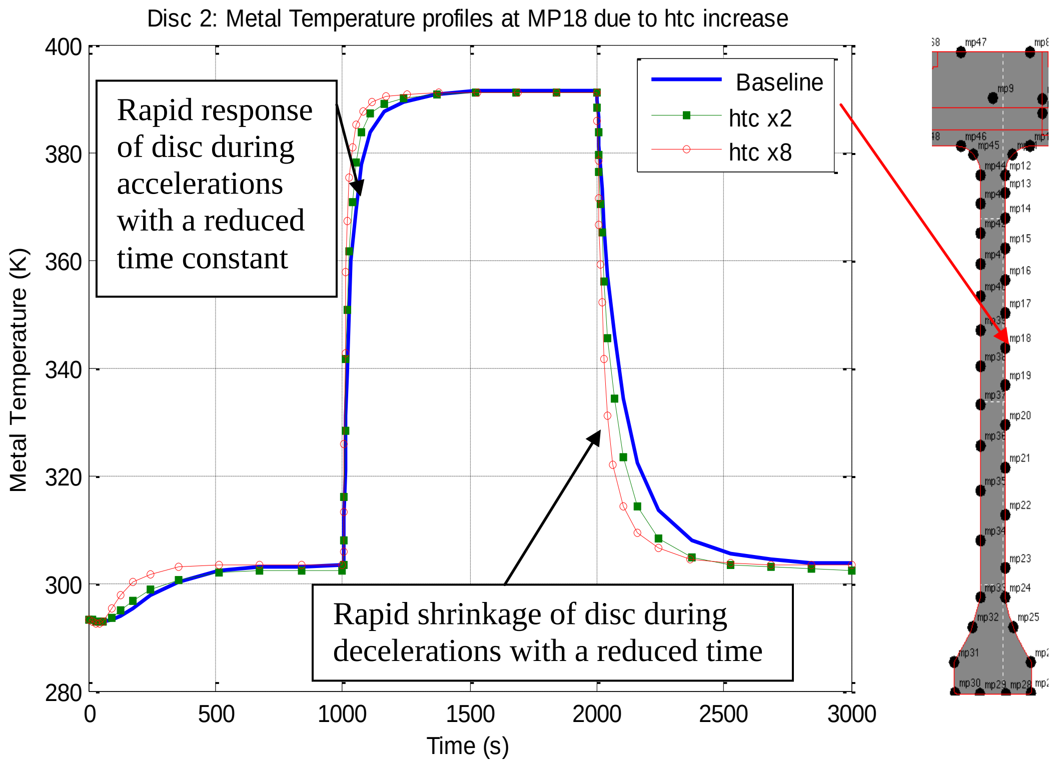

Figure 7.9: The variation of metal temperature with time for baseline model at MP18 on disc 2 upstream in cavity 3 of the MCR with increase in heat transfer coefficient during engine transient

During transient operation, there is a temperature change of 358.4K during acceleration from idle to max take-off and a temperature change of 335K during deceleration from max take-off to idle for heat transfer increase factor of 2.

Time constant reduction analysis for rotating-frame model point MP18						
htc increase factor	**τ_{accel} (s)**	**% reduction from baseline model**	**Time constant reduction factor**	**τ_{decel} (s)**	**% reduction from baseline model**	**Time constant reduction factor**
Baseline	35.34	0	1	97.78	0	1
2	24.23	31.43	1.46	65.39	33.13	1.50
4	18.28	48.27	1.93	47.64	51.29	2.05
6	16.39	53.62	2.16	40.99	58.08	2.39
8	15.35	56.58	2.30	37.67	61.47	2.60

Table 7.6: Time reduction analysis for rotating-frame model point MP18

The baseline model disc time constant at MP18 is reduced by approximately 31% during acceleration from Idle to MTO conditions and 33% during deceleration from MTO to Idle conditions with a heat transfer coefficient increased factor of 2 calculated against the baseline data.

Figure 7.10 shows the variation of temperature with time for baseline model at MP22 as a function of heat transfer coefficient. Confirmation of time constant reduction from the baseline model with increase heat transfer coefficient factor is documented in Table 7.7.

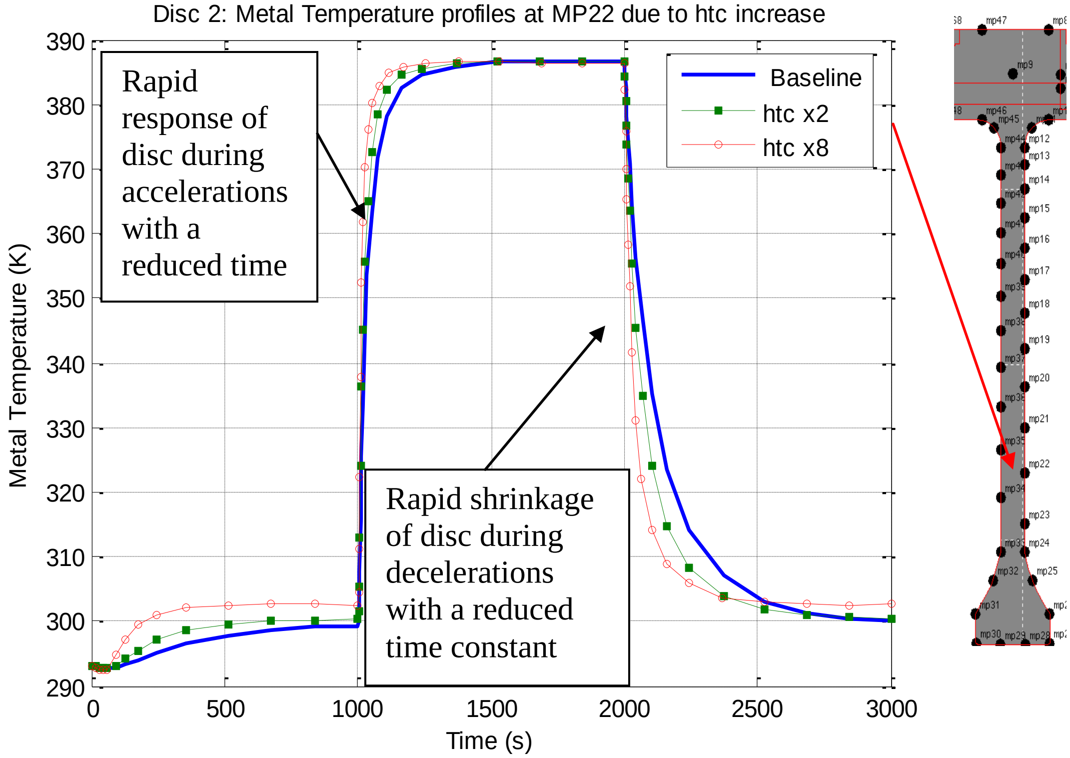

Figure 7.10: The variation of metal temperature with time for baseline model at MP22 on disc 2 upstream in cavity 3 of the MCR with increase in heat transfer coefficient during engine transient.

During transient operation, there is a temperature change of 354.8K during acceleration from idle to max take-off and a temperature change of 332.2K during deceleration from max take-off to idle for heat transfer increase factor of 2.

The baseline model disc time constant at MP22 is reduced by approximately 32% during acceleration from Idle to MTO conditions and 36% during deceleration from MTO to Idle conditions with a heat transfer coefficient increased factor of 2 calculated against the baseline data.

Time constant reduction analysis for rotating-frame model point MP22						
htc increase factor	**τ_{accel} (s)**	**% reduction from baseline model**	**Time constant reduction factor**	**τ_{decel} (s)**	**% reduction from baseline model**	**Time constant reduction factor**
Baseline	37.82	0	1	120.14	0	1
2	25.76	31.88	1.47	76.30	36.49	1.58
4	19.51	48.41	1.94	53.36	55.58	2.25
6	17.52	53.67	2.16	44.23	63.19	2.72
8	16.45	56.50	2.30	40.75	66.08	2.95

Table 7.7: Time reduction analysis for rotating-frame model point MP22

Figure 7.11 shows the variation of temperature with time for baseline model at MP28 as a function of heat transfer coefficient. Proof of time constant reduction from the baseline model with increase heat transfer coefficient factor is accessible in Table 7.8.

Time constant reduction analysis for rotating-frame model point MP28						
htc increase factor	**τ_{accel} (s)**	**% reduction from baseline model**	**Time constant reduction factor**	**τ_{decel} (s)**	**% reduction from baseline model**	**Time constant reduction factor**
Baseline	34.27	0	1	158.2	0	1
2	26.2	23.54	1.31	115.8	26.77	1.37
4	20.78	39.36	1.65	84.65	46.47	1.87
6	18.19	46.93	1.88	70.85	55.2	2.23
8	16.68	51.33	2.05	63.66	59.75	2.48

Table 7.8: Time reduction analysis for rotating-frame model point MP28

During transient operation, there is a temperature change of 298.6K during acceleration from idle to max take-off and a temperature change of 298.7K during deceleration from max take-off to idle for heat transfer increase factor of 2.

The baseline model disc time constant at MP28 is reduced by approximately 24% during acceleration from Idle to MTO conditions and 27% during deceleration from MTO to Idle conditions with a heat transfer coefficient increased factor of 2 calculated against the baseline data.

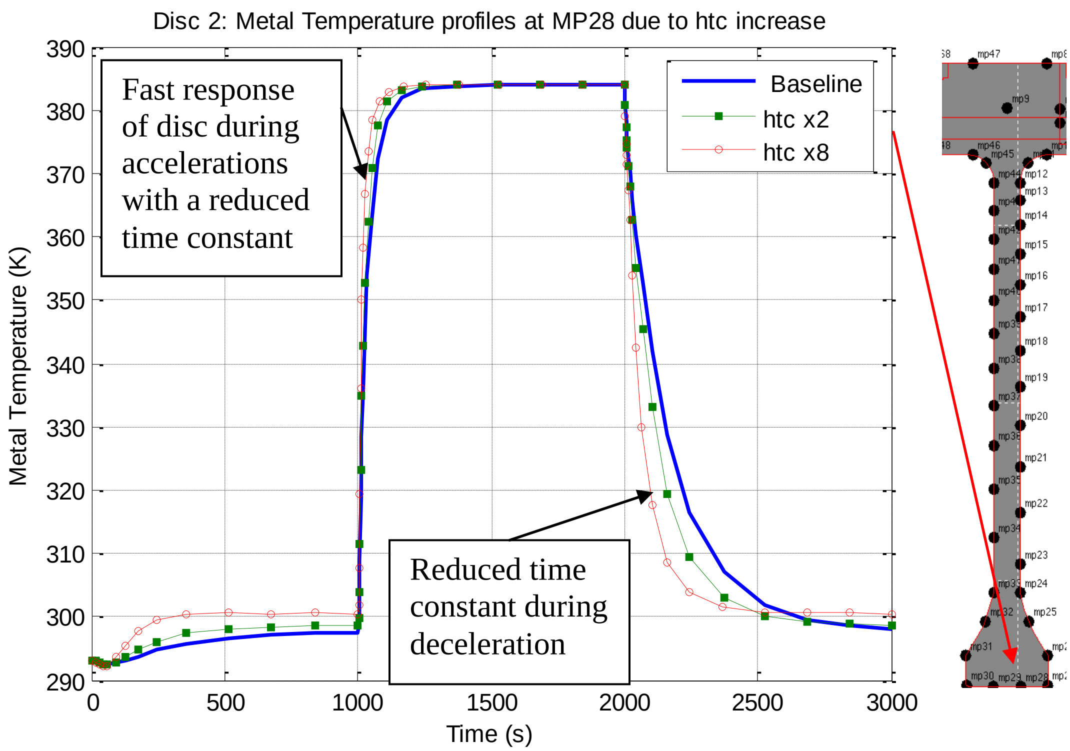

Figure 7.11: The variation of temperature with time for baseline model at MP28 on disc 2 upstream in cavity 3 of the MCR with increase in heat transfer coefficient during engine transient

Figure 7.12 shows the time constant reduction factor as a function of heat transfer coefficient for the baseline model during acceleration from “Idle to MTO” and deceleration from “MTO to Idle” over a square cycle for model points MP12, MP18, MP22 and MP28 on disc 2 upstream of the MCR drum.

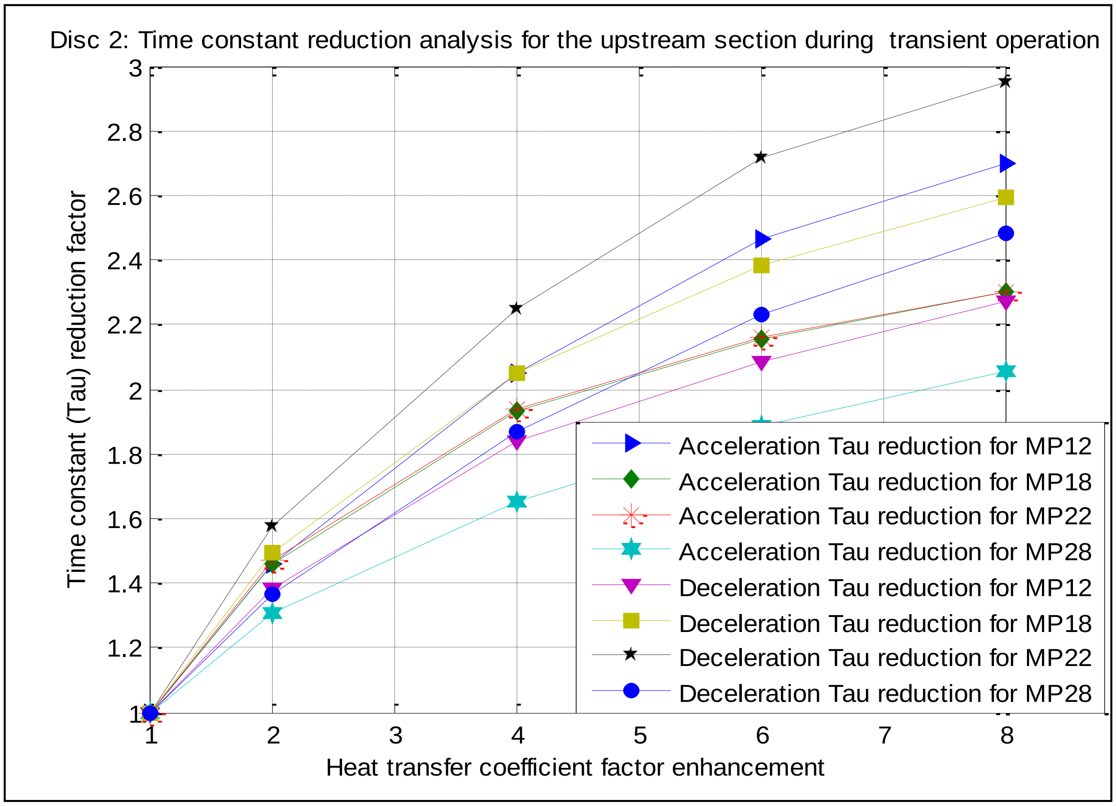

Figure 7.12: Time constant reduction factor as a function of heat transfer coefficient for the baseline model during acceleration from “Idle to MTO” and deceleration from “MTO to Idle” over a square cycle for model points MP12, MP18 and MP28 on disc 2 upstream of the MCR drum

For instance, the baseline model disc time constant at model points MP12, MP18, MP22 and MP28 has time constant reduction factor of approximately 1.46, 1.46, 1.47 and 1.31 during acceleration from Idle to MTO with a heat transfer coefficient increased factor of

2 which is equivalent to approximately 31%, 31%, 32%, and 25% reduction respectively. And a disc time constant of 1.38, 1.50, 1.58 and 1.37 during deceleration from MTO to Idle with a heat transfer coefficient increased factor of 2 which is equivalent to approximately 28%, 33%, 37% and 23% reduction respectively. A summary of other results for heat transfer coefficient multiplicative factor of 4, 6 and 8 for model points MP12, MP18, MP22 and MP28 during engine transient can be assessed from Table 7.5 through to Table 7.8.

Finally, metal temperature time profiles for baseline model for disc 2 upstream and downstream during acceleration and deceleration are shown in Figure 7.13 and Figure 7.14 respectively. The profiles give an indication of the time constant during engine transient for disc 2 with the model without radial inflow.

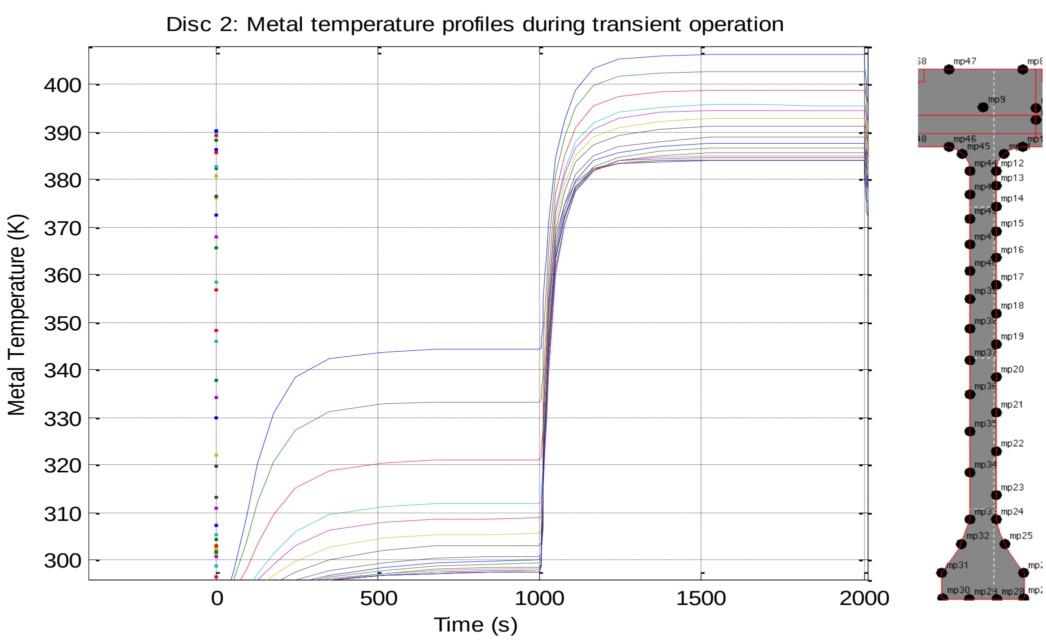

Figure 7.13: **Disc 2 metal temperature time profiles for baseline model during acceleration**

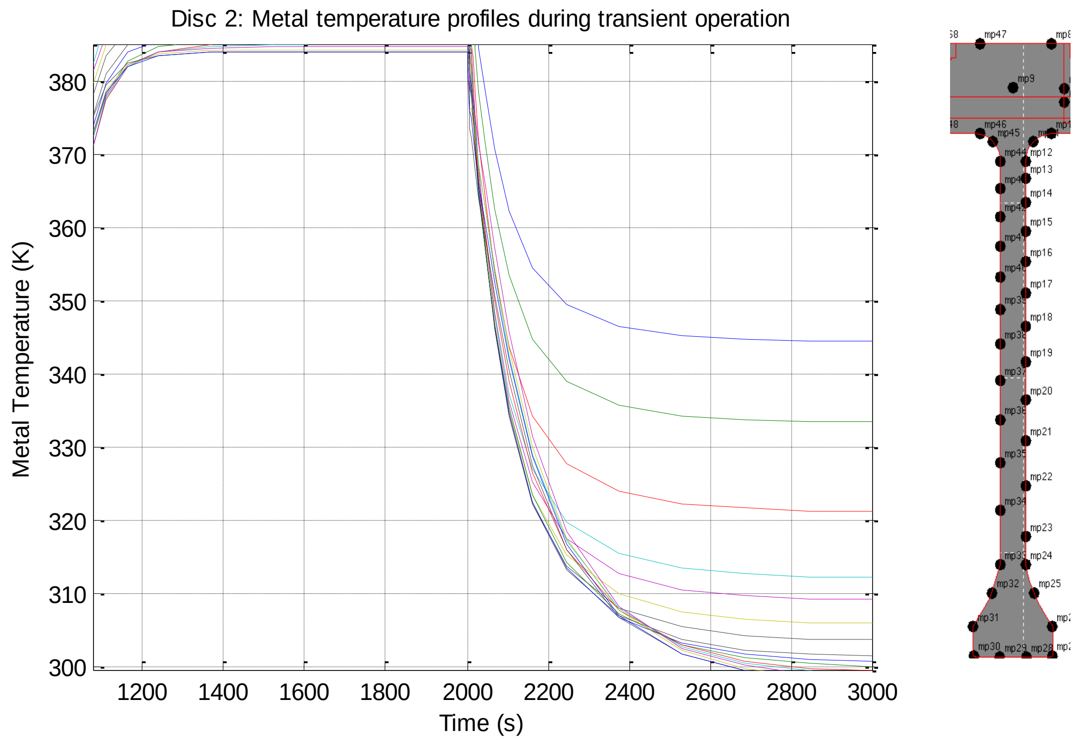

Figure 7.14: Disc 2 metal temperature time profiles for baseline model during deceleration

7.5 MCR results of Radial inflow model

Radial inflow is the bleed air from the compressor core flow which is ducted into the drum cavity to improve heat transfer in the cavity. The reductions of disc time constants are found to depend on the heat transfer coefficient increase of the disc. By introducing radial inflow into the cavity, an increase of the heat transfer coefficient of the disc is achieved and hence a reduction in the disc time constant. Five different radial inflow regimes were used for the analyses which are 1.6%, 2%, 3%, 4% and 6% of the bore mass flow. In the analysis presented in thesis, 6% radial inflow is used as the optimum value based on the pre-test computational fluid dynamic (CFD) analysis carry out by Dr. Atkins as part of the larger NEWAC programme. Figure 7.15 shows cavity 2 of the radial inflow model of the MCR remodelled with streams in place of the voids to allow for finite flow of fluid in the cavity. In this study, cavity 2 and 3 of the drum were remodelled to allow for a finite flow of fluid in the cavity. This was achieved by replacing the voids in the cavity with streams, and a radial inflow of fluid was supplied and ducted into the cavity through the radial inflow channels. Disc 2 of the MCR was used to demonstrate a proof of the concept. This was achieve through the reduction in the disc 2 heat expansion time constant by improving MCR drum heat transfer using bleed air from the MCR core flow.

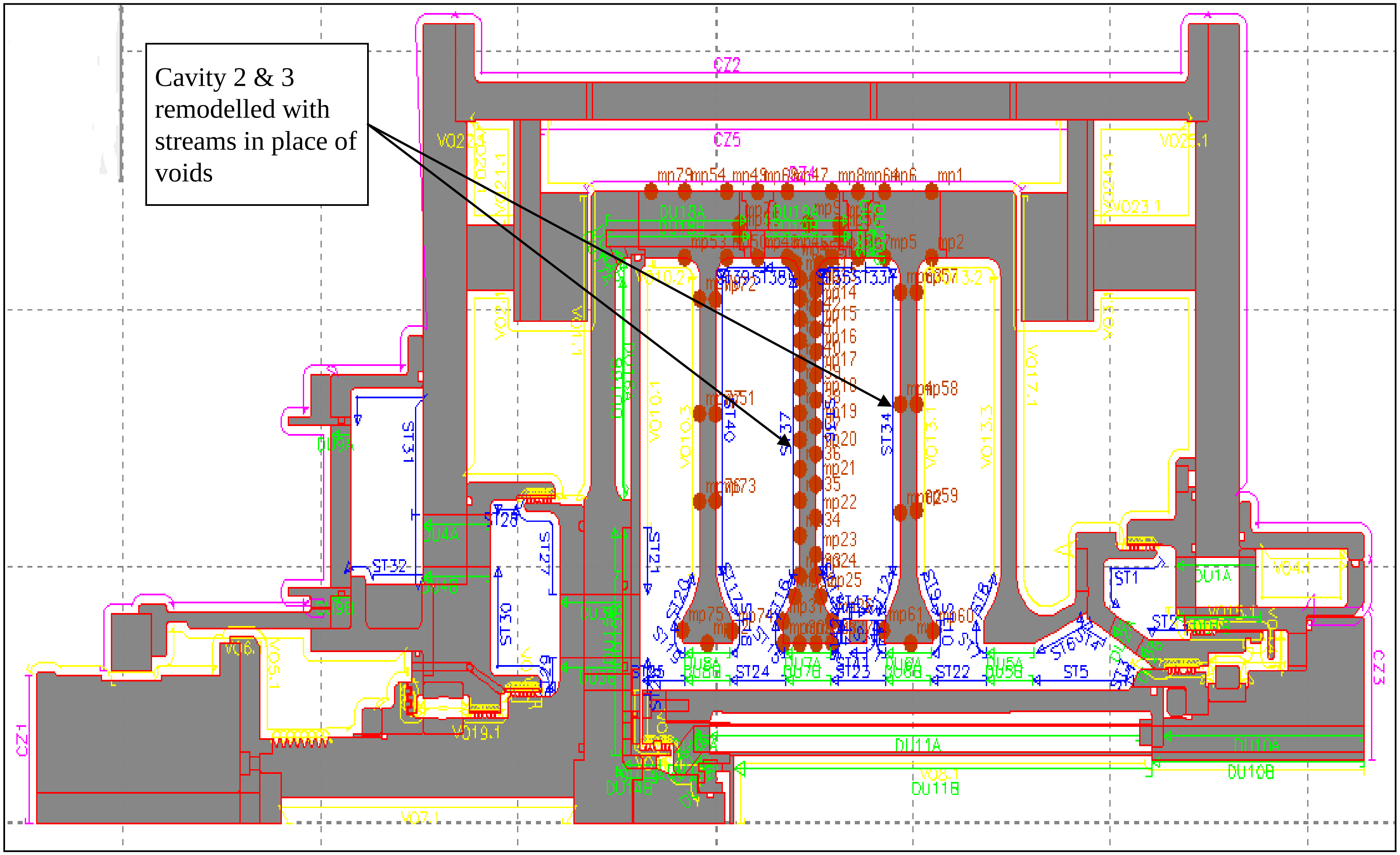

Figure 7.15: A finite element model of the MCR with cavity 2 remodelled with streams in place of the voids

7.5.1 MCR results of disc 2 upstream with radial inflow model

The results of the analysis for disc 2 upstream for model with radial inflow are presented in this section. The time constant analyses for radial inflow model were obtained by the introducing radial inflow into the cavity to increase heat transfer in the drum cavity. The rotating-frame model points used for the analysis in the cavity are MP12, MP18 and MP22 while MP28 used for the cob of the disc. Figure 7.16 shows the variation of rotating-frame metal temperature with time over the square cycle with 6% radial inflow for the seven model points on disc 2 upstream.

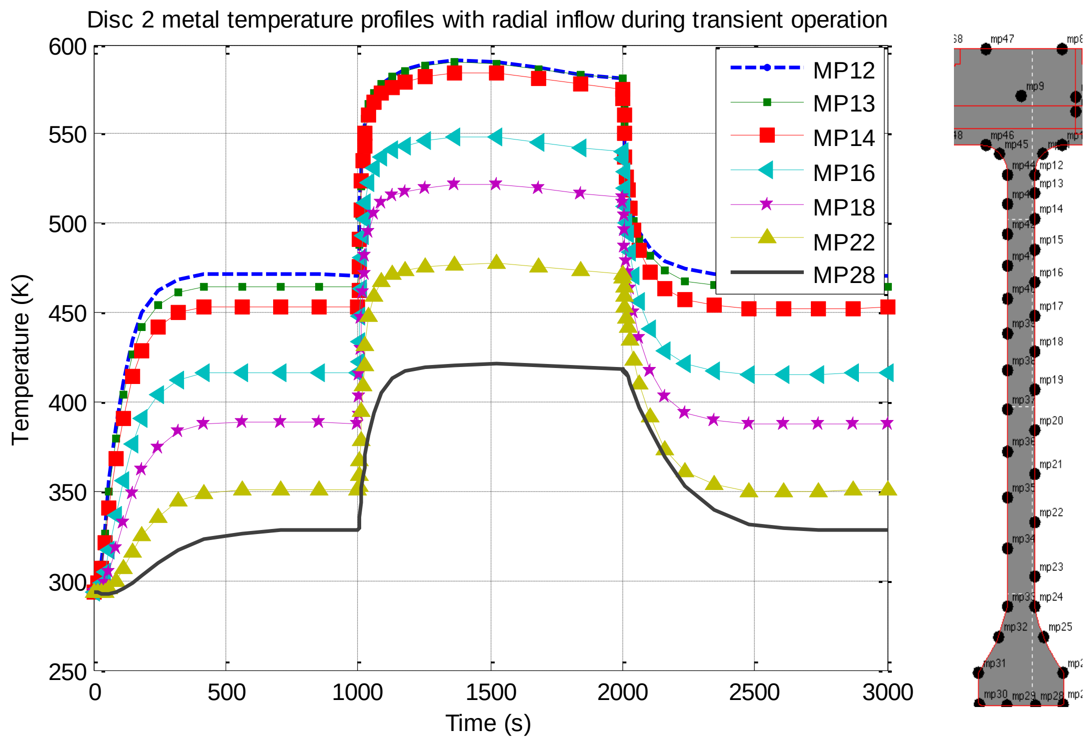

Figure 7.16: The variation of rotating-frame metal temperature with time over the square cycle with 6% radial inflow for four model points on disc 2 upstream.

This illustrates the metal temperature profiles during engine transient with radial inflow. The temperature time characteristic of Figure 7.16 shows different time constant during acceleration and deceleration for each model point location.

7.5.1.1 MCR results for model points MP12, MP18, MP22 and MP28 with radial inflow model

Figure 7.17 shows the variation of temperature with time for model with radial inflow at rotating-frame model point MP12 for various radial inflow regimes. Evidence of a significant time constant reduction with radial inflow model for different radial inflow percentage is presented in Table 7.9 for rotating-frame model point MP12.

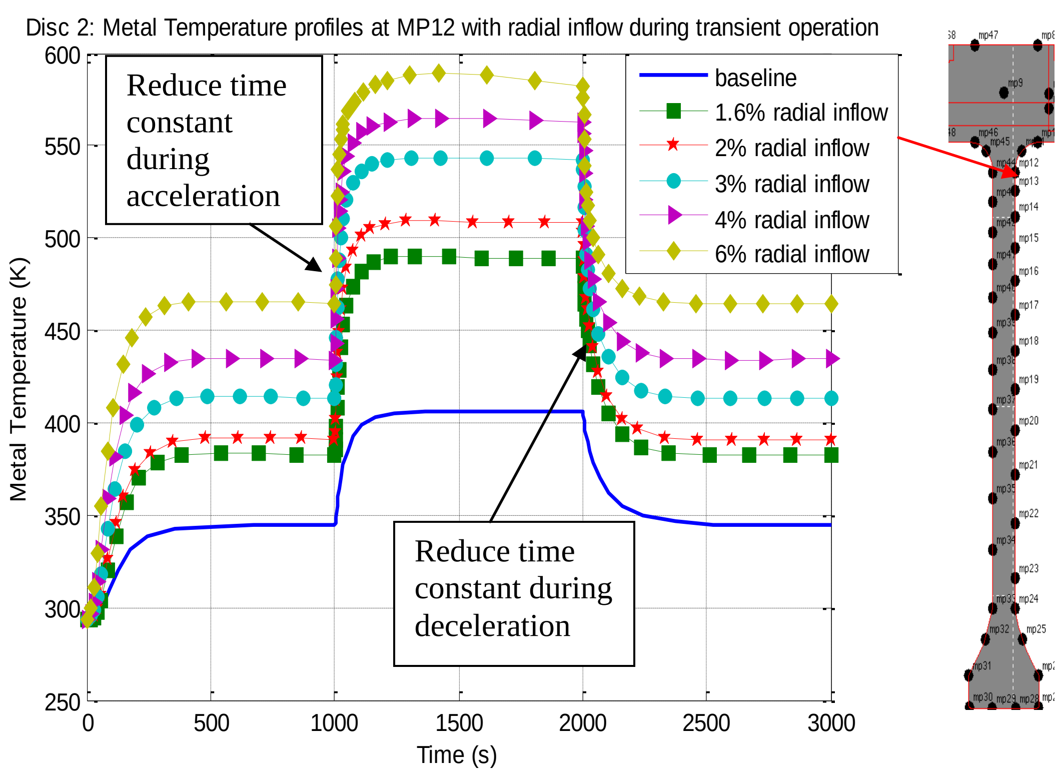

Figure 7.17: The variation of temperature with time for model with radial inflow at model point location MP12 on disc 2 upstream in cavity 3 of the MCR

During transient operation with radial inflow, there is a temperature change of 539.1K during acceleration from idle to max take-off and a temperature change of 508.0K during deceleration from max take-off to idle with a 6 % radial inflow. This gives a temperature difference of 155.7K and 140.9K for acceleration and deceleration when calculated against the baseline temperature change of 383.4K and 367.1K for acceleration and deceleration respectively. It is at this temperature change that the time constant is obtained. The temperature changes for all model points on disc 2 with different percentage radial inflows can be assessed from individual Table in appendix 7.9.

Time constant reduction analysis for rotating-frame model point MP12 with radial inflow						
Flow regimes (% of bore mass flow)	**τ_{accel} (s)**	**% reduction from baseline model**	**Time constant reduction factor**	**τ_{decel} (s)**	**% reduction from baseline model**	**Time constant reduction factor**
Baseline	48.92	0	1	81.93	0	1
1.6	32.69	33.18	1.50	61.65	24.75	1.33
2	28.68	41.38	1.71	55.29	32.51	1.48
3	22.25	54.51	2.20	44.29	45.94	1.85
4	18.60	62.00	2.63	38.63	52.85	2.12
6	15.20	68.92	3.22	31.19	61.93	2.63

Table 7.9: Time reduction analysis for rotating-frame model point MP12 with radial inflow

Radial inflow introduction into the cavity shows a significant reduction in disc time constant. For instance, with radial inflow, the disc time constant at MP12 is significantly reduced by approximately 69% during acceleration from Idle to MTO conditions and 62% during deceleration from MTO to Idle conditions with 6% radial inflow calculated against the baseline data. Figure 7.18 shows the variation of temperature with time for model with radial inflow at rotating-frame model point MP18 for various radial inflow regimes. Evidence of time constant reduction from the radial inflow model with different radial inflow percentage is presented in Table 7.10 for rotating-frame model point MP18.

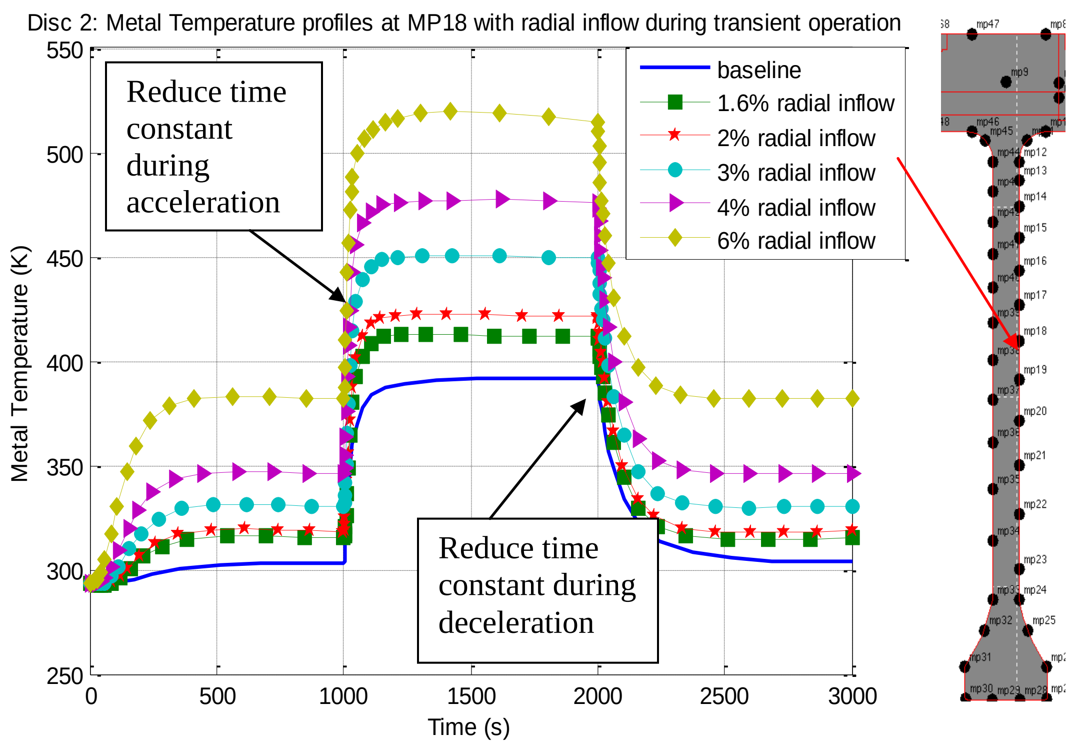

Figure 7.18: The variation of temperature with time for model with radial inflow at model point location MP18 on disc 2 upstream in cavity 3 of the MCR with increase in radial inflow

During transient operation with radial inflow, there is a temperature change of 465.8K during acceleration from idle to max take-off and a temperature change of 430.9K during deceleration from max take-off to idle with a 6 % radial inflow.

The disc time constant at MP18 with radial inflow is reduced significantly by approximately 36% during acceleration from Idle to MTO conditions and 33% during deceleration from MTO to Idle conditions with 6% radial inflow calculated against the baseline data.

Time constant reduction analysis for rotating-frame model point MP18 with radial inflow						
Flow regimes (% of bore mass flow)	**τ_{accel} (s)**	**% reduction from baseline model**	**Time constant reduction factor**	**τ_{decel} (s)**	**% reduction from baseline model**	**Time constant reduction factor**
Baseline	35.34	0	1	97.78	0	1
1.6	32.70	7.47	1.08	87.96	10.04	1.11
2	32.72	7.41	1.08	86.68	11.35	1.13
3	30.20	14.57	1.17	82.50	15.63	1.19
4	26.93	23.80	1.31	76.12	22.15	1.29
6	22.77	35.56	1.55	65.67	32.84	1.50

Table 7.10: Time reduction analysis for rotating-frame model point MP18 with radial inflow

Figure 7.19 shows the variation of temperature with time for model with radial inflow at rotating-frame model point MP22 for various radial inflow regimes. Table 7.11 shows proof of time constant reduction for the radial inflow model with different radial inflow regimes in the form percentage reduction and time constant reduction factor for rotating-frame model point MP22.

Time constant reduction analysis for rotating-frame model point MP22 with radial inflow						
Flow regimes (% of bore mass flow)	**τ_{accel} (s)**	**% reduction from baseline model**	**Time constant reduction factor**	**τ_{decel} (s)**	**% reduction from baseline model**	**Time constant reduction factor**
Baseline	37.82	0	1	120.14	0	1
1.6	35.51	6.10	1.07	110.50	8.023	1.09
2	36.25	4.14	1.04	110.88	7.71	1.08
3	34.93	7.63	1.08	109.82	8.60	1.10
4	32.90	13.00	1.15	104.10	13.36	1.15
6	27.70	26.76	1.37	93.64	22.06	1.28

Table 7.11: Time reduction analysis for rotating-frame model point MP22 with radial inflow

During transient operation with radial inflow, there is a temperature change of 425.2K during acceleration from idle to max take-off and a temperature change of 392.1K during deceleration from max take-off to idle with a 6 % radial inflow.

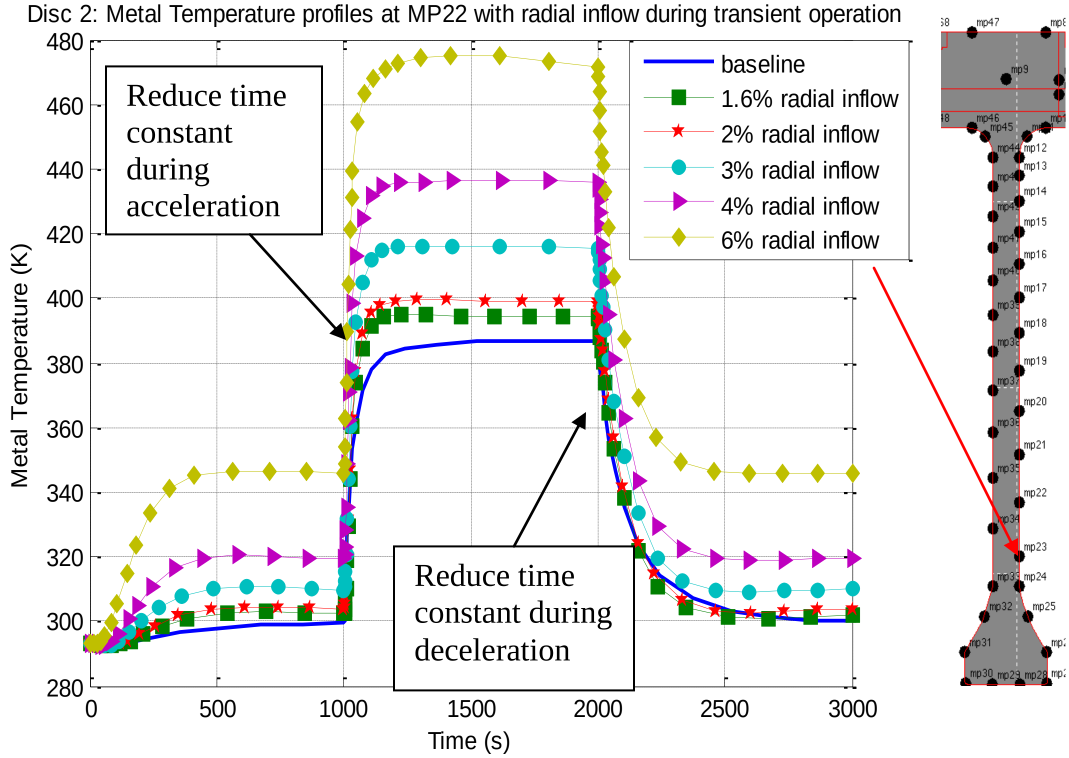

Figure 7.19: The variation of temperature with time for model with radial inflow at model point location MP22 on disc 2 upstream in cavity 3 of the MCR with increase in radial inflow.

The radial inflow model disc time constant at MP22 is reduced by approximately 27% during acceleration from IDLE to MTO conditions and 22% during deceleration from MTO to IDLE conditions with 6% radial inflow calculated against the baseline data.

Figure 7.20 shows the variation of temperature with time for model with radial inflow at rotating-frame model point MP28 as a function of heat transfer coefficient. With radial inflow, the heat transfer around the disc cob is less when compared to other parts of the disc as such no reduction in disc time constant in the cob region as expected. Evidence of time constant increase in the disc cob region for the model with radial inflow at rotating-frame model point MP28 is accessible in Table 7.12 in the form percentage reduction and time constant reduction factor.

Time constant reduction analysis for rotating-frame model point MP28 with radial inflow						
Flow regimes (% of bore mass flow)	**τ_{accel} (s)**	**% reduction from baseline model**	**Time constant reduction factor**	**τ_{decel} (s)**	**% reduction from baseline model**	**Time constant reduction factor**
Baseline	34.27	0	1	158.16	0	1
1.6	45.30	-32.14	0.76	190.36	-20.36	0.83
2	45.62	-33.12	0.75	190.75	-20.61	0.83
3	46.44	-35.51	0.74	196.20	-24.06	0.81
4	46.80	-36.57	0.73	198.77	-25.68	0.80
6	46.65	-36.12	0.74	198.76	-25.67	0.80

Table 7.12: Time reduction analysis for rotating-frame model point MP28 with radial inflow

During transient operation with radial inflow, there is a temperature change of 383.5K during acceleration from idle to max take-off and a temperature change of 357.3K during deceleration from max take-off to idle with a 6 % radial inflow. The introduction of radial inflow into the cavity does not increase the heat transfer (has less effect) around the disc cob region. This is so because the disc cob region comes into contact with the bore flow more than other part of the disc during engine operation resulting in a significant increase in the disc time constant. For instance, the disc time constant at MP28 is increased by approximately 36% during acceleration from Idle to MTO conditions and 25% during deceleration from MTO to Idle conditions with 6 % radial inflow calculated against the baseline data.

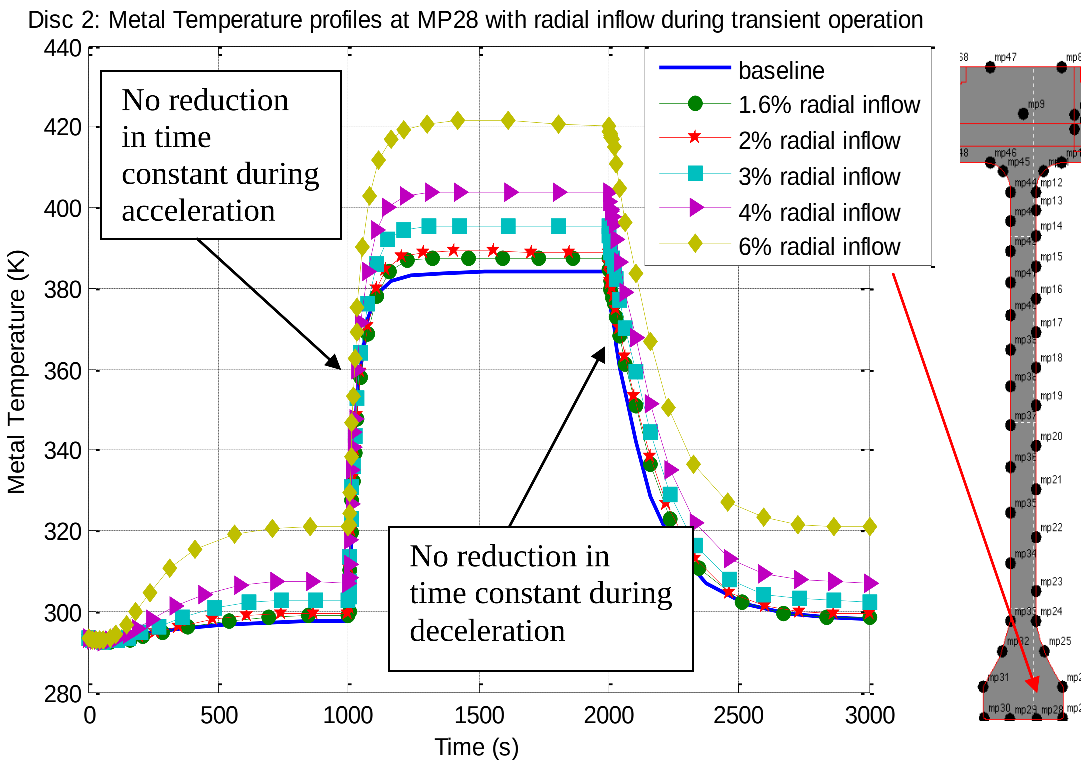

Figure 7.20: The variation of temperature with time for model with radial inflow at model point location MP28 on disc 2 upstream in cavity 3 of the MCR with increase in radial inflow.

Figure 7.21 shows the time constant reduction factor as a function of radial inflow during acceleration from "Idle to MTO" and deceleration from "MTO to Idle" over a square cycle for model points MP12, MP18, MP22 and MP28 on disc 2 upstream of the MCR drum. For instance, with 6% radial inflow, the disc time constant at MP12, MP18, MP22 and the disc cob model point MP28 has time constant reduction factor of approximately

3.22, 1.31, 1.37 and 0.74 respectively during acceleration from Idle to MTO conditions. This is equivalent to approximately 69%, 36%, and 27% reduction with a 36% increase for the disc cob respectively calculated against the baseline data. And approximately 2.63, 1.50, 1.28 and 0.80 which is equivalent to approximately 62%, 33%, and 22% reduction with a 26% increase for the disc cob respectively during deceleration from MTO to Idle conditions with 6% radial inflow calculated against the baseline data.

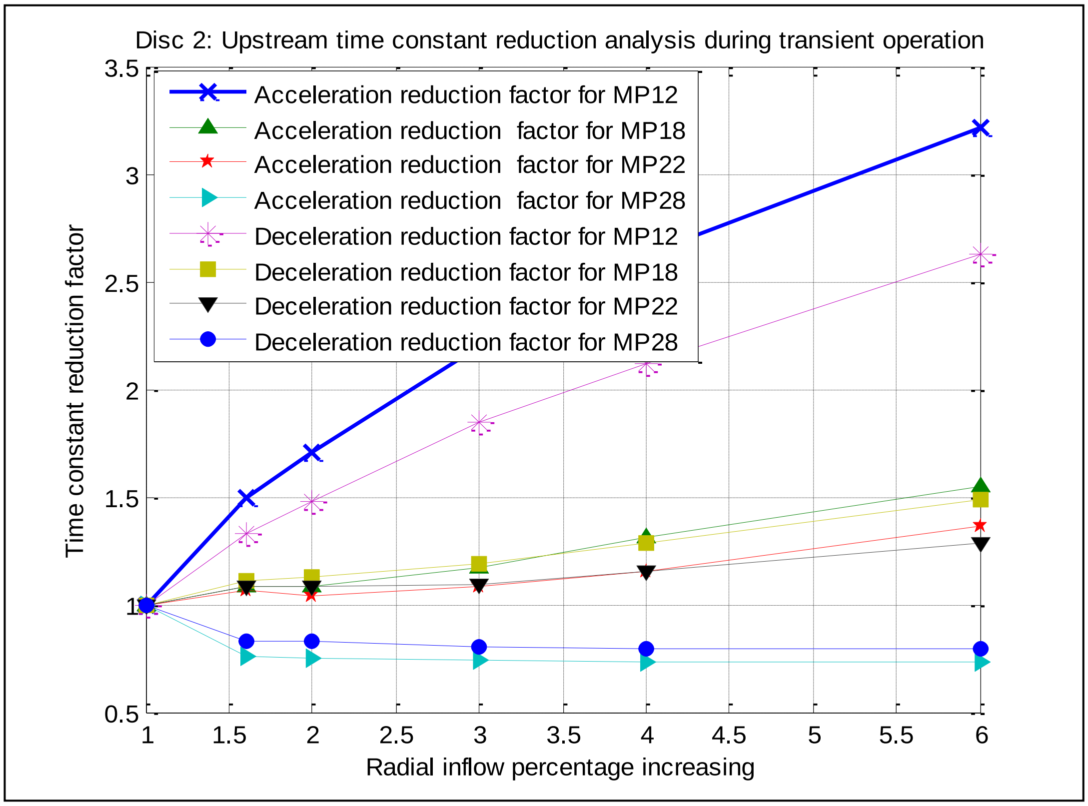

Figure 7.21: Time constant reduction factor as a function of radial inflow during acceleration from "Idle to MTO" and deceleration from "MTO to Idle" over a square cycle for model points MP12, MP18, MP22 and MP28 on disc 2 upstream of the MCR drum.

A summary of other results for radial inflow percentage of 1.6, 2, 3 and 4 for model points MP12, MP18, MP22 and MP28 during engine transient can be assessed from

Table 7.9 through to Table 7.12. As expected, the introduction of radial inflow into the cavity does not increase the heat transfer around the disc cob region as shown in the MP28 model point time constant reduction plot and data of Figure 7.25 and Table 7.17 respectively.

Finally, metal temperature time profiles for model with radial inflow for disc 2 upstream and downstream during acceleration and deceleration are shown in Figure 7.22 and Figure 7.23 respectively. The profiles give an indication of the time constant during engine transient for disc 2 with model with radial inflow.

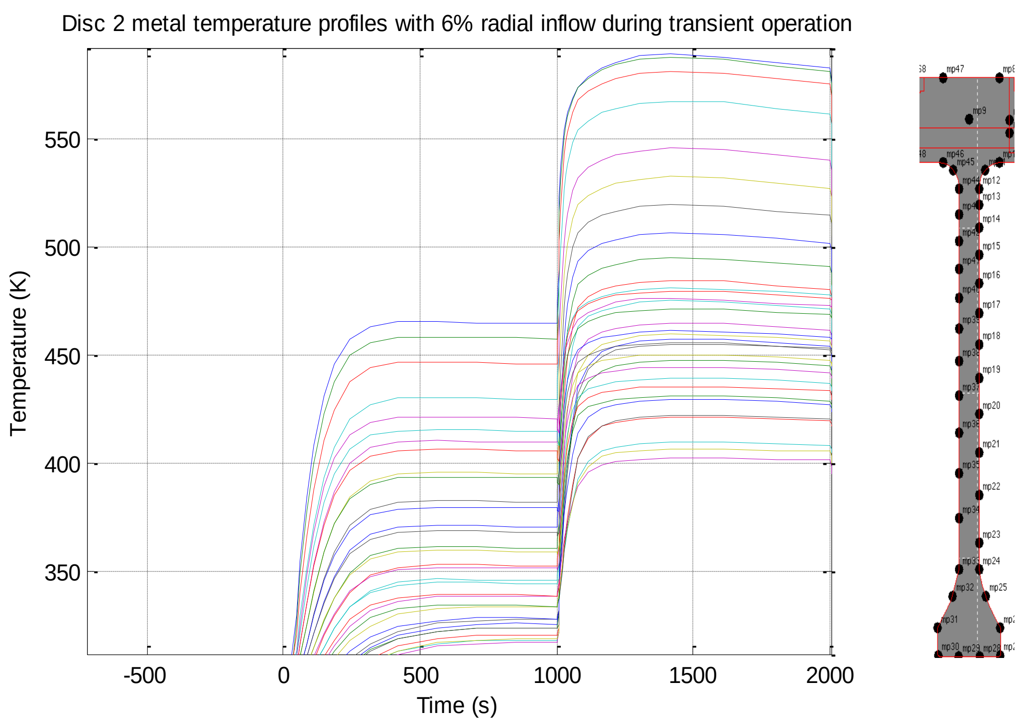

Figure 7.22: Disc 2 metal temperature time profiles for model with 6% radial inflow during acceleration.

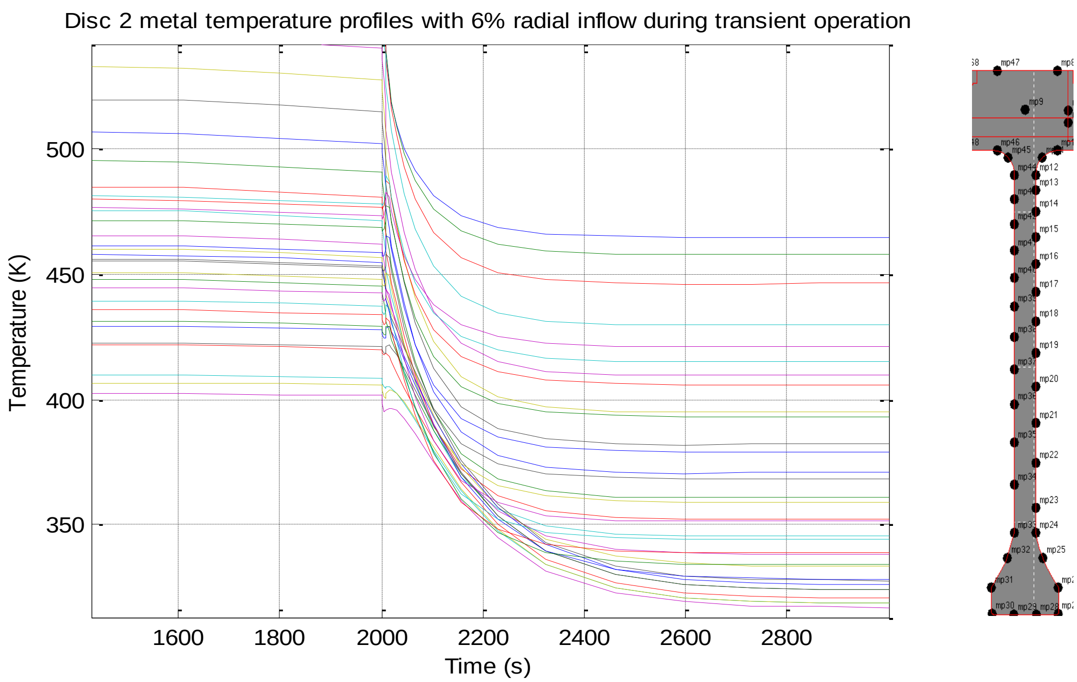

Figure 7.23: Disc 2 metal temperature time profiles for model with 6% radial inflow during deceleration.

7.6 Discussion of results

In SC03 predictions, the transients between the IDLE and MTO conditions during acceleration and between MTO and IDLE during deceleration were achieved in approximately 60 seconds. In the SC03, the radial inflow intensities shown indicate a noticeable and considerable reduction in the disc time constant. As expected, the concept of reducing disc time constant through the introduction of radial inflow is achieved. The SC03 result for the heat transfer shows that the radial inflow does not have as much effect in the disc cob region as in other parts of the disc as expected. The reason is that the tip area of the disc cob region comes into contact with the bore flow more in comparison to the rest of the disc. This effect is less for MTO than for IDLE conditions.

At both IDLE and MTO conditions, the location near rim region such as MP1 and MP79 are less affected in terms of time constant reduction. The absence of this effect implies that the time constant reduction at this point is controlled by the thermal mass of the thick outer rim of the drum at lower power. Nevertheless, a reduction in thermal mass of the rim was discarded due to the increased complication and risk such reduction would introduce to the overall project.

With the introduction of radial inflow into the drum cavity, the average temperature of the complete disc is elevated. There is also a significant effect of radial inflow on the radial temperature profile, even at very low levels of bore flow per cavity. For instance, with as low as 1.6% bore mass flow (radial inflow), MP12 has radial temperature of 44 K more than the baseline model and 2 K more at MP28 of the disc cob. The clarification of this effect is that immediately away from the viscous boundary layers the Coriolis forces become dominant (Atkins, 2013). Due to continuous rotation of the disc, the radial inflow fluid is restrained to the thin layers on the disc surfaces, which is in good agreement with Owen et al. (1989). During this process the angular momentum is conserved, the circumferential velocity of radial inflow is enhanced as it advances down the disc. The relative velocity in the circumferential direction causes an increase in the heat transfer coefficient. From the analysis of the five regimes of radial inflow, comparing to the baseline model, the radial inflow causes an increase in the radial temperature gradients in the cob region. As the intensity radial inflow is increased, the normalised temperature of the disc is increased and there a reduction in the temperature gradient on the outer parts of the disc. This manner is most prominent in the near shroud and diaphragm regions, but reduces towards the cob region as the axial flow becomes dominant.

7.7 Summary

Increasing the inbuilt heat transfer coefficient in the cavity and around the disc cob region would reduce the disc time constant. The reduction in disc time constant can be enhanced by introducing radial inflow into the drum. The radial inflow which is the bleed air from the core flow will increase the heat transfer in the drum cavity hence improving the heat transfer coefficient. From the baseline model, the continuous increase of the inbuilt heat transfer coefficient will not in a long term guarantee continuous reduction in disc time constant hence the need for a bleed air from the core flow. By introducing the radial inflow into cavity 3, the average temperature of the disc 2 is raised. Relative to the baseline model, there is also a reduction in temperature gradient along the disc downward from the shroud. The analysis with radial inflow in cavity 3 shows a possible reduction in disc 2 time constant by approximately 69%, 36% and 27% during acceleration and 62%, 33% and 22% during deceleration with 6% radial inflow at MP12, MP18 and MP22 respectively on disc 2 upstream calculated against the baseline nominal data. This is equivalent to a time constant reduction of 3.22, 1.31 and 1.37 during acceleration and 2.63, 1.50 and 1.28 during deceleration from the baseline model for model points MP12, MP18 and MP22 respectively. Taking an average of the time constant reduction values for model points (MP12, MP18 and MP22) along the disc, it shows that with 6% radial inflow, the disc time constant may be reduce by approximately 2.0 during acceleration and 1.80 during deceleration.

However, the effect of heat transfer increase is less at the disc cob region than other part of the disc because the disc cob region comes into contact with the bore flow more. As expected, the introduction of radial inflow into the cavity does not increase the heat transfer (has less effect) around the disc cob region. This is evidence in the MP28 model point time constant with 36% and 26% increase for the disc cob during acceleration and deceleration respectively calculated against the baseline data.

Finally, the concept of disc time constant reduction using the radial inflow works as anticipated. With the quantity of radial inflow employed in the analysis, there is an evident and significant reduction in the disc time constant.

Chapter 8

CONCLUSIONS AND RECOMMENDATIONS FOR FUTURE WORK

Section 8.1 provides general remarks on tip clearance control concepts with an overview of the models, experimental apparatus and the range of analysis carried out. The conclusions from the sensitivity analysis are presented in section 8.2. Section 8.3 provides the conclusions from 1-D analysis. This is the validation of the SC03 results with a lumped parameter model while the conclusions on 2-D modelling of MCR are presented in section 8.4. Finally, Section 8.5 gives some recommendations for possible future work.

8.1 General remarks

This thesis presents the results for tip clearance control concepts using Rolls-Royce Trent 1000 engine thermo-mechanical drum and casing models, lumped parameter models, and multiple cavity rotating rig (MCR) models representing the internal air system flows within a high-pressure (HPC) compressor. In the internal air system, air extracted from the intermediate-pressure (IPC) compressor and destined for the low-pressure (LPC) turbine discs and seals flows axially through the annular passage between the HP compressor disc bores and the enclosed IP drive shaft. The multiple cavity rig was modelled to be geometrically similar (approximately 70% of full size) to current Rolls-Royce Trent 1000 gas turbine aero-engines. It had a titanium-318 rotor comprising three discs. The completed rotor assembly of the MCR formed four cylindrical cavities. Each cylindrical cavity had an outer radius of b = 220 mm and the axial distance between the discs was s = 42.9 mm, giving a gap ratio G = s/b = 0.195 with an inner radius a = 70.1 mm. The drum was modelled with 82 model point for disc temperature measurement and ducts were also modelled for the supply and delivery of the radial inflow into the cavity. The mechanical design of the test facility allows the simulation of flow conditions in the HP compressor cavity equivalent to the Trent 1000 aero-engine, with a rotational speed of up to 10000 rpm. The idle and maximum take-off conditions in the square cycle correspond to in-cavity rotational Reynolds numbers of $3.1\times10^{6} \le \mathrm{Re}_{\varphi} \le 1.0\times10^{7}$.

The thermo-mechanical analysis software used is in this study is called SC03. This is the Rolls-Royce in-house modelling software. The SC03 software computes component temperatures, stresses, engine movement, and the deflections of axisymmetric or plane structures, as well as clearance optimisation using a priori knowledge of all the system's heat transfer coefficients. The finite element thermo-mechanical model of the multiple cavity rig (MCR) is calibrated against the lumped parameter model and the results compare with engine analysis.

Another study undertaken was the review of patent relevant to tip clearance control in H.P. compressor. This patents review gave correct interpretation of patents in terms of the type of control system, the area of application on the engine, and the control scheme. They were generally grouped into passive clearance control system and active clearance control system. The reviews help to outline the possible methods for tip clearance control. The patent documents were very useful during the TRIZ sessions. It was in the TRIZ sessions that the choice of the method for this study was chosen. A passive clearance control method was chosen for this study. Following the choice of the scheme for the study, a sensitivity study was undertaken using RB211-524 and Trent 1000 casing and drum models. Two analyses were performed, one without radial inflow (baseline model) and another with radial inflow. Finally, a 2-D modelling of MCR analysis with and without radial inflow of air was carried out to ascertain the effect of radial inflow on drum time constant.

The objective of this research was to develop a concept for tip clearance control in the H.P. compressor. A passive clearance control scheme was employed for this project. This involves the control of disc and casing thermal response during engine transient. This was achieved by increasing the heat transfer coefficient of the drum through the modelling of radial inflow of air into the compressor cavity. This will speed up the thermal response of the drum hence controlling the clearance between casing and the blade tip during engine transient.

8.2 Conclusions from Sensitivity analysis

Based on the results from the TRIZ session, a sensitivity analysis was carried out. This was to determine the quantitative effects of various parameters on the closure behaviour of the various high-pressure compressor stages. The parameters investigated include heat transfer coefficient, cavity mass flow and time constants. The most promising ideas generated during the session were analysed using the drum and casing models of the RB211-524 model and Trent 1000 engine.

The intention of this study was to decrease the time constant of the drum by increasing the relevant heat transfer coefficients. This will cause the compressor drum to heat up faster, hence narrowing the large gap that existed at the beginning of engine transient operation between the casing and the blade. This would effect a reduction in the cruise clearance and a reduction in clearance at first acceleration (max take-off) and hence a reduction in the overall specific fuel consumption, giving rise to higher engine efficiency. The sensitivity analysis was based on the lumped parameter concept for tip clearance control presented in detail in Chapter 4. Two basic analyses were employed over an engine square cycle to determine the compressor clearance during engine transients, namely the closure and the clearance analyses.

The time constant analysis for the RB211-524 drum and casing model shows that a reduction in the rotor time constant reduces the re-slam characteristics. This will result in a reduced clearance throughout the cycle and vice versa. An increase in the casing time constant also reduces the re-slam characteristics giving rise to reduced clearance throughout the cycle and vice versa. Hence, a proper closure and clearance, requires the reduction in drum time constant with an increase in casing time constant.

The heat transfer coefficient was improved by introducing radial inflow into the drum cavity. The sensitivity study for Trent 1000 engine shows that, with 6% radial inflow, there are potential reductions of stabilised cruise clearance and clearance at worst case acceleration (max take-off) when compare to the baseline model.

The overall results show significant enhancement with radial inflow on tip clearance. With 6% radial inflow, the clearance at worst case acceleration (max take off overshoot) is reduced by approximately 33%, 56%, 70%, 77% and 80%. The clearance at stabilised cruise is reduced at 6%, 17 %, 25 %, 30% and 33%. These results are for heat transfer coefficient multiplicative factors of 1, 2, 4, 6 and 8 respectively calculated against the baseline clearance. The blade tip time constant reduction analysis comparison between the model without radial inflow and the model with radial inflow shows a higher time constant reduction for the model with radial inflow, and hence a better compressor clearance control.

In the case with heat transfer coefficient, (50W/ (m^2K), 100W/ (m^2K) and 150 W/ (m^2K)), the results of the analysis indicate that with 6% radial inflow of air, it is possible to reduce the baseline cruise clearance by approximately 13%, 18% and 21% respectively. Finally, an increase in the heat transfer coefficient will reduce the time constant of the drum. This will reduce the reslam characteristics in the cycle, hence, a proper clearance throughout the cycle during transient operation.

8.3 Conclusions from 1-D analysis

The lumped parameter model (1-D modelling) was used in the validation of the results from the finite element thermo-mechanical model (SC03 model). The 1-D modelling involves the use of the lumped parameter method in the development of the concept for tip clearance control. The analysis makes use of a heat transfer and fluid flow based lumped parameter spreadsheet in combination with a full axisymmetric thermo-mechanical finite element high-pressure compressor (HPC) casing and drum model. The HPC model was used to investigate the effects of various parameters on the closure behaviour of the various HPC stages.

The variation of total thermal growth of casing and drum with time over the extended square cycle for Trent 1000 casing and drum models were studied. This variation gives the closure characteristics of the system during engine transient. The lumped parameter model closure was matched with SC03 closure over the extended square cycle for all stages of Trent 1000 casing and drum models. The lumped parameter model was used to predict the temperature profiles, closure and clearance profiles for tip clearance control in H.P. compressor.

The overall result of the matching process shows that the results of the lumped model are in good agreement with the results (time constant and closure data) of the SC03 model.

8.4 Conclusions from 2-D modelling of MCR

The 2-D modelling of the MCR is presented in this section. The aim of the modelling was to develop a reliable thermal model suitable to validate the experimental data obtained for the MCR for tip clearance control analysis. The model simulates the matched non-dimensional parameters. The non-dimensional quantities considered are rotational Reynolds number $Re_{Ø}$, axial Reynolds number Re_z, Grashof number Gr, and Rossby number Ro. The model was run at a rotational speed not exceeding 10,000 rpm, with a shroud temperature not exceeding 200 °C.

It was used to study the effect of heat transfer coefficient increase on drum time constant. Increasing the inbuilt heat transfer coefficient in the cavity and around the disc cob region reduces the disc time constant. The reduction in disc time constant was further enhanced by introducing radial inflow into the drum. The radial inflow, which is the bleed air from the core flow, increases the heat transfer in the drum cavity, hence improving the heat transfer coefficient. From the baseline model, the continuous increase of the inbuilt heat transfer coefficient does not guarantee continuous reduction in disc time constant in the long term, hence the need for bleed air from the core flow. According to the analysis with radial inflow, it is possible to reduce disc 2 upstream disc time constant by approximately 69%, 36%, and 27% during acceleration and 62%, 33%, and 22% during deceleration at the disc rim, mid–disc, and further down the disc near the disc cob (MP12, MP18, MP22), respectively, with 6% radial inflow calculated against the baseline nominal data.

However, the effect is less at the disc cob region than at other parts of the disc because the disc cob region comes into more contact with the bore flow. As expected, the introduction of radial inflow into the cavity does not increase the heat transfer (has less effect) around the disc cob region. This is evidenced by the MP28 model point time constant, which is increased by 36% and 26% for the disc cob during acceleration and deceleration, respectively, calculated against the baseline data.

The contribution of this work is to the ideas during Idea generation sessions that were considered in the present design. Also the adaptation of the original 40 inventive principles to problem solving in gas turbine engines. Two models have been built of the multiple cavity rig using the SCO3 software: one without radial inflow (baseline model) and another with radial inflow channels (ducts) that modelled the radial inflow into the drum cavity. A 1-D lump parameter model has also been developed and used to predict the temperature profiles, the closure and clearance of the H.P. compressor cycle during engine transient in an engine square cycle. This was used to validate the 2-D SCO3 models. The 2-D modelling results shows that 6% (of bore flow) radial inflow is capable of reducing the disc time constant by approximately 44% during acceleration at high power and 39% during deceleration at low power. This is equivalent to a time constant reduction factors of 2 during acceleration and 1.8 during deceleration. The efficiency has been improved by 0.2% points. The cruise clearance is reduced by 0.22mm. This 0.22mm would give a corresponding increase in compressor efficiency by 0.2% points and the specific fuel consumption (SFC) of the engine would be reduced by approximately 0.1% points. This could save a total of $16M per year in fuel costs for one airline.

From the analysis, the concept of disc time constant reduction using the radial inflow works as anticipated. With the quantity of radial inflow employed in the analysis, there is an evident and significant reduction in the disc time constant, hence the reduction in tip clearance H.P. compressor during engine transient.

8.5 Recommendations for future work

The tip clearance results presented in this thesis have been obtained from the analysis of surface temperatures measured by thermocouples positioned on the faces of the discs denoted on the models as model point (MP). The disc temperatures obtained from the model points were used to analyse the effect on time constant of the disc and hence the overall effect on tip clearance. For the radial inflow case in this study, the disc temperature and subsequent analysis of the effect on time constants results have been obtained with five different radial inflow regimes of 1.6%, 2%, 3%, 4% and 6% of bore flow, it is recommended that further tests be carried out by increasing the radial inflow conditions to ascertain the effect on heat transfer coefficient increase hence the effect on disc time constant. Other inlet conditions such as bore mass flow, inlet temperature and pressure could also be varied over a wide range to determine the effect on disc time constant hence the overall effect on tip clearance. Another study is to examine the effect of a change in disc cob width on the temperature distributions of the compressor disc since the heat transfer may be influenced by increasing or decreasing the bore diameter of discs.

The finite element software used for the modelling is the property of Rolls-Royce and not available for general use. It is proposed that attempt be made to develop the use of other finite element software such as ANSY for this study.

It would also be useful to make measurement of the tangential velocity in the cavities between discs. This would be done using Laser Doppler Anemometry (LDA). This study will give a more detailed inside of the effect of radial inflow on flow velocity in the cavity hence the consequence on heat transfer coefficient of the disc. The result will be used to obtain the effect on drum time constant and hence overall outcome on compressor clearance during engine transient on the non-dimensional operating conditions of modern HP axial compressors. Furthermore, any unsteadiness in the flow could be detected by measuring the circumferential pressure gradient inside the cavity using rotating pressure transducers. These measurements from LDA and pressure transducers would provide data for computational fluid dynamics (CFD) validation.

Bibliography

Acharya, S., Yang, H., Ekkad, S. V., Prakash, C. and Ron Bunker, R. (2002) Numerical simulation of film cooling on the tip of a gas turbine blade. ASME. Paper number GT-2002-30553.

Alexiou, A. (2000) *Flow and heat transfer in gas turbine H.P. compressor internal air systems.* D.Phil. thesis, School of Science and Technology, University of Sussex.

Altshuller, G. S. (1984), Creativity as an exact science - The theory of the solution of inventive problems. New York.

Albers, R. J., Ruiz, R., Boyle, M. (2004) *High pressure turbine elastic clearance control system and method.* United States patent application, 029011 A1, 2004.

Anderson, J. D. (1997). Description of HP Compressor excel tip clearance spreadsheet, Technical design report TDR47914, Rolls-Royce Plc

Angus, T. J. (1997) *Gas turbine engine case coated with thermal barrier coating to control axial airfoil clearance*, United States patent application, 5645399, 1997.
Apte, P. R., Shah, H. & Mann, D. (2001) 5W's and an H of TRIZ Innovation. *TRIZ Journal* [Online]. Available from: http:// www.triz-journal.com/archives/[Accessed :31st December 2010].

Aungier, R. H. (2003) *Axial-Flow Compressors. A Strategy for Aerodynamic Design and Analysis.* The American Society of Mechanical Engineers, Three Park Avenue, New York, NY 10016. ISBN 0-7918-0192-6

Aurisicchio, M., Gourtovaia, M., Bracewell, R. H. & Wallace, K. M.(2007) *Evaluation Of How Dred Design Rationale Is Interpreted.* Proc. of International Conference on Engineering Design (ICED 07), Paris, France, Design Society.

Aurisicchio, M., Gourtovaia, M., Bracewell, R. H. & Wallace, K. M.(2008) *How to evaluate reading and interpretation of differently structured engineering design rationales.* Artificial Intelligence for Engineering Design, Analysis and Manufacturing (2008), 22, 345–358.

Auxier, T. A. (1995) *Aerodynamic tip sealing for rotor blade.* United States patent application, 5403158, 1995.

Azad, G. E., Han, J. & Boyle, R. (2000) *Heat transfer and flow on the squealer tip of gasturbine blade.* ASME. Paper number: 2000-GT-0195.

Azad, G. S., Han, J. C., Teng, S. & Boyle, R. (2000) *Heat transfer and pressure distribution on a gas turbine blade tip.* ASME. Paper number: 2000-GT-0194.

Atkins, N. (2013) *Investigation of a radial-inflow bleed as a potential for compressor clearance control*. ASME Paper number: GT2013-95768.

Bae, J., Breuer, K. S. & Tan, C. S. (2000) *Control of tip clearance flows in axial compressors.* AIAA. Paper number: 2000-2233.

Bae, J., Breuer, K. S. & Tan, C. S. (2003) *Active control of tip clearance flow in axial compressors.* ASME. Paper number: GT2003-38661.

Baslsdon, J. G. (2006) C*asing arrangement*. United States patent application 7140836 B2, 2006.

Beheshti, B. H., Teixeira, J. A., Ivey, P. C., Ghorbanian, K. & Farhanieh B. (2004) *Parametric study of tip clearance: Casing treatment on performance and stability of a transonic axial compressor.* ASME. Paper number: GT2004-53390.

Behr, T., Kalfas, A. I. & Abhari, R. S. (2007) *Control of rotor tip leakage through cooling injection from the casing in a high-work turbine: Experimental investigation.* ASME. Paper number: GT2007-27269.

Bessette, A. D., Davies, D. O. & Shade, J. L. (1991) *Combined turbine stator cooling and turbine tip clearance control*.United States patent application, 5048288, 1991.

Bligh, A. (2006) *The Overlap Between TRIZ and Lean IME 552*: Lean Manufacturing Systems University of Rhode Island, TRIZ Journal. http://www.innovation-triz.com/papers/TRIZ_Lean.pdf [Accessed 1st November 2010].

Bock, A. (2000) *Passive clearance control system for a gas turbine.*United States patent application, 6126390, 2000.

Boden, M. A. (1990) *The Creative Mind, Myths and Mechanisms*. London, Routledge.

Boden, M. A. (ed.) (1990). *What is Creativity*? *Dimensions of Creativity*. Cambridge, MA/ London, MIT Press, pp.75-117.

Boden, M. A. (1998) Creativity and artificial intelligence. *Artificial Intelligence*, 103 (1-2), 347-356.

Bonner, K. J. (1992) *Thermal blade tip clearance control for gas turbine engines.* United States patent application, 5154575, 1992.

Boyce, M.P. (2003) *Gas Turbine Engineering Handbook, Second Edition*. Butterworth-Hienemann.

Botje, J. M. (1961) *Tip clearance control system for turbomachine.* United States patent application, 2994472, 1961.

Bracewell, R. H., Wallace, K., Moss, M., Knott, D. (2009) *Capturing design rationale*. Computer-Aided Design 41 (2009) 173-186, Elsevier.com/locate/cad.

Bracewell, R. H., Ahmed, S. & Wallace, K. M. (2004) *DRed and design folders: a way of caputuring, storing and passing on - knowledge generated during design projects*. Design Automation Conference, ASME DETC, Salt Lake City, Utah, USA.

Brown, B. H., DeTolla, F. L. & Reilly, D. R. (1977) *Method and apparatus for controlling stator thermal growth.* United States patent application, 4005946, 1977.

Bucaro, M. T., Albers, R. J., Estridge, S.A & Wartner, R. F. (2007) T*hermal control of gas turbine engine rings for active clearance control*. United States patent application 0140839 A1, 2007.

Burns, D. W. & Fagan Jr., J. R. (1997) *Magnetic bearings actuation for compressor stability control*. United States patent application, 5658125, 1997.

Cameron, J. D., Bennington, M. A., Ross, M. H., Morris, S. C. & Corke, T. C. (2007) *Effects of steady tip clearance asymmetry and rotor whirl on stall inception in an axial compressor.* ASME. Paper number: GT2007-28278.

Candy, L. (1997) Computer and creativity supports: knowledge, visualisation and collaboration. *Knowledge-Based Systems*, 10, 3-13.

Cang, J. N., Gast, J. R., Hensley, J. J. & Waldhelm, C. M (1989) *Turbine blade tip clearance control system.* United States patent application, 4874290, 1989.

Casakin, H. & Kreitler, S. , (2005) The determinants of creativity. *Flexibility in design. Engineering and Product Design Education Conference, Napier University, September 15–16.* Edinburgh, UK: Crossing Design Boundaries (P. Rodgers, L. Brodhurst & D. Hepburn, Eds.), pp.303–308.

Cassina, G., Kammerer, A., Beheshti, B. H. & Abhari, R. S. (2007) *Parametric study of tip injection in an axial flow compressor stage.* ASME. Paper number: GT2007-27403.

Catlow, R. (1993) *Blade tip clearance control apparatus.* United States patent application, 5211534, 1993.

Chandrasekaran, B. (1989) *Design Problem Solving*: *A Task Analysis*. American Association for Artificial Intelligence. Available from://www.cse.ohio-state.edu/~chandra/ai-mag-design-ps.pdf [Accessed 20th December 2010].

Changqing, G., Kezheng, H. & Fei, M. (2005) Comparison of Innovation Methodologies and TRIZ. TRIZ Journal [Online] Available from: http:// www.triz-journal.com/archives/2005/09/07. pdf [Accessed 31st December 2010].

Chew, J. W. (1982). *Computation of flow and heat transfer in rotating cavities*. D.Phil. Thesis, School of Engineering, University of Sussex, UK.

Chew, J. W. (1985a) *Moment coefficients and flow entrainment rate for a cone rotating in an infinite environment.* Rolls-Royce PLC, Theoretical Science Group. Report number: TSG0225.

Chew, J. W. (1985b) Computation of convective laminar flow in rotating cavities. *J. Fluid Mech.*, 153, 339-360.

Chew, J. W. (1988) The effect of hub radius on the flow due to a rotating disc. Technical briefs. *J. Turbomachinery*, 110, 417-418.

Chew, J. W., Farthing, P. R., Owen, J. M. & Stratford, B. (1989) The use of fins to reduce the pressure drop in a rotating cavity with a radial inflow. *J. Turbomachinery*, 111, 349-356.

Chew, J. W., Owen, J. M. & Pincombe, J. R. (1984) Numerical predictions for laminar source-sink flow in a rotating cylindrical cavity. *J. Fluid Mech*., 143, 451-466.

Childs, P. R. N. (2011) *Rotating Flow*. Elsevier Inc. ISBN 978-0-12-382098-3

Childs, P.R.N., Dullenkopf, K., and Bohn, D. (2006) *Internal air systems experimental rig best practice*. ASME Paper GT2006-90215.

Childs, P.R.N., Atkins, N.R., Ekong, G., Mega, D., Knott, D. , Tsai, S.K. and Aurisicchio, M.L. (2008) Effective implementation of TRIZ (theory of inventive problem solving) for compressor clearance design options. Private communication

Childs, P.R.N. & Tsai, S-K. (2010) Creativity in the design process in the turbomachinery industry. *J. of Design Research*, 8, 145-164.

Ciokajlo, J. J. & Hauser, A. A. (1991) *Mechanical blade tip clearance control apparatus for a gas turbine engine.* United States patent application, 5018942, 1991.

Ciokajlo, J. J. & Hauser, A. A. (1992) *Clearance control assembly having thermally-controlled one-piece cylindrical housing for radially positioning shroud segments*. United States patent application, 5167488 A1, 1992.

Ciokajlo, J. J. (1992) *Blade tip clearance control apparatus annular support ring thermal expansion.* United States patent application, 5116199, 1992.

Cline, L. D., Hauser, A. A., Sidenstick, J. E. & Zlatic, M. S. (982) *Clearance control.* United States patent application, 4363599, 1982.

Clough, R. S. & Neal, P. F. (1989) *Gas turbine control system*. United States patent application, 4844688, 1989.

Cobb, E. C. & Saunders, O. A. (1956) Heat transfer from a rotating disc. *Proc. R. Soc. Lond. A.*, 236, 343-351.

Cochran, W. G. (1934) The flow due to a rotating disc. *Proc. Cambridge Phil. Soc.*, 30, 365-375.

Colley, R. H. (1982) *Rotor tip clearance control apparatus for gas turbine engine.* United States patent application, 4330234, 1982.

Corsmeier, R. J., Petsche, J. (1991) *Blade tip clearance control apparatus using bellcrank mechanism*, United States patent application, 5054997, 1991.

Corsmeier, R. J., Tseng, W. (1991) *Blade clearance apparatus using shroud segment position modulation.* United States patent application, 5056988, 1991.

Couger, J. D., Higgins, L. E. & Mcintyre, S. C. (1993) (Un)Structured Creativity in Information Systems Organizations. *MIS Quarterly*, 17 (4), 375-397.

Couger, J.D. (1995) *Creative Problem Solving and Opportunity Finding*. Danvers, MA, Boyd & Fraser Publishing Co.

Cross, N. (1989) *Engineering Design Methods.* The Open University, Milton Keynes, UK, John Wiley & Sons.

Cumpsty, N. A. (1989) *Compressor Aerodynamics*. Addison Wesley Longman Limited. England. ISBN 0-582-01364-X

Curtis, E. M., Denton, J. D., Longley, J. P. & Rosic, B. (2009) *Controlling tip leakage Effects of steady tip clearance asymmetry and rotor whirl on stall inception in an axial flow over a shrouded turbine rotor using an air-curtain*. ASME. Paper number: GT2009- *Fluid Mech.*, 153, 339-360.

Damlis, N., Zegarski, F. J. & Brayton, D. D. (1993) *Gas turbine engine clearance control apparatus*. United States patent application, 5,228,828, 1993.

Davison, S. H., Kast, K. H. & Clark, A. W. (1990) *Active clearance control.* United States patent application, 4928240, 1990.

Davison, S. H. (1980) *Rotor/shroud clearance control system.* United States patent application, 4230436, 1980.

Davison, S. H. & William, F. M. (1990) *Clearance control system.* United States patent application, 4893984, 1990.

de Bono, E. (1996) *Teach Yourself to Think*. London, UK, Penguin Books.

Deng, X., Zhang, H., Chen, J. & Huang, W. (2005) *Unsteady tip clearance flow in a lowspeed axial compressor rotor with upstream and downstream stators.* ASME. Paper number: GT2005-68571.

Dennis, R. W., Newstead, C. & Ede, A. J. (1970) *Heat Transfer from a Rotating Disc in Cross-Flow*. 4th International Heat Transfer Conference, Versailles III F C 7 1.

Deveau, P. J., Greenberg, P. B. & Paolillo, R. E. (1985) *Gas turbine engine active clearance control*. United States patent application, 4513567, 1985.

Dey, D. & Camci, C. (2001) *Aerodynamic tip desensitization of an axial turbine rotor using tip platform extensions.* ASME. Paper number: 2001-GT-484.

Dobrzynski, B., Saathoff, H., Kosyna, G., Clemen, C. & Gümmer, V. (2008) *Active flow control in a single-stage axial compressor using tip injection and endwall boundary layer removal.* ASME. Paper number: GT2008-50214.

Dodd, A. G. & Pellow, T. R. (1991) *Turbomachine clearance control.* United States patent application, 5044881, 1991.

Domb, E. (1997) 40 Inventive Principles With Examples. *TRIZ Journal*. [Online] Available from: http://www.triz-journal.com/archives/1997/07/b/index.html [Accessed 8th December 2010].

Domb, E., Terninko, J., Miller, J. & MacGran, E. (2001) *The Seventy-Six Standard Solutions: How They Relate to the 40 Principles of Inventive Problem Solving*. TRIZ Journal. [Online] Available from: http://www.triz-journal.com/archives/1999/05/e/index.htm [Accessed 29th November 2010].

Dorfman, L. A. (1963) *Hydrodynamic resistance and the heat loss of rotating solids.* Edinburgh, Oliver and Boyd.

Dorst, K. & Cross, N. (2001) *Creativity in the Design Process*: *Co-evolution of Problem - Solution*. *Design Studies*, 22 (5), 425-437.

Down, J. P. & Haigh, R. C. (1997) *Turbine blade passive clearance control.* United States patent application, 5688107, 1997.

Du, J., Lin, F., Zhang, H. & Chen, J. (2008) *Numerical investigation on the originating mechanism of unsteadiness in tip leakage flow for a transonic fan rotor*. ASME. Paper number: GT2008-51463.

Ekong, G. I., Long, C. A., Atkins, N. R. & Childs, P. R. N. (2011) The development of concepts for the control of tip clearance in Gas turbine HP compressors using TRIZ.TRIZ. In: Gaetano Cascini, Tom Vaneker, ed. *TRIZ Future Conference 2011, Dublin, Ireland November 2-4*. ITT, Dublin: ETRIA, pp.437-440.

Evan, D. E. (2007) Variable stator vane arrangement for a compressor. United States patent application 7198454 B2, 2007.

Evans, D. H. (1993) *Tip clearance control apparatus for a turbo-machine blade*, United States patent application, 5203673, 1993.

Farthing, P. R. (1988) *The effect of geometry on flow and heat transfer in a rotating cavity*. D.Phil. thesis, School of Engineering, University of Sussex, UK.

Farthing, P. R., Chew, J. W. & Owen, J. M. (1991) The use of de-swirl nozzles to reduce the pressure drop in a rotating cavity with a radial inflow. *J. Turbomachinery*, 113, 106-114.

Farthing, P. R., Long, C. A., Owen, J. M. & Pincombe, J. R. (1992a) Rotating cavity with axial throughflow of cooling air: Flow structure. *J. Turbomachinery*, 114, 237-246.

Farthing, P. R., Long, C. A., Owen, J. M. & Pincombe, J. R. (1992b) Rotating cavity with axial throughflow of cooling air: Heat transfer. *J. Turbomachinery*, 114, 229-236.

Farthing, P. R., Long, C. A. & Rogers, R. H. (1991) *Measurement and prediction of heat transfer from compressor discs with a radial inflow of cooling air*. ASME. Paper number: 91-GT-53.

Farthing, P. R. & Owen, J. M. (1988) The effect of disc geometry on heat transfer in a rotating cavity with a radial outflow of fluid. *J. Eng. Gas Turbine and Power*, 110, 70-77.

Farthing, P. R. & Owen, J. M. (1991) De-swirled radial inflow in a rotating cavity. *Int. J. Heat Fluid Flow*, 12, 63-70.

Farthing, P. R. & Rogers, R. H. (1987) *Heat transfer from the discs of a rotating cavity with a radial inflow of air. Part 1: Comparison between theory and experiment*. Thermo-Fluid Mechanics Research Centre, School of Engineering, University of Sussex, UK. Report number: 87/TFMRC/109a.

Firouzian, M. (1986) *Flow and heat transfer in a rotating cylindrical cavity with a radial inflow of fluid.* M.Phil. thesis, School of Engineering, University of Sussex, UK.

Firouzian, M., Owen, J. M., Pincombe, J. R. & Rogers, R. H. (1985) Flow and heat transfer in a rotating cylindrical cavity with a radial inflow of fluid. Part 1: The flow structure. *Int. J. Heat and Fluid Flow*, 6, 228-234.

Freeman, C. (1985) *Effect of tip clearance flow on compressor stability and engine performance.* [Lecture series] Von Karman Institute for Flow Dynamics, 1985-05.

Fuller, J. R. D. & Bell, J. K. A. (1989) *Clearance control apparatus for a bladed fluid flow machine.* United States patent application, 4804310, 1989.

Gaul, G. R. (1997) *Method for reducing steady state rotor blade tip clearance in land-based gas turbine to improve efficiency*. United States patent application, 5667358, 1997.

Gero, J. S. & Maher, M. L. (1993), *Modelling Creativity and Knowledge-Based Creative Design*, New Jersey: Lawrence Erlbaum Associates, Inc.

Glezer, B. & Bagheri, H. (1998) *Turbine blade clearance control system*. United States patent application, 5779436, 1998.

Glover, J. (1993) *Tip clearance control apparatus and method*. United States patent application, 5,212,940, 1993.

Glover, J.(1992) *Impingement manifold.* United States patent application, 5100291, 1992.

Goel, P. S. & Singh, N. (1998). Creativity and Innovation in Durable Product Development. *Computers & Industrial Engineering*, 35, (1-2), 5-8.

Gregory, N., Stuart, J. T. & Walker, W. S. (1955) On the stability of three-dimensional boundary layers with application to the flow due to a rotating disc. *Phil. Trans. R. Soc. A.*, 248, 155-199.

Griffin, J. G. & Schwarz, F. M. (1981) *External gas turbine engine cooling for clearance control*. United States patent application, 4279123, 1981.

Günther A., Uffrecht, W., Heller, L. and Odenbach, S. (2013) Experimental and numerical analysis of heat transfer in compressor-disc cavities for a transition between heating and cooling flow[Online] Available from: http://www.mtu.de/en/technologies/engineering_news/development/Heller_Experimental_an_Numerical_en.pdf [Accessed 03rd February 2013].

Hagi, N. (2000) *Seal clearance control system for gas turbine stationary blade.*United States patent application, 6152685, 2000.

Hall, D. J. (1996) The role of creativity within best practice manufacturing. *Technovation*, 16 (3), 115-121.

Hallinger, C. C. & Kervistin, R. (1976) *Device for regulating blade tip clearance.* United States patent application, 3975901, 1976.

Halsey, R. W. P. (1999) *Tip clearance control.* United States patent application, 5871333, 1999.

Harris, D. J. (2007) *Methods and apparatus for maintaining rotor assembly tip clearances.* United States patent application 7246996 B2, 2007.

Harris, R. (1998) *Introduction to Creative Thinking*. [Online] Available from: http://www.virtualsailt.com/crebookl.htm [Accessed 1st December 2010].

Hassanvand, M., Tao, W. S., Tai, F. G. & Qi, W. S. (2004) *Simulation and investigation of tip leakage flow based on dissipation function.* ASME. Paper number: GT2004-54283.

Herron, W. L. (2007) M*ethod for controlling blade tip clearance in a gas turbine*. European patent application, 1 860 281 A2, 2007.

Hide, R. (1958) An experimental study of thermal convection in a rotating liquid. *Phil. Trans. R. Soc. A.*, 250, 441-478.

Hide, R. (1968) On source-sink flows in a rotating fluid. *J. Fluid Mech.*, 32 (4), 737-764.

Higgins, J. M. (2006) *101 Creative Problem Solving Techniques.* Florida, New Management Publishing Company, Inc.

Higgins, L. F. (1999) Applying Principles of Creativity Management to Marketing Research Efforts in High-Technology Markets Industrial. *Marketing Management*, 28, 305-317.

Hipple, J. (2005) The integration and strategic use of TRIZ with the CPS (Creative Problem Solving) process. *TRIZ Journal*. [Online] Available from: *TRIZ Journal*, March 2005. http://www.triz-journal.com/archives/2005/03/03.pdf [Accessed 23rd November 2010].

Hohlfeld, E. M., Christophel, J. R., Couch, E. L. & Thole, K. A. (2003) *Predictions of cooling from dirt purge holes along the tip of a turbine blade.* ASME. Paper number: GT2003-38251.

Hovan, E. J. (1985) *Clearance control in turbine seals.* United States patent application, 4541775, 1985.

Hsiao, H., Liang, Y. & Lin, T. (2004) A creative thinking teaching model in a computer network course for vocational high school students.*World Transactions on Engineering and Technology Education*, 3 (2), pp. 243-248.

Huber, F. W. & Dietrich, D. J. (1997) *Clearance control for the turbine of a gas turbine.* United States patent application, 5667359, 1997.

Incropera; DeWitt, Bergman, Lavine (2007). *Fundamentals of Heat and Mass Transfer* (6th edition ed.). John Wiley & Sons. pp. 260–261. ISBN 978-0-471-45728-2.

Illingworth, J. B. (2006). *Fluid-Solid heat transfer coupling*. D.Phil. thesis, School of Engineering, University of Sussex, UK.

Ingleson, J. F. (1963) *Variable clearance shroud structure for gas turbine engine.* United States patent application, 3058398, 1963.

Inoue, M., Kuroumaru, M., Yoshida, S., Minami, T., Yamaha, K. & Furukawa, M. (2004) *Effect of tip clearance on stall evolution process in a low axial compressor stage.* ASME. Paper number: GT2004-53354.

Johnson, D. M. (1993) *Gas turbine engine case thermal control flange*. United States patent application, 5219268, 1993.

Johnston, R. P., Knapp, M. H. & Coulson, C. E. (1982) *Active control system for a turbomachine*. United States patent application, 4329114, 1982.

Jothiprasad, G., Murray, R. C., Essenhigh, K., Bennett, G. A., Saddoughi, S., Wadia, A. & Breeze-Stringfellow, A. (2010) *Control of tip-clearance flow in a low speed axial compressor rotor with plasma actuation.* ASME. Paper number: GT2010-22345.

Kervistin, R. (1989) *System for adjusting radial clearance between rotor and stator elements.* United States patent application, 4849895, 1989.

Kildea, R. J. (1994) *Passive clearance control system for turbine blades.* United States patent application, 5282721, 1994.

Kim, I. (2002) *40 principles as a problem finder*. [Online] Available from: http://www.triz-journal.com/archives/2005/03/04.pdf [Accessed 11th November 2010]

Kim, I. (2005) 40 Principles as a Problem Finder. *TRIZ Journal* [Online]. Available from: http://www.triz-journal.com/archives/2005/03/04.pdf[Accessed 10th November 2010]

Knott, D. (2008) A practical TRIZ process, private communication.

Kolodner, J. L. (1999) An Introduction to Case-Based Reasoning. *Artificial Intelligence Review*, 6, 3-34.

Kraev, V. (2006) Kreav's Korner: Technical and Physical contradictions-Lesson 3. *TRIZ Journal*. [Online]. Available from: http://www.triz-journal.com/archives/2006/12/01.pdf [Accessed 16th November 2010]

Kraev, V. (2007) Kreav's Korner: Inventive Standards & S-Field Models-Lesson 8. *TRIZ Journal*. [Online]. Available from: http://www.triz-journal.com/archives/2007/05/06/ [Accessed 31st December, 2010]

Kreith, F., and Bohn, M. S. (1993) *Principles Heat Transfer (5th ed.)*. West Publishing Company. pp. 119-126. ISBN 0-314-01360-1

Kreitler, S. & Casakin, H. (2009) Motivation for Creativity in Design Students. *Creativity Research Journal*, 21(2–3), 282-293.

Kusterer, K., Moritz, N., Bohn, D., Sugimoto, T. & Tanaka, R. (2007) *Reduction of tipclearance losses in an axial turbine by shaped design of the blade tip region.* ASME.Paper number: GT2007-27303.

Lapworth, B. L. & Chew, J. W. (1992) A numerical study of the influence of disc geometry on the flow and heat transfer in a rotating cavity. *J. Turbomachinery*, 114, 256-263.

Lattime, S. B. & Steinetz, B. M. (2002) *Turbine Engine Clearance Control Systems: Current Practices and Future Directions.* National Aeronautics and Space Administration (NASA). NASA/TM—2002-211794.

Lau, K. Y. (1992) *Blade tip clearance control arrangement for a gas turbine.* United States patent application, 5092737, 1992.

Laurello, V. P. (1989) *Turbine cooling and thermal control*. United States patent application, 4,815,272, 1989.

Lee J. Design rationale systems: Understanding the issues. IEEE Expert 1997; (May/June):78-85.

Lenahan, D. T., Shotts, L. D., Shetty, B. S. & Glover, J. (1994) *Clearance control system separately expanding or contracting portion of annulus shroud.* United States patent application, 5281085, 1994.

Leogrande, J. A., Jalbert, P. L., Wood, C. B. & Schryver, M. J. (2007) S*ystem and method for monitoring thermal growth and controlling*. United States patent application 0043497A1, 2007.

Leonard, J. F. & Maggs, P. J. (1994) *Turbine engines*. United States patent application, 5295787, 1994.

Lewis, R. W., Nithiarasu, P., Seetharamu, K. N. (2004). *Fundamentals of the finite element method for heat and fluid flow*. Wiley. p. 151. ISBN 0-470-84789-1

Long, C. A. (1984) *Transient heat transfer in a rotating cylindrical cavity*. D.Phil. thesis, School of Engineering, University of Sussex, UK.

Long, C. A. (1994) Disc heat transfer in a rotating cavity with an axial throughflow of cooling air. *Int. J. Heat Fluid Flow*, 15, 307-316.

Long, C. A. (1999) *Essential heat transfer.* London, Longman.

Long, C. A. & Childs, P. R. N (2007) Shroud heat transfer measurements inside a heated multiple rotating cavity with an axial throughflow of air. *International Journal of Heat and Fluid Flow***,** Volume 28, Issue 6, Pages 1405–1417

Long, C. A., Morse, A. P. & Tucker, P. G. (1997) Measurement and computation of heat transfer in high pressure compressor drum geometries with axial throughflow. *J. Turbomachinery*, 119, 51-60.

Long, C. A., Morse, A. P. & Zafiropoulos, N. (1993) *Buoyancy-affected flow and heat transfer in asymmetrically-heated rotating cavities.* ASME. Paper number: 93-GT-88.

Long, C. A., Miché, N.D.D., Childs, P.R.N. (2007) Flow measurements inside a heated multiple rotating cavity with axial throughflow. *International Journal of Heat and Fluid Flow***,** Volume 28, Issue 6, Pages 1391–1404

Long, C. A. & Owen, J. M. (1986) The effect of inlet conditions on heat transfer in a rotating cavity with a radial outflow of fluid. *J. Turbomachinery*, 108, 145-152.

Long, C. A. & Tucker, P. G. (1994a) Numerical computation of laminar flow in a heated rotating cavity with an axial throughflow of air. *Int. J. Num. Meth. Heat Fluid Flow*, 4, 347-365.

Long, C. A. & Tucker, P. G. (1994b) Shroud heat transfer measurements from a rotating cavity with an axial throughflow of air. *J. Turbomachinery*, 116, 525-534.

Lu, X., Chu, W., Zhu J. & Wu, Y. (2007) *Mechanism of the interaction between casing treatment and tip leakage flow in a subsonic axial compressor.* ASME. Paper number: GT2007-90077.

Lu, X., Zhu, J., Chu, W. & Wang, R. (2005) *The effects of stepped tip gap on performance and flowfield of a subsonic axial-flow compressor rotor.* ASME. Paper number: GT2005-69106.

Lyon, B. V. (1995) *Dynamic control of tip clearance.* United States patent application, 5456576, 1995.

Mann, D.L., (2001) Laws Of System Completeness. *TRIZ Journal*. [Online] Available from: *TRIZ Journal*, http://www.triz-journal.com/archives/2001/05/d/index.htm [Accessed 16th November 2010].

Mann, D. L. (2002) *Hands-on Systematic Innovation*. Belgium, CREAX Press.

Martin, N. F., Crum, G. A. & McCallum, A. (2006) *Compressor bleed air manifold for blade clearance control.* United States patent application 7090462 B2, 2006.

Martin, A. N. (1996) *Engine blade clearance control system with piezoelectric actuator.* United States patent application, 5545007, 1996.

McFadzean, E.S. (1996) *New Ways of Thinking: An Evaluation of K-Groupware and Creative Problem Solving*. Doctoral Dissertation. Henley-on-Thames, Henley Management College/Brunel University.

McFadzean, E. S. (1998) Enhancing creative thinking within organisations. *Management Decision*, 36 (5), 309-315.

McGeehan, W. F. (1990) *Active clearance control*. United States patent application, 4893983, 1990.

Meylan, P. (1997) *Compressor and method of operating it*. United States patent application, 5605437, 1997.

Mich´e, N. D. D. (2008) *Flow and heat transfer measurements inside a heated multiple rotating cavity with axial throughflow*. PhD thesis, University of Sussex.

Mills, S. J., Monico, R. D. & Bradley, A. J. (1994) *Gas turbine clearance control.* United States patent application, 5351732, 1994.

Mills, S.J. (1991) *Gas turbine with turbine tip clearance control device and method of operation*. United States patent application, 5064343, 1991.

Mitchell, W. E. & Kowalik, T. F. (1989) *Creative problem solving*. [Online] Available from: http://www.roe11.k12.il.us/.pdf [Accessed 4th December 2012].

Monico, R. D and Chew, J. W (1993) Modelling thermal behaviour of turbomachinery discs and casings. *Proceedings of Agard Conference 527 held in Antalya, Turkey12th - 16th October 1992* ISBN 92-835-0701-0 Published Febraury 1993.

Monsarrat, W. G. & Neal, W. F. (1981) *Compressor structure adapted for active clearance control.* United States patent application, 4268221, 1981.

Morris, S. C., Corke, T. C., Van Ness, D., Stephens, J. & Douvillev, T. (2005) *Tip clearance control using plasma actuators*. AIAA. Paper number: 2005-782

Mossey, P. W. (1982) *Apparatus and method for optical clearance determination.* United States patent application, 4326804, 1982.

Ness II, D. K. V. (2009) *A study of tip clearance flow loss mitigation in a linear turbine cascade using active and passive flow control*. D.Phil. thesis, the Graduate School of the University of Notre Dame.

Nikkanen, J. P. & Griffin, J. G. (1985) *Pressurized nacelle compartment for active clearance controlled gas turbine engines*. United States patent application, 4493184, 1985.

Niu, M. & Zang, S. (2009) Influences of tip cooling injection on tip clearance control at design and off-design incidences. IJRM. Paper number: 2009-160423.

Northrop, A. & Owen, J. M. (1988a) Heat transfer measurements in rotating-disc systems. Part 1: The free disc. *Int. J. Heat Fluid Flow*, 9 (1), 19-26.

Northrop, A. & Owen, J. M. (1988b) Heat transfer measurements in rotating-disc systems. Part 2: The rotating cavity with a radial outflow of cooling air. *Int. J. Heat Fluid Flow*, 9 (1), 27-36.

Osborn, A.F. (1953) *Applied Imagination*. New York, Scribner's.

Owen, B. C. (1998) *Blade tip clearance control apparatus.* United States patent application, 5791872, 1998.

Owen, J. M. (1971) The Reynolds analogy applied to flow between a rotating and a stationary disc. *Int. J. Heat Mass Transfer,* 14, 451-460.

Owen, J. M. (1979) On the computation of heat transfer coefficients from imperfect temperature measurements. *J. Mech. Eng. Sci.*, 21 (5), 323-334.

Owen, J. M. & Bilimoria, E. D. (1977) Heat transfer in rotating cylindrical cavities. *J. Mech. Eng. Sci.*, 19, 175-187.

Owen, J. M., Haynes, C. M. & Bayley, F. J. (1974) Heat transfer from an air-cooled rotating disc. *Proc. R. Soc. Lond. A.*, 336, 453-473.

Owen, J. M. & Onur, H. S. (1983) Convective heat transfer in a rotating cylindrical Cavity. *J. Eng. Power*, 105, 265-271.

Owen, J. M. & Pincombe, J. R. (1979) Vortex breakdown in a rotating cylindrical cavity. *J. Fluid Mech.*, 90, 109-127.

Owen, J. M. & Pincombe, J. R. (1980) Velocity measurements inside a rotating cylindrical cavity with a radial outflow of fluid. *J. Fluid Mech*., 99, 111-127.

Owen, J. M., Pincombe, J. R. & Rogers, R. H. (1985) Source-sink flow inside a rotating cylindrical cavity. *J. Fluid Mech.*, 155, 233-265.

Owen, J. M. & Rogers, R. H. (1989) *Flow and heat transfer in rotating-disc systems: Vol. 1, rotor-stator systems.* Taunton, UK & Wiley, NY, Research Studies Press.

Owen, J. M. & Rogers, R. H. (1995) Flow and heat transfer in rotating-disc systems: Vol. 2, rotating cavities. Taunton, UK & Wiley, NY, Research Studies Press.

Papa, M., Goldstein R. J. & Gori, F. (2002) *Effects of tip geometry and tip clearance on the mass/heat transfer from a large-scale gas turbine blade.* ASME. Paper number: GT-2002-30192.

Patterson, W. R. (1976) *Thermal actuated valve for clearance control*. United States patent application, 3966354, 1976.

Patterson, W. R. (1978) *Variable shroud for a turbomachine*. United States patent application, 4127357, 1978.

Pierre, S. & Dobson, M. J. (2000) *Turbine passive thermal valve for improved tip clearance control.* United States patent application, 6116852, 2000.

Pincombe, J. R. (1983) *Optical measurements of the flow inside a rotating cylinder.* D.Phil. thesis, School of Engineering, University of Sussex, UK.

Plemmons, L. W., Proctor. R., Albers, R. J. and Gardner, D. L. (1993) *Gas turbine engine case counterflow thermal control.* United States patent application, 5205115, 1993.

Proctor, R., Linger, D. R., DiSalle, D. A, Brassfield, S. R. & Plemmons, J. W. (1996) *Isolated turbine shroud.* United States patent application, 5562408, 1996.

Proctor, R., Linger, D. R., DiSalle, D. A, Brassfield, S. R. & Plemmons, J. W. (1997) *Smart turbine shroud.* United States patent application, 5593277, 1997.

Putman, R. L. & Dinse, M. L. (1987) *Active clearance control.* United States patent application, 4648241, 1987.

Putman, R. L. & Hovan, E. J. (1989) *Method for maintaining blade tip clearance*. United States patent application, 4856272, 1989.

Radomski, M. A. (1982) *High pressure compressor clearance investigation.* CF6 Jet Engine Diagnostics Program. National Aeronautics and Space Administration (NASA). NASA CR-165580.

Rantanen, K. & Domb, E. (2002) *Simplified TRIZ: New Problem-Solving Applications for Engineers and Manufacturing Professionals*. Boca Raton, FL, St. Lucie Press.

Rao, N. M. & Camci, C. (2004) *Axial turbine tip desensitization by injection from a tip trench. Part 1: Effect of injection mass flow rate*. ASME. Paper number: GT2004-53256.

Redinger Jr., I. H., Sadowsky, D. & Stripinis, P. S. (1978) *Clearance control for gas turbine.* United States patent application, 4069662, 1978.

Redinger Jr., I. H., Sadowsky, D. & Stripinis, P. S. (1977) *External gas turbine engine cooling for clearance control.* United States patent application, 4019320, 1977.

Ress, R. A. (2001) *Blade clearance control for turbomachinery*. United States patent application, 6273671 B1, 2001.

Richardson, P. D. & Saunders, O. A. (1963) Studies of flow and heat transfer associated with a rotating disc. *J. Mech. Eng. Sci.*, 5, 336-342.

Ritchie, J. A., Schleue, J. H., Glover, J. & Tegarden, F. W. (1995) *Integral clearance control impingement manifold and environmental shield.* United States patent application, 5399066, 1995.

Rolls-Royce plc. (2004) SC03 Thermo-Mechanics Quality System Rolls-Royce. capability Intranet.

Rolls Royce plc. (2005) *The Jet Engine*. ISBN 0 902121 2 35, Rolls Royce Technical Publications Department, Derby, U.K.

Saha, A. K., Acharya, S., Bunker, R. & Prakash, C. (2006) Blade tip leakage flow and heat transfer with pressure-side winglet. IJRM. Paper number: 2006-17079.

Sakulkaew, S., Tan, C. S., Donahoo, E., Cornelius, C., Montgomery, M. (2013) *Compressor Efficiency Variation with Rotor Tip Gap from Vanishing to Large Clearance*, ASME Journal of Turbomachinery May 2013, Vol. 135 / 031030.

Saravanamuttoo, H. I. H, Rogers, G. F. C, Cohen, H. (2001) *Gas Turbine Theory*. 5th edition. Pearson education Limited. ISBN 0130-15847-X

Savransky, S. D. (1999) Lesson 4-Contradictions. *TRIZ Journal*. [Online] Available from: http://www.triz-journal.com/archieves/1991/11/b/index.htm [Accessed 16th November 2010].

Schlange, L. E. & Juttner, U. (1997) Helping Managers to Identify the Key Strategic Issues. *Longe Range Planning*, 30 (5), 777-786.

Schlicting, H., (1979) Boundary *Layer Theory*. 4th Edition, McGraw Hill.

Schroder, M. S. (2002) *Bucket tip clearance control system*. United States patent application, 6435823 B1, 2002.

Schulze, W. M. (1981) *Variable clearance control for gas turbine engine.* United States patent application, 4304093, 1981.

Schwarz, F. M. & Griffin, J. G. (1984) *Modulated clearance control for an axial rotary machine*. United States patent application, 4487016, 1984.

Schwarz, F. M. & Crawley Jr., C. J. (1991) *Thermal clearance method for gas turbine engine*. United States patent application, 5076050, 1991.

Schwarz, F. M., Crawley Jr., C. J., Rauseo, A. F. & Laqueux, K. R. (1992) *Active clearance control with cruise mode*. United States patent application, 5090193, 1992.

Schwarz, F. M. & Smith, J. W. (2006) *Gas turbine engine blade tip clearance apparatus and method.* United States patent application, 0140756 A1, 2006.

Schwarz, F. M. (1980a) *Seal clearance control for a gas turbine.* United States patent application, 4213296, 1980.

Schwarz, F. M. (1980b) *Temperature control of engine case for clearance control,* United States patent application, 4242042, 1980.

Schwarz, F. M. (1985) *Clearance control for gas turbine*. United States patent application, 4525998, 1985.

Sefertzi, E. (2000) *Creativity*. Report produced for the EC funded project "INNOREGIO: dissemination of innovation and knowledge management techniques," Stockholm School of Economics in Riga. http://www.urenio.org/tools/en/creativity.pdf[Accessed 1st December 2010].

Sexton, B. F., Knuijt, H. M., Eldrid, S. Q., Myers, A., Coneybeer, K. E., Johnson, D. M. & Kellock, I. R. (1998) *Removable inner turbine shell with bucket tip clearance control.* United States patent application, 5779442, 1998.

Shuba, B. H. (1993) *Apparatus for bleeding air*. United States patent application, 5261228, 1993.

Shuba, B. H. (1994) Method *for air bleeding.* United States patent application, 5351473, 1994.

Sirakov, B. T. & Tan, C. S. (2002) *Effect of upstream unsteady flow conditions on rotor tip leakage flow.* ASME. Paper number: GT2002-30358.

Smith, G. J. W. (2005) How should creativity be defined? *Creativity Research Journal*, 17 (2/3), 293-295.

Spakovszky, Z. S., Paduano, J. D., Larsonneur, R., Traxler, A. & Bright, M. M. (2001) Tip clearance actuation with magnetic bearings for high-speed compressor stall control. *J. Eng. Gas Turbines and Power*, 123, 464.

Stone, K. M. (1996) *Review of Literature on Heat Transfer Enhancement in Compact Heat Exchangers* ACRC TR-105 Air Conditioning and Refrigeration Center University of Illinois Mechanical & Industrial Engineering Dept. 1206 West Green Street Urbana, IL 61801 (217) 333-3115

Stowell, W. R. (1989) Active clearance control. United States patent application, 4,842,477, 1989.

Stueber, H. B., Baehre, E. E., Alberecht, R. W., Glynn, C. C. & Hemmelgarn, R. J. (1994) *Stator seal assembly providing improved clearance control.* United States patent application, 5333993, 1994.

Tallman, J. & Lakshminarayana, B. L. (2001) *Methods for desensitizing tip clearance effects in turbines.* ASME. Paper number: 2001-GT-0486.

Terninko, J. (2000) Su-Field Analysis. *TRIZ Journal*. [Online] Available from: http://www.triz-journal.com/archives/2000/02/article 4_02-2000.pdf[Accesssed 29th November 2010].

Thai Technics (2001) *Single spool*.
[online] Available http://www.thaitechnics.com/engine/engine_type.html

Theodorsen, T. & Regier, A. (1944) *Experiments on drag of revolving discs, cylinders and streamline rods at high speeds.* NACA. Report number: 793.

Therbert, G. W. (1981) *Blade tip clearance control.* United States patent application, 4247247, 1981.

Thompson, G. & Lordan, M. (. (1999). Review of creativity principles applied to engineering design. *Proceedings of the Institution of Mechanical Engineers*. **213, 1**, 17-31.

Tritton, D. J. (1988) *Physical fluid dynamics.* Oxford, Oxford University Press.

Tsai, S. K. & Childs, P. R. N. (2008) TRIZ incorporating the BRIGHT process in design. *TRIZ Future 2008 Conference, Enschede,* Netherlands, pp. 243-250.

Tseng, W. & Hauser, A. A. (1991) *Blade tip clearance control apparatus with shroud segment position adjustment by unison ring movement*. United States patent application, 5035573, 1991.

Tucker, P. G. (1993) *Numerical and experimental investigation of flow structure and heat transfer in a rotating cavity with an axial throughflow of cooling air.* D.Phil. thesis, School of Engineering, University of Sussex, UK.

Tucker, P. G. & Long, C. A. (1996) Numerical investigation into influence of geometry on flow in a rotating cavity with an axial throughflow. *Int. Comm. Heat Mass Transfer,* 23 (3), 335-344.

Vakhtin, A. B., Chen, S. J. & Massick, S. M. (2009) *Optical probe for monitoring blade tip clearance.* AIAA. Paper number: 2009-507.

Vidal, R. V. V. (2005) Creativity for Operational Researchers. *Investegacao Operational*, 25 (1),1-24.

Villalba, E. (2008) *On Creativity, Towards an Understanding of Creativity and its Measurements*, JRC Scientific and Technical Reports, European Commission http://publications.jrc.ec.europa.eu/repository/bitstream/111111111/11605/1/eur_on%20creativity_new_.pdf [Accessed 1st December, 2010].

Wakemen, T. G. & Corsmeier, R. J. (1997) *Turbo machine shroud-to-rotor blade dynamic clearance control.* United States patent application, 5601402, 1997.

Walker, R. C., Reese, S. P., Joyce, D. L. & Kastrup, D. A. (1991) *Active clearance control for gas turbine engine*. United States patent application, 5012420, 1991.

Walker, A., Wakeman, T. G., Lenahan, D. T., Plemmons, L. W. & Elovic, A. P. (1992) *Turbine shroud clearance control assembly.* United States patent application, 5127793, 1992.

Wallis, A. M., Denton, J. D. & Demargne, A. J. (2000) *The control of shroud leakage flows to reduce aerodynamic losses in a low aspect ratio, shroud axial flow turbine.* ASME. Paper number: 2000-GT-0475.

Weimer, M. M. & Klusman, S. A. (1993) *Turbomachine with active tip clearance control*. United States patent application, 5263816, 1993.

Weiner, H. I. & Allard, K. L. (1986) *Active clearance control.* United States patent application, 4576547, 1986.

White, F. M. (1984). *Heat Transfer*. Addison-Wesley Publishing Company. pp. 158-164. ISBN 0-201-08324-8

Williams, R., Smith, D. G. & He, L. (2006) *A study of large tip clearance flows in an axial compressor blade row.* ASME. Paper number: GT2006-90463.

Wilson, J. W. (2004) *Passive clearance control.* United States patent application, 6877952 B2, 2004.

Wilson, D. G. (1993) *The design of high-efficiency turbomachinery and gas turbines.* The MIT Press Cambridge, Massachussetts London, England. ISBN 0-262-23114-X

Wikipedia (2013) *Multi-spool*
Available [Online] http://en.wikipedia.org/wiki/Turbine_blade [Assesed on 22nd July 2013]

Wright, W. B. & Flatman, R. J. (1987) *Blade tip clearance control.* United States patent application, 4,683,716, 1987.

Xia, J. (2002) *Active control system for gas turbine blade tip clearance*. United States patent application, 6401460 B1, 2002.

Yamaha, K., Funazaki K. & Furukawa, M. (2007) *The behaviour of tip clearance flow at near-stall condition in a transonic axial compressor rotor.* ASME. Paper number: GT2007-27725.

Yang, H., Acharya, S., Ekkad, S. & Prakash, C. (2002) *Numerical simulation of film cooling on the tip of a gas turbine blade*. ASME. Paper number: 2002-GT-30553.

Zadworna, M., Musator, M. & Obrezkovs, R. (2008) *TRIPS Agreement's Impact on the Accessibility of Pharmaceuticals in the Developing Countries: Developed Game-Theoretic Model*. Bachelor Thesis in Business Administration Final Seminar date: School of Sustainable Development of Society and Technology, Malardalen University, Sweden.

Zhao, S., Lu, X., Zhu, J. & Zhang, H. (2010) *Investigation of the effects of circumferential grooves on the unsteadiness of tip clearance flow to enhance compressor flow instability.* ASME. Paper number: GT2010-22652.

Zlotin, B. ,& Zusman, A. (2001) *Directed Evolution: Philosophy, Theory and Practice*. Southfield, MI, USA, Ideation International Inc.

Zusman, A. (1998) *Overview of Creative Methods*. Southfield, MI, USA, Ideation International Inc.

APPENDICES

APPENDIX 1.1: Publications

Prior to completion of this thesis some of the results and findings had been presented and published at various conferences. They are included within this appendix for completeness.

Ekong, G.I, Long, C.A, Atkins, N.R. and Childs, P.R.N, The development of concepts for the control of tip clearance control concepts in Gas turbine H.P compressor, Proceedings of the TRIZ (Theory of Inventive Problem Solving) Future Conference 2011, 2–4 November 2011, Dublin-Ireland, page 437-440. ISBN: 978-0-9551218-2-1.

Ekong, G.I, Exploring Compressor Clearance control concepts using Heat transfer coefficient Approach, American Society of Mechanical Engineers (ASME) International Mechanical Engineering Congress and Exposition, November 11-17, 2011, Colorado Convention Center & Hyatt Regency Denver, Denver, Colorado, USA, IMECE2011-66224.

Ekong, G.I, Long, C.A, Atkins, N.R. and Childs, P.R.N, Developing Compressor Clearance control concepts using Time Constant Reduction Approach, American Society of Mechanical Engineers (ASME) International Mechanical Engineering Congress and Exposition, November 11-17, 2011, Colorado Convention Center & Hyatt Regency Denver, Denver, Colorado, USA, IMECE2011-66226.

Ekong, G.I, The application of 40 inventive principles in tip clearance control concepts in Gas turbine H.P compressor, Proceedings of the TRIZ (Theory of Inventive Problem Solving) Future Conference 2012, 24 – 26 October 2012, Lisbon-Portugal, page 447-459. ISBN: 978-989-95683-1-0.

Ekong, G.I, Long, C.A, and Childs, P.R.N., Tip Clearance control concept in H.P compressor, American Society of Mechanical Engineers (ASME) International Mechanical Engineering Congress and Exposition, November 9-15, 2012, Houston, Texas, USA, IMECE2012-93063.

Ekong, G.I, Long, C.A, and Childs, P.R.N, The Effect of Heat Transfer Coefficient increase on Tip Clearance control concept in H.P compressors in Gas Turbine Engine, American Society of Mechanical Engineers (ASME) International Mechanical Engineering Congress and Exposition, November 15-21, 2013, San Diego, CA, USA, IMECE2012-64958.

Ekong, G.I, Childs, P.R.N. and Long, C.A., Application of creativity tools to Gas Turbine Engine Compressor Clearance Control, American Society of Mechanical Engineers (ASME) International Mechanical Engineering Congress and Exposition, November 15-21, 2013, San Diego, CA, USA, IMECE2012-64932.

ETRIA EUROPEAN TRIZ ASSOCIATION

TRIZ Future 2011, Dublin, Ireland

The development of concepts for the control of tip clearance in Gas turbine HP compressors using TRIZ

G.I.Ekong[a*], C. A. Long,[a*], N. R. Atkins[b], P. R. N. Childs[c]

[a] *Thermo-Fluid Mechanics Research Centre, University of Sussex, Brighton, BN1 9QT, UK*
[b] *Dept. of Engineering, University of Cambridge, Cambridge CB3 0DY, UK*
Dept. of Mech. Engineering, Imperial College London, South Kensington, London, SW7 2AZ, UK

Abstract

The control of tip clearance in high pressure (HP) compressors has been a continuing issue in the gas turbine industry. The gap varies significantly during different operating conditions of the engine due to centrifugal forces on the rotor and differential thermal expansions in the discs and casing. The relevance of TRIZ to this was the need for new forms of solution to the design problem and it was also selected in order to surmount a perceived conflict during the selection of a solution to the design problem. This paper presents the development of concepts and the evaluation of the concept for the reduction and control of tip clearance using the TRIZ (theory of inventive problem solving) process. A design process was carried out and a series of theoretical solutions has been developed and their prospective practicality in tip clearance control investigated with thermal modelling.

Keywords: Compressors; Tip clearance control; Innovation

1. Introduction

Tip clearance is the radial gap between the stationary compressor casing and the rotating blades. The gap varies significantly during different operating conditions of the engine due to centrifugal forces on the rotor and differential thermal expansions in the discs and casing. In general, as the clearance between the compressor blade tips and the casing increases, the aerodynamic efficiency will decrease and therefore the specific fuel consumption and operating costs will increase, and the clearance is therefore of critical importance to civil airline operators and their customers alike.

In compressors, an efficient control scheme for the tip gap between the rotor blade and casing is necessary for engine stability; this would help reduce surge occurrence and reduction in cruise clearance during the engine operating cycle.

2. Application of TRIZ technique to tip clearance concepts

TRIZ is the Russian acronym for "Teoriya Resheniya Izobretatelskikh Zadatch" meaning the 'Theory of Inventive Problem-solving.' TRIZ is sometimes referred to as a model-based technology for generating new ideas, the refinement of old ideas and solutions for problem-solving and has been identified as potentially useful in turbo machinery design applications (see [2]). Following completion of a review of tip clearance patents, a TRIZ session took place at Rolls-Royce (plc) to determine the issues relating to tip clearance. During these sessions, resource definition was carried out and problem definition was captured using an Issue Based Information System called DRed (See [1]). An indication of some of the issues and ideas arising is shown in Figure 1. These includes thermal effects, casing out-of round, dynamic and static loads, manufacture and build issues, measurement and control issues, and design and validation issues.

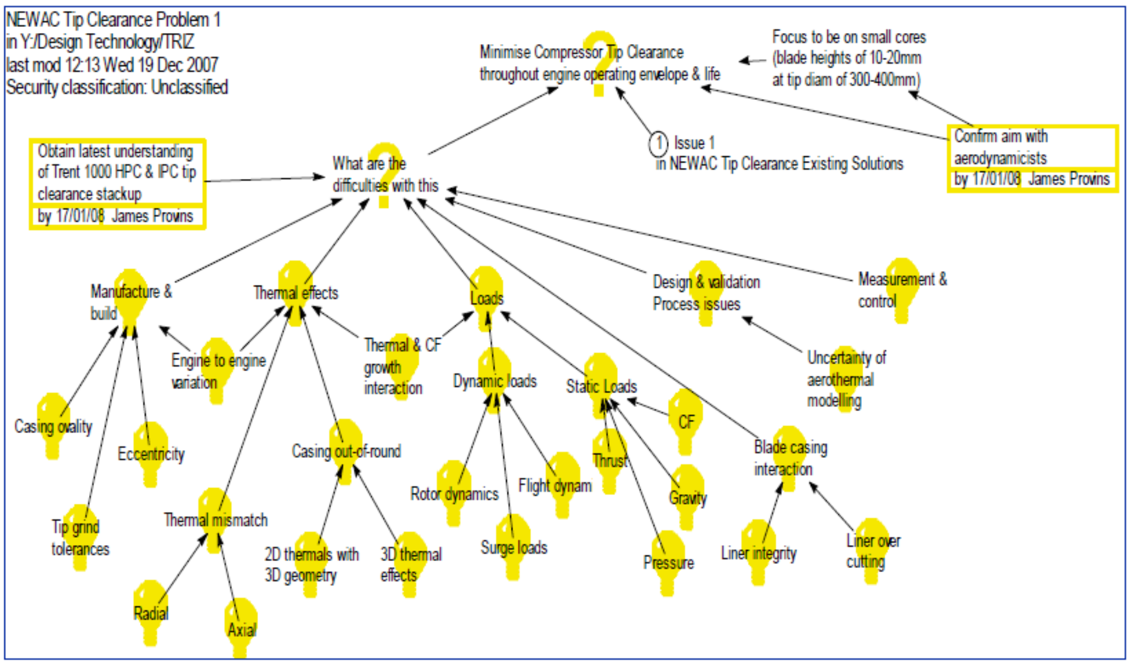

Fig. 1: Tip clearance problems

Some creative techniques such as brainstorming, Ideal Final Result, checklist, and creative thinking were utilised in conjunction with the 40 TRIZ Inventive Principles to determine suitable principles to deploy in developing tip clearance control concepts for compressors. During the TRIZ session, 'Post-it' brainstorming was used to collect ideas generated by participants with the originator of the idea identified by use of initials. In all, 162 raw ideas were generated, subsequently scanned and assembled into an idea database called the NEWAC Tip Clearance Control System Idea Database. The ideas were then categorised and rated in terms of viability, risk, and potential benefit, and hence 41 of the ideas were identified and considered for further investigation. These included both passive and active concepts which can be summarised by the following general areas:

- Control of the disc/casing thermal response;
- Control of the blade/casing mechanical response;
- Asymmetry reduction.

A sensitivity analysis was carried out based on the TRIZ results to determine the quantitative effect of various parameters such as the heat transfer coefficient and time constants on the closure behaviour of the various high-pressure compressor stages. The results are presented in Section 3.

3. Sensitivity analysis results

Based on the results from the TRIZ session, a sensitivity analysis was carried out in order to determine the quantitative effect of various parameters such as the heat transfer coefficient and time constants on the closure behaviour of the various high-pressure compressor stages. The most promising ideas generated during the session were analysed for use on the Trent 1000 engine. An example analysis is shown in Figure 2 which illustrates the effect of increasing the heat transfer coefficient on the clearance behaviour of stage three of an engine compressor drum model. The corresponding finite element model is illustrated in Figure 3. Due to commercial constraints, the extent of information provided here is limited as the project is on-going.

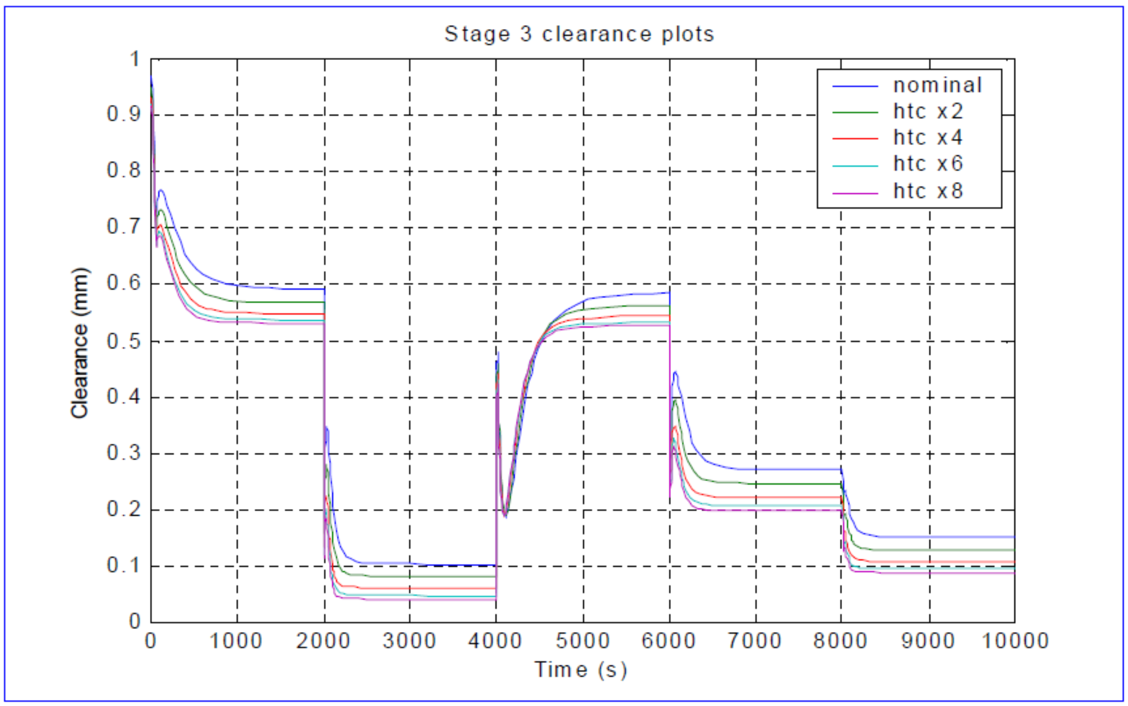

Figure 2: Clearance as a function of time over the square cycle for the Trent 1000 HP compressor stage 3 drum and casing model

As shown in Figure 2, increasing the heat transfer coefficient will reduce the drum time constant, which provides an indication of the speed of response of the equipment to changes in boundary conditions. This will reduce the 're-slam,' or sudden change in operating speed, characteristics of the drum and hence the reduction in clearance throughout the cycle. The effect is not very large but will improve significantly by the introduction of radial air inflow into the drum cavity to increase the thermal response of the HP compressor drum.

Figure 3: Trent 1000 drum model

4. Conclusion

A better tip clearance control can be achieved by reducing the high pressure compressor (HPC) drum time constant. The drum time constant can be reduced by increasing the heat transfer coefficient of the drum. In order to surmount a perceived conflict during the selection of a solution to the design concepts of tip clearance control it was decided that TRIZ be used. The TRIZ process adopted was to categorise ideas generated during the brainstorming session thereby reducing the number of ideas carried forward for further engineering analysis. TRIZ was found to be highly useful in provoking ideas in an area that had previously been tackled several times using traditional approaches. The work described here is targeted on the development of alternative engine configurations in order to achieve significant and robust reduction of tip clearance through out engine operating cycle.

References

[1] Aurisicchio M., Gourtovaia M., Bracewell R. H., and Wallace K. M., 2007, "Evaluation Of How Dred Design Rationale Is Interpreted," Proc. of International Conference on Engineering Design (ICED 07), Paris, France, Design Society.

[2] Childs, P.R.N., Tsai, S.K. Creativity in the design process in the turbomachinery industry. Journal of Design Research, Vol. 8, pp. 145-164, 2010.

APPENDIX 2.1: NEWAC Clearance Control Patent Database

NEWAC
Clearance Control Patent Database, Godwin Ekong, Nick Atkins, December 2007

Summary Table

Company	Short Name	Total
Rolls-Royce	R-R	15
General Electric	GE	39
United Technologies	P&W	30
General Motors	GMC	2
SNECMA	SNEC	2
Mitsubishi Heavy Industries	MHI	1
Solar Turbines	SOLAR	2
Westinghouse Electric	WEC	2
Allison	ALL	2
NASA, USAF, SIEMENS, ABB, Florida Turbine		1 each

Patent Table

	Date	Company	Number	Title
100	2007	GE	7,246,996 B2	METHODS AND APPARATUS FOR MAINTAINING ROTOR ASSEMBLY TIP CLEARANCES
99	2007	R-R	7,198,454 B2	VARIABLE STATOR VANE ARRANGEMENT FOR A COMPRESSOR
98	2007	GE	2007/0140839 A1	THERMAL CONTROL OF GAS TURBINE ENGINE RINGS FOR ACTIVE CLEARANACE CONTROL
97	2007	GE	EP 1 860 281 A2	METHOD FOR CONTROLLING BLADE TIP CLEARANCE IN A GAS TURBINE
96	2007	P&W	2007/0043497A1	SYSTEM AND METHOD FOR MONITORING THERMAL GROWTH AND CONTROLLING
95	2006	GE	7,090,462 B2	COMPRESSOR BLEED AIR MANIFOLD FOR BLADE CLEARANCE CONTROL
94	2006	R-R	7140836 B2	CASING ARRANGMENT
93	2006	P&W	2006/0140756 A1	GAS TURBINE ENGINE BLADE TIP CLEARANCE APPARATUS AND METHOD
92	2004	GE	2004/029011 A1	HIGH PRESSURE TURBINE ELASTIC CLEARANCE CONTROL SYSTEM AND METHOD
91	2004	Florida Turbine Technologies	6,877,952	PASSIVE CLEARANCE CONTROL

90	2002	GE	6,435,823 B1	BUCKET TIP CLEARANCE CONTROL SYSTEM
89	2002	SIEMENS	6,401,460 B1	ACTIVE CONTROL SYSTEM FOR GAS TURBINE BLADE TIP CLEARANCE
88	2001	ALL	6,273,671 B1	BLADE CLEARANCE CONTROL FOR TURBOMACHINERY
87	1992	GE	5,167,488A1	CLEARANCE CONTROL ASSEMBLY HAVING THERMALLY-CONTROLLED ONE-PIECE ………
86	2000	MHI	6,152,685	SEAL CLEARANCE CONTROL SYSTEM FOR GAS TURBINE STATIONARY BLADE
85	2000	R-R	6,126,390	PASSIVE CLEARANCE CONTROL SYSTEM FOR A GAS TURBINE
84	2000	P&W	6,116,852	TURBINE PASSIVE THERMAL VALVE FOR IMPROVED TIP CLEARANCE CONTROL
83	1999	R-R	5,871,333	TIP CLEARANCE CONTROL
82	1998	R-R	5,791,872	BLADE TIP CLEARANCE CONTROL APPARATUS
81	1998	GE	5,779,442	REMOVABLE INNER TURBINE SHELL WITH BUCKET TIP CLEARANCE CONTROL
80	1998	SOLAR	5,779,436	TURBINE BLADE CLEARANCE CONTROL SYSTEM
79	1997	P&W	5,688,107	TURBINE BLADE PASSIVE CLEARANCE CONTROL
78	1997	P&W	5,667,359	CLEARANCE CONTROL FOR THE TURBINE OF A GAS TURBINE
77	1997	WEC	5,667,358	METHOD FOR REDUCING STEADY STATE ROTOR BLADE TIP CLEARANCE IN LAND-BASED…
76	1997	ALL	5,658,125	MAGNETIC BEARINGS ACTUATION FOR COMPRESSOR STABILITY CONTROL
75	1997	P&W	5,645,399	GAS TURBINE ENGINE CASE COATED WITH THERMAL BARRIER COATING TO CONTROL…….
74	1997	ABB	5,605,437	COMPRESSSOR AND METHOD OF OPERATING IT
73	1997	USAF	5,601,402	TURBO MACHINE SHROUD-TO- ROTOR BLADE DYNAMIC CLEARANCE CONTROL
72	1997	GE	5,593,277	SMART TURBINE SHROUD
71	1996	GE	5,562,408	ISOLATED TURBINE SHROUD
70	1996	P&W	5,545,007	ENGINE BLADE CLEARANCE CONTROL SYSTEM WITH PIEZOELECTRIC ACTUATOR
69	1995	P&W	5,456,576	DYNAMIC CONTROL OF TIP CLEARANCE
68	1995	P&W	5,403,158	AERODYNAMIC TIP SEALING FOR ROTOR BLADES
67	1995	GE	5,399,066	INTERGRAL CLEARANCE CONTROL IMPINGEMENT MANIFOLD AND ENVIR. SHIELD
66	1994	R-R	5,351,732	GAS TURBINE CLEARANCE CONTROL
65	1994	GE	5,351,473	METHOD FOR AIR BLEEDING
64	1994	GE	5,333,993	STATOR SEAL ASSEMBLY PROVIDING IMPROVED CLEARANCE CONTRO
63	1994	R-R	5, 295, 787	TURBINE ENGINES
62	1994	P&W	5,282,721	PASSIVE CLEARANCE CONTROL SYSTEM FOR TURBINE BLADES
61	1994	GE	5,281,085	CLEARANCE CONTROL SYSTEM SEPARATELY EXPANDING OR CONTRACTING PORTION…..
60	1993	GMC	5,263,816	TURBOMACHINE WITH ACTIVE TIP CLEARANCE CONTROL
59	1993	GE	5,261,228	APPARATUS FOR BLEEDING AIR
58	1993	GE	5,228,828	GAS TURBINE ENGINE CLEARANCE CONTROL APPARATUS
57	1993	GE	5,219,268	GAS TURBINE ENGINE CASE THERMAL CONTROL FLANGE
56	1993	GE	5,212,940	TIP CLEARANCE CONTROL APPARATUS AND METHOD
55	1993	R-R	5,211,534	BLADE TIP CLEARANCE CONTROL APPARATUS
54	1993	GE	5,205,115	GAS TURBINE ENGINE CASE COUNTERFLOW THERMAL CONTROL

53	1993	WEC	5,203,673	TIP CLEARANCE CONTROL APPARATUS FOR A TURBO-MACHINE BLADE
52	1992	P&W	5,154,575	THERMAL BLADE TIP CLEARANCE CONTROL FOR GAS TURBINE ENGINES
51	1992	GE	5,127,793	TURBINE SHROUD CLEARANCE CONTROL ASSEMBLY
50	1992	GE	5,116,199	BLADE TIP CLEARANCE CONTROL APP. ANNULAR SUPPORT RING THERMAL EXPANSION
49	1992	GE	5,100,291	IMPINGEMENT MANIFOLD
48	1992	R-R	5,092,737	BLADE TIP CLEARANCE CONTROL ARRANGEMENT FOR A GAS TURBINE
47	1992	P&W	5,090,193	ACTIVE CLEARANCE CONTROL WITH CRUISE MODE
46	1991	P&W	5,076,050	THERMAL CLEARANCE METHOD FOR GAS TURBINE ENGINE
45	1991	R-R	5,064,343	GAS TURBINE WITH TURBINE TIP CLEARANCE CONTROL DEVICE & METHOD OF OPERATION
44	1991	GE	5,056,988	BLADE CLEARANCE APPARATUS USING SHROUD SEGMENT POSITION MODULATION
43	1991	GE	5,054,997	BLADE TIP CLEARANCE CONTROL APPARATUS USING BELLCRANK MECHANISM
42	1991	P&W	5,048,288	COMBINED TURBINE STATOR COOLING AND TURBINE TIP CLEARANCE CONTROL
41	1991	R-R	5,044,881	TURBOMACHINE CLEARANCE CONTROL
40	1991	GE	5,035,573	BLADE TIP CLEARANCE CONTROL APP. WITH SHROUD SEGMENT POSTION ADJUSTMENT…
39	1991	GE	5,018,942	MECHANICAL BLADE TIP CLEARANCE CONTROL APPARATUS FOR A GAS TURBINE ENGINE
38	1991	GE	5,012,420	ACTIVE CLEARANCE CONTROL FOR GAS TURBINE ENGINE
37	1990	GE	4,928,240	ACTICE CLEARANCE CONTROL
36	1990	GE	4,893,984	CLEARANCE CONTROL SYSTEM
35	1990	GE	4,893,983	ACTIVE CLEARANCE CONTROL
34	1990	GE	3,966,354	THERMAL ACTUATED VALVE FOR CLEARANCE CONTROL
33	1989	SOLAR	4,874,290	TURBINE BLADE TIP CLEARANCE CONTROL SYSTEM
32	1989	P&W	4,856,272	METHOD FOR MAINTAINING BLADE TIP CLEARANCE
31	1989	SNEC	4,849,895	SYSTEM FOR ADJUSTING RADIAL CLEARANCE BETWEEN ROTOR AND STATOR ELEMENTS
30	1989	R-R	4,844,688	GAS TURBINE CONTROL SYSTEM
29	1989	GE	4,842,477	ACTIVE CLEARANCE CONTROL
28	1989	P&W	4,815,272	TURBINE COOLING AND THERMAL CONTROL
27	1989	R-R	4,804,310	CLEARANCE CONTROL APPARATUS FOR A BLADED FLUID FLOW MACHINE
26	1987	R-R	4,683,716	BLADE TIP CLEARANCE CONTROL
25	1987	P&W	4,648,241	ACTIVE CLEARANCE CONTROL
24	1986	P&W	4,576,547	ACTIVE CLEARANCE CONTROL
23	1985	P&W	4,541,775	CLEARANCE CONTROL IN TURBINE SEALS
22	1985	P&W	4,525,998	CLEARANCE CONTROL FO GAS TURBINE
21	1985	P&W	4,513,567	GASTURBINE ENGINE ACTIVE CLEARANCE CONTROL
20	1985	P&W	4,493,184	PRESSURIZED NACELLE COMP. FOR ACTIVE CLEARANCE CONTROLLED GAS TURBINE ENG.
19	1984	P&W	4,487,016	MODULATED CLEARANCE CONTROL FOR AN AXIAL ROTARY MACHINE
18	1982	GE	4,363,599	CLEARANCE CONTROL
17	1982	R-R	4,330,234	ROOR TIP CLEARNCE CONTROL APPARATUS FOR GAS TURBINE ENGINE
16	1982	NASA	4,329,114	ACTIVE CONTROL SYSTEM FOR A TURBOMACHINE

15	1982	GE	4,326,804	APPARATUS AND METHOD FOR OPTICAL CLEARANCE DETERMINATION
14	1981	GE	4,304,093	VARIABLE CLEARNCE CONTROL FOR GAS TURBINE ENGINE
13	1981	P&W	4,279,123	EXTERNAL GAS TURBINE ENGINE COOLING FOR CLEARANCE CONTROL
12	1981	P&W	4,268,221	COMPRESSOR STRUCTURE ADAPTED FOR ACTIVE CLEARANCE CONTROL
11	1981	GMC	4,247,247	BLADE TIP CLEARANCE CONTROL
10	1980	P&W	4,242,042	TEMPERATURE CONTROL OFENGINE CASE FOR CLEARANCE CONTROL
9	1980	GE	4,230,436	ROTOR/SHROUD CLEARANCE CONTROL SYSTEM
8	1980	P&W	4,213,296	SEAL CLEARANCE CONTROL FOR A GAS TURBINE
7	1978	GE	4,127,357	VARIABLE SHROUD FOR A TURBOMACHINE
6	1978	P&W	4,069,662	CLEARANCE CONTROL FOR GAS TURBINE
5	1977	P&W	4,019,320	EXTERNAL GAS TURBINE ENGINE COOLING FOR CLEARANCE CONTROL
4	1977	P&W	4,005,946	METHOD AND APPARATUS FOR CONTOLLING STATOR THERMAL GROWTH
3	1976	SNEC	3,975,901	DEVICE FOR REGULATING BLADE TIP CLEARANCE
2	1963	GE	3,058,398	VARIABLE CLEARANCE SHROUD STRUCTURE FOR GAS TURBINE ENGINE
1	1961	GE	2,994,472	TIP CLEARANCE CONTROL SYSTEM FOR TUROMACHINE

Appendix 4: Matching data for stage 3 (Matlab files)

MATCHING DATA FOR TRENT 1000 STAGES

```
% Stage 3

function [stab_cruise_clr,stab_MTO_clr,worst_decel_clr,worst_accel_clr] =
func_closure_mm_stage3_new(dfact,cfact)

% Load the environemtal parameters
[rpm_IDLE,rpm_MTO,rpm_CRUISE,T26_IDLE,T26_MTO,T26_CRUISE,T30_IDLE,T30_MTO,T3
0_CRUISE,t,t0,t1,t2,t3] = envParams('T1000');
pulse_train = ones(1,length(t));

stage = 3;

% stage 3 parameters
radius = 0.3587;
blade_height = 0.036;
alpha_casing = 0.99e-6;
k_drum = 659;
E = 110e9; % Pa

tau_casing_idle = 45;
tau_drum_idle = 280;
Xd_idle = 1.4;
Xc_idle = 1.456;
casing_delay_idle = 17; drum_delay_idle = casing_delay_idle;

tau_casing_accel = 17;
tau_drum_accel = 90;
Xd_accel=0.48;
Xc_accel=1.1;

tau_casing_decel = 40;
tau_drum_decel = 300;
Xd_decel=0.7300;
Xc_decel=1.6540;

tau_drum_cruise = 160;
tau_casing_cruise = 26;
Xd_cruise=0.3929;
Xc_cruise=1.220;

% cfact
cfact=1;
% dfact
dfact=1;

% speed setup
rpm = rpm_IDLE ...
    + ClosureModel_delay((rpm_MTO-rpm_IDLE)*pulse_train,t1)...
    - ClosureModel_delay((rpm_MTO-rpm_IDLE)*pulse_train,t2)...
    + ClosureModel_delay((rpm_CRUISE-rpm_IDLE)*pulse_train,t3);
```

```
% CF growth of the drum
d_cf = k_drum/E*rpm.^2;

% Thermal growths.
t_casing = 288.15+[ClosureModel_delay(Xc_idle*(T30_IDLE - 288.15)*(1-exp(-(t-t0-
casing_delay_idle)./(cfact*tau_casing_idle))),t0+casing_delay_idle) ...
   + ClosureModel_delay(Xc_accel*(T30_MTO-T30_IDLE)*(1-exp(-(t-
t1)./(cfact*tau_casing_accel))),t1) ...
   - ClosureModel_delay(Xc_decel*(T30_MTO-T30_IDLE)*(1-exp(-(t-
t2)./(cfact*tau_casing_decel))),t2) ...
   + ClosureModel_delay(Xc_cruise*(T30_CRUISE-T30_IDLE)*(1-exp(-(t-
t3)./(cfact*tau_casing_cruise))),t3)]*1000;

d_casing = alpha_casing*t_casing;

Trotor_idle = Xd_idle*(T26_IDLE - 288.15)+288.15;
Trotor_acel = Xd_accel*(T26_MTO-T26_IDLE)+288.15;
Trotor_decel = Xd_decel*(T26_MTO-T26_IDLE)+288.15;
Trotor_cruise = Xd_cruise*(T26_CRUISE-T26_IDLE)+288.15;

t_drum = 288.15+[ClosureModel_delay((Trotor_idle-288.15)*(1-exp(-(t-t0-
drum_delay_idle)./(dfact*tau_drum_idle))),t0+drum_delay_idle)  ...
   + ClosureModel_delay((Trotor_acel-288.15)*(1-exp(-(t-t1)./(dfact*tau_drum_accel))),t1) ...
   - ClosureModel_delay((Trotor_decel-288.15)*(1-exp(-(t-t2)./(dfact*tau_drum_decel))),t2) ...
   + ClosureModel_delay((Trotor_cruise-288.15)*(1-exp(-(t-
t3)./(dfact*tau_drum_cruise))),t3)]*1000;

% Variable alpha
alphaD = alphaDrum(t_drum);

% drum displacement
d_drum = radius*alphaD'.*t_drum;

closure = d_casing-(d_cf+d_drum);

% Plot the characteristics

lw = 1; % line width

%plotting
plot(t,closure,'k','linewidth',lw);
hold on
load Stage3.mat
plot(t,clo)
title('Stage 3 - Closure behaviour')
xlabel('Time (s)')
ylabel('Closure (mm)')
legend('Lumped model', 'SC03 model')
grid on
axis([0 8000 -1 0])
```

APPENDIX 5.1: STAGE 3 CLOSURE DATA WITHOUT RADIAL INFLOW

Stage 3	2000-Stabilised Idle		
htc factor	Data	Reduction	%reduction
nominal	-0.40667	1	0
2	-0.40737	0.998272	-0.17305
4	-0.40925	0.993698	-0.63419
6	-0.41099	0.989496	-1.06159
8	-0.41241	0.986085	-1.4111

Stage 3	Worst case acceleration closure (MTO overshoot)		
htc factor	Data	Reduction	%reduction
nominal	-0.6485	1	0
2	-0.6935	0.935116	-6.93857
4	-0.73121	0.886883	-12.7544
6	-0.74782	0.867194	-15.3145
8	-0.75788	0.855674	-16.8669

Stage 3	4000-Stabilised MTO		
htc factor	Data	Reduction	%reduction
nominal	**-0.89425**	1	0
2	**-0.89427**	0.99997	-0.00301
4	**-0.8979**	0.995929	-0.40876
6	**-0.90095**	0.992563	-0.74927
8	**-0.90329**	0.989987	-1.01145

Stage 3	6000-Stabilised idle		
htc factor	Data	Reduction	%reduction
nominal	-0.41176	1	0
2	-0.41183	0.999832	-0.01682
4	-0.41335	0.996143	-0.38722
6	-0.41482	0.99262	-0.74346
8	-0.41618	0.989365	-1.07489

Stage 3	8000-Stabilised cruise closure		
htc factor	Data	Reduction	%reduction
nominal	-0.72626	1	0
2	-0.72917	0.996012	-0.40038
4	-0.73588	0.986929	-1.32446
6	-0.74092	0.980226	-2.01727
8	-0.74476	0.97516	-2.54725

APPENDIX 5.2: STAGE 3 CLEARANCE DATA WITHOUT RADIAL INFLOW

Stage 3	**2000-Stabilised Idle**		
htc factor	Data	Reduction	%reduction
nominal	0.591462	1	0
2	0.568235	1.040875	3.926948
4	0.549362	1.076634	7.117887
6	0.537844	1.099689	9.065212
8	0.531769	1.112253	10.0924

Stage 3	**Worst case acceleration clearance (MTO overshoot)**		
htc factor	Data	Reduction	%reduction
nominal	0.349631	1	0
2	0.28211	1.239341	19.31196
4	0.227395	1.537545	34.96125
6	0.201015	1.739329	42.50655
8	0.186293	1.876779	46.71721

Stage 3	**4000-Stabilised MTO**		
htc factor	Data	Reduction	%reduction
nominal	0.103885	1	0
2	0.081334	1.277259	21.70737
4	0.060707	1.711257	41.56341
6	0.047884	2.169538	53.90724
8	0.040885	2.54092	60.64417

Stage 3	**6000-Stabilised idle**		
htc factor	Data	Reduction	%reduction
nominal	0.586374	1	0
2	0.563781	0.184265	3.853019
4	0.545256	0.190525	7.012125
6	0.534011	0.194537	8.929889
8	0.527992	0.196755	9.956331

Stage 3	**8000-Stabilised cruise clearance**		
htc factor	Data	Reduction	%reduction
nominal	0.271867	1	0
2	0.246436	1.103198	9.354439
4	0.222725	1.220639	18.07571
6	0.207915	1.307587	23.52324
8	0.199412	1.363344	26.65092

APPENDIX 5.3: STAGE 3 CLOSURE DATA WITH RADIAL INFLOW

Stage 3	**2000-Stabilised Idle**		
htc factor	Data	Reduction	%reduction
nominal	-0.40667	1	0
2	**-0.37813**	1.075476	7.017892
4	**-0.37554**	1.082885	7.654061

6	**-0.37367**	1.088321	8.115385
8	**-0.37256**	1.09156	8.388018
	-0.37232	1.09225	8.445827

Stage 3	**Worst case acceleration closure (MTO overshoot)**		
htc factor	Data	Reduction	%reduction
nominal	-0.6485	1	0
2	-0.66376	0.97701	-2.3531
4	-0.70206	0.923712	-8.25888
6	-0.72682	0.892242	-12.0773
8	-0.73531	0.881945	-13.3857
	-0.73912	0.877392	-13.9742

Stage 3	**4000-Stabilised MTO**		
htc factor	Data	Reduction	%reduction
nominal	-0.89425	1	0
2	**-0.79592**	1.123535	10.99524
4	**-0.78608**	1.137601	12.09573
6	**-0.78008**	1.146348	12.76647
8	**-0.77789**	1.149584	13.01199
	-0.77673	1.151293	13.14115

Stage 3	**6000-Stabilised idle**		
htc factor	Data	Reduction	%reduction
nominal	-0.41176	1	0
2	**-0.38379**	1.072882	6.793078
4	-0.38124	1.080059	7.412437
6	-0.37886	1.086822	7.988575
8	-0.37776	1.090011	8.257769
	-0.37668	1.093124	8.519028

Stage 3	**8000-Stabilised cruise closure**		
htc factor	Data	Reduction	%reduction
nominal	-0.72626	1	0
2	-0.64004	1.134717	11.8723
4	-0.63137	1.150308	13.06678
6	-0.62676	1.158759	13.70077
8	-0.62516	1.161731	13.92154
	-0.62457	1.162828	14.00276

APPENDIX 5.4: STAGE 3 CLEARANCE DATA WITH RADIAL INFLOW

Stage 3	**2000-Stabilised Idle**		
htc factor	Data	Reduction	%reduction
nominal	0.591462	1	0
2	0.518429	1.140873	12.34782
4	0.481689	1.227892	18.55959
6	0.457488	1.292847	22.6513
8	0.444042	1.331994	24.92461
	0.435749	1.357345	26.32675

Stage 3	**Worst case acceleration clearance (MTO overshoot)**		
htc factor	Data	Reduction	%reduction
nominal	0.349631	1	0
2	0.232797	1.501867	33.41621
4	0.155171	2.253198	55.61865
6	0.104332	3.35115	70.1595
8	0.081292	4.300929	76.74921
	0.068947	5.071021	80.28011

Stage 3	**4000-Stabilised MTO**		
htc factor	Data	Reduction	%reduction
nominal	0.103885	1	0
2	0.100636	1.032284	3.127409
4	0.07115	1.460087	31.51095
6	0.051071	2.034132	50.83899
8	0.038712	2.683528	62.73562
	0.031338	3.314962	69.83374

Stage 3	**6000-Stabilised idle**		
htc factor	Data	Reduction	%reduction
nominal	0.586374	1	0
2	0.512771	0.202595	12.55211
4	0.475994	0.218249	18.8241
6	0.452289	0.229687	22.8667
8	0.438843	0.236725	25.15975
	0.43139	0.240815	26.43082

Stage 3	**8000-Stabilised cruise clearance**		
htc factor	Data	Reduction	%reduction
nominal	0.271867	1	0
2	0.256518	1.059835	5.645681
4	0.225866	1.203666	16.92048
6	0.204393	1.330117	24.81866
8	0.191442	1.420099	29.58237
	0.183503	1.481538	32.50257

APPENDIX 5.5: STAGE 3 CLEARANCE DATA FOR SPECIFIC HEAT TRANSFER COEFFICIENT

Stage 3	8000-Stabilised cruise clearance		
htc factor	Data	Reduction	%reduction
nominal	0.271867	1	0
50	0.235368	1.155072	13.4253
100	0.222431	1.222253	18.18385
150	0.214419	1.267924	21.13091

APPENDIX 6: SC03 model validation against lumped model (Matlab files)

BASELINE: SC03 MODEL VALIDATION AGAINST LUMPED MODEL	
MP12	MP18

% MP12 analysis
% Load the environemtal parameters
 	
% Spool speed in rpm
rpm_IDLE = 314.16/(2*pi)*60; % NH
rpm_MTO = 837.76/(2*pi)*60; % NH
 	
% Fluid Temperatures in Kelvin
% let T26 = inlet temp
% let T30 = outlet temp
T26_IDLE = 344; % T26 ???
T26_MTO = 440; % T26 ???
 	
T30_IDLE = 344;
T30_MTO = 406;
 	
% Time vector setup
t = 1:3000;
t0 = 0;
t1 = 1005;
t2 = 2010;
t3 = 3000;
 	
pulse_train = ones(1,length(t));
 	
% MP12 parameters
 	
tau_drum_idle = 152; % s
Xd_idle = 1.006;
 	
tau_drum_accel = 48.91809;
Xd_accel=0.64511;
 	
tau_drum_decel = 81.92736;
Xd_decel=0.6300;
 	
ClosureModel_delay_idle=1;
% speed setup
rpm = rpm_IDLE ...
+ ClosureModel_delay((rpm_MTO-
	% MP18 analysis
	% Load the environemtal parameters
	
	% Spool speed in rpm
	rpm_IDLE = 314.16/(2*pi)*60; % NH
	rpm_MTO = 837.76/(2*pi)*60; % NH
	
	% Fluid Temperatures in Kelvin
	% let T26 = inlet temp
	% let T30 = outlet temp
	T26_IDLE = 344; % T26 ???
	T26_MTO = 440; % T26 ???
	
	T30_IDLE = 344;
	T30_MTO = 406;
	
	% Time vector setup
	t = 1:3000;
	t0 = 0;
	t1 = 1005;
	t2 = 2010;
	t3 = 3000;
	
	pulse_train = ones(1,length(t));
	
	% MP18 parameters
	
	tau_drum_idle = 525; % s
	Xd_idle = 0.226;
	
	tau_drum_accel = 35.34131;
	Xd_accel=0.91891;
	
	tau_drum_decel = 97.77802;
	Xd_decel=0.8990;
	;
	
	ClosureModel_delay_idle=1;
	
	% speed setup
	rpm = rpm_IDLE ...
	+ ClosureModel_delay((rpm_MTO-
	rpm_IDLE)*pulse_train,t1)...
	- ClosureModel_delay((rpm_MTO-

<table>
<tr>
<td>rpm_IDLE)*pulse_train,t1)...
   - ClosureModel_delay((rpm_MTO-rpm_IDLE)*pulse_train,t2);

Trotor_idle = Xd_idle*(T26_IDLE - 291)+291;
Trotor_acel = Xd_accel*(T26_MTO-T26_IDLE)+291;
Trotor_decel = Xd_decel*(T26_MTO-T26_IDLE)+291;

t_drum = 291+[ClosureModel_delay((Trotor_idle-291)*(1-exp(-(t-t0-ClosureModel_delay_idle)./(tau_drum_idle))),t0+ClosureModel_delay_idle) ...
   + ClosureModel_delay((Trotor_acel-291)*(1-exp(-(t-t1)./(tau_drum_accel))),t1) ...
   - ClosureModel_delay((Trotor_decel-291)*(1-exp(-(t-t2)./(tau_drum_decel))),t2)];

% Variable alpha
%alphaD = alphaDrum(t_drum);

lw = 1; % line width

%plotting
plot(t,(t_drum),'k','linewidth',lw);
hold on
load MP12_temp.mat
plot(Time,Temp)

title('MP12 - SC03 model validation against Lumped model')
legend('Lumped model','SC03 model')
xlabel('Time (s)')
ylabel('Temperature (K)')

grid on</td>
<td>rpm_IDLE)*pulse_train,t2);

Trotor_idle = Xd_idle*(T26_IDLE - 291)+291;
Trotor_acel = Xd_accel*(T26_MTO-T26_IDLE)+291;
Trotor_decel = Xd_decel*(T26_MTO-T26_IDLE)+291;

t_drum = 291+[ClosureModel_delay((Trotor_idle-291)*(1-exp(-(t-t0-ClosureModel_delay_idle)./(tau_drum_idle))), t0+ClosureModel_delay_idle) ...
   + ClosureModel_delay((Trotor_acel-291)*(1-exp(-(t-t1)./(tau_drum_accel))),t1) ...
   - ClosureModel_delay((Trotor_decel-291)*(1-exp(-(t-t2)./(tau_drum_decel))),t2)];

% Variable alpha
%alphaD = alphaDrum(t_drum);

lw = 1; % line width

%plotting
plot(t,(t_drum),'k','linewidth',lw);
hold on
load MP18_temp.mat
plot(Time,Temp)

title('MP18 - SC03 model validation against Lumped model')
legend('Lumped model','SC03 model')
xlabel('Time (s)')
ylabel('Temperature (K)')

grid on</td>
</tr>
</table>

<table>
<tr><th colspan="2">BASELINE: SC03 MODEL VALIDATION AGAINST LUMPED MODEL</th></tr>
<tr><th>MP22</th><th>MP28</th></tr>
<tr>
<td>
% MP22 analysis
% Load the environemtal parameters

% Spool speed in rpm
   rpm_IDLE = 314.16/(2*pi)*60; % NH
   rpm_MTO = 837.76/(2*pi)*60; % NH</td>
<td>
% MP28 analysis
% Load the environemtal parameters

% Spool speed in rpm
   rpm_IDLE = 314.16/(2*pi)*60; % NH
   rpm_MTO = 837.76/(2*pi)*60; % NH</td>
</tr>
</table>

<table>
<tr>
<td>

```
   % Fluid Temperatures in Kelvin
    % let T26 = inlet temp
   % let T30 = outlet temp
   T26_IDLE = 344; % T26 ???
   T26_MTO = 440; % T26 ???

   %T30_IDLE = 344;
   %T30_MTO = 406;


   % Time vector setup
   t = 1:3000;
   t0 = 0;
   t1 = 1005;
   t2 = 2010;
   t3 = 3000;

pulse_train = ones(1,length(t));



% MP22 parameters


tau_drum_idle =416; % s
Xd_idle = 0.146;

tau_drum_accel = 37.81574;
Xd_accel=0.9150;

tau_drum_decel = 120.1379;
Xd_decel=0.8970;

ClosureModel_delay_idle=1;

% speed setup
rpm = rpm_IDLE ...
   + ClosureModel_delay((rpm_MTO-
rpm_IDLE)*pulse_train,t1)...
   - ClosureModel_delay((rpm_MTO-
rpm_IDLE)*pulse_train,t2);


Trotor_idle = Xd_idle*(T26_IDLE - 291)+291;
Trotor_acel = Xd_accel*(T26_MTO-
T26_IDLE)+291;
Trotor_decel = Xd_decel*(T26_MTO-
T26_IDLE)+291;

t_drum = 291+[ClosureModel_delay((Trotor_idle-
291)*(1-exp(-(t-t0-
```

</td>
<td>

```
   % Fluid Temperatures in Kelvin
    % let T26 = inlet temp
   % let T30 = outlet temp
   T26_IDLE = 344; % T26 ???
   T26_MTO = 440; % T26 ???

   T30_IDLE = 344;
   T30_MTO = 406;


   % Time vector setup
   t = 1:3000;
   t0 = 0;
   t1 = 1005;
   t2 = 2010;
   t3 = 3000;

pulse_train = ones(1,length(t));



% MP28 parameters

 tau_drum_idle =368; % s
Xd_idle = 0.106;


tau_drum_accel = 34.27152;
Xd_accel=0.9050;

tau_drum_decel =158.1572;
Xd_decel=0.8900;

ClosureModel_delay_idle=1;

% speed setup
rpm = rpm_IDLE ...
   + ClosureModel_delay((rpm_MTO-
rpm_IDLE)*pulse_train,t1)...
   - ClosureModel_delay((rpm_MTO-
rpm_IDLE)*pulse_train,t2);


Trotor_idle = Xd_idle*(T26_IDLE - 291)+291;
Trotor_acel = Xd_accel*(T26_MTO-
T26_IDLE)+291;
Trotor_decel = Xd_decel*(T26_MTO-
T26_IDLE)+291;

t_drum =
291+[ClosureModel_delay((Trotor_idle-
291)*(1-exp(-(t-t0-
```

</td>
</tr>
</table>

ClosureModel_delay_idle)./(tau_drum_idle))),t0+ClosureModel_delay_idle) ... + ClosureModel_delay((Trotor_acel-291)*(1-exp(-(t-t1)./(tau_drum_accel))),t1) ... - ClosureModel_delay((Trotor_decel-291)*(1-exp(-(t-t2)./(tau_drum_decel))),t2)]; % Variable alpha %alphaD = alphaDrum(t_drum); lw = 1; % line width %plotting plot(t,(t_drum),'k','linewidth',lw); hold on load MP_22_temp.mat plot(Time,Temp) title('MP22 - SC03 model validation against Lumped model') legend('Lumped model','SC03 model') xlabel('Time (s)') ylabel('Temperature (K)') grid on	ClosureModel_delay_idle)./(tau_drum_idle))),t0+ClosureModel_delay_idle) ... + ClosureModel_delay((Trotor_acel-291)*(1-exp(-(t-t1)./(tau_drum_accel))),t1) ... - ClosureModel_delay((Trotor_decel-291)*(1-exp(-(t-t2)./(tau_drum_decel))),t2)]; % Variable alpha %alphaD = alphaDrum(t_drum); lw = 1; % line width %plotting plot(t,(t_drum),'k','linewidth',lw); hold on load MP_28_temp.mat plot(Time,Temp) title('MP28 - SC03 model validation against Lumped model') legend('Lumped model','SC03 model') xlabel('Time (s)') ylabel('Temperature (K)') grid on

RADIAL INFLOW: SC03 MODEL VALIDATION AGAINST LUMPED MODEL	
MP12	MP18

% MP12 analysis
% Load the environemtal parameters
% Spool speed in rpm
rpm_IDLE = 314.16/(2*pi)*60; % NH
rpm_MTO = 837.76/(2*pi)*60; % NH
% Fluid Temperatures in Kelvin
% let T26 = inlet temp
% let T30 = outlet temp
T26_IDLE = 344;
T26_MTO = 440;
T30_IDLE = 344;
T30_MTO = 406;
% Time vector setup
t = 1:3000;
t0 = 0;
t1 = 1005;
t2 = 2010;
t3 = 3000;
pulse_train = ones(1,length(t));
	% MP18 analysis
	% Load the environemtal parameters
	% Spool speed in rpm
	rpm_IDLE = 314.16/(2*pi)*60; % NH
	rpm_MTO = 837.76/(2*pi)*60; % NH
	% Fluid Temperatures in Kelvin
	% let T26 = inlet temp
	% let T30 = outlet temp
	T26_IDLE = 344;
	T26_MTO = 440;
	T30_IDLE = 344;
	T30_MTO = 406;
	% Time vector setup
	t = 1:3000;
	t0 = 0;
	t1 = 1005;
	t2 = 2010;
	t3 = 3000;
	pulse_train = ones(1,length(t));
	% MP18 parameters

% MP12 parameters
tau_drum_idle = 101.43; % s
Xd_idle = 3.306;
tau_drum_accel = 15.20;
Xd_accel=1.1991;
tau_drum_decel = 31.19;
Xd_decel=1.2150;
ClosureModel_delay_idle=1;
% speed setup
rpm = rpm_IDLE ...
+ ClosureModel_delay((rpm_MTO-rpm_IDLE)*pulse_train,t1)...
- ClosureModel_delay((rpm_MTO-rpm_IDLE)*pulse_train,t2);
Trotor_idle = Xd_idle*(T26_IDLE - 291)+291;
Trotor_acel = Xd_accel*(T26_MTO-T26_IDLE)+291;
Trotor_decel = Xd_decel*(T26_MTO-T26_IDLE)+291;
t_drum = 291+[ClosureModel_delay((Trotor_idle-291)*(1-exp(-(t-t0-ClosureModel_delay_idle)./(tau_drum_idle))),t0+ClosureModel_delay_idle) ...
+ ClosureModel_delay((Trotor_acel-291)*(1-exp(-(t-t1)./(tau_drum_accel))),t1) ...
- ClosureModel_delay((Trotor_decel-291)*(1-exp(-(t-t2)./(tau_drum_decel))),t2)];
% drum displacement
lw = 1; % line width
%plotting
plot(t,(t_drum),'k','linewidth',lw);
hold on
load MP12_rad.mat
plot(Time6,Temp6)
title('MP12 - SC03 model with 6% radial inflow validation against Lumped model')
legend('Lumped model','SC03 model')
xlabel('Time (s)')
ylabel('Temperature (K)')
grid on
	tau_drum_idle = 153.78; % s
	Xd_idle = 1.806;
	tau_drum_accel = 22.77;
	Xd_accel=1.2991;
	tau_drum_decel = 65.67;
	Xd_decel=1.3750;
	ClosureModel_delay_idle=1;
	% speed setup
	rpm = rpm_IDLE ...
	+ ClosureModel_delay((rpm_MTO-rpm_IDLE)*pulse_train,t1)...
	- ClosureModel_delay((rpm_MTO-rpm_IDLE)*pulse_train,t2);
	Trotor_idle = Xd_idle*(T26_IDLE - 291)+291;
	Trotor_acel = Xd_accel*(T26_MTO-T26_IDLE)+291;
	Trotor_decel = Xd_decel*(T26_MTO-T26_IDLE)+291;
	t_drum = 291+[ClosureModel_delay((Trotor_idle-291)*(1-exp(-(t-t0-ClosureModel_delay_idle)./(tau_drum_idle))),t0+ClosureModel_delay_idle) ...
	+ ClosureModel_delay((Trotor_acel-291)*(1-exp(-(t-t1)./(tau_drum_accel))),t1) ...
	- ClosureModel_delay((Trotor_decel-291)*(1-exp(-(t-t2)./(tau_drum_decel))),t2)];
	% drum displacement
	lw = 1; % line width
	%plotting
	plot(t,(t_drum),'k','linewidth',lw);
	hold on
	load MP18_rad.mat
	plot(Time6,Temp6)
	title('MP18 - SC03 model with 6% radial inflow validation against Lumped model')
	legend('Lumped model','SC03 model')
	xlabel('Time (s)')
	ylabel('Temperature (K)')
	grid on

RADIAL INFLOW: SC03 MODEL VALIDATION AGAINST LUMPED MODEL	
MP22	MP28
% MP22 analysis % Load the environemtal parameters % Spool speed in rpm rpm_IDLE = 314.16/(2*pi)*60; % NH rpm_MTO = 837.76/(2*pi)*60; % NH % Fluid Temperatures in Kelvin % let T26 = inlet temp	% MP28 analysis % Load the environemtal parameters % Spool speed in rpm rpm_IDLE = 314.16/(2*pi)*60; % NH rpm_MTO = 837.76/(2*pi)*60; % NH % Fluid Temperatures in Kelvin % let T26 = inlet temp

```
    % let T30 = outlet temp
    T26_IDLE = 344;
    T26_MTO = 440;
    T30_IDLE = 344;
    T30_MTO = 406;
   % Time vector setup
    t = 1:3000;
    t0 = 0;
    t1 = 1005;
    t2 = 2010;
    t3 = 3000;
 pulse_train = ones(1,length(t));
 % MP12 parameters
 tau_drum_idle = 199.05;
Xd_idle = 1.066;
 tau_drum_accel = 27.70;
Xd_accel=1.2991;
 tau_drum_decel = 93.64;
Xd_decel=1.3150;
 ClosureModel_delay_idle=1;
% speed setup
rpm = rpm_IDLE ...
    + ClosureModel_delay((rpm_MTO-
rpm_IDLE)*pulse_train,t1)...
    - ClosureModel_delay((rpm_MTO-
rpm_IDLE)*pulse_train,t2);
 Trotor_idle = Xd_idle*(T26_IDLE - 291)+291;
Trotor_acel = Xd_accel*(T26_MTO-
T26_IDLE)+291;
Trotor_decel = Xd_decel*(T26_MTO-
T26_IDLE)+291;
 t_drum =
291+[ClosureModel_delay((Trotor_idle-291)*(1-
exp(-(t-t0-
ClosureModel_delay_idle)./(tau_drum_idle))),t0
+ClosureModel_delay_idle)  ...
    + ClosureModel_delay((Trotor_acel-291)*(1-
exp(-(t-t1)./(tau_drum_accel))),t1) ...
    - ClosureModel_delay((Trotor_decel-
291)*(1-exp(-(t-t2)./(tau_drum_decel))),t2)];
% drum displacement
lw = 1; % line width
 %plotting
plot(t,(t_drum),'k','linewidth',lw);
hold on
load MP22_rad.mat
plot(Time6,Temp6)
 title('MP22 - SC03 model with 6% radial inflow
validation against Lumped model')
legend('Lumped model','SC03 model')
xlabel('Time (s)')
ylabel('Temperature (K)')
 grid on
```

```
    % let T30 = outlet temp
    T26_IDLE = 344;
    T26_MTO = 440;
    T30_IDLE = 344;
    T30_MTO = 406;
   % Time vector setup
    t = 1:3000;
    t0 = 0;
    t1 = 1005;
    t2 = 2010;
    t3 = 3000;
 pulse_train = ones(1,length(t));
 % MP28 parameters
 tau_drum_idle = 320.31;
Xd_idle = 0.5866;
 tau_drum_accel = 46.65;
Xd_accel=1.0341;
 tau_drum_decel = 198.76;
Xd_decel=1.0790;
 ClosureModel_delay_idle=1;
% speed setup
rpm = rpm_IDLE ...
    + ClosureModel_delay((rpm_MTO-
rpm_IDLE)*pulse_train,t1)...
    - ClosureModel_delay((rpm_MTO-
rpm_IDLE)*pulse_train,t2);
 Trotor_idle = Xd_idle*(T26_IDLE - 291)+291;
Trotor_acel = Xd_accel*(T26_MTO-
T26_IDLE)+291;
Trotor_decel = Xd_decel*(T26_MTO-
T26_IDLE)+291;
 t_drum =
291+[ClosureModel_delay((Trotor_idle-291)*(1-
exp(-(t-t0-
ClosureModel_delay_idle)./(tau_drum_idle))),t0
+ClosureModel_delay_idle)  ...    +
ClosureModel_delay((Trotor_acel-291)*(1-exp(-
(t-t1)./(tau_drum_accel))),t1) ...    -
ClosureModel_delay((Trotor_decel-291)*(1-
exp(-(t-t2)./(tau_drum_decel))),t2)];
 % drum displacement
%d_drum = radius*alphaD'.*t_drum;
 lw = 1; % line width
 %plotting
plot(t,(t_drum),'k','linewidth',lw);
hold on
load MP28_rad.mat
plot(Time6,Temp6)
 title('MP28 - SC03 model with 6% radial inflow
validation against Lumped model')
legend('Lumped model','SC03 model')
xlabel('Time (s)')
ylabel('Temperature (K)')
 grid on
```

APPENDIX 7.1

Thermal boundary conditions for sc03 calibration

The position and definition of the thermal boundary conditions applied in the SC03 model with radial inflow, for the results presented in Chapter 7 are given below.

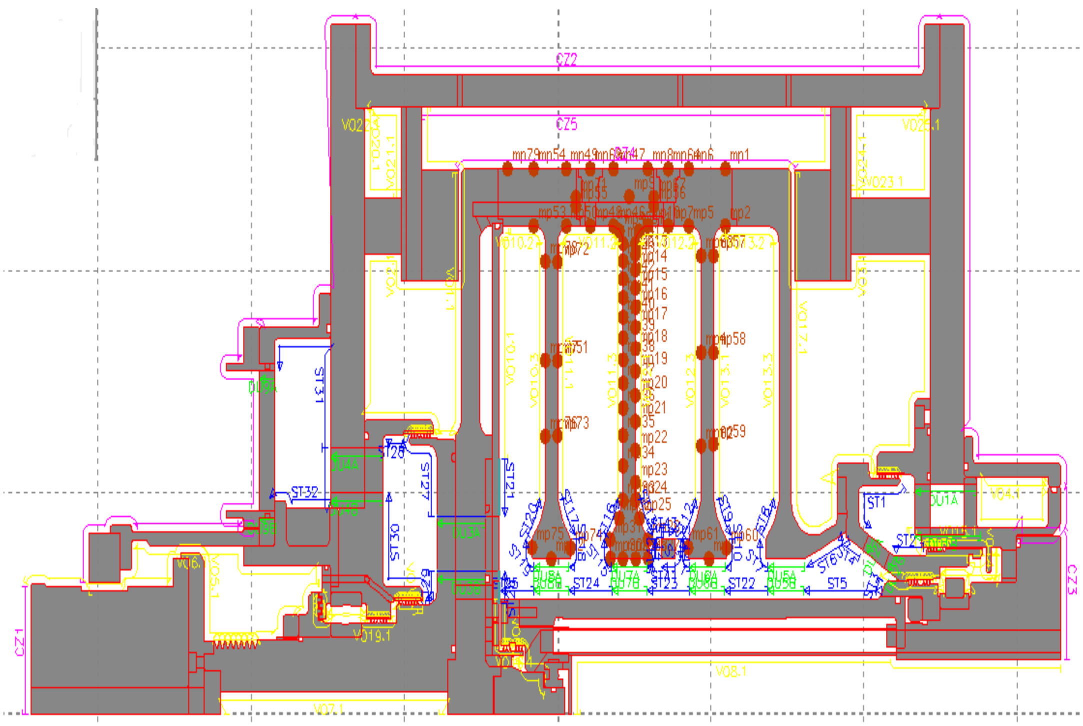

Baseline model

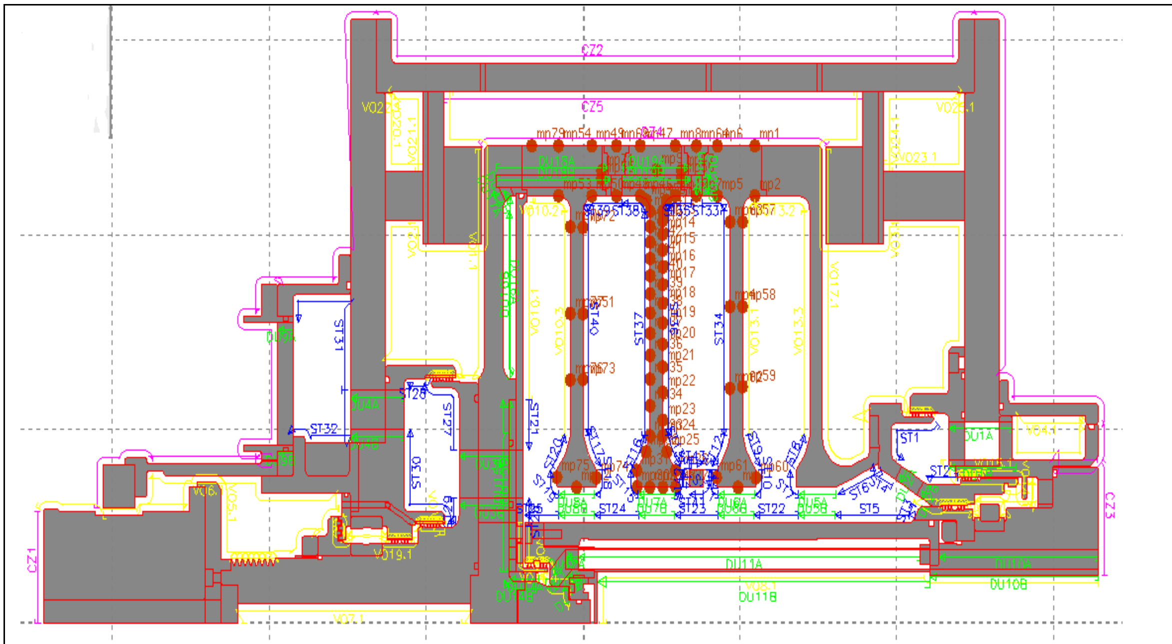

Model with radial inflow

BOUNDARY CONDITIONS	
CONVECTING ZONE	CZ
THERMAL VOID	VO
STREAM	ST
DUCT	DU

```
                    MODEL BOUNDARY CONDITIONS
------------------------------------------------------------------------------

CONVECTING ZONES
----------------

| INDEX          |    1
| FLUID TYPE     |  air
| TEMPERATURE    |  288
| PRESSURE       |  P_amb
| HTC            |  NCY(59)

| INDEX          |    2
| FLUID TYPE     |  air
| TEMPERATURE    |  288
| PRESSURE       |  P_amb
| HTC            |  NVP(1077)

| INDEX          |    3
| FLUID TYPE     |  air
| TEMPERATURE    |  288
| PRESSURE       |  P_amb
| HTC            |  NVP(56)

| INDEX          |    4
| FLUID TYPE     |  air
| TEMPERATURE    |  T_rim
| PRESSURE       |  P_rim
| HTC            |  10000

| INDEX          |    5
| FLUID TYPE     |  air
| TEMPERATURE    |  288
| PRESSURE       |  P_bore
| HTC            |  NVP(370)

| INDEX          |    6
| FLUID TYPE     |  air
| TEMPERATURE    |  288
| PRESSURE       |  P_bore
| HTC            |  NVP(122)

| INDEX          |    7
| FLUID TYPE     |  air
| TEMPERATURE    |  288
| PRESSURE       |  P_bore
| HTC            |  NVP(254)

| INDEX          |    8
| FLUID TYPE     |  air
| TEMPERATURE    |  288
| PRESSURE       |  P_bore
| HTC            |  NVP(145)

| INDEX          |    9
| FLUID TYPE     |  air
| TEMPERATURE    |  288
| PRESSURE       |  P_bore
| HTC            |  0
```

```
THERMAL VOIDS
-------------

 | INDEX        |    4                             | INDEX        |    5
 | SUB-INDEX    |    1                             | SUB-INDEX    |    1
 | FLUID TYPE   |  air                             | FLUID TYPE   |  air
 | VOLUME       |  0                               | VOLUME       |  0
 | POWER INPUT  |  PWR(-1)                         | POWER INPUT  |  PWR(18)
 | PRESSURE     |  P_bore                          | PRESSURE     |  0
 | HTC          |  FRGEND(NH)                      | HTC          |  FRGEND(NH)
 | SWIRL VEL    |  0                               | SWIRL VEL    |  0

 | INDEX        |    6                             | INDEX        |    7
 | SUB-INDEX    |    1                             | SUB-INDEX    |    1
 | FLUID TYPE   |  air                             | FLUID TYPE   |  air
 | VOLUME       |  0                               | VOLUME       |  0
 | POWER INPUT  |  PWR(19)                         | POWER INPUT  |  0
 | PRESSURE     |  0                               | PRESSURE     |  P_bore
 | HTC          |  FRGEND(NH)                      | HTC          |  FRGEND(NH)
 | SWIRL VEL    |  0                               | SWIRL VEL    |  0

 | INDEX        |    8                             | INDEX        |    9
 | SUB-INDEX    |    1                             | SUB-INDEX    |    1
 | FLUID TYPE   |  air                             | FLUID TYPE   |  air
 | VOLUME       |  0                               | VOLUME       |  0
 | POWER INPUT  |  0                               | POWER INPUT  |  PWR(26)
 | PRESSURE     |  0                               | PRESSURE     |  P_bore
 | HTC          |  FRGEND(NI)                      | HTC          |  FRGEND(NH)
 | SWIRL VEL    |  0                               | SWIRL VEL    |  0

 | INDEX        |   10                             | INDEX        |   10
 | SUB-INDEX    |    1                             | SUB-INDEX    |    2
 | FLUID TYPE   |  air                             | FLUID TYPE   |  air
 | VOLUME       |  0                               | VOLUME       |  0
 | POWER INPUT  |  PWR(20)                         | POWER INPUT  |  PWR(20)
 | PRESSURE     |  SP20                            | PRESSURE     |  SP20
 | HTC          |  1.8*NVP(240)                    | HTC          |  1.8*NUS(108)
 | SWIRL VEL    |  0.5*NH*110**2/y                 | SWIRL VEL    |  0.5*NH*110**2/y
```

```
| INDEX          |   10                          | INDEX          |   13
| SUB-INDEX      |    3                          | SUB-INDEX      |    1
| FLUID TYPE     |  air                          | FLUID TYPE     |  air
| VOLUME         |  0                            | VOLUME         |  0
| POWER INPUT    |  PWR(20)                      | POWER INPUT    |  PWR(8)
| PRESSURE       |  SP20                         | PRESSURE       |  SP8
| HTC            |  1.8*NVP(240)                 | HTC            |  1.8*NVP(240)
| SWIRL VEL      |  0.5*NH*110**2/y              | SWIRL VEL      |  0.5*NH*110**2/y

| INDEX          |   13                          | INDEX          |   13
| SUB-INDEX      |    2                          | SUB-INDEX      |    3
| FLUID TYPE     |  air                          | FLUID TYPE     |  air
| VOLUME         |  0                            | VOLUME         |  0
| POWER INPUT    |  PWR(8)                       | POWER INPUT    |  PWR(8)
| PRESSURE       |  SP8                          | PRESSURE       |  SP8
| HTC            |  1.8*NUS(108)                 | HTC            |  1.8*NVP(240)
| SWIRL VEL      |  0.5*NH*110**2/y              | SWIRL VEL      |  0.5*NH*110**2/y

| INDEX          |   14                          | INDEX          |   15
| SUB-INDEX      |    1                          | SUB-INDEX      |    1
| FLUID TYPE     |  air                          | FLUID TYPE     |  air
| VOLUME         |  0                            | VOLUME         |  0
| POWER INPUT    |  PWR(-1)                      | POWER INPUT    |  PWR(2)
| PRESSURE       |  P_bore                       | PRESSURE       |  P_bore
| HTC            |  FRGEND(NH)                   | HTC            |  FRGEND(NH)
| SWIRL VEL      |  0                            | SWIRL VEL      |  0

| INDEX          |   16                          | INDEX          |   18
| SUB-INDEX      |    1                          | SUB-INDEX      |    1
| FLUID TYPE     |  air                          | FLUID TYPE     |  air
| VOLUME         |  0                            | VOLUME         |  0
| POWER INPUT    |  PWR(25)                      | POWER INPUT    |  PWR(29)
| PRESSURE       |  P_bore                       | PRESSURE       |  SP29
| HTC            |  FRGEND(NI)                   | HTC            |  FRGEND(NH)
| SWIRL VEL      |  0                            | SWIRL VEL      |  0

| INDEX          |   19
| SUB-INDEX      |    1
| FLUID TYPE     |  air
| VOLUME         |  0
| POWER INPUT    |  PWR(29)
| PRESSURE       |  SP29
| HTC            |  FRGEND(NH)
| SWIRL VEL      |  0
```

```
STREAMS
-------

 | INDEX         |    1                          | INDEX         |    2
 | FLUID TYPE    |  air                          | FLUID TYPE    |  air
 | MASS FLOW     |  DM1*0.5                      | MASS FLOW     |  DM1*0.5
 | INLET TEMP.   |  T_bore                       | INLET TEMP.   |  T_bore
 | HEAT PICKUP   |  0                            | HEAT PICKUP   |  0
 | PRESSURE      |  P_bore                       | PRESSURE      |  P_bore
 | HTC           |  FRGEND(NH)                   | HTC           |  FRGEND(NH)
 | SWIRL VEL     |  0                            | SWIRL VEL     |  0
 | FLOW VECTOR   |  S                            | FLOW VECTOR   |  S

 | INDEX         |    3                          | INDEX         |    4
 | FLUID TYPE    |  air                          | FLUID TYPE    |  air
 | MASS FLOW     |  DM2*0.5                      | MASS FLOW     |  DM2*0.5
 | INLET TEMP.   |  DT2                          | INLET TEMP.   |  T_bore
 | HEAT PICKUP   |  0                            | HEAT PICKUP   |  0
 | PRESSURE      |  P_bore                       | PRESSURE      |  P_bore
 | HTC           |  FRGEND(NH)                   | HTC           |  FRGEND(NH)
 | SWIRL VEL     |  0                            | SWIRL VEL     |  0
 | FLOW VECTOR   |  S                            | FLOW VECTOR   |  S

 | INDEX         |    5                          | INDEX         |    6
 | FLUID TYPE    |  air                          | FLUID TYPE    |  air
 | MASS FLOW     |  SM3                          | MASS FLOW     |  SM4
 | INLET TEMP.   |  ST3                          | INLET TEMP.   |  ST4
 | HEAT PICKUP   |  0                            | HEAT PICKUP   |  0
 | PRESSURE      |  P_bore                       | PRESSURE      |  P_bore
 | HTC           |  FRGEND(NI)                   | HTC           |  FRGEND(NH)
 | SWIRL VEL     |  0                            | SWIRL VEL     |  0
 | FLOW VECTOR   |  S                            | FLOW VECTOR   |  S


| INDEX         |    7                          | INDEX         |    8
| FLUID TYPE    |  air                          | FLUID TYPE    |  air
| MASS FLOW     |  DM5                          | MASS FLOW     |  SM7
| INLET TEMP.   |  DT5                          | INLET TEMP.   |  ST7
| HEAT PICKUP   |  vorx(nh)                     | HEAT PICKUP   |  vorx(nh)
| PRESSURE      |  P_bore                       | PRESSURE      |  P_bore
| HTC           |  1.35*FRGEND(NH)              | HTC           |  FRGEND(NH)
| SWIRL VEL     |  0                            | SWIRL VEL     |  0
| FLOW VECTOR   |  S                            | FLOW VECTOR   |  S

| INDEX         |    9                          | INDEX         |   10
| FLUID TYPE    |  air                          | FLUID TYPE    |  air
| MASS FLOW     |  SM8                          | MASS FLOW     |  SM9
| INLET TEMP.   |  VT13                         | INLET TEMP.   |  ST9
| HEAT PICKUP   |  -vorx(nh)                    | HEAT PICKUP   |  -vorx(nh)
| PRESSURE      |  P_bore                       | PRESSURE      |  P_bore
| HTC           |  FRGEND(NH)                   | HTC           |  1.35*FRGEND(NH)
| SWIRL VEL     |  0                            | SWIRL VEL     |  0
| FLOW VECTOR   |  S                            | FLOW VECTOR   |  S

| INDEX         |   11                          | INDEX         |   12
| FLUID TYPE    |  air                          | FLUID TYPE    |  air
| MASS FLOW     |  SM12+(0.5*DM6)               | MASS FLOW     |  SM40
| INLET TEMP.   |  ST12+DT6                     | INLET TEMP.   |  ST40
| HEAT PICKUP   |  -vorx(nh)                    | HEAT PICKUP   |  -vorx(nh)
| PRESSURE      |  SP12                         | PRESSURE      |  SP40
| HTC           |  1.35*FRGEND(NH)              | HTC           |  FRGEND(NH)
| SWIRL VEL     |  0                            | SWIRL VEL     |  0
| FLOW VECTOR   |  S                            | FLOW VECTOR   |  S

| INDEX         |   13                          | INDEX         |   14
| FLUID TYPE    |  air                          | FLUID TYPE    |  air
| MASS FLOW     |  SM38                         | MASS FLOW     |  SM13+(0.5*SM23)
| INLET TEMP.   |  ST38                         | INLET TEMP.   |  ST13+ST23
| HEAT PICKUP   |  -vorx(nh)                    | HEAT PICKUP   |  -vorx(nh)
| PRESSURE      |  SP38                         | PRESSURE      |  SP13
| HTC           |  FRGEND(NH)                   | HTC           |  1.35*FRGEND(NH)
| SWIRL VEL     |  0                            | SWIRL VEL     |  0
| FLOW VECTOR   |  S                            | FLOW VECTOR   |  S
```

```
| INDEX         |   15
| FLUID TYPE    |  air
| MASS FLOW     |  DM7
| INLET TEMP.   |  DT7
| HEAT PICKUP   |  vorx(nh)
| PRESSURE      |  DP7
| HTC           |  1.35*FRGEND(NH)
| SWIRL VEL     |  0
| FLOW VECTOR   |  S

| INDEX         |   16
| FLUID TYPE    |  air
| MASS FLOW     |  SM15
| INLET TEMP.   |  ST15
| HEAT PICKUP   |  vorx(nh)
| PRESSURE      |  SP15
| HTC           |  FRGEND(NH)
| SWIRL VEL     |  0
| FLOW VECTOR   |  S

| INDEX         |   17
| FLUID TYPE    |  air
| MASS FLOW     |  SM36
| INLET TEMP.   |  ST36
| HEAT PICKUP   |  -vorx(nh)
| PRESSURE      |  SP36
| HTC           |  FRGEND(NH)
| SWIRL VEL     |  0
| FLOW VECTOR   |  S

| INDEX         |   18
| FLUID TYPE    |  air
| MASS FLOW     |  0.5*SM17
| INLET TEMP.   |  ST17
| HEAT PICKUP   |  -vorx(nh)
| PRESSURE      |  P_bore
| HTC           |  1.35*FRGEND(NH)
| SWIRL VEL     |  0
| FLOW VECTOR   |  S

| INDEX         |   19
| FLUID TYPE    |  air
| MASS FLOW     |  DM8
| INLET TEMP.   |  DT8
| HEAT PICKUP   |  vorx(nh)
| PRESSURE      |  P_bore
| HTC           |  1.35*FRGEND(NH)
| SWIRL VEL     |  0
| FLOW VECTOR   |  S

| INDEX         |   20
| FLUID TYPE    |  air
| MASS FLOW     |  SM19
| INLET TEMP.   |  ST19
| HEAT PICKUP   |  vorx(nh)
| PRESSURE      |  P_bore
| HTC           |  FRGEND(NH)
| SWIRL VEL     |  0
| FLOW VECTOR   |  S

| INDEX         |   21
| FLUID TYPE    |  air
| MASS FLOW     |  SM20
| INLET TEMP.   |  VT10
| HEAT PICKUP   |  -vorx(nh)
| PRESSURE      |  P_bore
| HTC           |  FRGEND(NH)
| SWIRL VEL     |  0
| FLOW VECTOR   |  S

| INDEX         |   22
| FLUID TYPE    |  air
| MASS FLOW     |  DM5
| INLET TEMP.   |  DT5
| HEAT PICKUP   |  0
| PRESSURE      |  P_bore
| HTC           |  FRGEND(NI)
| SWIRL VEL     |  0
| FLOW VECTOR   |  S
```

```
| INDEX        |  23                              | INDEX        |  24
| FLUID TYPE   | air                              | FLUID TYPE   | air
| MASS FLOW    | DM6                              | MASS FLOW    | DM7
| INLET TEMP.  | DT6                              | INLET TEMP.  | DT7
| HEAT PICKUP  | 0                                | HEAT PICKUP  | 0
| PRESSURE     | P_bore                           | PRESSURE     | P_bore
| HTC          | FRGEND(NI)                       | HTC          | FRGEND(NI)
| SWIRL VEL    | 0                                | SWIRL VEL    | 0
| FLOW VECTOR  | S                                | FLOW VECTOR  | S

| INDEX        |  25                              | INDEX        |  26
| FLUID TYPE   | air                              | FLUID TYPE   | air
| MASS FLOW    | DM8                              | MASS FLOW    | SM25
| INLET TEMP.  | DT8                              | INLET TEMP.  | ST25
| HEAT PICKUP  | 0                                | HEAT PICKUP  | 0
| PRESSURE     | P_bore                           | PRESSURE     | P_bore
| HTC          | FRGEND(NI)                       | HTC          | FRGEND(NH)
| SWIRL VEL    | 0                                | SWIRL VEL    | 0
| FLOW VECTOR  | S                                | FLOW VECTOR  | S

| INDEX        |  27                              | INDEX        |  28
| FLUID TYPE   | air                              | FLUID TYPE   | air
| MASS FLOW    | DM3                              | MASS FLOW    | SM27
| INLET TEMP.  | DT3                              | INLET TEMP.  | ST27
| HEAT PICKUP  | 0                                | HEAT PICKUP  | 0
| PRESSURE     | P_bore                           | PRESSURE     | P_bore
| HTC          | FRGEND(NH)                       | HTC          | FRGEND(NH)
| SWIRL VEL    | 0                                | SWIRL VEL    | 0
| FLOW VECTOR  | S                                | FLOW VECTOR  | S

| INDEX        |  29                              | INDEX        |  30
| FLUID TYPE   | air                              | FLUID TYPE   | air
| MASS FLOW    | DM3                              | MASS FLOW    | SM29
| INLET TEMP.  | DT3                              | INLET TEMP.  | ST29
| HEAT PICKUP  | 0                                | HEAT PICKUP  | 0
| PRESSURE     | P_bore                           | PRESSURE     | P_bore
| HTC          | FRGEND(NH)                       | HTC          | FRGEND(NH)
| SWIRL VEL    | 0                                | SWIRL VEL    | 0
| FLOW VECTOR  | S                                | FLOW VECTOR  | S
```

```
| INDEX          |  31
| FLUID TYPE     | air
| MASS FLOW      | DM4
| INLET TEMP.    | DT4
| HEAT PICKUP    | 0
| PRESSURE       | P_bore
| HTC            | FRGEND(NH)
| SWIRL VEL      | 0
| FLOW VECTOR    | S

| INDEX          |  32
| FLUID TYPE     | air
| MASS FLOW      | DM4
| INLET TEMP.    | DT4
| HEAT PICKUP    | 0
| PRESSURE       | P_bore
| HTC            | FRGEND(NH)
| SWIRL VEL      | 0
| FLOW VECTOR    | S

| INDEX          |  33
| FLUID TYPE     | air
| MASS FLOW      | SM16
| INLET TEMP.    | ST16
| HEAT PICKUP    | vorx(nh)
| PRESSURE       | SP16
| HTC            | 1.8*NVP(240)
| SWIRL VEL      | 0
| FLOW VECTOR    | S

| INDEX          |  34
| FLUID TYPE     | air
| MASS FLOW      | SM33
| INLET TEMP.    | ST33
| HEAT PICKUP    | vorx(nh)
| PRESSURE       | SP33
| HTC            | 1.8*NUS(108)
| SWIRL VEL      | 0
| FLOW VECTOR    | S

| INDEX          |  35
| FLUID TYPE     | air
| MASS FLOW      | SM34
| INLET TEMP.    | ST34
| HEAT PICKUP    | -vorx(nh)
| PRESSURE       | SP34
| HTC            | 1.8*NUS(108)
| SWIRL VEL      | 0
| FLOW VECTOR    | S

| INDEX          |  36
| FLUID TYPE     | air
| MASS FLOW      | SM35
| INLET TEMP.    | ST35
| HEAT PICKUP    | -vorx(nh)
| PRESSURE       | SP35
| HTC            | 1.8*NVP(240)
| SWIRL VEL      | 0
| FLOW VECTOR    | S

| INDEX          |  37
| FLUID TYPE     | air
| MASS FLOW      | DM20
| INLET TEMP.    | T_rim +DT20
| HEAT PICKUP    | -vorx(nh)
| PRESSURE       | DP20
| HTC            | 1.8*NUS(108)
| SWIRL VEL      | 0
| FLOW VECTOR    | S

| INDEX          |  38
| FLUID TYPE     | air
| MASS FLOW      | SM37
| INLET TEMP.    | ST37
| HEAT PICKUP    | -vorx(nh)
| PRESSURE       | SP37
| HTC            | 1.8*NVP(240)
| SWIRL VEL      | 0
| FLOW VECTOR    | S

| INDEX          |  39
| FLUID TYPE     | air
| MASS FLOW      | DM20
| INLET TEMP.    | T_rim + DT20
| HEAT PICKUP    | -vorx(nh)
| PRESSURE       | DP20
| HTC            | 1.8*NUS(108)
| SWIRL VEL      | 0
| FLOW VECTOR    | S

| INDEX          |  40
| FLUID TYPE     | air
| MASS FLOW      | SM39
| INLET TEMP.    | ST39
| HEAT PICKUP    | -vorx(nh)
| PRESSURE       | SP39
| HTC            | 1.8*NVP(240)
| SWIRL VEL      | 0
| FLOW VECTOR    | S

| INDEX          |  41
| FLUID TYPE     | air
| MASS FLOW      | DM6
| INLET TEMP.    | DT6
| HEAT PICKUP    | 0
| PRESSURE       | 0
| HTC            | 0
| SWIRL VEL      | 0
| FLOW VECTOR    | S

| INDEX          |  42
| FLUID TYPE     | air
| MASS FLOW      | SM41
| INLET TEMP.    | ST41
| HEAT PICKUP    | 0
| PRESSURE       | 0
| HTC            | 0
| SWIRL VEL      | 0
| FLOW VECTOR    | S

| INDEX          |  43
| FLUID TYPE     | air
| MASS FLOW      | SM42
| INLET TEMP.    | ST42
| HEAT PICKUP    | 0
| PRESSURE       | 0
| HTC            | 0
| SWIRL VEL      | 0
| FLOW VECTOR    | S

| INDEX          |  44
| FLUID TYPE     | air
| MASS FLOW      | SM43
| INLET TEMP.    | ST43
| HEAT PICKUP    | 0
| PRESSURE       | 0
| HTC            | 0
| SWIRL VEL      | 0
| FLOW VECTOR    | S
```

```
DUCTS
-----

 | INDEX          |    1
 | FLUID TYPE     |  air
 | MASS FLOW      |  0.5*W_bore
 | INLET TEMP.    |  T_bore
 | HEAT PICKUP A  |  0
 | PRESSURE A     |  P_bore
 | HTC A          |  MNUN(3139.68,20,39.96,W_bore)
 | HEAT PICKUP B  |  0
 | PRESSURE B     |  P_bore
 | HTC B          |  MNUN(3139.68,20,39.96,W_bore)
 | SWIRL VEL      |  0

 | INDEX          |    2
 | FLUID TYPE     |  air
 | MASS FLOW      |  SM1+SM2
 | INLET TEMP.    |  MIX(1,2,0)
 | HEAT PICKUP A  |  0
 | PRESSURE A     |  P_bore
 | HTC A          |  MNUN(428.88,7,16,W_bore)
 | HEAT PICKUP B  |  0
 | PRESSURE B     |  P_bore
 | HTC B          |  MNUN(428.88,7,16,W_bore)
 | SWIRL VEL      |  0

 | INDEX          |    3
 | FLUID TYPE     |  air
 | MASS FLOW      |  SM21+SM26
 | INLET TEMP.    |  MIX(21,26,0)
 | HEAT PICKUP A  |  0
 | PRESSURE A     |  P_bore
 | HTC A          |  MNUN(3492.01,25,31.96,W_bore)
 | HEAT PICKUP B  |  0
 | PRESSURE B     |  P_bore
 | HTC B          |  MNUN(3492.01,25,31.96,W_bore)
 | SWIRL VEL      |  0

 | INDEX          |    4
 | FLUID TYPE     |  air
 | MASS FLOW      |  SM28+SM30
 | INLET TEMP.    |  MIX(28,30,0)
 | HEAT PICKUP A  |  0
 | PRESSURE A     |  P_bore
 | HTC A          |  MNUN(2764.96,20,34,W_bore)
 | HEAT PICKUP B  |  0
 | PRESSURE B     |  P_bore
 | HTC B          |  MNUN(2764.96,20,34,W_bore)
 | SWIRL VEL      |  0

 | INDEX          |    5
 | FLUID TYPE     |  air
 | MASS FLOW      |  SM5+SM6
 | INLET TEMP.    |  MIX(5,6,0)
 | HEAT PICKUP A  |  0
 | PRESSURE A     |  P_bore
 | HTC A          |  (FRGEND(NH)**2)+MNUN(7586,30,35,W_bore)
 | HEAT PICKUP B  |  0
 | PRESSURE B     |  P_bore
 | HTC B          |  (FRGEND(NI)**2)+MNUN(7586,30,35,W_bore)
 | SWIRL VEL      |  0

 | INDEX          |    6
 | FLUID TYPE     |  air
 | MASS FLOW      |  SM10+SM22
 | INLET TEMP.    |  MIX(10,22,0)
 | HEAT PICKUP A  |  0
 | PRESSURE A     |  P_bore
 | HTC A          |  (FRGEND(NH)**2)+MNUN(7586,30,35,W_bore)
 | HEAT PICKUP B  |  0
 | PRESSURE B     |  P_bore
 | HTC B          |  (FRGEND(NI)**2)+MNUN(7586,30,35,W_bore)
 | SWIRL VEL      |  0


| INDEX          |    7
| FLUID TYPE     |  air
| MASS FLOW      |  MIX(14,23,0)
| INLET TEMP.    |  MIX(14,23,0)
| HEAT PICKUP A  |  0
| PRESSURE A     |  P_bore
| HTC A          |  (FRGEND(NH)**2)+MNUN(7586,30,35,W_bore)
| HEAT PICKUP B  |  0
| PRESSURE B     |  P_bore
| HTC B          |  (FRGEND(NI)**2)+MNUN(7586,30,35,W_bore)
| SWIRL VEL      |  0

| INDEX          |    8
| FLUID TYPE     |  air
| MASS FLOW      |  MIX(18,24,0)
| INLET TEMP.    |  MIX(18,24,0)
| HEAT PICKUP A  |  0
| PRESSURE A     |  P_bore
| HTC A          |  (FRGEND(NH)**2)+MNUN(7586,30,35,W_bore)
| HEAT PICKUP B  |  0
| PRESSURE B     |  P_bore
| HTC B          |  (FRGEND(NI)**2)+MNUN(7586,30,35,W_bore)
| SWIRL VEL      |  0

| INDEX          |    9
| FLUID TYPE     |  air
| MASS FLOW      |  SM31+SM32
| INLET TEMP.    |  MIX(31,32,0)
| HEAT PICKUP A  |  0
| PRESSURE A     |  P_bore
| HTC A          |  MNUN(8329.84,63.5,10,W_bore)
| HEAT PICKUP B  |  0
| PRESSURE B     |  P_bore
| HTC B          |  MNUN(8329.84,63.5,10,W_bore)
| SWIRL VEL      |  0

| INDEX          |   10
| FLUID TYPE     |  air
| MASS FLOW      |  0.06*W_bore
| INLET TEMP.    |  T_radial
| HEAT PICKUP A  |  0
| PRESSURE A     |  P_radial
| HTC A          |  MNUN(314.2,20,107.7,0.06*W_bore)
| HEAT PICKUP B  |  0
| PRESSURE B     |  P_radial
| HTC B          |  MNUN(314.2,20,107.7,0.06*W_bore)
| SWIRL VEL      |  0

| INDEX          |   11
| FLUID TYPE     |  air
| MASS FLOW      |  DM10
| INLET TEMP.    |  DT10
| HEAT PICKUP A  |  0
| PRESSURE A     |  DP10
| HTC A          |  MNUN(314.2,20,224,0.06*W_bore)
| HEAT PICKUP B  |  0
| PRESSURE B     |  DP10
| HTC B          |  MNUN(314.2,20,224,0.06*W_bore)
| SWIRL VEL      |  0

| INDEX          |   12
| FLUID TYPE     |  air
| MASS FLOW      |  DM11
| INLET TEMP.    |  DT11
| HEAT PICKUP A  |  0
| PRESSURE A     |  DP11
| HTC A          |  MNUN(314.2,20,7.9,0.06*W_bore)
| HEAT PICKUP B  |  0
| PRESSURE B     |  DP11
| HTC B          |  MNUN(314.2,20,7.9,0.06*W_bore)
| SWIRL VEL      |  0
```

```
| INDEX          |   13
| FLUID TYPE     |  air
| MASS FLOW      |  DM12
| INLET TEMP.    |  DT12
| HEAT PICKUP A  |  0
| PRESSURE A     |  DP12
| HTC A          |  MNUN(314.2,20,10.5,0.06*W_bore)
| HEAT PICKUP B  |  0
| PRESSURE B     |  DP12
| HTC B          |  MNUN(314.2,20,10.5,0.06*W_bore)
| SWIRL VEL      |  0

| INDEX          |   14
| FLUID TYPE     |  air
| MASS FLOW      |  DM13
| INLET TEMP.    |  DT13
| HEAT PICKUP A  |  0
| PRESSURE A     |  DP13
| HTC A          |  MNUN(78.6,10,16.6,0.06*W_bore)
| HEAT PICKUP B  |  0
| PRESSURE B     |  DP13
| HTC B          |  MNUN(78.6,10,16.6,0.06*W_bore)
| SWIRL VEL      |  0

| INDEX          |   15
| FLUID TYPE     |  air
| MASS FLOW      |  DM14
| INLET TEMP.    |  DT14
| HEAT PICKUP A  |  0
| PRESSURE A     |  DP14
| HTC A          |  MNUN(50.3,8,88.5,0.06*W_bore)
| HEAT PICKUP B  |  0
| PRESSURE B     |  DP14
| HTC B          |  MNUN(50.3,8,88.5,0.06*W_bore)
| SWIRL VEL      |  0

| INDEX          |   16
| FLUID TYPE     |  air
| MASS FLOW      |  DM15
| INLET TEMP.    |  DT15
| HEAT PICKUP A  |  0
| PRESSURE A     |  DP15
| HTC A          |  MNUN(50.3,8,94.4,0.06*W_bore)
| HEAT PICKUP B  |  0
| PRESSURE B     |  DP15
| HTC B          |  MNUN(50.3,8,94.4,0.06*W_bore)
| SWIRL VEL      |  0

| INDEX          |   17
| FLUID TYPE     |  air
| MASS FLOW      |  DM16
| INLET TEMP.    |  DT16
| HEAT PICKUP A  |  0
| PRESSURE A     |  DP16
| HTC A          |  MNUN(85,10.4,7.5,0.06*W_bore)
| HEAT PICKUP B  |  0
| PRESSURE B     |  DP16
| HTC B          |  MNUN(85,10.4,7.5,0.06*W_bore)
| SWIRL VEL      |  0

| INDEX          |   18
| FLUID TYPE     |  air
| MASS FLOW      |  DM17
| INLET TEMP.    |  DT17
| HEAT PICKUP A  |  0
| PRESSURE A     |  DP17
| HTC A          |  MNUN(113.1,12,73.3,0.06*W_bore)
| HEAT PICKUP B  |  0
| PRESSURE B     |  DP17
| HTC B          |  MNUN(113.1,12,73.3,0.06*W_bore)
| SWIRL VEL      |  0

| INDEX          |   19
| FLUID TYPE     |  air
| MASS FLOW      |  DM18
| INLET TEMP.    |  DT18
| HEAT PICKUP A  |  0
| PRESSURE A     |  DP18
| HTC A          |  MNUN(113.1,12,73.3,0.06*W_bore)
| HEAT PICKUP B  |  0
| PRESSURE B     |  DP18
| HTC B          |  MNUN(113.1,12,73.3,0.06*W_bore)
| SWIRL VEL      |  0

| INDEX          |   20
| FLUID TYPE     |  air
| MASS FLOW      |  DM19
| INLET TEMP.    |  DT19+0.2*(T_rim-DT19)
| HEAT PICKUP A  |  0
| PRESSURE A     |  DP19
| HTC A          |  MNUN(154,14,10.5,0.06*W_bore)
| HEAT PICKUP B  |  0
| PRESSURE B     |  DP19
| HTC B          |  MNUN(154,14,10.5,0.06*W_bore)
| SWIRL VEL      |  0
```

APPENDIX 7.2: Model Geometry and Environmental parameters

MODEL GEOMETRY

```
MODEL SIZES
------------------------------------------------------------------------
---------



Geometry Entities
  Type             Active    Total    Max ID
-------------------------------------------
Line                1196      1196      4410
Arc                  263       263      4129
-------------------------------------------
Total:                        1459


Topology Entities
  Type             Active    Total    Max ID
-------------------------------------------
Region               154       154      6980
Open Shell           154       154      6979
Face                 154       154      6977
Loop                2077      2077      6984
Edge                1456      1459      4412
Edge_Vertex         1459      1459      4411
Max edges on a face            161
Max faces on a region            1
-------------------------------------------
Total:                        5457


Mesh Entities
  Type             Active    Total    Max ID
-------------------------------------------
Tri 6              10007     10007     10007
-------------------------------------------
Total:                       10007
Nodes:                                 22504
```

ENVIRONMENT PARAMETERS

```
-----------------------------------------------------------------------

Refs.  Name

  122  NH
   11  NI
    4  T_bore
    4  T_rim
    1  T_radial
   54  P_bore
    1  P_rim
    2  P_radial
   42  W_bore
    0  W_radial
    0  T_amb
    3  P_amb

Number of environment parameters :   12
Number used in expressions       :   10
```

APPENDIX 7.3: MCR drum material

MULTIPLE CAVITY RIG DRUM MATERIAL

```
-----------------------------------------------------------------------
---------
                            MATERIAL QUALITY
-----------------------------------------------------------------------
---------


Material: TFF

Thermal and elastic properties.
Within the temperature range     0.0 to    0.0 minimum data quality was
'E'.
i.e. Quality is unknown.


-----------------------------------------------------------------------
---------
                                 MATERIAL DATA
-----------------------------------------------------------------------
---------

Prefix #  represents material mixture
Prefix ## represents advanced material mixture
```

Material Name TFF ISOTROPIC
WARNING. This is not current COMMIT materials data.
Data quality is unknown.
Zero Strain Ref Temp (deg C) 20.0000
Mass Density (Mg/mm3) 0.442878E-08

T(deg C)	E(MPa)	P.R.	Alpha	K(mW/mm/K)	Cp(mJ/Mg/K)
-200.0	1.3040E+05	3.2000E-01	7.4000E-06	4.1833E+00	5.0100E+08
-180.0	1.2900E+05	3.2000E-01	7.5368E-06	4.4167E+00	5.0500E+08
-160.0	1.2760E+05	3.2000E-01	7.6544E-06	4.6500E+00	5.0900E+08
-140.0	1.2620E+05	3.2000E-01	7.7400E-06	4.8833E+00	5.1300E+08
-120.0	1.2480E+05	3.2000E-01	7.8200E-06	5.1167E+00	5.1700E+08
-100.0	1.2340E+05	3.2000E-01	7.9000E-06	5.3500E+00	5.2100E+08
-80.0	1.2200E+05	3.2000E-01	7.9800E-06	5.5833E+00	5.2500E+08
-60.0	1.2060E+05	3.2000E-01	8.0600E-06	5.8167E+00	5.2900E+08
-40.0	1.1920E+05	3.2000E-01	8.1470E-06	6.0500E+00	5.3300E+08
-20.0	1.1780E+05	3.2000E-01	8.2733E-06	6.2833E+00	5.3700E+08
0.0	1.1640E+05	3.2000E-01	8.4200E-06	6.5167E+00	5.4100E+08
20.0	1.1500E+05	3.2000E-01	8.5600E-06	6.7500E+00	5.4500E+08
40.0	1.1374E+05	3.2000E-01	8.6945E-06	6.9804E+00	5.4889E+08
60.0	1.1266E+05	3.2000E-01	8.8319E-06	7.2228E+00	5.5320E+08
80.0	1.1166E+05	3.2000E-01	8.9558E-06	7.4730E+00	5.5760E+08
100.0	1.1060E+05	3.2000E-01	9.0500E-06	7.7200E+00	5.6200E+08
120.0	1.0948E+05	3.2000E-01	9.1108E-06	7.9600E+00	5.6630E+08
140.0	1.0836E+05	3.2000E-01	9.1570E-06	8.1993E+00	5.7067E+08
160.0	1.0724E+05	3.2000E-01	9.2040E-06	8.4417E+00	5.7540E+08
180.0	1.0612E+05	3.2000E-01	9.2520E-06	8.6862E+00	5.8020E+08
200.0	1.0500E+05	3.2000E-01	9.3000E-06	8.9300E+00	5.8500E+08
220.0	1.0396E+05	3.2000E-01	9.3480E-06	9.1706E+00	5.8980E+08
240.0	1.0295E+05	3.2000E-01	9.3960E-06	9.4098E+00	5.9460E+08
260.0	1.0182E+05	3.2000E-01	9.4440E-06	9.6523E+00	5.9940E+08
280.0	1.0066E+05	3.2000E-01	9.4920E-06	9.9022E+00	6.0420E+08
300.0	9.9500E+04	3.2000E-01	9.5400E-06	1.0150E+01	6.0900E+08
320.0	9.8335E+04	3.2000E-01	9.5915E-06	1.0380E+01	6.1380E+08
340.0	9.7174E+04	3.2000E-01	9.6450E-06	1.0602E+01	6.1860E+08
360.0	9.6034E+04	3.2000E-01	9.6940E-06	1.0844E+01	6.2340E+08
380.0	9.4915E+04	3.2000E-01	9.7420E-06	1.1100E+01	6.2820E+08
400.0	9.3800E+04	3.2000E-01	9.7900E-06	1.1350E+01	6.3300E+08
420.0	9.2680E+04	3.2000E-01	9.8375E-06	1.1590E+01	6.3796E+08
440.0	9.1560E+04	3.2000E-01	9.8854E-06	1.1830E+01	6.4324E+08
460.0	9.0442E+04	3.2000E-01	9.9354E-06	1.2070E+01	6.4880E+08
480.0	8.9291E+04	3.2000E-01	9.9875E-06	1.2311E+01	6.5440E+08
500.0	8.8000E+04	3.2000E-01	1.0040E-05	1.2550E+01	6.6000E+08
520.0	8.6192E+04	3.2000E-01	1.0091E-05	1.2786E+01	6.6560E+08
540.0	8.3776E+04	3.2000E-01	1.0143E-05	1.3022E+01	6.7120E+08
560.0	8.1064E+04	3.2000E-01	1.0198E-05	1.3258E+01	6.7700E+08
580.0	7.8368E+04	3.2000E-01	1.0254E-05	1.3494E+01	6.8385E+08
600.0	7.6000E+04	3.2000E-01	1.0310E-05	1.3730E+01	6.9100E+08
620.0	7.3916E+04	3.2000E-01	1.0366E-05	1.3969E+01	6.9807E+08
640.0	7.1928E+04	3.2000E-01	1.0422E-05	1.4211E+01	7.0532E+08
660.0	7.0000E+04	3.2000E-01	1.0477E-05	1.4448E+01	7.1292E+08
680.0	6.8000E+04	3.2000E-01	1.0528E-05	1.4684E+01	7.2170E+08
700.0	6.6000E+04	3.2000E-01	1.0580E-05	1.4920E+01	7.3100E+08
720.0	6.4000E+04	3.2000E-01	1.0635E-05	1.5156E+01	7.4125E+08
740.0	6.2000E+04	3.2000E-01	1.0691E-05	1.5392E+01	7.5334E+08
760.0	6.0000E+04	3.2000E-01	1.0749E-05	1.5629E+01	7.6765E+08
780.0	5.8000E+04	3.2000E-01	1.0809E-05	1.5873E+01	7.8698E+08

```
 800.0  5.6000E+04  3.2000E-01  1.0870E-05  1.6120E+01  8.1000E+08
 820.0  5.4000E+04  3.2000E-01  1.0933E-05  1.6364E+01  8.3000E+08
 840.0  5.2000E+04  3.2000E-01  1.0997E-05  1.6608E+01  8.5000E+08
 860.0  5.0000E+04  3.2000E-01  1.1063E-05  1.6852E+01  8.7000E+08
 880.0  4.8000E+04  3.2000E-01  1.1131E-05  1.7096E+01  8.9000E+08
 900.0  4.6000E+04  3.2000E-01  1.1200E-05  1.7340E+01  9.1000E+08
--------------------------------------------------------------------
--------
```

APPENDIX 7.4: Time constant and percentage analysis for disc 2 upstream

Time constant reduction analysis for rotating-frame model point MP13						
Flow regimes (% of bore mass flow)	**τ_{accel} (s)**	**% reduction from baseline model**	**Time constant reduction factor**	**τ_{decel} (s)**	**% reduction from baseline model**	**Time constant reduction factor**
Baseline	43.66	0	1	81.25	0	1
2	28.47	34.79	1.53	57.78	28.88	1.41
4	19.36	55.67	2.26	42.31	47.93	1.92
6	16.92	61.26	2.58	37.22	54.19	2.18
8	15.54	64.4	2.81	34.11	58.02	2.38

Time constant reduction analysis for rotating-frame model point MP14						
Flow regimes (% of bore mass flow)	**τ_{accel} (s)**	**% reduction from baseline model**	**Time constant reduction factor**	**τ_{decel} (s)**	**% reduction from baseline model**	**Time constant reduction factor**
Baseline	38.62	0	1	81.96	0	1
2	24.93	35.45	1.55	37.5	54.24	2.19
4	18.02	53.33	2.14	41.96	48.8	1.95
6	15.88	58.88	2.43	36.96	54.9	2.22
8	14.74	61.82	2.62	33.94	58.59	2.41

Time constant reduction analysis for rotating-frame model point MP15						
Flow regimes (% of bore mass flow)	**τ_{accel} (s)**	**% reduction from baseline model**	**Time constant reduction factor**	**τ_{decel} (s)**	**% reduction from baseline model**	**Time constant reduction factor**
Baseline	35.74	0	1	84.79	0	1
2	23.65	33.83	1.51	58.46	31.06	1.45
4	18.05	49.51	1.98	43.29	48.94	1.96
6	16.05	55.08	2.23	38.2	54.95	2.22
8	14.95	58.17	2.39	35.13	58.57	2.41

Time constant reduction analysis for rotating-frame model point MP16						
Flow regimes (% of bore mass flow)	**τ_{accel} (s)**	**% reduction from baseline model**	**Time constant reduction factor**	**τ_{decel} (s)**	**% reduction from baseline model**	**Time constant reduction factor**
Baseline	35.22	0	1	89.87	0	1
2	24.02	31.81	1.47	61.83	31.2	1.45
4	18	48.9	1.96	44.51	50.47	2.02
6	16.05	54.43	2.19	39.22	56.36	2.29
8	14.99	57.46	2.35	36.06	59.87	2.49

Time constant reduction analysis for rotating-frame model point MP17						
Flow regimes (% of bore mass flow)	**τ_{accel} (s)**	**% reduction from baseline model**	**Time constant reduction factor**	**τ_{decel} (s)**	**% reduction from baseline model**	**Time constant reduction factor**
Baseline	35.24	0	1	94	0	1
2	24.1	31.6	1.46	63.63	32.31	1.48
4	18.13	48.54	1.94	46.06	51.01	2.04
6	16.23	53.95	2.17	40.11	57.33	2.34
8	15.17	56.94	2.32	36.87	60.78	2.55

Time constant reduction analysis for rotating-frame model point MP19						
Flow regimes (% of bore mass flow)	**τ_{accel} (s)**	**% reduction from baseline model**	**Time constant reduction factor**	**τ_{decel} (s)**	**% reduction from baseline model**	**Time constant reduction factor**
Baseline	35.56	0	1	101.4	0	1
2	24.46	31.21	1.45	67.37	33.55	1.5
4	18.46	48.1	1.93	49.11	51.57	2.06
6	16.54	53.47	2.15	41.84	58.74	2.42
8	15.5	56.41	2.29	38.49	62.04	2.63

Time constant reduction analysis for rotating-frame model point MP20						
Flow regimes (% of bore mass flow)	**τ_{accel} (s)**	**% reduction from baseline model**	**Time constant reduction factor**	**τ_{decel} (s)**	**% reduction from baseline model**	**Time constant reduction factor**
Baseline	35.99	0	1	105.9	0	1
2	24.82	31.03	1.45	70.03	33.89	1.51
4	18.78	47.83	1.92	50.49	52.33	2.1
6	16.91	53.01	2.13	42.6	59.78	2.49
8	15.87	55.91	2.27	39.2	62.99	2.7

Time constant reduction analysis for rotating-frame model point MP21						
Flow regimes (% of bore mass flow)	**τ_{accel} (s)**	**% reduction from baseline model**	**Time constant reduction factor**	**τ_{decel} (s)**	**% reduction from baseline model**	**Time constant reduction factor**
Baseline	36.69	0	1	112.5	0	1
2	25.17	31.41	1.46	73.37	34.77	1.53
4	18.93	48.4	1.94	52.37	53.44	2.15
6	17.02	53.62	2.16	43.71	61.14	2.57
8	15.97	56.47	2.3	40.23	64.23	2.8

Time constant reduction analysis for rotating-frame model point MP23						
Flow regimes (% of bore mass flow)	**τ_{accel} (s)**	**% reduction from baseline model**	**Time constant reduction factor**	**τ_{decel} (s)**	**% reduction from baseline model**	**Time constant reduction factor**
Baseline	39.18	0	1	140.00	0	1
2	26.12	33.33	1.5	88.94	36.46	1.57
4	19.67	49.79	1.99	59.66	57.38	2.35
6	17.6	55.09	2.23	49.12	64.91	2.85
8	16.52	57.84	2.37	43.39	69.00	3.23

Time constant reduction analysis for rotating-frame model point MP24						
Flow regimes (% of bore mass flow)	**τ_{accel} (s)**	**% reduction from baseline model**	**Time constant reduction factor**	**τ_{decel} (s)**	**% reduction from baseline model**	**Time constant reduction factor**
Baseline	39.89	0	1	155.5	0	1
2	25.97	34.9	1.54	100.8	35.16	1.54
4	18.97	52.44	2.1	66.72	57.1	2.33
6	16.88	57.68	2.36	55.06	64.6	2.82
8	15.82	60.33	2.52	48.01	69.13	3.24

Time constant reduction analysis for rotating-frame model point MP25						
Flow regimes (% of bore mass flow)	**τ_{accel} (s)**	**% reduction from baseline model**	**Time constant reduction factor**	**τ_{decel} (s)**	**% reduction from baseline model**	**Time constant reduction factor**
Baseline	41.23	0	1	170.4	0	1
2	27.11	34.25	1.52	117	31.32	1.46
4	19.08	53.72	2.16	79.11	53.56	2.15
6	16.63	59.66	2.48	62.96	63.04	2.71
8	15.29	62.91	2.7	55.3	67.54	3.08

Time constant reduction analysis for rotating-frame model point MP26						
Flow regimes (% of bore mass flow)	**τ_{accel} (s)**	**% reduction from baseline model**	**Time constant reduction factor**	**τ_{decel} (s)**	**% reduction from baseline model**	**Time constant reduction factor**
Baseline	33.79	0	1	162.5	0	1
2	22.61	33.1	1.49	112.2	30.93	1.45
4	16.47	51.26	2.05	75.5	53.52	2.15
6	14.59	56.83	2.32	60.25	62.91	2.7
8	14.1	58.27	2.4	52.64	67.6	3.09

Time constant reduction analysis for rotating-frame model point MP27						
Flow regimes (% of bore mass flow)	**τ_{accel} (s)**	**% reduction from baseline model**	**Time constant reduction factor**	**τ_{decel} (s)**	**% reduction from baseline model**	**Time constant reduction factor**
Baseline	25.45	0	1	152.5	0	1
2	17.45	31.43	1.46	102.6	32.69	1.49
4	13.75	45.98	1.85	69.57	54.37	2.19
6	12.93	49.2	1.97	56.51	62.94	2.7
8	12.62	50.39	2.02	49.22	67.72	3.1

Time constant reduction analysis for rotating-frame model point MP29						
Flow regimes (% of bore mass flow)	**τ_{accel} (s)**	**% reduction from baseline model**	**Time constant reduction factor**	**τ_{decel} (s)**	**% reduction from baseline model**	**Time constant reduction factor**
Baseline	34.08	0	1	157.9	0	1
2	25.94	23.87	1.31	115.1	27.12	1.37
4	20.39	40.17	1.67	83.52	47.11	1.89
6	17.89	47.51	1.91	69.1	56.24	2.29
8	16.68	51.05	2.04	63.66	59.69	2.48

APPENDIX 7.5: Time constant and percentage analysis for disc 2 upstream

Time constant reduction analysis for rotating-frame model point MP30						
Flow regimes (% of bore mass flow)	**τ_{accel} (s)**	**% reduction from baseline model**	**Time constant reduction factor**	**τ_{decel} (s)**	**% reduction from baseline model**	**Time constant reduction factor**
Baseline	24.76	0	1	151.6	0	1
2	16.3	34.19	1.52	100.9	33.46	1.5
4	12.5	49.5	1.98	65.51	56.8	2.31
6	11.2	54.78	2.21	51.36	66.13	2.95
8	10.48	57.66	2.36	42.86	71.74	3.54

Time constant reduction analysis for rotating-frame model point MP31						
Flow regimes (% of bore mass flow)	**τ_{accel} (s)**	**% reduction from baseline model**	**Time constant reduction factor**	**τ_{decel} (s)**	**% reduction from baseline model**	**Time constant reduction factor**
Baseline	32.54	0	1	161.2	0	1
2	20.77	36.17	1.57	109.2	32.27	1.39
4	14.46	55.56	2.25	70.67	56.15	2.15
6	13.11	59.72	2.48	55.15	65.78	2.75
8	11.41	64.93	2.85	45.48	71.78	3.33

Time constant reduction analysis for rotating-frame model point MP32						
Flow regimes (% of bore mass flow)	**τ_{accel} (s)**	**% reduction from baseline model**	**Time constant reduction factor**	**τ_{decel} (s)**	**% reduction from baseline model**	**Time constant reduction factor**
Baseline	41.12	0	1	170	0	1
2	26.71	35.05	1.54	116.4	31.5	1.46
4	18.28	55.54	2.25	77.88	54.2	2.18
6	15.07	63.34	2.73	61.51	63.8	2.76
8	13.36	67.52	3.08	52.32	69.2	3.25

Time constant reduction analysis for rotating-frame model point MP33						
Flow regimes (% of bore mass flow)	**τ_{accel} (s)**	**% reduction from baseline model**	**Time constant reduction factor**	**τ_{decel} (s)**	**% reduction from baseline model**	**Time constant reduction factor**
Baseline	39.01	0	1	155.7	0	1
2	25.09	35.68	1.55	100.7	35.3	1.55
4	17.98	53.91	2.17	66.43	57.33	2.34
6	15.67	59.83	2.49	54.5	64.99	2.86
8	15.26	60.88	2.56	47.79	69.3	3.26

Time constant reduction analysis for rotating-frame model point MP34						
Flow regimes (% of bore mass flow)	**τ_{accel} (s)**	**% reduction from baseline model**	**Time constant reduction factor**	**τ_{decel} (s)**	**% reduction from baseline model**	**Time constant reduction factor**
Baseline	38.55	0	1	128.1	0	1
2	26.14	32.2	1.47	80.83	36.88	1.58
4	20.09	47.88	1.92	55.56	56.62	2.31
6	18.07	53.14	2.13	46.01	64.07	2.78
8	16.94	56.05	2.28	41.91	67.28	3.06

Time constant reduction analysis for rotating-frame model point MP36						
Flow regimes (% of bore mass flow)	**τ_{accel} (s)**	**% reduction from baseline model**	**Time constant reduction factor**	**τ_{decel} (s)**	**% reduction from baseline model**	**Time constant reduction factor**
Baseline	36.33	0	1	109.1	0	1
2	25.07	30.99	1.45	71.74	34.26	1.52
4	18.95	47.83	1.92	51.63	52.69	2.11
6	17.16	52.76	2.12	43.46	60.18	2.51
8	16.12	55.62	2.25	40.08	63.27	2.72

Time constant reduction analysis for rotating-frame model point MP37						
Flow regimes (% of bore mass flow)	**τ_{accel} (s)**	**% reduction from baseline model**	**Time constant reduction factor**	**τ_{decel} (s)**	**% reduction from baseline model**	**Time constant reduction factor**
Baseline	35.8	0	1	103.1	0	1
2	24.71	30.97	1.45	68.77	33.31	1.5
4	18.71	47.72	1.91	50.01	51.51	2.06
6	16.92	52.74	2.12	42.54	58.75	2.42
8	15.88	55.65	2.25	39.24	61.95	2.63

Time constant reduction analysis for rotating-frame model point MP39						
Flow regimes (% of bore mass flow)	**τ_{accel} (s)**	**% reduction from baseline model**	**Time constant reduction factor**	**τ_{decel} (s)**	**% reduction from baseline model**	**Time constant reduction factor**
Baseline	35.36	0	1	96.01	0	1
2	24.24	31.45	1.46	64.61	32.71	1.49
4	18.29	48.29	1.93	47.12	50.93	2.04
6	16.46	53.44	2.15	40.89	57.41	2.35
8	15.42	56.4	2.29	37.71	60.73	2.55

Time constant reduction analysis for rotating-frame model point MP40						
Flow regimes (% of bore mass flow)	**τ_{accel} (s)**	**% reduction from baseline model**	**Time constant reduction factor**	**τ_{decel} (s)**	**% reduction from baseline model**	**Time constant reduction factor**
Baseline	35.37	0	1	92.17	0	1
2	24.23	31.49	1.46	62.93	31.72	1.46
4	18.15	48.69	1.95	45.46	50.68	2.03
6	16.29	53.93	2.17	40	56.61	2.3
8	15.24	56.91	2.32	36.9	59.96	2.5

Time constant reduction analysis for rotating-frame model point MP41						
Flow regimes (% of bore mass flow)	**τ_{accel} (s)**	**% reduction from baseline model**	**Time constant reduction factor**	**τ_{decel} (s)**	**% reduction from baseline model**	**Time constant reduction factor**
Baseline	35.32	0	1	87.08	0	1
2	23.66	33.01	1.49	59.95	31.16	1.45
4	18.07	48.85	1.96	44.02	49.44	1.98
6	16.16	54.26	2.19	38.99	55.22	2.23
8	15.06	57.36	2.35	36	58.65	2.42

Time constant reduction analysis for rotating-frame model point MP42						
Flow regimes (% of bore mass flow)	**τ_{accel} (s)**	**% reduction from baseline model**	**Time constant reduction factor**	**τ_{decel} (s)**	**% reduction from baseline model**	**Time constant reduction factor**
Baseline	36.54	0	1	83	0	1
2	23.99	34.35	1.52	57.55	30.67	1.44
4	18.29	49.95	2	42.9	48.31	1.93
6	16.37	55.2	2.23	38.07	54.13	2.18
8	15.27	58.2	2.39	35.21	57.58	2.36

Time constant reduction analysis for rotating-frame model point MP44						
Flow regimes (% of bore mass flow)	**τ_{accel} (s)**	**% reduction from baseline model**	**Time constant reduction factor**	**τ_{decel} (s)**	**% reduction from baseline model**	**Time constant reduction factor**
Baseline	49.13	0	1	82.38	0	1
2	33.84	31.12	1.45	59.73	27.5	1.38
4	23.99	51.16	2.05	44.68	45.76	1.84
6	20.17	58.94	2.44	39.67	51.85	2.08
8	18.36	62.63	2.68	36.6	55.57	2.25

APPENDIX 7.6: Time constant and percentage analysis for disc 2 upstream with different percentage (%) radial inflow

Time constant reduction analysis for rotating-frame model point MP12 with radial inflow						
Flow regimes (% of bore mass flow)	**τ_{accel} (s)**	**% reduction from baseline model**	**Time constant reduction factor**	**τ_{decel} (s)**	**% reduction from baseline model**	**Time constant reduction factor**
Baseline	48.92	0	1	81.93	0	1
1.6	32.69	33.18	1.5	61.65	24.75	1.33
2	28.68	41.38	1.71	55.29	32.51	1.48
3	22.25	54.51	2.2	44.29	45.93	1.85
4	18.6	61.98	2.63	38.63	52.85	2.12
6	15.2	68.92	3.22	31.19	61.93	2.63

Time constant reduction analysis for rotating-frame model point MP13 with radial inflow						
Flow regimes (% of bore mass flow)	**τ_{accel} (s)**	**% reduction from baseline model**	**Time constant reduction factor**	**τ_{decel} (s)**	**% reduction from baseline model**	**Time constant reduction factor**
Baseline	43.66	0	1	81.25	0	1
1.6	31.52	27.8	1.39	63.87	21.38	1.27
2	28.28	35.23	1.54	58.51	27.99	1.39
3	22.8	47.77	1.91	49.25	39.38	1.65
4	19.54	55.24	2.23	43.19	46.84	1.88
6	16.4	62.44	2.66	37.18	54.24	2.19

Time constant reduction analysis for rotating-frame model point MP14 with radial inflow						
Flow regimes (% of bore mass flow)	**τ_{accel} (s)**	**% reduction from baseline model**	**Time constant reduction factor**	**τ_{decel} (s)**	**% reduction from baseline model**	**Time constant reduction factor**
Baseline	38.62	0	1	81.96	0	1
1.6	30.73	20.42	1.26	67.53	17.61	1.21
2	28.38	26.51	1.36	62.8	23.38	1.31
3	23.66	38.75	1.63	55.09	32.78	1.49
4	20.66	46.51	1.87	49.65	39.42	1.65
6	17.61	54.41	2.19	42.99	47.54	1.91

Time constant reduction analysis for rotating-frame model point MP15 with radial inflow						
Flow regimes (% of bore mass flow)	**τ_{accel} (s)**	**% reduction from baseline model**	**Time constant reduction factor**	**τ_{decel} (s)**	**% reduction from baseline model**	**Time constant reduction factor**
Baseline	35.74	0	1	84.79	0	1
1.6	30.83	13.73	1.16	73.39	13.45	1.16
2	29.34	17.9	1.22	68.83	18.83	1.23
3	24.87	30.41	1.44	61.43	27.55	1.38
4	22.02	38.4	1.62	56.55	33.31	1.5
6	18.83	47.32	1.9	49.98	41.06	1.7

Time constant reduction analysis for rotating-frame model point MP16 with radial inflow						
Flow regimes (% of bore mass flow)	**τ_{accel} (s)**	**% reduction from baseline model**	**Time constant reduction factor**	**τ_{decel} (s)**	**% reduction from baseline model**	**Time constant reduction factor**
Baseline	35.22	0	1	89.87	0	1
1.6	31.96	9.265	1.1	80.23	10.73	1.12
2	31.27	11.24	1.13	77.38	13.89	1.16
3	27.38	22.28	1.29	69.89	22.23	1.29
4	23.8	32.44	1.48	63.76	29.05	1.41
6	20.46	41.91	1.72	57.12	36.44	1.57

Time constant reduction analysis for rotating-frame model point MP17 with radial inflow						
Flow regimes (% of bore mass flow)	**τ_{accel} (s)**	**% reduction from baseline model**	**Time constant reduction factor**	**τ_{decel} (s)**	**% reduction from baseline model**	**Time constant reduction factor**
Baseline	35.24	0	1	94.00	0	1
1.6	32.21	8.592	1.09	84.23	10.4	1.12
2	31.92	9.406	1.1	82.24	12.51	1.14
3	28.77	18.35	1.22	76.53	18.59	1.23
4	25.11	28.75	1.4	69.63	25.93	1.35
6	21.59	38.74	1.63	61.42	34.66	1.53

Time constant reduction analysis for rotating-frame model point MP18 with radial inflow						
Flow regimes (% of bore mass flow)	**τ_{accel} (s)**	**% reduction from baseline model**	**Time constant reduction factor**	**τ_{decel} (s)**	**% reduction from baseline model**	**Time constant reduction factor**
Baseline	35.34	0	1	97.78	0	1
1.6	32.7	7.472	1.08	87.96	10.04	1.11
2	32.72	7.408	1.08	86.68	11.35	1.13
3	30.19	14.57	1.17	82.49	15.63	1.19
4	26.93	23.79	1.31	76.12	22.15	1.28
6	22.77	35.56	1.55	65.67	32.84	1.49

Time constant reduction analysis for rotating-frame model point MP19 with radial inflow						
Flow regimes (% of bore mass flow)	**τ_{accel} (s)**	**% reduction from baseline model**	**Time constant reduction factor**	**τ_{decel} (s)**	**% reduction from baseline model**	**Time constant reduction factor**
Baseline	35.56	0	1	101.4	0	1
1.6	33.52	5.74	1.06	91.61	9.64	1.11
2	33.76	5.06	1.05	90.94	10.3	1.11
3	31.77	10.66	1.12	88.19	13.01	1.15
4	28.89	18.74	1.23	82.44	18.69	1.23
6	24.13	32.15	1.47	71.8	29.19	1.41

Time constant reduction analysis for rotating-frame model point MP20 with radial inflow						
Flow regimes (% of bore mass flow)	**τ_{accel} (s)**	**% reduction from baseline model**	**Time constant reduction factor**	**τ_{decel} (s)**	**% reduction from baseline model**	**Time constant reduction factor**
Baseline	35.99	0	1	105.90	0	1
1.6	34.05	5.40	1.06	95.42	9.92	1.11
2	34.43	4.35	1.05	95.07	10.24	1.11
3	32.85	8.72	1.1	93.32	11.9	1.14
4	30.28	15.86	1.19	88.02	16.91	1.2
6	25.13	30.17	1.43	77.33	26.99	1.37

Time constant reduction analysis for rotating-frame model point MP21 with radial inflow						
Flow regimes (% of bore mass flow)	**τ_{accel} (s)**	**% reduction from baseline model**	**Time constant reduction factor**	**τ_{decel} (s)**	**% reduction from baseline model**	**Time constant reduction factor**
Baseline	36.69	0	1	112.5	0	1
1.6	35.1	4.33	1.05	100.5	10.62	1.12
2	35.73	2.61	1.03	100.4	10.75	1.12
3	34.33	6.43	1.07	99.48	11.55	1.13
4	32.06	12.63	1.14	94.63	15.87	1.19
6	26.79	26.99	1.37	84.03	25.29	1.34

Time constant reduction analysis for rotating-frame model point MP22 with radial inflow						
Flow regimes (% of bore mass flow)	**τ_{accel} (s)**	**% reduction from baseline model**	**Time constant reduction factor**	**τ_{decel} (s)**	**% reduction from baseline model**	**Time constant reduction factor**
Baseline	37.82	0	1	120.1	0	1
1.6	35.51	6.10	1.06	110.5	8.02	1.09
2	36.25	4.14	1.04	110.9	7.71	1.08
3	34.93	7.63	1.08	109.8	8.59	1.09
4	32.9	12.99	1.15	104.1	13.36	1.15
6	27.7	26.76	1.37	93.64	22.06	1.28

Time constant reduction analysis for rotating-frame model point MP23 with radial inflow						
Flow regimes (% of bore mass flow)	**τ_{accel} (s)**	**% reduction from baseline model**	**Time constant reduction factor**	**τ_{decel} (s)**	**% reduction from baseline model**	**Time constant reduction factor**
Baseline	39.18	0	1	140.0	0	1
1.6	40.24	-2.71	0.97	137.7	1.619	1.02
2	40.72	-3.94	0.96	137.1	2.04	1.02
3	39.43	-0.64	0.99	135.4	3.29	1.03
4	36.25	7.47	1.08	130.7	6.62	1.07
6	31.08	20.68	1.26	119.7	14.5	1.17

Time constant reduction analysis for rotating-frame model point MP24 with radial inflow						
Flow regimes (% of bore mass flow)	**τ_{accel} (s)**	**% reduction from baseline model**	**Time constant reduction factor**	**τ_{decel} (s)**	**% reduction from baseline model**	**Time constant reduction factor**
Baseline	39.89	0	1	155.5	0	1
1.6	46.49	-16.5	0.86	161.3	-3.69	0.96
2	46.67	-17	0.85	160	-2.9	0.97
3	45.41	-13.9	0.88	157.3	-1.15	0.99
4	42.84	-7.41	0.93	152.6	1.866	1.02
6	36.43	8.663	1.09	142.8	8.193	1.09

Time constant reduction analysis for rotating-frame model point MP25 with radial inflow						
Flow regimes (% of bore mass flow)	**τ_{accel} (s)**	**% reduction from baseline model**	**Time constant reduction factor**	**τ_{decel} (s)**	**% reduction from baseline model**	**Time constant reduction factor**
Baseline	41.23	0	1	170.4	0	1
1.6	58.23	-41.2	0.71	197.0	-15.6	0.86
2	57.82	-40.2	0.71	193.7	-13.7	0.88
3	55.48	-34.6	0.74	190.7	-11.9	0.89
4	51.68	-25.4	0.8	183.2	-7.6	0.93
6	46.18	-12	0.89	166.8	2.08	1.02

Time constant reduction analysis for rotating-frame model point MP26 with radial inflow						
Flow regimes (% of bore mass flow)	**τ_{accel} (s)**	**% reduction from baseline model**	**Time constant reduction factor**	**τ_{decel} (s)**	**% reduction from baseline model**	**Time constant reduction factor**
Baseline	33.79	0	1	162.5	0	1
1.6	58.98	-74.5	0.57	203.3	-25.1	0.8
2	57.99	-71.6	0.58	199.0	-22.5	0.82
3	54.51	-61.3	0.62	194.2	-19.5	0.84
4	49.93	-47.8	0.68	184.5	-13.5	0.88
6	43.02	-27.3	0.79	163.2	-0.44	1

Time constant reduction analysis for rotating-frame model point MP27 with radial inflow						
Flow regimes (% of bore mass flow)	**τ_{accel} (s)**	**% reduction from baseline model**	**Time constant reduction factor**	**τ_{decel} (s)**	**% reduction from baseline model**	**Time constant reduction factor**
Baseline	25.45	0	1	152.5	0	1
1.6	50.19	-97.2	0.51	194.4	-27.5	0.78
2	49.48	-94.5	0.51	191.1	-25.4	0.8
3	47.39	-86.2	0.54	188.3	-23.5	0.81
4	44.48	-74.8	0.57	181	-18.7	0.84
6	37.27	-46.5	0.68	163.8	-7.46	0.93

Time constant reduction analysis for rotating-frame model point MP28 with radial inflow						
Flow regimes (% of bore mass flow)	**τ_{accel} (s)**	**% reduction from baseline model**	**Time constant reduction factor**	**τ_{decel} (s)**	**% reduction from baseline model**	**Time constant reduction factor**
Baseline	34.27	1	0	158.2	1	0
1.6	45.29	0.76	-32.1	190.4	0.83	-20.4
2	45.62	0.75	-33.1	190.7	0.83	-20.6
3	46.44	0.74	-35.5	196.2	0.81	-24.1
4	46.8	0.73	-36.6	198.8	0.8	-25.7
6	46.65	0.74	-36.1	198.8	0.8	-25.7

Time constant reduction analysis for rotating-frame model point MP29 with radial inflow						
Flow regimes (% of bore mass flow)	**τ_{accel} (s)**	**% reduction from baseline model**	**Time constant reduction factor**	**τ_{decel} (s)**	**% reduction from baseline model**	**Time constant reduction factor**
Baseline	34.08	0	1	157.9	0	1
1.6	37.72	-10.67	0.904	185.9	-17.69	0.85
2	38.43	-12.75	0.887	186.3	-17.94	0.848
3	40.59	-19.1	0.84	195.5	-23.8	0.808
4	42.54	-24.82	0.801	202.7	-28.34	0.779
6	45.42	-33.28	0.75	210.5	-33.32	0.75

APPENDIX 7.7: Time constant and percentage analysis for disc 2 downstream with different percentage (%) radial inflow

Time constant reduction analysis for rotating-frame model point MP30 with radial inflow						
Flow regimes (% of bore mass flow)	**τ_{accel} (s)**	**% reduction from baseline model**	**Time constant reduction factor**	**τ_{decel} (s)**	**% reduction from baseline model**	**Time constant reduction factor**
Baseline	24.76	0	1	151.6	0	1
1.6	24.29	1.91	1.02	175.6	-15.8	0.86
2	24.75	0.04	1	177.2	-16.9	0.86
3	26.76	-8.09	0.93	188.9	-24.6	0.8
4	29.14	-17.7	0.85	199.3	-31.4	0.76
6	33.11	-33.7	0.75	212.6	-40.2	0.71

Time constant reduction analysis for rotating-frame model point MP31 with radial inflow						
Flow regimes (% of bore mass flow)	**τ_{accel} (s)**	**% reduction from baseline model**	**Time constant reduction factor**	**τ_{decel} (s)**	**% reduction from baseline model**	**Time constant reduction factor**
Baseline	32.54	0	1	161.2	0	1
1.6	32.63	-0.27	1	187.3	-16.3	0.81
2	33.24	-2.13	0.98	188	-16.6	0.81
3	35.16	-8.05	0.93	198.4	-23.1	0.76
4	37.74	-16	0.86	207	-28.4	0.73
6	42.21	-29.7	0.77	217.5	-35	0.7

Time constant reduction analysis for rotating-frame model point MP32 with radial inflow						
Flow regimes (% of bore mass flow)	**τ_{accel} (s)**	**% reduction from baseline model**	**Time constant reduction factor**	**τ_{decel} (s)**	**% reduction from baseline model**	**Time constant reduction factor**
Baseline	41.12	0	1	170	0	1
1.6	47.18	-14.7	0.87	191.4	-12.6	0.89
2	47.72	-16.1	0.86	190.8	-12.2	0.89
3	48.92	-19	0.84	197.4	-16.1	0.86
4	49.67	-20.8	0.83	201	-18.3	0.85
6	50.71	-23.3	0.81	203.9	-20	0.83

Time constant reduction analysis for rotating-frame model point MP33 with radial inflow						
Flow regimes (% of bore mass flow)	**τ_{accel} (s)**	**% reduction from baseline model**	**Time constant reduction factor**	**τ_{decel} (s)**	**% reduction from baseline model**	**Time constant reduction factor**
Baseline	39.01	0	1	155.7	1	0
1.6	36.07	7.53	1.08	158.6	0.98	-1.85
2	36.82	5.6	1.06	159.2	0.98	-2.25
3	38.24	1.98	1.02	165.5	0.94	-6.3
4	38.73	0.7	1.01	169.8	0.92	-9.08
6	38.41	1.52	1.02	175.4	0.89	-12.7

Time constant reduction analysis for rotating-frame model point MP34 with radial inflow						
Flow regimes (% of bore mass flow)	**τ_{accel} (s)**	**% reduction from baseline model**	**Time constant reduction factor**	**τ_{decel} (s)**	**% reduction from baseline model**	**Time constant reduction factor**
Baseline	38.55	0	1	128.1	0	1
1.6	25.34	34.3	1.52	114.1	10.9	1.12
2	26.06	32.4	1.48	116.6	8.92	1.1
3	27.8	27.9	1.39	124	3.21	1.03
4	28.61	25.8	1.35	128.3	-0.14	1
6	28.51	26	1.35	132.5	-3.5	0.97

Time constant reduction analysis for rotating-frame model point MP35 with radial inflow						
Flow regimes (% of bore mass flow)	**τ_{accel} (s)**	**% reduction from baseline model**	**Time constant reduction factor**	**τ_{decel} (s)**	**% reduction from baseline model**	**Time constant reduction factor**
Baseline	37.26	0	1	116.4	0	1
1.6	25.28	32.17	1.47	97.62	16.11	1.19
2	26.05	30.1	1.43	99.32	14.64	1.17
3	27.74	25.55	1.34	106.2	8.73	1.1
4	28.48	23.56	1.31	109.2	6.18	1.07
6	28.42	23.72	1.31	109	6.35	1.07

Time constant reduction analysis for rotating-frame model point MP36 with radial inflow						
Flow regimes (% of bore mass flow)	**τ_{accel} (s)**	**% reduction from baseline model**	**Time constant reduction factor**	**τ_{decel} (s)**	**% reduction from baseline model**	**Time constant reduction factor**
Baseline	36.33	0	1	109.1	0	1
1.6	24.03	33.9	1.51	92.56	15.2	1.18
2	24.69	32	1.47	94.61	13.3	1.15
3	26.38	27.4	1.38	100.2	8.15	1.09
4	27.1	25.4	1.34	102.1	6.44	1.07
6	27.3	24.9	1.33	101.9	6.61	1.07
Time constant reduction analysis for rotating-frame model point MP37 with radial inflow						
Flow regimes (% of bore mass flow)	**τ_{accel} (s)**	**% reduction from baseline model**	**Time constant reduction factor**	**τ_{decel} (s)**	**% reduction from baseline model**	**Time constant reduction factor**
Baseline	35.8	0	1	103.1	0	1
1.6	23.25	35.1	1.54	88.88	13.8	1.16
2	23.99	33	1.49	91.13	11.6	1.13
3	25.45	28.9	1.41	96.66	6.27	1.07
4	26.13	27	1.37	98.46	4.52	1.05
6	26.64	25.6	1.34	98.93	4.06	1.04

Time constant reduction analysis for rotating-frame model point MP38 with radial inflow						
Flow regimes (% of bore mass flow)	**τ_{accel} (s)**	**% reduction from baseline model**	**Time constant reduction factor**	**τ_{decel} (s)**	**% reduction from baseline model**	**Time constant reduction factor**
Baseline	35.47	0	1	99.65	0	1
1.6	22.98	35.21	1.54	86.81	12.88	1.15
2	23.78	32.95	1.49	89.11	10.57	1.12
3	25.12	29.18	1.41	94.24	5.42	1.06
4	25.64	27.71	1.38	95.82	3.84	1.04
6	26.36	25.68	1.35	96.77	2.89	1.03

Time constant reduction analysis for rotating-frame model point MP39 with radial inflow						
Flow regimes (% of bore mass flow)	**τ_{accel} (s)**	**% reduction from baseline model**	**Time constant reduction factor**	**τ_{decel} (s)**	**% reduction from baseline model**	**Time constant reduction factor**
Baseline	35.36	0	1	96.01	0	1
1.6	22.98	35.0	1.54	85.42	11	1.12
2	23.82	32.6	1.48	87.69	8.67	1.09
3	25.09	29	1.41	92.43	3.73	1.04
4	25.56	27.7	1.38	93.91	2.19	1.02
6	26.51	25.0	1.33	95.61	0.42	1

Time constant reduction analysis for rotating-frame model point MP40 with radial inflow						
Flow regimes (% of bore mass flow)	**τ_{accel} (s)**	**% reduction from baseline model**	**Time constant reduction factor**	**τ_{decel} (s)**	**% reduction from baseline model**	**Time constant reduction factor**
Baseline	35.37	0	1	92.17	0	1
1.6	23	35	1.54	83.88	9	1.1
2	23.87	32.5	1.48	86.08	6.61	1.07
3	25.13	28.9	1.41	90.59	1.71	1.02
4	25.7	27.3	1.38	92.3	-0.14	1
6	27.08	23.4	1.31	95.34	-3.43	0.97

Time constant reduction analysis for rotating-frame model point MP41 with radial inflow						
Flow regimes (% of bore mass flow)	**τ_{accel} (s)**	**% reduction from baseline model**	**Time constant reduction factor**	**τ_{decel} (s)**	**% reduction from baseline model**	**Time constant reduction factor**
Baseline	35.32	0	1	87.08	0	1
1.6	23.04	34.8	1.53	82.44	5.32	1.06
2	23.85	32.5	1.48	83.98	3.56	1.04
3	24.91	29.5	1.42	87.45	-0.43	1
4	25.36	28.2	1.39	89.15	-2.39	0.98
6	27.18	23.1	1.3	93.48	-7.35	0.93

Time constant reduction analysis for rotating-frame model point MP42 with radial inflow						
Flow regimes (% of bore mass flow)	**τ_{accel} (s)**	**% reduction from baseline model**	**Time constant reduction factor**	**τ_{decel} (s)**	**% reduction from baseline model**	**Time constant reduction factor**
Baseline	36.54	0	1	83	1	0
1.6	23.83	34.8	1.53	82.6	1	0.48
2	24.42	33.2	1.5	83.13	1	-0.15
3	25.11	31.3	1.45	85.12	0.98	-2.55
4	25.51	30.2	1.43	86.4	0.96	-4.09
6	27.34	25.2	1.34	91.23	0.91	-9.92

Time constant reduction analysis for rotating-frame model point MP43 with radial inflow						
Flow regimes (% of bore mass flow)	**τ_{accel} (s)**	**% reduction from baseline model**	**Time constant reduction factor**	**τ_{decel} (s)**	**% reduction from baseline model**	**Time constant reduction factor**
Baseline	41.19	0	1	81.33	0	1
1.6	25.97	36.95	1.59	84.53	-3.93	0.96
2	26.37	35.98	1.56	84.2	-3.52	0.97
3	26.8	34.94	1.54	85.19	-4.74	0.95
4	27.16	34.07	1.52	86.14	-5.91	0.94
6	28.71	30.3	1.43	91.3	-12.26	0.89

Time constant reduction analysis for rotating-frame model point MP44 with radial inflow						
Flow regimes (% of bore mass flow)	**τ_{accel} (s)**	**% reduction from baseline model**	**Time constant reduction factor**	**τ_{decel} (s)**	**% reduction from baseline model**	**Time constant reduction factor**
Baseline	49.13	1	0	82.38	1	0
1.6	30.97	1.59	37	88.37	0.93	-7.27
2	30.76	1.6	37.4	87.39	0.94	-6.08
3	30.62	1.6	37.7	88.06	0.94	-6.9
4	31.02	1.58	36.9	89.03	0.93	-8.07
6	32.42	1.52	34	94.56	0.87	-14.8

APPENDIX 7. 8: Temperature changes (baseline)
Upstream

MP12	ΔT during acceleration	ΔT during deceleration
Baseline	383.3987	367.1112
2	376.3607	357.4794
4	371.0491	350.1147
6	368.9561	347.1707
8	367.8078	345.5442

MP18	ΔT during acceleration	ΔT during deceleration
Baseline	358.8829	335.8435
2	358.3598	335.0372
4	358.4149	335.1828
6	358.582	335.4405
8	358.6962	335.6345

MP22	ΔT during acceleration	ΔT during deceleration
Baseline	354.4759	331.8785
2	354.76	332.1533
4	355.1623	332.7932
6	355.3985	333.1912
8	355.54	333.4466

MP28	ΔT during acceleration	ΔT during deceleration
Baseline	297.4899	298.0188
2	298.5551	298.7106
4	299.5907	299.6668
6	300.1267	300.1778
8	300.4735	300.5077

Downstream

MP43	ΔT during acceleration	ΔT during deceleration
Baseline	373.8518	354.6189
2	368.5955	347.2484
4	365.0654	342.2711
6	364.0426	340.8077
8	363.5626	340.1099

MP38	ΔT during acceleration	ΔT during deceleration
Baseline	358.1808	335.1219
2	357.8425	334.5786
4	357.9997	334.8709
6	358.1903	335.1585
8	358.3126	335.3686

MP35	ΔT during acceleration	ΔT during deceleration
Baseline	354.9547	332.2637
2	355.1957	332.4983
4	355.5919	333.1051
6	355.8338	333.4951
8	355.9799	333.7415

APPENDIX 7.9: Temperature changes (with radial inflow)

Upstream

MP12	ΔT during acceleration	ΔT during deceleration
Baseline	383.3987	367.1112
1.6	449.7264	421.6951
2	464.914	434.0771
3	494.968	460.9936
4	515.3493	481.5189
6	539.1146	507.9802

MP18	ΔT during acceleration	ΔT during deceleration
Baseline	358.8829	335.8435
1.6	376.4354	350.8253
2	383.6222	356.4496
3	405.6377	374.1686
4	428.1679	393.9515
6	465.8016	430.8752

MP22	ΔT during acceleration	ΔT during deceleration
Baseline	354.4759	331.8785
1.6	360.4488	335.9516
2	363.7687	338.6919
3	376.6539	348.7759
4	392.8429	362.2362
6	425.1802	392.0889

MP28	ΔT during acceleration	ΔT during deceleration
Baseline	352.1386	329.6449
1.6	354.623	331.2778
2	355.9765	332.2606
3	361.1908	336.6104
4	368.1615	342.6659
6	383.467	357.3181

Downstream

MP43	ΔT during acceleration	ΔT during deceleration
Baseline	373.8518	354.6189
1.6	397.78	376.7324
2	405.0016	383.3386
3	421.838	399.9964
4	435.5531	415.062
6	454.694	438.0826

MP38	ΔT during acceleration	ΔT during deceleration
Baseline	358.1808	335.1219
1.6	366.3142	342.3544
2	369.7234	345.3926
3	380.7178	355.3194
4	392.8504	367.299
6	415.2243	391.8723

MP35	ΔT during acceleration	ΔT during deceleration
Baseline	354.9547	332.2637
1.6	359.3219	335.2388
2	361.4434	337.1872
3	369.2082	343.9676
4	378.8484	353.0239
6	398.7607	373.7948

Appendix 7.10

A.7.10. 1: MCR results of disc 2 downstream without radial inflow (baseline model)

The time constant analysis results for disc 2 downstream for model without radial inflow is presented in this section. The rotating-frame model points used are MP43, MP38 and MP35. Figure A.7.10.13 shows the variation of rotating-frame metal temperature with time over the square cycle without radial inflow for disc 2 downstream.

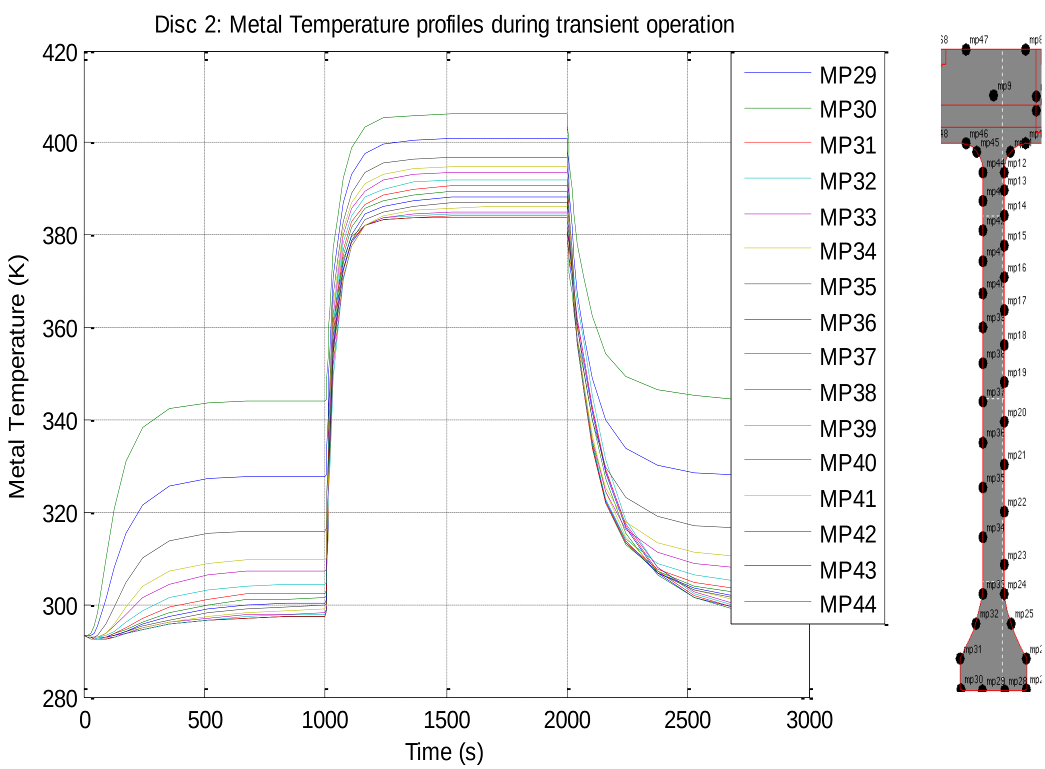

Figure A.7.10.13: The variation of rotating-frame metal temperature with time over the square cycle without radial inflow for disc 2 downstream.

The temperature time characteristic shows an indication of different time constant during acceleration and deceleration for each model point location. As discussed in Section

A.7.10.4.1., the baseline model growth characteristics and time constant analysis for rotating-frame model points were obtained by increasing the inbuilt heat transfer coefficient in the drum cavity and around the disc cob by a factor of 2, 4, 6 and 8.

Figure A.7.10.14 shows the variation of temperature with time for baseline model at MP43 as a function of heat transfer coefficient. Evidence of time constant reduction from the baseline model with increase heat transfer coefficient factor is presented in Table A.7.10.12 in the form percentage reduction and time constant reduction factor.

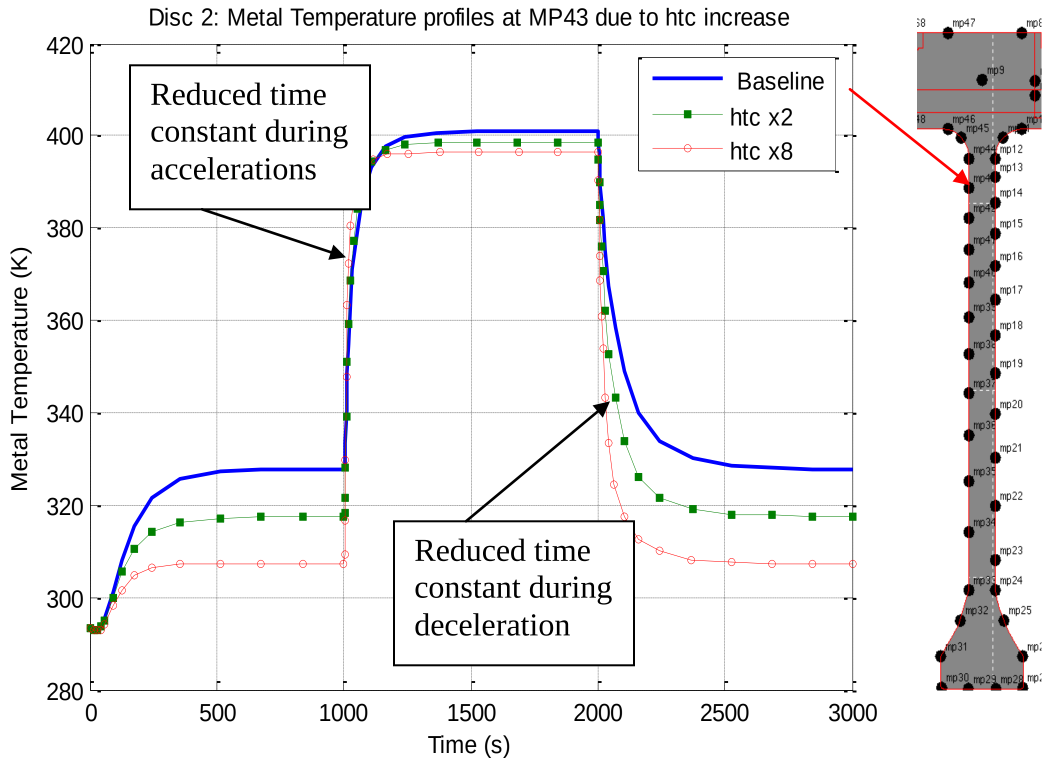

Figure A.7.10.14: The variation of temperature with time for baseline model at MP43 on disc 2 downstream in cavity 2 of the MCR with increase in heat transfer coefficient during engine transient.

During transient operation, there is a temperature change of 368.6K during acceleration from idle to max take-off and a temperature change of 347.2K during deceleration from max take-off to idle for heat transfer increase factor of 2.

The baseline model disc time constant at MP43 is reduced by approximately 36% during acceleration from Idle to MTO conditions and 29% during deceleration from MTO to Idle conditions with a heat transfer coefficient increased factor of 2 calculated against the baseline data.

Time constant reduction analysis for rotating-frame model point MP43						
htc increase factor	**τ_{accel} (s)**	**% reduction from baseline model**	**Time constant reduction factor**	**τ_{decel} (s)**	**% reduction from baseline model**	**Time constant reduction factor**
Baseline	41.19	0	1	81.33	0	1
2	26.28	36.19	1.57	57.38	29.45	1.42
4	18.50	55.09	2.23	41.97	48.40	1.94
6	16.26	60.52	2.53	37.06	54.43	2.20
8	14.96	63.68	2.75	34.16	58.01	2.38

Table A.7.10.12: Time reduction analysis for rotating-frame model point MP43

Time reduction analysis for rotating-frame model point MP38 during engine transient operations is presented in Table A.7.10.13. Figure A.7.10.15 shows the variation of temperature with time for baseline model at MP38 as a function of heat transfer coefficient.

During transient operation, there is a temperature change of 357.8K during acceleration from idle to max take-off and a temperature change of 334.6K during deceleration from max take-off to idle for heat transfer increase factor of 2.

The results indicate a reduction in disc time constant by approximately 31% during acceleration from Idle to MTO conditions and 33% during deceleration from MTO to Idle conditions with a heat transfer coefficient increased factor of 2 calculated against the baseline data.

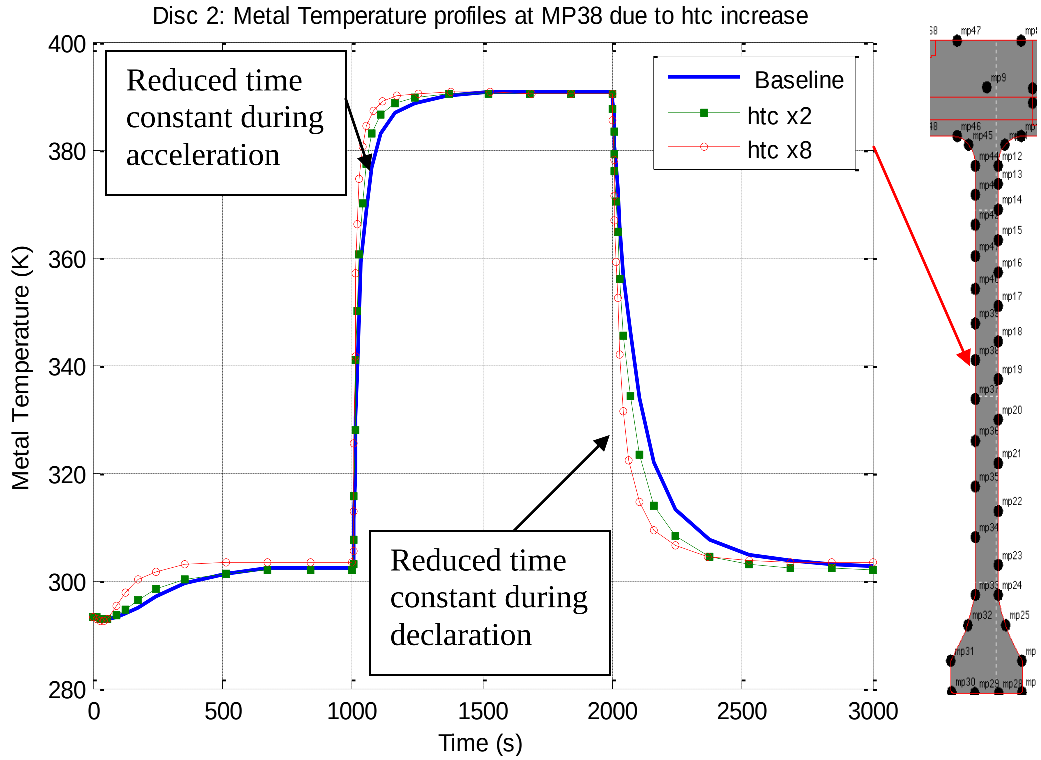

Figure A.7.10.15: The variation of temperature with time for baseline model at MP38 on disc 2 downstream in cavity 2 of the MCR with increase in heat transfer coefficient during engine transient.

Time constant reduction analysis for rotating-frame model point MP38						
htc increase factor	**τ_{accel} (s)**	**% reduction from baseline model**	**Time constant reduction factor**	**τ_{decel} (s)**	**% reduction from baseline model**	**Time constant reduction factor**
Baseline	35.47	0	1	99.65	0	1
2	24.39	31.25	1.46	66.38	33.39	1.50
4	18.44	48.00	1.92	48.64	51.19	2.05
6	16.62	53.15	2.14	41.75	58.10	2.39
8	15.58	56.08	2.28	38.51	61.36	2.59

Table A.7.10.13: Time reduction analysis for rotating-frame model point MP38

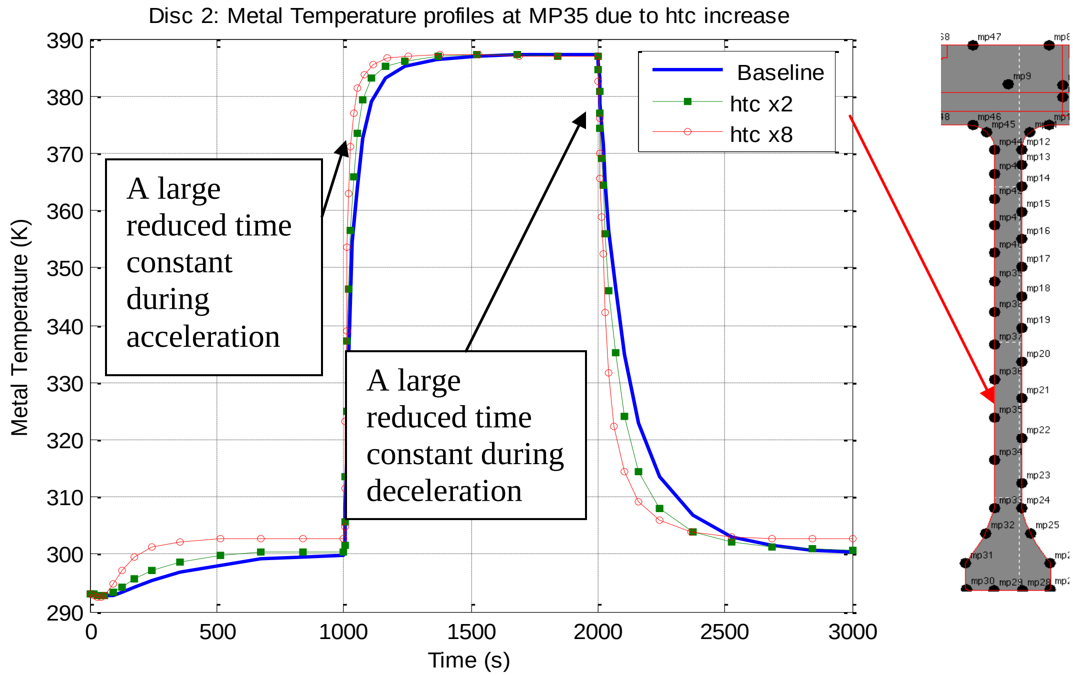

Figure A.7.10.16: The variation of metal temperature with time for baseline model at MP35 on disc 2 downstream in cavity 2 of the MCR with increase in heat transfer coefficient during engine transient.

Time reduction analysis for rotating-frame model point MP35 during engine transient operations is presented in Table A.7.10.14. Figure A.7.10.16 shows the variation of temperature with time for baseline model at MP35 as a function of heat transfer coefficient.

During transient operation, there is a temperature change of 355.2K during acceleration from idle to max take-off and a temperature change of 332.5K during deceleration from max take-off to idle for heat transfer increase factor of 2.

The results show a reduction in disc time constant by approximately 32% during acceleration from Idle to MTO conditions and 35% during deceleration from MTO to

Idle conditions with a heat transfer coefficient increased factor of 2 calculated against the baseline data.

Time constant reduction analysis for rotating-frame model point MP35						
htc increase factor	**τ_{accel} (s)**	**% reduction from baseline model**	**Time constant reduction factor**	**τ_{decel} (s)**	**% reduction from baseline model**	**Time constant reduction factor**
Baseline	37.26	0	1	116.36	0	1
2	25.37	31.92	1.47	75.49	35.13	1.54
4	18.95	49.15	1.97	53.76	53.80	2.16
6	17.00	54.40	2.19	44.73	61.56	2.60
8	16.01	57.05	2.33	41.25	64.55	2.82

Table A.7.10.14: Time reduction analysis for rotating-frame model point MP35

Figure A.7.10.17 shows the time constant reduction factor as a function of heat transfer coefficient for the baseline model during acceleration from "Idle to MTO" and deceleration from "MTO to Idle" over a square cycle for model points MP35, MP38 and MP43 on disc 2 downstream of the MCR drum. For example, the baseline model disc time constant at MP43, MP38 and MP35 has time constant reduction factor of approximately 1.57, 1.46 and 1.47 during acceleration from Idle to MTO which is equivalent to approximately 36%, 31% and 32% reduction respectively with a heat transfer coefficient increased factor of 2 calculated against the baseline data. And approximately 1.42, 1.50 and 1.54 during deceleration from MTO to Idle which is equivalent to approximately 30%, 33% and 35% respectively with a heat transfer coefficient increased factor of 2 calculated against the baseline data. A summary of other results for heat transfer coefficient increased factor of 4, 6 and 8 for model points MP35, MP38 and MP43 during engine transient can be assessed from Table A.7.10.12 through to Table A.7.10.14.

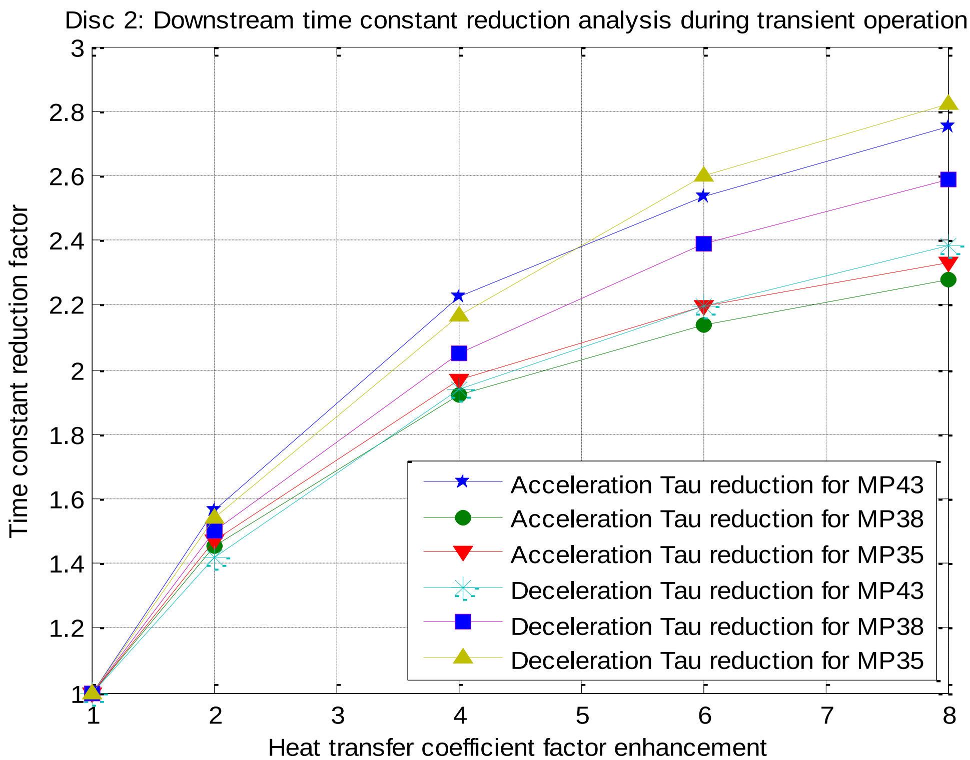

Figure A.7.10.17: Time constant reduction factor as a function of heat transfer coefficient for the baseline model during acceleration from "Idle to MTO" and deceleration from "MTO to Idle" over a square cycle for model points MP35, MP38 and MP43 on disc 2 downstream of the MCR drum.

A.7.10.2 MCR results of disc 2 downstream with radial inflow model

The disc time constant analysis results for disc 2 downstream for model with radial inflow is presented in this section. The rotating-frame model points used are MP43, MP38 and MP35. Figure A.7.10.28 shows the variation of rotating-frame metal temperature with time over the square cycle with 6% radial inflow for disc 2 downstream. This demonstrates the metal temperature profiles during engine transient with radial inflow. The thermal growth characteristic shows different time constant during acceleration and deceleration for each model point location.

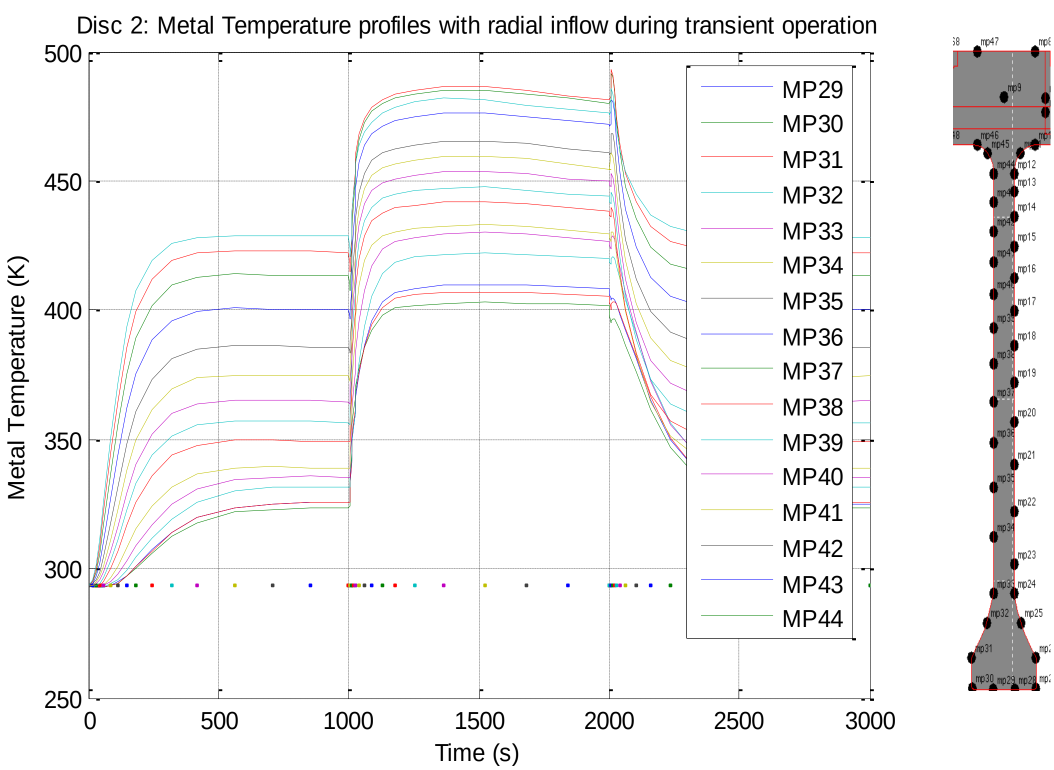

Figure A.7.10.28: The variation of rotating-frame metal temperature with time over the square cycle with 6% radial inflow for disc 2 downstream.

Figure A.7.10.29 shows the variation of temperature with time for radial inflow model disc time constant at MP43. Table A.7.10.19 shows facts of time constant reduction for the radial inflow model with different radial inflow regimes in the form percentage reduction and time constant reduction factor for MP43.

Time constant reduction analysis for rotating-frame model point MP43 with radial inflow						
Flow regimes (% of bore mass flow)	**τ_{accel} (s)**	**% reduction from baseline model**	**Time constant reduction factor**	**τ_{decel} (s)**	**% reduction from baseline model**	**Time constant reductio n factor**
Baseline	41.20	0	1	81.33	0	1
1.6	25.97	36.95	1.60	84.53	-3.93	0.96
2	26.37	35.98	1.56	84.20	-3.52	0.97
3	26.80	34.94	1.54	85.20	-4.74	0.96
4	27.16	34.07	1.52	86.14	-5.91	0.94
6	28.71	30.30	1.44	91.30	-12.26	0.89

Table A.7.10.19: Time reduction analysis for rotating-frame model point MP43 with radial inflow

During transient operation with radial inflow, there is a temperature change of 454.7K during acceleration from idle to max take-off and a temperature change of 438.1K during deceleration from max take-off to idle with a 6 % radial inflow. With radial inflow, the heat transfer is increased leading to a significant reduction the disc time constant during acceleration. For instance, the radial inflow model disc time constant at MP43 is reduced by approximately 30% during acceleration from Idle to MTO conditions with an increase of 12% during deceleration from MTO to Idle conditions with 6% radial inflow calculated against the baseline data. This may be due the chunky thermal mass of outer rim at lower power during deceleration resulting in lower heat transfer coefficients.

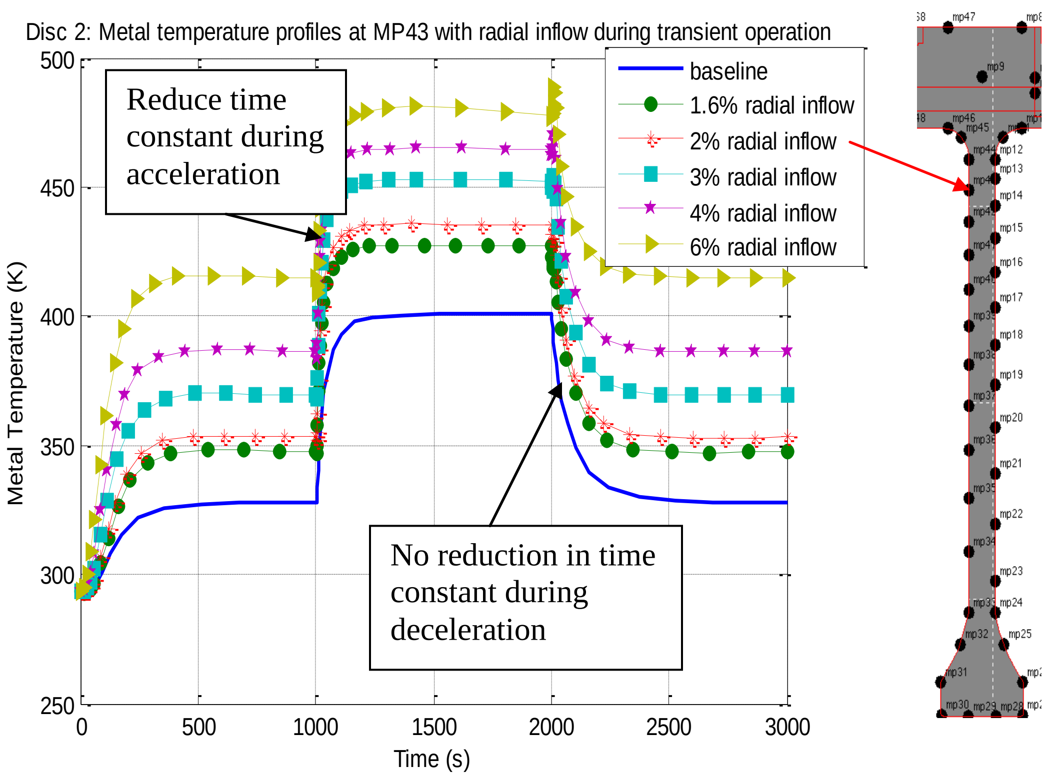

Figure A.7.10.29: The variation of temperature with time for model with radial inflow at model point location MP43 on disc 2 downstream in cavity 2 of the MCR with increase in radial inflow.

Time reduction analysis for rotating-frame model point MP38 during engine transient operations is presented in Table A.7.10.20. Figure A.7.10.30 shows the variation of temperature with time for radial inflow model at MP38. During transient operation with radial inflow, there is a temperature change of 415.2K during acceleration from idle to max take-off and a temperature change of 391.9K during deceleration from max take-off to idle with a 6 % radial inflow. The results indicate a reduction in disc time constant at MP38 by approximately 26% during acceleration from Idle to MTO conditions and 3% during deceleration from MTO to Idle conditions with 6% radial inflow calculated against the baseline data.

Time constant reduction analysis for rotating-frame model point MP38 with radial inflow						
Flow regimes (% of bore mass flow)	**τ_{accel} (s)**	**% reduction from baseline model**	**Time constant reduction factor**	**τ_{decel} (s)**	**% reduction from baseline model**	**Time constant reductio n factor**
Baseline	35.47	0	1	99.65	0	1
1.6	22.98	35.21	1.54	86.81	12.88	1.15
2	23.78	32.95	1.49	89.12	10.57	1.12
3	25.12	29.18	1.41	94.24	5.42	1.06
4	25.64	27.71	1.38	95.82	3.84	1.04
6	26.36	25.68	1.35	96.77	2.90	1.03

Table A.7.10.20: Time reduction analysis for rotating-frame model point MP38 with radial inflow

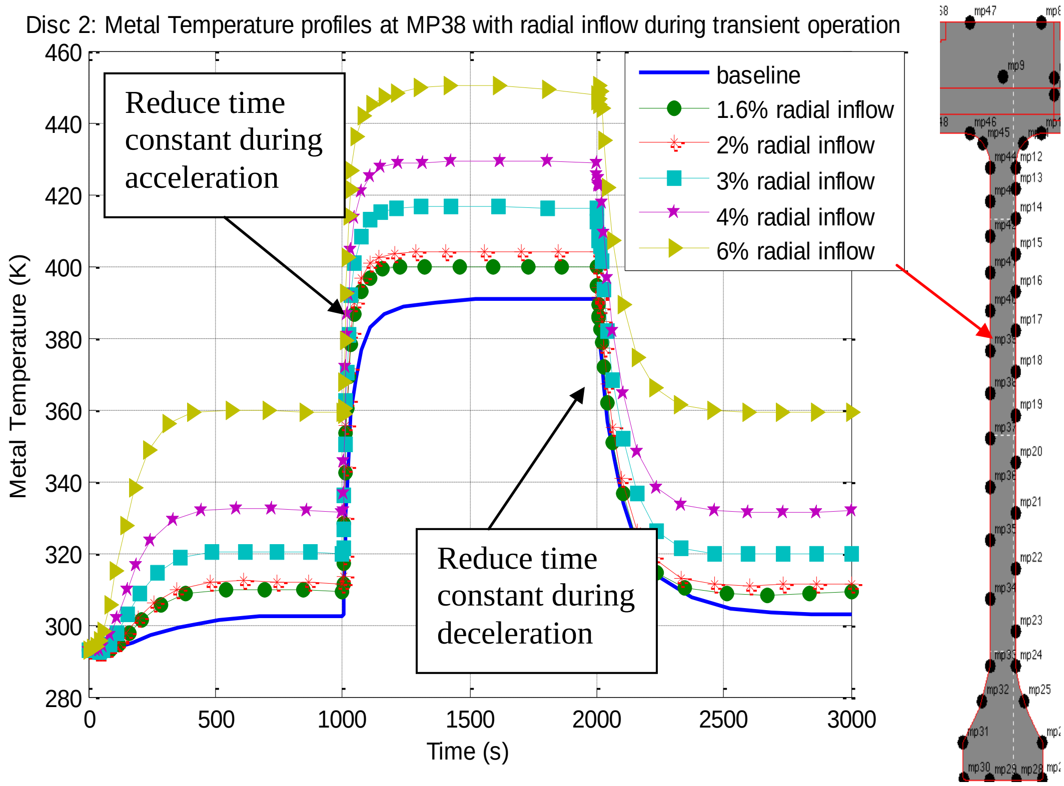

Figure A.7.10.30: The variation of temperature with time for model with radial inflow at model point location MP38 on disc 2 downstream in cavity 2 of the MCR with increase in radial inflow.

Time reduction analysis for rotating-frame model point MP35 during engine transient operations is presented in Table A.7.10.21. Figure A.7.10.31 shows the variation of temperature with time at MP35 for model with radial inflow. During transient operation with radial inflow, there is a temperature change of 398.8K during acceleration from idle to max take-off and a temperature change of 373.8K during deceleration from max take-off to idle with a 6 % radial inflow. The results show a reduction in disc time constant at MP35 by approximately 24% during acceleration from Idle to MTO conditions and 6% during deceleration from MTO to Idle conditions with 6% radial inflow calculated against the baseline data.

Time constant reduction analysis for rotating-frame model point MP35 with radial inflow						
Flow regimes (% of bore mass flow)	**τ_{accel} (s)**	**% reduction from baseline model**	**Time constant reduction factor**	**τ_{decel} (s)**	**% reduction from baseline model**	**Time constant reduction factor**
Baseline	37.26	0	1	116.36	0	1
1.6	25.28	32.17	1.47	97.62	16.11	1.19
2	26.05	30.10	1.43	99.32	14.65	1.17
3	27.74	25.55	1.34	106.21	8.73	1.10
4	28.48	23.56	1.31	109.17	6.18	1.07
6	28.42	23.72	1.31	108.98	6.35	1.07

Table A.7.10.21: Time reduction analysis for rotating-frame model point MP35 with radial inflow

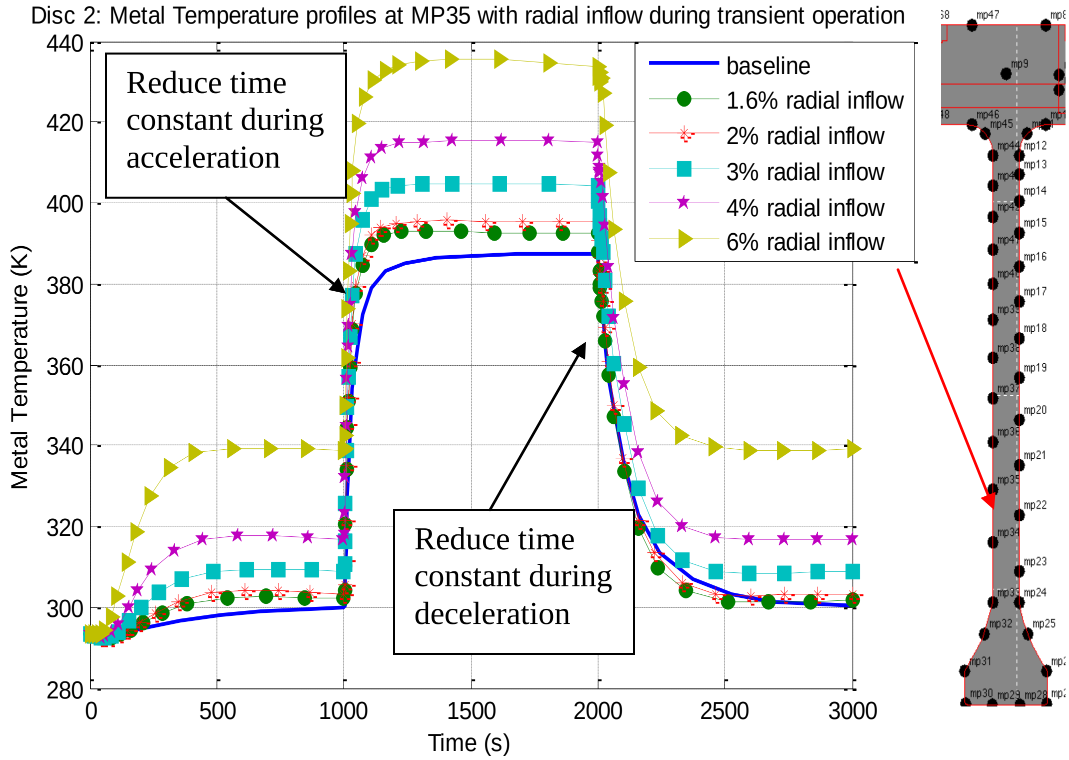

Figure A.7.10.31: The variation of temperature with time for model with radial inflow at model point location MP35 on disc 2 downstream in cavity 2 of the MCR with increase in radial inflow.

Figure A.7.10.32 shows the time constant reduction factor as a function of radial inflow during acceleration from "Idle to MTO" and deceleration from "MTO to Idle" over a square cycle for model points MP35, MP38 and MP43 on disc 2 downstream of the MCR drum. For instance, the radial inflow model disc time constant at MP43, MP38 and MP35 has time constant reduction factor of approximately 1.43, 1.35 and 1.31 respectively during acceleration from Idle to MTO conditions. This is equivalent to approximately 30%, 26%, and 24% reduction respectively calculated against the baseline data. And approximately 0.89, 1.03 and 1.06 respectively during deceleration from MTO to Idle conditions with 6% radial inflow calculated against the baseline data. This is equivalent to approximately 12% increase in time constant with 3%, and 6% reduction respectively calculated against the baseline data. However, 1.6% radial inflow gave a higher time constant reduction during acceleration when compare to other flow regimes at model points MP38 and MP35 but there were no reduction in disc time constant at model point MP43 during deceleration. A summary of other results for radial inflow percentage of 1.6, 2, 3 and 4 for model points MP35, MP38 and MP43 during engine transient can be assessed from Table A.7.10.19 through to Table A.7.10.21.

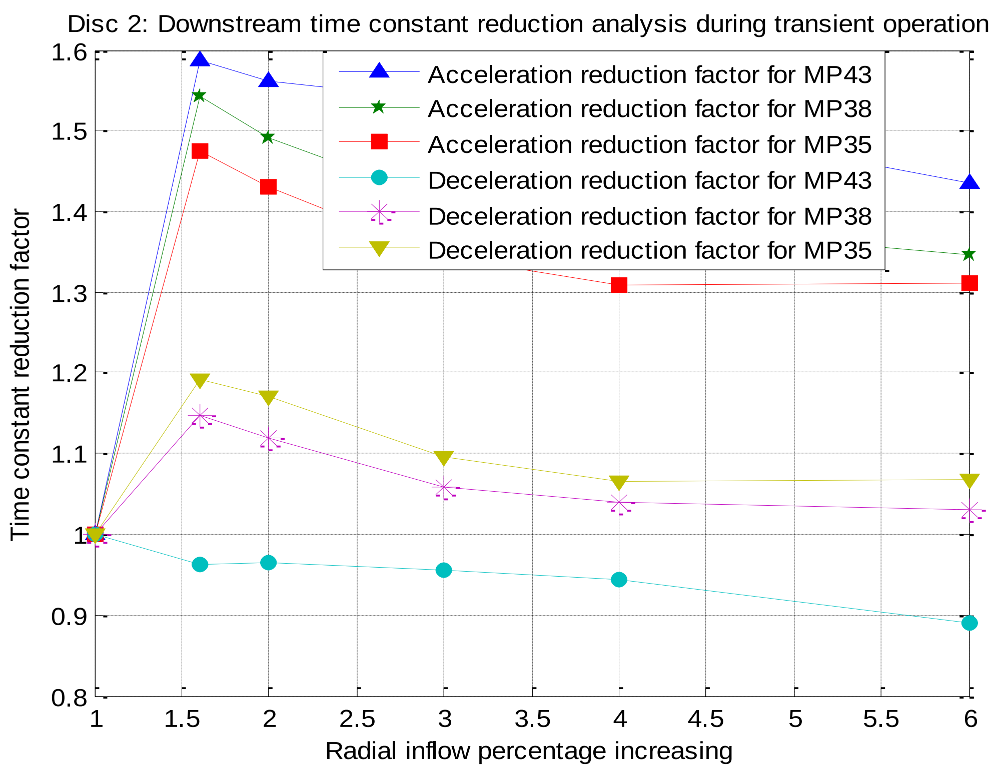

Figure A.7.10.32: Time constant reduction factor as a function of radial inflow during acceleration from "Idle to MTO" and deceleration from "MTO to Idle" over a square cycle for model points MP35, MP38 and MP43 on disc 2 downstream of the MCR drum.

APPENDIX 8: The 40 Inventive Principles

The original forty inventive principles have been adapted for problem solving in gas turbine engine. The forty (40) Inventive Principles and the accompanying examples for gas turbine engines are presented in Appendix 8.

SN	Principles	Examples
1	Segmentation	The arrangement where an axial compressor, a combustor and an axial turbine are integrated to form a gas turbine engine. The partitioning of a gas turbine engine into a compressor, combustor and turbine. The linking of individual arcuate nozzle segments to form a gas turbine nozzle guide vane assembly.
2	Taking out	The removal of combustion products from gas turbine engines. The removal of heat resistant coatings on blades, vanes and liners in gas turbine engines.
3	Local quality	The use of flexible elements capable of withstanding high temperature and pressure fluctuations for gas turbine expansion joints, which are intended to withstand thermal movements and vibration without imposing any loads on the connected components.
4	Asymmetry	The casing housing a compressor with flanges defining passages having an asymmetrical cross section, that are connectable to pipes to provide secondary air to the combustion chamber in a gas turbine engine. The occurrence of non-uniform flow in a compressor due to asymmetric tip clearance in gas turbine engines.
5	Merging	To bring together compressed air and fuel, which are then ignited in the combustor of gas turbine engines, through which energy is added to the gas stream.
6	Universality	The use of a row of stationary blades at the compressor inlet known as the Inlet Guide Vanes (IGV), to ensure that air enters the first-stage rotors at the desired flow angle. These vanes are pitch variable, thus can be adjusted to the varying flow requirements of the engine.

Table A.8: 40 Inventive Principles for Gas turbine engines with examples for each one.

7	Nested doll	The use of a turbine blade damper-seal assembly. This is a seal nested within a damper, such that both the seal and damper are disposed to provide sealing between adjacent blade platforms.
8	Anti-weight	The use of titanium-based alloys for compressor blades, fans blades, discs and hubs for high strength and low weight in gas turbines.
9	Preliminary anti-action	The covering with an abradable material of the casing of a high pressure compressor (HPC) to prevent harmful effects (rubbing) of rotor blades on casing during movement.
10	Preliminary action	The use of auxiliary power units (APU) to provide power to start the main engines of a gas turbine engine.
11	Beforehand cushioning	The use of an internal air system for cooling in gas turbine engines.
12	Equi-potentiality	The operation of a gas turbine engine over a design cycle such as the Square cycle, with different operational conditions at start, idle and maximum take-off.
13	The other way round	The use of radial inflow to increase the heat transfer in a high pressure compressor (HPC) cavity, thereby causing a reduction in the time constant of the drum.
14	Spheroidality-Curvature	The use of ball and roller bearings in gas turbine engines. The use of centrifugal forces to spin rotor blades to compress air inside the compressor in a gas turbine engine.
15	Dynamics	The use of an obturator to selectively regulate hot and cold flow in a gas turbine engine.
16	Partial or excessive actions	The use of high inlet temperature in gas turbines for higher efficiency.
17	Another dimension	The use of an axial compressor with several stages, instead of a centrifugal compressor, to increase engine pressure and efficiency.

Table A.8 (Continued): 40 Inventive Principles for Gas turbine engines with examples for each one.

18	Mechanical vibration	The use of molybdenum coated titanium blades to dampen vibrations on some stages of rotor blades. The detection of failures in gas turbines such as; wear at combustor assembly interfaces, blade rub and Thermal Barrier Coating (TBC) spalling by mechanical vibration. The detection of stall, or surge development in the axial compressor of gas turbine engines by mechanical vibration. The control of stall, or surge development in the axial compressor of gas turbine engines by the measurement of its frequency.
19	Periodic action	The use of ON / OFF type micro switch rub detectors to monitor tip clearance in gas turbine engines. Re-circulation of bleeds in individual compressor cavities to speed rotor response.
20	Continuity of useful action	The continuous ducting of bypass air through slots on the casing to mix with the mainstream flow and reduce clearance in gas turbine engines.
21	Skipping	The rotation of a rotor of a high pressure compressor (HPC) at high rotational speeds for higher efficiency in gas turbines engines. The extraction of air from the intermediate stages of a pressure compressor used for the cooling and sealing of the low pressure turbine stages, thereby diverting it from the main flow, and hence bypassing the high pressure compressor.
22	Blessing in disguise	The use of combustion products by turbines in the form of shaft power to drive the compressor in gas turbine engines and to generate thrust. The use of magnetic attraction to hold abradable dust in the liner of the down-stream stages, thus reducing clearance in service.

Table A.8 (Continued): 40 Inventive Principles for Gas turbine engines with examples for each one.

23	Feedback	The use of an active clearance control mechanism in a gas turbine engine with a proximity sensor for feedback.
24	Intermediary	The use of a thermal lining to insulate the casing from the rotor. Thermal coating on aerofoil to reduce thermal growth.
25	Self-service	The use of combustion products by turbines to generate thrust and shaft power to drive a compressor in gas turbine engines. The use of pressurised air as a seal in aero-engines.
26	Copying	Virtual monitoring of the workings of gas turbine engines via a computer.
27	Cheap short-living objects	The use of ceramic blades for minimal centrifugal force and thermal growth.
28	Mechanics substitution	The application of electrical heating to the casing to modulate tip gap, instead of using mechanical systems such as screw thread devices (actuators) to selectively move axial rotor assemblies to alter the clearance.
29	Pneumatics and hydraulics	The use of a fluid pressure-controlled shroud mechanism for control of the rotor to stator clearance in a gas turbine engine.
30	Flexible shells and thin films	A flexible casing with an actuating system to squeeze it inwards / pull outwards using circumferential wires / bands. The use of a segmented blade tip with slots to increase flexibility and reduce loads during rub.
31	Porous materials	The creation of slots on the casing makes the casing porous, thereby allowing the ducting of bypass air through to mix with the mainstream flow to reduce clearance.
32	Colour changes	The use of a colour coating on turbine blades to resist high temperature (e.g., Ipcote IP9183-R1). The use of coloured layers of abradable material together with borescope testing to check wear in gas turbine engines.

Table A.8 (Continued): 40 Inventive Principles for Gas turbine engines with examples for each one.

33	Homogeneity	To use the same material for the shaft of both the turbine and IP compressor for durability (to reduce wear and tear) when they engage each other during rotation.
34	Discarding and recovering	Gas turbines recover the combustion products from the combustion chambers as shaft power and use it to drive the compressor and other components in gas turbine engines.
35	Parameters	The use of high inlet temperatures in aero-engines for higher efficiency. Increasing the pressure ratio of the compressor in aero-engines for higher efficiency.
36	Phase transitions	Insertion of a thermal ring containing a fluid with a defined thermal capacity, so that the temperature of a key component is maintained at a constant level during the period of the phase transition.
37	Thermal expansion	The application of passive blade tip clearance control in gas-turbine engines. The use of a thermal coating on an aerofoil to reduce thermal growth. The coating of a soft material on the inner surface of the compressor case that can be worn away by the blades as they expand due to the heat generated from compressing the air.
38	Strong oxidants	The use of anti-oxidants to inhibit the formation of peroxide compounds in certain gas turbine fuels. The use of coatings to protect hot components in gas turbine engines.
39	Inert atmosphere	The use of fuel additives in gas turbine engines to control high temperature corrosion of blades and vanes. The addition of fire retardent elements to titanium parts in gas turbines to reduce the possibility of titanium fire.
40	Composite materials	The use of a polymer matrix composite (PMC), such as carbon fibre composites, for fan blades in gas turbines.

Table A.8 (Continued): 40 Inventive Principles for Gas turbine engines with examples for each one.